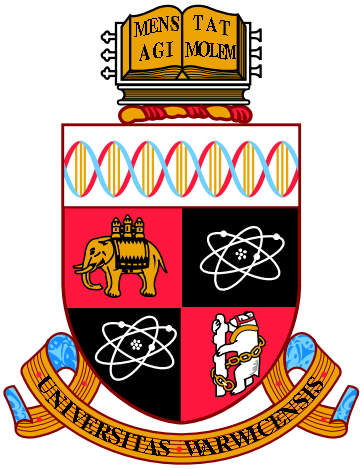

Modelling and interpreting the coupling between coherent nonlinear structures and ambient turbulence in fusion plasmas using approaches derived from the Lotka-Volterra equations

by

Hao Zhu

Thesis

Submitted to the University of Warwick

for the degree of

Doctor of Philosophy

Department of Physics

May 2015

THE UNIVERSITY OF WARWICK

Contents

List of Tables **iv**

List of Figures **v**

Acknowledgments **xvi**

Declarations **xvii**

Abstract **xviii**

Summary **xix**

Chapter 1 Introduction to fusion plasma physics **1**

1.1 Lawson criterion 1
1.2 Fundamental plasma physics 2
1.2.1 Fluid description 2
1.2.2 Magnetohydrodynamics description 8
1.2.3 L-mode 13
1.2.4 H-mode 14
1.2.5 Interactions of drift wave turbulence and zonal flow 17
1.2.6 Heat pulse experiments and anomalous transport 22
1.3 Magnetic confinement fusion devices 26
1.3.1 Tokamaks 26
1.3.2 Stellarators 30
1.4 Instability in Tokamaks 33
1.4.1 Disruption 33
1.4.2 Sawtooth instability 33
1.4.3 Tearing modes 34
1.4.4 Ballooning modes 35
1.4.5 Edge localised modes(ELMs) 36

Chapter 2 Introduction to nonlinear dynamics **38**
2.1 Reviews of reduced models in magnetic confinement fusion 38
2.2 Lotka-Volterra models 41
2.2.1 Lotka-Volterra model 42
2.2.2 Limit cycle manifold 48
2.2.3 Period-doubling bifurcation 51
2.2.4 Chaos 56
2.3 Computational methodology 58
2.3.1 Taylor series solver 58
2.3.2 Other ODE solvers 63
2.3.3 Stiffness 65
2.4 Reduced models for magnetic confinement regimes 67
2.4.1 Model proposed by Malkov et al. 67
2.4.2 Model proposed by Itoh et al. 72
2.5 Reduced models for heat pulse experiments 74
2.5.1 Model proposed by Dendy et al. 74

Chapter 3 Predator-prey models for confinement in fusion plasmas **77**
3.1 Introduction 77
3.2 Modelling confinement transitions 81
3.3 Phase space evolution 86
3.4 Stability analysis in MD and ZCD models 91
3.5 Limit cycle analysis in ZCD model 94
3.6 Conclusions 97

Chapter 4 Heating induced confinement transitions in MD and ZCD models **99**
4.1 Introduction 99
4.2 Analytical confinement properties of the models 102
4.3 Confinement transition induced by heating in MD model 105
4.4 Confinement transition induced by heating in ZCD model 108
4.5 Impact of smoothed changes of external heating flux on MD model . 111
4.6 Impact of oscillating heating rate on ZCD model 113
4.7 Conclusions 118

Chapter 5 Heat pulse model in the Large Helical Device **120**
5.1 Introduction 120
5.2 Travelling wave transformations on the model 123

5.3 Comparison of model results with the LHD experimental data 125
5.4 Conclusion 132

Chapter 6 Conclusion **134**

Chapter 7 Publications during Ph.D. studies **136**
7.1 Peer-reviewed journals 136
7.2 Conference proceedings 136

List of Tables

2.1 The physical meaning of the terms and parameters in the r.h.s of the MD model. 68
2.2 The physical meaning of the terms and parameters in the r.h.s of the II model. 73

3.1 The physical meanings of terms and parameters in r.h.s of ZCD model equations(3.1.1-3.1.4). 79
3.2 Summary of Figs.3.2.1 to 3.3.5 90
3.3 Properties of stability analysis of MD system 94
3.4 Properties of stability analysis of ZCD system 95

5.1 Experimentally inferred parameter values[Dendy et al., 2013] for both T_e rise and T_e drop cases. We have $\partial\kappa_T/\partial x_1 = \partial\kappa_T/\partial x_3$, $\partial\kappa_Q/\partial x_1 = \partial\kappa_Q/\partial x_3$. 126
5.2 Boundary conditions of both T_e rise and T_e drop cases. We have $y_1(\xi = 0) = y_1(\xi = 10)$. 126

List of Figures

1.2.1 Fig.3.4 in [Chen, 1975], the diamagnetic drifts in a cylindrical plasma 7
1.2.2 Fig.2(a) in [Yushmanov et al., 1990], the comparisons of confinement times($\tau_E^{ITER89-P}$ and τ_E^{exp}) in different fusion devices. 14
1.2.3 Fig.7 in [Doyle et al., 2007], the comparison of experimental power threshold for L-H transition with the scaling expression Eq.(1.2.81)[Wesson, 2011]. 15
1.2.4 Fig.3 in [Cheng et al., 2013], the transitions of L-I-H and L-I. 16
1.2.5 Fig.6-13 in [Chen, 1975], the geometry of drift instability in a cylinder. The rectangular region is also shown in Fig.1.2.6. 18
1.2.6 Fig.6-14 in [Chen, 1975], the physical mechanism of drift waves. . . . 19
1.2.7 Fig.3.3 in [Horton et al., 2012], the diagram of the Carnot cycle for ∇T driven drift waves. W is the maximum energy released to the plasma turbulence. 20
1.2.8 Fig.18.2 in [Itoh et al., 1999], the effect of a sheared $\boldsymbol{E} \times \boldsymbol{B}$ flow, $V_{\boldsymbol{E}\times\boldsymbol{B}}$ on a turbulent eddy. (a) illustrates the Cartesian coordinate with magnetic field and shear velocity. (b) the circular turbulent eddy with the size L. (c) distorted turbulent eddy by sheared flow. 21
1.2.9 Fig.1 in [Diamond et al., 2005], classic and new paradigm for plasma turbulence. 22
1.2.10 Fig.1 in [Mantica et al., 1999], the time evolution of electron temperature T_e, the averaged electron density $\bar{n}_e$ and the electron energy stored in the plasmas W_e for RTP discharge r19970224.024. A hydrogen pellet is injected at $t = 0.2054$ second in target plasmas. . . . 23
1.2.11 Fig.1 in [Inagaki et al., 2010], typical electron temperature T_e response to the pellet injection in (a) the local diffusive case (b) the abrupt T_e rise case and (c) the abrupt T_e drop case. 24

1.2.12 Fig.2 in [Inagaki et al., 2010], the bifurcation diagram containing stationary and dynamic state. This is expressed by the relationship between heat flux average by electron density q_e/n_e and electron temperature gradient ∇T_e in the core plasma($\rho = 0.19$) in LHD. The green arrows denote the variation directions. 25
1.3.1 Schematic diagram of a Tokamak device from Wikipedia. 26
1.3.2 Figure 1.6.3 in [Wesson, 2011]. (a) The change of flux through the torus induces toroidal electric field which drives the toroidal current. (b) The flux change is produced by primary winding using a transformer core. 27
1.3.3 Figure 5.2 in [Freidberg, 2007]. The cross section of a Tokamak. . . . 28
1.3.4 Fig.12.3.1 in [Wesson, 2011]. The configuration of the Joint European Torus(JET) Tokamak. 29
1.3.5 Schematic diagram of structure of Stellarator from the Wikipedia. . 31
1.3.6 Comparison of Tokamak and Stellarator from the Wikipedia. 31
1.3.7 Schematic diagram of Large Helical Device(LHD). 32
1.4.1 Fig.7.7.2 in [Wesson, 2011]. Four phases of plasma disruption. 34
1.4.2 Fig.7.6.1 in [Wesson, 2011]. The X-ray emission from (a) the central region (b) the outer region of plasma. 34
1.4.3 Schematic diagram of tearing mode in a poloidal cross section of a Tokamak from Richard Fitzpatrick's report. 35
1.4.4 Fig.6.13.1 in [Wesson, 2011]. Showing the destabilizing curvature on the outer side of the Tokamak and stabilizing on the inner side. . . . 36
1.4.5 Fig.7.17.1 in [Wesson, 2011]. This figure demonstrates the falling in temperature, density and pressure respectively resulting from ELMs in JET. 36

2.2.1 2-ODE Lotka-Volterra model. Defining R as rabbits, F as foxes. Left panel: time series of 2-ODE Lotka-Volterra model. Right panel: phase plot of 2-ODE Lotka-Volterra model. The parameters and initial conditions are given as $\alpha = 1, \beta = 0.1, \gamma = 2, \delta = 0.15, R_0 = 35, F_0 = 40$. 45
2.2.2 Pendulum oscillation model with small angle approximation. Left panel: time series of pendulum oscillation model. Right panel: phase plot of pendulum oscillation model. The parameter and initial conditions are $A = 2, x_0 = 0, v_0 = 1.2$. 47

2.2.3 Pendulum oscillation model with large angle. Left panel: time series of pendulum oscillation model. Right panel: phase plot of pendulum oscillation model. The parameter and initial conditions are $A = 2, x_0 = 0, v_0 = 2.8$. 47
2.2.4 Pendulum oscillation model in critical angle condition. Left panel: time series of pendulum oscillation model. Right panel: phase plot of pendulum oscillation model. The parameter and initial conditions are $A = 2, x_0 = 0, v_0 = 2.8285$. 48
2.2.5 Figure 7.0.1 in [Strogatz, 2014]. Three types of limit cycles, which are stable limit cycle, unstable limit cycle and half-stable limit cycle. 49
2.2.6 Van der Pol oscillation model. Left Panel: time series of Van der Pol oscillation model. Right Panel: phase plot of Van der Pol oscillation model. The parameter and initial conditions are $\eta = 2, x_0 = 0, v_0 = 1.2$. 50
2.2.7 Van der Pol oscillation model. Left panel: time series of Van der Pol oscillation model. Right panel: phase plot of Van der Pol oscillation model. The parameter and initial conditions are $\eta = 8, x_0 = 0, v_0 = 1.2$. 50
2.2.8 Figure 7.1.4 and Figure 7.1.5 in [Strogatz, 2014]. Numerical solution of Van der Pol equation for $\eta = 1.5$ and starting from $(\dot{x}, x) = (0.5, 0)$ at $t = 0$. 51
2.2.9 Figure 1.1 in [Hilborn, 1994]. The inductor-diode circuit. $i(t)$ is the electric current. $V_d(t)$ is the electric potential difference across the diode. 52
2.2.10 Figure 1.3 in [Hilborn, 1994]. The time series of diode voltage. Upper panel shows period-1, while lower panel illustrates period-2. 52
2.2.11 Figure 1.4 in [Hilborn, 1994]. The time series of diode voltage. Upper panel shows period-4, while lower panel indicates period-8. 53
2.2.12 Figure 1.5 in [Hilborn, 1994]. Upper panel is period-4 time series of diode voltage. Lower panel is the corresponding time series of current. 53
2.2.13 Figure 1.6 in [Hilborn, 1994]. Diode voltage as a function of time. Both of upper and lower panels are no longer periodic. 54
2.2.14 Figure 1.7 in [Hilborn, 1994]. Upper panel is period-3 time series of diode voltage. Lower panel is the signal generator voltage as a function of time. 54
2.2.15 Figure 1.8 in [Hilborn, 1994]. Bifurcation diagram for the diode circuit. 55
2.2.16 Figure 1.9 in [Hilborn, 1994]. Another bifurcation diagram for a smaller signal generator amplitude. 56

2.2.17 Lorenz chaotic model. Left panel: irregular time series of Lorenz chaotic model. Right panel: phase plot of Lorenz chaotic model in the type of butterfly. The parameters and initial conditions are $\sigma = 10, b = \frac{8}{3}, r = 28, x_0 = z_0 = 0, y_0 = 1$. 57
2.2.18 Reconstruction of phase plot of Lorenz attractor with Takens' Theorem. 58
2.3.1 Deviations of the constant of motion in Eq.(2.2.18) with various fixed step sizes. 61
2.3.2 Bifurcation diagram in Chapter 4.4 with step size $\delta t = 0.5$ 61
2.3.3 Bifurcation diagram in Chapter 4.4 with step size $\delta t = 0.1$ 62
2.3.4 Bifurcation diagram in Chapter 4.4 with step size $\delta t = 0.01$ 62
2.3.5 Bifurcation diagram in Chapter 4.4 with step size $\delta t = 0.001$. This figure is from Fig.4.6.6 in Chapter 4.4. 63
2.3.6 Fig.17.1.3 in [Press, 2007]. For fourth-order Runge-Kutta method, in each step the derivative is evaluated four times. 64
2.3.7 Fig.17.3.1 in [Press, 2007]. This is extrapolation used in the Bulirsch-Stoer method. A large interval H is spanned by various sequences of finer and finer substeps. 65
2.4.1 Fig.2 in [Malkov and Diamond, 2009]. Upper panel indicates time evolution of E(normalised micro-scale turbulence intensity) and N(normalised electron temperature gradient). Lower panel demonstrates the time series of U(energy of zonal flow). The system starts from overpowered H-mode then unstable L-mode then transient oscillatory T-mode. . . 69
2.4.2 Fig.3 in [Malkov and Diamond, 2009]. Limit cycle oscillation of E(normalised micro-scale turbulence intensity), N(normalised electron temperature gradient) and U(energy of zonal flow) when $q = 0.58$. 70
2.4.3 Fig.4 in [Malkov and Diamond, 2009]. Collapse of limit cycle oscillation and transition to quiescent H-mode(QH-mode), in which only N(normalised electron temperature gradient) exists when $q = 0.582$. 70
2.4.4 Fig.6 in [Malkov and Diamond, 2009]. The external heating rate slowly varies from $q = 0.47$(stable L-mode) to $q = 0.62$(stable QH-mode) and back. It is found that the final state is not identical with the initial state, which is identified as hysteresis of the dynamical system. 71
2.4.5 Fig.7 in [Malkov and Diamond, 2009]. The average and oscillatory parts of q value are 0.54 and 0.08 respectively. The modulation frequency ω is 0.31. The time evolutions of E, U and N indicate apparent irregularity when applying periodic external heating flux. 71

2.5.1 Fig.1 in [Dendy et al., 2013], time series of normalised (a)$\delta\nabla T_e$, (b)δq and (c)δT_e for the T_e rise case in LHD in $\rho = 0.19$. Blue lines are experimental data and red lines are model outputs. Parameters are: $\chi_0 = 3.2\mathrm{m}^2\mathrm{s}^{-1}$, $T_{e0} = 3.5\mathrm{keV}$, $L_c = 1.1\mathrm{m}$, $\kappa_{T0} = 15, \partial\kappa_T/\partial x_1 = \partial\kappa_T/\partial x_3 = 1.5, \kappa_{Q0} = 225, \partial\kappa_Q/\partial x_1 = \partial\kappa_Q/\partial x_3 = 22.5, \gamma_{L1} = \gamma_{L2} = 35$ and $\eta/\tau_c\chi_0 = 10.5$. 75

2.5.2 Fig.2 in [Dendy et al., 2013], time series of normalised (a)$\delta\nabla T_e$, (b)δq and (c)δT_e for the T_e drop case in LHD in $\rho = 0.19$. Blue lines are experimental data and red lines are model outputs. Parameters are: $\chi_0 = 2.4\mathrm{m}^2\mathrm{s}^{-1}$, $T_{e0} = 2.9\mathrm{keV}$, $L_c = 1.1\mathrm{m}$, $\kappa_{T0} = 20, \partial\kappa_T/\partial x_1 = \partial\kappa_T/\partial x_3 = 2.0, \kappa_{Q0} = 400, \partial\kappa_Q/\partial x_1 = \partial\kappa_Q/\partial x_3 = 40, \gamma_{L1} = \gamma_{L2} = 35$ and $\eta/\tau_c\chi_0 = 10.5$. 76

3.2.1 Upper panel: From a state near overpowered H-mode to unstable H-mode then to unstable L-mode then to T-mode. Lower panel: Transition to T-mode for U_1 and U_2 showing intersection at $t \simeq 750$ time units followed by gradual energy reversal. The model parameters are $\nu_1 = 19$, $\nu_2 = 1.01\nu_1$, $\eta_1 = 0.12$, $\eta_2 = 1.01\eta_1$, $q = 0.47$, $\rho = 0.55$, $\sigma = 0.6$, $\zeta = 1.7$. 82

3.2.2 Upper panel: Transition from unstable fixed point state(T-mode) to unstable limit cycle oscillation state. Lower panel: Zoomed in version from $t = 300$ to $t = 800$. The model parameters are $\nu_1 = 19$, $\nu_2 = 0.01\nu_1$, $\eta_1 = 0.12$, $\eta_2 = 0.1\eta_1$, $q = 0.47$, $\rho = 0.55$, $\sigma = 0.6$, $\zeta = 1.7$. 83

3.2.3 Burst energy transfer from U_2 to U_1 during strong nonlinear oscillation, followed by limit cycle oscillation in N, E and U_1. The model parameters are $\nu_1 = 19$, $\nu_2 = 1.01\nu_1$, $\eta_1 = 0.12$, $\eta_2 = 1.01\eta_1$, $q = 0.58$, $\rho = 0.55$, $\sigma = 0.6$, $\zeta = 1.7$. 83

3.2.4 Upper panel: Collapse of limit cycle in N, E and U_1. Lower panel: Stair increasing of U_2 between every two pulses. The model parameters are $\nu_1 = 19$, $\nu_2 = 0.01\nu_1$, $\eta_1 = 0.12$, $\eta_2 = 0.01\eta_1$, $q = 0.58$, $\rho = 0.55$, $\sigma = 0.6$, $\zeta = 1.7$. 84

3.2.5 Upper panel: Collapse of limit cycle with positively correlated growth of pulses of U_1 and U_2. Lower panel: Zoomed in version from $t = 240$ to $t = 400$. The model parameters are $\nu_1 = 19$, $\nu_2 = 1.0001\nu_1$, $\eta_1 = 0.12$, $\eta_2 = 1.0001\eta_1$, $q = 0.582$, $\rho = 0.55$, $\sigma = 0.6$, $\zeta = 1.7$. . . . 85

3.2.6 Evolution to the finite N attractor for different η_2 values. Upper panel: $\eta_2 = 0.05$. Middle upper panel: $\eta_2 = 0.06$. Middle lower panel: $\eta_2 = 0.10$. Lower panel: $\eta_2 = 0.11$. The remaining parameters are identical: $\nu_1 = 19$, $\nu_2 = 1.001\nu_1$, $\eta_1 = 0.12$, $q = 0.582$, $\rho = 0.55$, $\sigma = 0.6$, $\zeta = 1.7$. 85
3.3.1 First panel: Fig.2 in MD. The parameters are $\nu = 19$, $\eta = 0.12$, $q = 0.47$, $\rho = 0.55$, $\sigma = 0.6$, $\zeta = 1.7$. Second panel: Projection of first panel on E-U plane. Third panel: Phase plot of Fig.3.2.1. Last panel: Phase plot of Fig.3.2.1 with 81 initial conditions. Stars denote initial values, blue dots denote trajectories and red diamonds denote final states. 87
3.3.2 First panel: Projection of Fig.2 in MD on E-U plane. The parameters are $\nu = 19$, $\eta = 0.12$, $q = 0.47$, $\rho = 0.55$, $\sigma = 0.6$, $\zeta = 1.7$. Second panel: Phase plot of Fig.3.2.2. Last panel: Phase plot of Fig.3.2.2 with 81 initial conditions. Stars denote initial values, blue dots denote trajectories and red diamonds denote final states. 88
3.3.3 First panel: Fig.3 in MD. The parameters are $\nu = 19$, $\eta = 0.12$, $q = 0.58$, $\rho = 0.55$, $\sigma = 0.6$, $\zeta = 1.7$. Second panel: Projection of first panel on E-U plane. Third panel: Phase plot of Fig.3.2.3. Last panel: Phase plot of Fig.3.2.3 with 81 initial conditions. Stars denote initial values, blue dots denote trajectories and red diamonds denote final states. 88
3.3.4 First panel: Projection of Fig.3 in MD on E-U plane. The parameters are $\nu = 19$, $\eta = 0.12$, $q = 0.58$, $\rho = 0.55$, $\sigma = 0.6$, $\zeta = 1.7$. Middle panel: Phase plot of Fig.3.2.4. Last panel: Phase plot of Fig.3.2.4 with 81 initial conditions. Stars denote initial values, blue dots denote trajectories and red diamonds denote final states. 89
3.3.5 First panel: Phase plot for Fig.4 of MD. Second panel: Projection of Fig.4 in MD on E-U plane. The parameters are $\nu = 19$, $\eta = 0.12$, $q = 0.582$, $\rho = 0.55$, $\sigma = 0.6$, $\zeta = 1.7$. Third panel: Phase plot of Fig.3.2.5. Last panel: Phase plot of Fig.3.2.5 with 81 initial conditions. Stars denote initial values, blue dots denote trajectories and red diamonds denote final states. 90
3.3.6 Time series of Fig.3.2.2 in Chapter 3.2, annotated in light of Fig.3.3.7. 91
3.3.7 Phase plot of Fig.3.3.2 in Chapter 3.2. 91
3.5.1 Parameter space of ν_2/ν_1 and η_2/η_1 when $q = 0.47$. 96
3.5.2 Parameter space of ν_2/ν_1 and η_2/η_1 when $q = 0.58$. 96

3.5.3 Parameter space of ν_2/ν_1 and η_2/η_1 when $q = 0.582$. 97

4.2.1 KD/MD model dependence of ratios of confinement time τ_{QH}/τ_T (blue stars; left scale) and temperature gradient N_{QH}/N_T (red crosses; right scale) on the normalised increase in heating rate $\delta q/q_0$. Solid line for τ_{QH}/τ_T is inferred from Eqs.(4.2.5) and (4.2.6). Points are obtained from numerical results for $\delta q = 0.495$, $\tau_{QH} = 1.8182$, q_0 values are shown in figure; other parameter values are $\nu = 19$, $\eta = 0.12$, $\rho = 0.55$, $\sigma = 0.6$, $\zeta = 1.7$. 103

4.2.2 ZCD model dependence of ratios of confinement time τ_{QH}/τ_O (blue stars; left scale) and temperature gradient N_{QH}/N_O (red crosses; right scale) on the normalised increase in heating rate $\delta q/q_0$. Solid line is inferred from Eqs.(4.2.4) and (4.2.9). Points are obtained from numerical results for $\delta q = 0.20$, $\tau_{QH} = 1.8182$, q_0 values are shown in figure; other parameter values are $\nu_1 = 19$, $\nu_2 = 0.19$, $\eta_1 = 0.12$, $\eta_2 = 0.012$, $\rho = 0.55$, $\sigma = 0.6$, $\zeta = 1.7$. 104

4.3.1 Time traces and phase space evolution for the KD/MD model, Eqs(4.1.1) to (4.1.3), with a discontinuous increase in heating rate q by amount $\delta q = 0.16$ from $q_0 = 0.45$ at $t = 2000$ time units; q reverts to q_0 at $t = 3000$ time units. Upper left plot shows time traces of variables N (black), q (dashed magenta), U (red) and E (green). Lower left plot shows time trace of energy confinement time τ_c defined by Eq.(4.2.1). Right plot shows time evolution of the system in (N, E, U) phase space. The sequence of key phases is labelled in all three plots in this Figure as follows. A is the initial transient evolution from the over-powered H-mode point I, leading to convergent cyclic motion towards fixed point attractor B corresponding to T-mode. At C the instantaneous increase in heating rate q induces rapid departure from the T-mode attractor B to the QH-mode (increased N; $E = U = 0$) attractor D with improved confinement time. Instantaneous reversion of q to initial value q_0 brings the end of phase D and results in immediate transition to a QH-mode by exponential decrease in N, labelled E, with a lower value of N and the same confinement time as phase D. There is later a spontaneous back transition from E at $t = 4000$ time units, followed by convergent cyclic motion F to the T-mode attractor B. 106

4.3.2 As Fig.4.3.1, for the case where $q_0 = 0.47$. The major difference is the longer duration of the post-heating QH-mode phase E, after reversion of q to its initial value. 107
4.3.3 As Fig.4.3.2, for the case where $q_0 = 0.49$. The major difference is that the back transition from the post-heating QH-mode phase E, which is not a stable attractor, has not yet occurred by the end of this run. 108
4.4.1 As Fig.4.3.1, for the two-predator ZCD model, Eqs(4.1.4) to (4.1.7), with a sharp heating transition where $q_0 = 0.45$, $\delta q = 0.16$. The second predator field U_2 is traced in blue in the upper left plot. The major difference from Fig.4.3.1 is that the post-heating T-mode state F is a repulsive fixed point, from which the system spontaneously transitions and converges cyclically to the fixed point G. This is known from [Zhu et al., 2013] and has enhanced N and finite U_2, with E very small. Here we refer to the attractive fixed point G as an example of O-mode. 109
4.4.2 As Fig.4.3.2, for the two-predator ZCD model[Zhu et al., 2013] with a sharp heating transition where $q_0 = 0.47$, $\delta q = 0.16$. The major difference from Fig.4.3.2 is that the post-heating T-mode state F is a repulsive fixed point, from which the system spontaneously transitions and converges cyclically to the limit cycle G. This is known from [Zhu et al., 2013] and has oscillations of enhanced N and finite U_2, accompanied by small pulses of E. Here we refer to the attractive limit cycle G as an example of O-mode. 110
4.4.3 As Fig.4.3.3, for the two-predator ZCD model[Zhu et al., 2013] with a sharp heating transition where $q_0 = 0.49$, $\delta q = 0.16$. There is insufficient run time for the phase E QH-mode to transition to T-mode and then to the O-mode attractor, unlike Figs.4.4.1 and 4.4.2. 111
4.5.1 Time traces and phase space evolution for the MD model, Eqs(4.1.1) to (4.1.3), with a smooth increase, represented by the tanh function in Eqs.(4.5.1) and (4.5.2), in the heating rate q by an amount $\delta q = 0.16$ from $q_0 = 0.45$ around $t = 2000$ time units; q reverts to q_0 around $t = 3000$ time units. Upper left plot shows time traces of variables N (black), q (dashed magenta), U (red) and E (green). Lower left plot shows time trace of energy confinement time defined by Eq.(4.2.1). Right plot shows time evolution of the system in (N, E, U) phase space. 112

4.5.2 As Fig.4.5.1, for the case where $q_0 = 0.49$. There are two major differences from Fig.4.3.3. First, confinement time τ_c during phase C experiences a transient drop before jumping to higher confinement regime. Second, a spontaneous back-transition F to T-mode appears after long duration phase E QH-mode. 113
4.6.1 Period-1 oscillation in ZCD system dynamics in response to the varying heating rate defined by Eq.(4.6.1) with $A = 0.0215$; other parameter values are as for Fig.4.4.2. Left, the power spectrum of N; right, the full attractor in (N, U_2, E) space; inset, the time series of N. . . 115
4.6.2 As Fig.4.6.1, showing period-2 oscillation in ZCD system dynamics when $A = 0.0240$. 115
4.6.3 As Fig.4.6.1, showing period-4 oscillation in ZCD system dynamics when $A = 0.0270$. 116
4.6.4 Period-doubling illustrated by the power spectra of N from Figs.4.6.1 to 4.6.3, over-plotted in the frequency range from 0.04 to 0.08. Blue, red and black dash lines denote spectra of period-1, period-2 and period-4 respectively. 116
4.6.5 As Fig.4.6.1, showing chaotic attractor of the ZCD system dynamics when $A = 0.0295$. 117
4.6.6 Period-doubling bifurcation path to chaos of ZCD system dynamics. Micro-turbulence level E is plotted versus amplitude A of oscillatory heating component in Eq.(4.6.1), in the range 0.0215 to 0.0295. The first four arrows indicate successive bifurcations, which occur at values $A = 0.0230, 0.0265, 0.0272$ and 0.0273. These yield Feigenbaum's ratio to within 0.05 per cent. The fifth arrow marks a period-6 window within the chaotic region. 117

5.3.1 Time evolution of electron temperature at multiple radial locations, derived from LHD data(blue) and the model(red) for the core temperature rise(R) heat pulse propagation experiment in plasma 49708. Radial locations range from edge($\rho = 0.703$) to core($\rho = 0.015$), where $\rho = r/a$, r is the radial co-ordinate and $a \sim 0.6$m is minor radius of LHD. Model results match experimental data well from $\rho = 0.450$ inwards to the plasma core, especially amplitudes and the time structure of pulse decay. The amplitudes of model time traces increase from edge to core, as in the measured electron temperature profiles. Model results do not fit experimental data outwards from $\rho = 0.546$ to $\rho = 0.703$, implying that different physics applies in the outer LHD plasma. 127

5.3.2 Time evolution of electron temperature at multiple radial locations, derived from LHD data(blue) and the model(red) for the core temperature drop(D) heat pulse propagation experiment in plasma 49719. Radial locations range from edge($\rho = 0.703$) to core($\rho = 0.015$), where $\rho = r/a$, r is the radial co-ordinate and $a \sim 0.6$m is minor radius of LHD. As in Fig.5.3.1, model results match experimental data well from $\rho = 0.450$ inwards to the plasma core. Again, model results do not fit experimental data outwards from $\rho = 0.546$ to $\rho = 0.703$, reinforcing that different physics dominates in the outer LHD plasma. 128

5.3.3 Time evolution of electron temperature at three specific radii selected from Fig.5.3.1 for the central temperature rise(R) case, during the heat pulse propagation experiment in LHD plasma #Te49708. Data and model output are denoted by blue and red lines respectively. . . 128

5.3.4 Time evolution of electron temperature at three specific radii selected from Fig.5.3.2 for the central temperature drop(D) case, during the heat pulse propagation experiment in LHD plasma #Te49719. Data and model output are denoted by blue and red lines respectively. . . 129

5.3.5 Data analysis underpinning calculation of pulse velocity from the experimental data, which requires a statistically robust identification of the time of the pulse peak from the noisy data at each radius $0.450 \geq \rho \geq 0.015$. Blue lines show timeseries of electron temperature data versus time from the R case(Te49708). Red lines denote timeseries smoothed over a window whose span is 5% of the total sample points, so that approximately 50 sample points generate the moving average. Black dots mark the maximum values, at each radius, of each smoothed time-evolving electron temperature pulse. The width of the horizontal error bars is defined by span of the moving window. The black dash line is the best fit straight line joining all the peaks. From it we infer the pulse propagation speed, which is nearly independent of radius, to be $(32.62 \pm 9.89)\text{ms}^{-1}$. 130

5.3.6 As Fig.5.3.5, demonstrating the calculation of the pulse velocity for the electron temperature data for the D case. Despite data which is more noisy than in Fig.5.3.5, the pulse propagation velocity calculated from the dashed line is approximately constant across all radii in this region $0.450 \geq \rho \geq 0.015$ of LHD plasma 49719. We infer a pulse velocity $(53.50 \pm 20.97)\text{ms}^{-1}$. 131

5.3.7 Variation and robustness of nonlinear pulse phenomenology in the model, for three different values of pseudo-velocity v_0 at three radial locations(Left panel). Blue lines show experimental data for R case in plasma 49708. Solid, dash and dot magenta lines denote simulation outputs for $v_0 = 15, v_0 = 30$ and $v_0 = 45$ respectively. The boundary condition for R case is $y_2(0) = 1.5$, and no horizontal or vertical shift is applied to the model outputs. Right panel: Phase plot of model outputs from left plots, all of which lie on the same orbit. Circulation direction of this phase plot is identical with Fig.6(a) of [Dendy et al., 2013], where the sign of the horizontal axis is reversed. 131

5.3.8 Impact of different ξ values on the heat pulse model in R case, four cases($\xi = 5; \xi = 10; \xi = 15; \xi = 20$) are examined. Red solid, dash blue and dash magenta lines denote y_1, y_2 and y_3 respectively. 132

Acknowledgments

I would like to thank my supervisors Professor Sandra C Chapman and Professor Richard O Dendy for their support over the three and half years. I am grateful for helpful discussions with Professor Shigeru Inagaki, Professor Sanae-I. Itoh, Professor Kimitaka Itoh and Professor George Rowlands. Moreover, of course, I will also be thankful for the unwavering support from my parents.

Chapter 3 was part-funded by the EPSRC and the RCUK Energy Programme under grant EP/I501045 and the European Communities under the contract of Association between EURATOM and CCFE.

Chapter 4 was part-funded by the support by KAKENHI (21224014, 23244113) from JSPS and the EPSRC and the RCUK Energy Programme under grant EP/I501045 and the European Communities under the contract of Association between EURATOM and CCFE.

Chapter 5 was part-funded by the RCUK Energy Programme under grant EP/I501045. This project has received funding from the Euratom under grant agreement number 633053. This work was also supported in part by the grant-in-aid for scientific research of JSPF, Japan (23244113) and KAKENHI (21224014) from JSPS, Japan.

This thesis was typeset with LaTeX 2$_\varepsilon$[1] by the author.

[1] LaTeX 2$_\varepsilon$ is an extension of LaTeX. LaTeX is a collection of macros for TeX. TeX is a trademark of the American Mathematical Society. The style package *warwickthesis* was used.

Declarations

I hereby declare that this thesis is my own work, except where explicitly stated, and that it has not been submitted for another degree at the University of Warwick, or any other university.

Chapters 1 and 2 do not include original work but provide theoretical and experimental backgrounds. The results presented in Chapters 3 and 4 have been published in [Zhu et al., 2013] and [Zhu et al., 2014] respectively. Moreover, results in Chapter 5 have been submitted to [Zhu et al., 2015].

H. Zhu May, 2015

Abstract

Turbulent transport in magnetized plasmas is one of the fundamental issues in fusion plasma physics. It is recognized that the interactions between zonal flows(ZFs) and micro-scale drift wave turbulence can influence plasma transport in both Tokamaks and Stellarators. These interactions are believed to play a significant role in the transition from low energy confinement regime(L-mode) to high confinement regime(H-mode). In the desired H-mode, the temperatures and densities are higher than those in L-mode, and this can typically generate a doubling of the confinement time. Anomalous, turbulent-linked transport between the plasma edge and the core is also significant in fusion plasma physics. Heat pulse experiments, which involve strongly nonlinear localised perturbation of the plasma, probe the character of anomalous transport in both Tokamaks and Stellarators. In this thesis, we interpret the zonal flow-turbulence interactions in terms of the Lotka-Volterra model, which is derived in ecology and is widely utilized in many fields of science. We discover a novel limit cycle manifold for the plasma state as characterised by micro-scale drift wave turbulence, the electron temperature gradient and the energy of meso-scale structures such as zonal flows. In fusion experiments, an apparent limit cycle manifold called the I-phase has been found in many Tokamaks during L-H transitions. We investigate the possible links between this phenomenology and our model, and also report transitions between different confinement regimes in the model. Finally, we describe heat pulse propagation experiments in Large Helical Device(LHD), which is a Stellarator, in terms of a new model for anomalous transport phenomena from the plasma edge to the core.

Summary

When facing the energy crisis, it is recognised worldwide that nuclear fusion is one of the most promising potential solutions. However, plenty of unexplored topics still exist in fusion plasma physics. This thesis focuses primarily on one of those issues: modelling and interpreting the coupling relationships between coherent nonlinear structures and ambient micro-scale turbulence in fusion plasmas, using approaches derived from the Lotka-Volterra(or predator-prey) model. Additionally, we interpret heat pulse propagation experiments in the Large Helical Device(LHD), which is a type of fusion device called Stellarator, in terms of a new travelling wave transformation of an existing model. Introductions to fundamental plasma physics, L-H transitions, drift wave turbulence–zonal flows interactions, heat pulse propagation experiments, MHD description and instabilities in Tokamaks are given in **Chapter 1**. In **Chapter 2**, we introduce some key aspects of nonlinear dynamics that are helpful in analysing those phenomena in nuclear fusion. Terminologies of nonlinear dynamics such as the Lotka-Volterra(or predator-prey) model, limit cycle manifold, bifurcation theory and chaos will be described. The specific methodology applied throughout this thesis will be introduced as well.

We know that energy transport and confinement in Tokamak fusion plasmas is partly governed by the coupled nonlinear interactions between micro-scale drift wave turbulence and meso-scale coherent nonlinear structures, such as zonal flows, together with free energy sources such as temperature gradients. Zero-dimensional models, designed to embody mathematically some of the supposed physical narratives for these interactions, can help to identify the origin of enhanced energy con-

finement and of transitions between confinement regimes. A prime zero-dimensional paradigm is Lotka-Volterra or predator-prey. Within this framework, we propose a novel model. This requires a fourth coupled nonlinear ordinary differential equation, together with a fourth variable which we treat as geodesic acoustic modes(GAMs). We investigate the degree of invariance of the phenomenology generated by the model of Malkov *et al.*(3-ODE), given this additional physics. We study and compare the long-time behaviour of the three-equation and four-equation systems, their evolution towards the final state, and their attractive fixed points and limit cycles. We explore the sensitivities of paths to attractors. It is demonstrated that an attractive fixed point of the three-equation system can become a limit cycle manifold of the four-equation system. Addressing these questions is particularly important for models that generate sharp transitions in the values of system variables which may replicate some key features of confinement transitions. Our results help to establish the robustness of the zero-dimensional model approach to capturing observed confinement phenomenology in Tokamak fusion plasmas. We report these results in **Chapter 3**, see also [Zhu et al., 2013].

It is well known experimentally that rapid substantial changes in heating rate can induce transitions to improved energy confinement regimes for Tokamak plasmas. We examine the effect of step changes in external heating rate in the models of Malkov *et al.*(3-ODE) which nonlinearly couple the evolving electron temperature gradient, micro-turbulence intensity and a meso-scale flow; and in the extension of Zhu *et al.*(4-ODE), which couples to a second meso-scale flow component. The electron temperature gradient rises, as does the confinement time defined by analogy with the fusion context, while micro-turbulence is suppressed. This outcome is robust against variation of heating rise time and against introduction of an additional variable into the model. It is also demonstrated that oscillating changes in heating rate can drive the level of micro-turbulence through a period-doubling route to chaos, where the amplitude of the oscillatory component of the external heating rate is the control parameter. We report these results in **Chapter 4**, see also [Zhu et al., 2014].

It is observed that rapid edge cooling of magnetically confined plasmas, induced by pellet injection, can trigger heat pulses that propagate rapidly inward. These can result in either large positive or negative deviations of the electron temperature at the plasma core. They represent a fairly extreme example of coherent nonlinear structures in plasmas, and as such are a particularly interesting challenge to theory. By applying a travelling wave transformations, we extend the model of Dendy *et al.*, which successfully describes local temporal evolution in these plasmas, to include also spatial dependence. The extended model comprises two coupled nonlinear first order ordinary differential equations for the (x, t) evolution of the deviation from steady state of two independent variables: the excess electron temperature gradient and the excess heat flux, both of which are measured in the LHD experiments. Pulse velocity is also defined in terms of plasma quantities. This enables us to model spatio-temporal pulse evolution in a way which yields as output the spatiotemporal evolution of the electron temperature, which is also measured in detail in the experiments. We compare the model results against LHD datasets using appropriate initial and boundary conditions. Sensitivities of this nonlinear model with respect to plasma parameters, initial conditions and boundary conditions are investigated. We conclude that this model can match experimental data for the time-evolving temperature profiles of pulses and their propagation velocities across a broad radial range from plasma edge to core. We report these results in **Chapter 5**, see also [Zhu et al., 2015].

We summarize in **Chapter 6** the ways in which our new models can successfully assist interpretation of the drift wave turbulence – zonal flows interactions and the heat pulse propagation experiments. These results appear to reinforce the validity of Lotka-Volterra models when modelling and interpreting this class of phenomenon observed in nuclear fusion plasmas.

In brief, the structure of this thesis is as follows. In **Chapter 1**, we give introductions to fundamental plasma physics, fusion devices, MHD description and instabilities in Tokamaks. **In Chapter 2**, we introduce the basics of nonlinear dynamics, including the Lotka-Volterra model and the methodology used throughout

this thesis. **In Chapter 3**, the reduced models to interpret the interactions between drift wave turbulence and zonal flows will be presented. **In Chapter 4**, we explore the impact of different levels of external heating flux on the reduced models. **In Chapter 5**, we interpret the heat pulse propagation experiments in the Large Helical Device using a novel model. **In Chapter 6**, we will provide a conclusion for this thesis.

Chapter 1

Introduction to fusion plasma physics

1.1 Lawson criterion

In order to reach the condition of nuclear fusion ignition, we have to satisfy the triple product, which is called the Lawson criterion[Lawson, 1955]:

$$nT\tau_E > 5 \times 10^{21} m^{-3} keVs \tag{1.1.1}$$

where n and T are the peak density and the peak temperature of the particles in the plasma, and τ_E is the confinement time of energy[Wesson, 2011].

Under this circumstance, the plasma will have achieved the power balance. The balance equation is

$$P_H + \frac{1}{4}\overline{n^2 < \sigma v >}\mathcal{E}_\alpha V = \frac{3\overline{nT}}{\tau_E}V \tag{1.1.2}$$

where P_H is the external heating power, n is the particle density, σ is the cross-section of the reaction, $< \sigma v >$ is the rate of nuclear reaction, $\mathcal{E}_\alpha$ is the α-particle heating per unit volume, V is the plasma volume, T is the temperature and τ_E is the confinement time[Freidberg, 2007]. The discovery of H-mode[Wagner et al., 1982] in the year 1982 on ASDEX in Germany realised an increase in both temperature and density at plasma edge. These phenomena also enhance the confinement time[Wagner, 2007], motivating research into high confinement mode(H-mode) physics. For discussions of H-mode, please see Chapter 1.2.4. For the models which

are utilized to interpret the transition to H-mode, please see Chapter 2.4.

Since such a high temperature is incompatible with confinement by material walls, another way of confinement is required. Magnetic confinement fusion(MCF) provides such a method, in which plasmas are confined in a toroidal region by the magnetic field, being held by the field in microscale gyrating orbit[Wesson, 2011]. For further information about magnetic confinement fusion devices like Tokamak and Stellarator, please see Chapter 1.3.

1.2 Fundamental plasma physics

1.2.1 Fluid description

The characteristic density of a plasma in medium-size MCF experiment would be $10^{19}\mathrm{m}^{-3}$[Dendy, 1990]. If each particle has a complex trajectory, it would be rather difficult to predict the behaviour of the plasma. Fortunately, the majority of the plasma phenomena observed, for example the drift wave in Chapter 1.2.5, can be described by a simple model. This model is utilized in fluid mechanics, and only the motion of the fluid elements is taken into consideration. The properties of each individual particle are implicitly summed and averaged. The only difference between the ordinary fluid description and the plasma fluid description is charged particles[Chen, 1975]. In this subchapter, the fundamental fluid description of plasma will be given. The fluid drift perpendicular to the magnetic field, which is not only a valid approximation of the fluid description but also linked to many fusion plasma phenomena, will be introduced as well. The discussions in the Chapter 1.2.1 appear in [Chen, 1975] and [Krall and Trivelpiece, 1986].

The equation of motion for a single particle is:

$$m\frac{d\boldsymbol{v}}{dt} = q(\boldsymbol{E} + \boldsymbol{v} \times \boldsymbol{B}) \tag{1.2.1}$$

Assume there are no thermal motions and no collisions. Then all particles in a fluid element move together, and the individual particle velocity $\boldsymbol{v}$ is identical with the average velocity $\boldsymbol{u}$ of the particles in the fluid element. Then the fluid equation is obtained by multiplying the density of particles n.

$$mn\frac{d\boldsymbol{u}}{dt} = qn(\boldsymbol{E} + \boldsymbol{u} \times \boldsymbol{B}) \tag{1.2.2}$$

In Eq.(1.2.1), the time derivative is to be taken at the position of the particles(called Langrange method). However, the equation for fluid elements relative to a co-ordinate system fixed in space(called Euler method) is more convenient for the present description.

To make this transformation to variables in the fixed frame, consider $\boldsymbol{G(x,t)}$ to be any physical quantity of a fluid element in one-dimensional space. The variance of $\boldsymbol{G(x,t)}$ with time in a frame moving with the fluid is:

$$\frac{d\boldsymbol{G}(x,t)}{dt} = \frac{\partial \boldsymbol{G}}{\partial t} + \frac{\partial \boldsymbol{G}}{\partial x}\frac{dx}{dt} = \frac{\partial \boldsymbol{G}}{\partial t} + u_x \frac{\partial \boldsymbol{G}}{\partial x} \tag{1.2.3}$$

In three-dimensional case, Eq.(1.2.3) has been changed as:

$$\frac{d\boldsymbol{G}}{dt} = \frac{\partial \boldsymbol{G}}{\partial t} + (\boldsymbol{u}\cdot\nabla)\boldsymbol{G} \tag{1.2.4}$$

This equation is called convective derivative and $\boldsymbol{u}\cdot\nabla$ is a scalar differential operator. In the plasma, we assume that the fluid velocity is $\boldsymbol{u}$, then we can rewrite Eq.(1.2.2) as:

$$mn\left[\frac{\partial \boldsymbol{u}}{\partial t} + (\boldsymbol{u}\cdot\nabla)\boldsymbol{u}\right] = qn(\boldsymbol{E} + \boldsymbol{u}\times\boldsymbol{B}) \tag{1.2.5}$$

The complete statistical description of a given system of N particles is given in terms of a distribution function

$$F \;=\; F(\boldsymbol{x}_1, \boldsymbol{x}_2, ..., \boldsymbol{x}_N, \boldsymbol{v}_1, \boldsymbol{v}_2, ..., \boldsymbol{v}_N, t) \tag{1.2.6}$$

where $\int F d\boldsymbol{x}_1, d\boldsymbol{x}_2, ..., d\boldsymbol{x}_N, d\boldsymbol{v}_1, d\boldsymbol{v}_2, ..., d\boldsymbol{v}_N = 1$.

The many-body distribution function Eq.(1.2.6) obeys the Liouville equation

$$\frac{\partial F}{\partial t} + \sum_i \left(\frac{\partial F}{\partial \boldsymbol{x}_i}\cdot\boldsymbol{v}_i + \frac{\partial F}{\partial \boldsymbol{v}_i}\cdot\boldsymbol{a}_i^T\right) = 0 \tag{1.2.7}$$

where $\boldsymbol{a}_i^T$ is the total acceleration of particle i due to the external and interparticle forces. The Liouville equation is well known from statistical mechanics. We can then get the kinetic equation of a plasma,

$$\frac{\partial}{\partial t} f_\alpha^{(1)} + \boldsymbol{v}_1 \cdot \frac{\partial}{\partial \boldsymbol{x}_1} f_\alpha^{(1)} + \frac{q_\alpha}{m_\alpha} \langle \boldsymbol{E} + \boldsymbol{v_1} \times \boldsymbol{B} \rangle \cdot \frac{\partial}{\partial \boldsymbol{v}_1} f_\alpha^{(1)} = \left. \frac{\partial f_\alpha^{(1)}}{\partial t} \right|_c \tag{1.2.8}$$

where $\boldsymbol{E}$ and $\boldsymbol{B}$ are electric and magnetic fields respectively, $f_\alpha^{(1)}$ is the distribution function of particle of type α at $\boldsymbol{x}_1$ and $\boldsymbol{v}_1$. The equation above is Boltzmann equation. If we neglect the collisional term on the right-hand side, the equation becomes Vlasov equation.

The integral of Eq.(1.2.8) over all velocity space is

$$\int \left(\frac{\partial}{\partial t} f_\alpha + \boldsymbol{v} \cdot \frac{\partial}{\partial \boldsymbol{x}} f_\alpha + \frac{q_\alpha}{m_\alpha} \langle \boldsymbol{E} + \boldsymbol{v} \times \boldsymbol{B} \rangle \cdot \frac{\partial}{\partial \boldsymbol{v}} f_\alpha \right) d\boldsymbol{v} = \int \left. \frac{\partial f_\alpha}{\partial t} \right|_c d\boldsymbol{v} \tag{1.2.9}$$

where $f_\alpha \equiv f_\alpha(\boldsymbol{x}, \boldsymbol{v}, t)$. The Eq.(1.2.9) is called equation of continuity.

The integral over all velocity space of the product of the plasma kinetic equation Eq.(1.2.8) and the momentum $m_\alpha \boldsymbol{v}$ of a particle of species α is

$$\int m_\alpha \boldsymbol{v} \left(\frac{\partial f_\alpha}{\partial t} + \boldsymbol{v} \cdot \frac{\partial f_\alpha}{\partial \boldsymbol{x}} + \frac{q_\alpha}{m_\alpha} \langle \boldsymbol{E} + \boldsymbol{v} \times \boldsymbol{B} \rangle \cdot \frac{\partial f_\alpha}{\partial \boldsymbol{v}} \right) d\boldsymbol{v} = \int m_\alpha \boldsymbol{v} \left. \frac{\partial f_\alpha}{\partial t} \right|_c d\boldsymbol{v} \tag{1.2.10}$$

With the aid of equation of continuity, Eq.(1.2.10) reduces to the momentum transfer equation for particles of species α; that is,

$$\begin{aligned} & n_\alpha m_\alpha \frac{\partial \boldsymbol{V}_\alpha}{\partial t} + n_\alpha m_\alpha \boldsymbol{V}_\alpha \cdot \nabla \boldsymbol{V}_\alpha - n_\alpha q_\alpha \langle \boldsymbol{E} + \boldsymbol{v} \times \boldsymbol{B} \rangle + \nabla \cdot \boldsymbol{P}_\alpha \\ & = -\sum_\beta n_\alpha m_\alpha (\boldsymbol{V}_\alpha - \boldsymbol{V}_\beta) \langle \nu_{\alpha\beta} \rangle \end{aligned} \tag{1.2.11}$$

where $\langle \nu_{\alpha\beta} \rangle$ is a mean collision frequency for momentum transfer from all other types of plasma particles[Krall and Trivelpiece, 1986]. This equation has an alternative form as given below,

$$mn \left[\frac{\partial \boldsymbol{u}}{\partial t} + (\boldsymbol{u} \cdot \nabla) \boldsymbol{u} \right] = qn(\boldsymbol{E} + \boldsymbol{u} \times \boldsymbol{B}) - \nabla \cdot \boldsymbol{P} - \frac{mn(\boldsymbol{u} - \boldsymbol{u_0})}{\tau} \tag{1.2.12}$$

where $\boldsymbol{P}$ is defined as stress tensor($\nabla \cdot \boldsymbol{P} = \nabla p$ in most of the cases, where p is the pressure), $\boldsymbol{u}_0$ is the velocity of the neutral fluid, $\boldsymbol{u} - \boldsymbol{u_0}$ is the relative velocity in collisions and τ is the mean free time between collisions.

We also have the equation of continuity

$$\frac{\partial n}{\partial t} + \nabla \cdot (n\boldsymbol{u}) = 0 \tag{1.2.13}$$

A conservation of energy equation is also required. This is represented by the equation of state,

$$p = C\rho^{\gamma} \tag{1.2.14}$$

where C is a constant and γ is the ratio of specific heats C_p/C_v. The term ∇p is then given by

$$\frac{\nabla p}{p} = \gamma \frac{\nabla n}{n} \tag{1.2.15}$$

where $p = nKT$. Hence, we consider the ions and electrons in plasma fluid description. Then the charges and the current densities are given by

$$\sigma = n_i q_i + n_e q_e \tag{1.2.16}$$

$$\boldsymbol{j} = n_i q_i \boldsymbol{v}_i + n_e q_e \boldsymbol{v}_e \tag{1.2.17}$$

Since the single particle motion will not be considered, we then use $\boldsymbol{v}$ instead of $\boldsymbol{u}$ for the velocity of fluid. We also neglect the terms representing the viscosity and collisions. Thus we get the complete set of fluid equations in this plasma fluid description.

$$\begin{aligned}
\epsilon_0 \nabla \cdot \boldsymbol{E} &= n_i q_i + n_e q_e && (1.2.18)\\
\nabla \times \boldsymbol{E} &= -\dot{\boldsymbol{B}} && (1.2.19)\\
\nabla \cdot \boldsymbol{B} &= 0 && (1.2.20)\\
\mu_0^{-1} \nabla \times \boldsymbol{B} &= n_i q_i \boldsymbol{v}_i + n_e q_e \boldsymbol{v}_e + \epsilon_0 \dot{\boldsymbol{E}} && (1.2.21)\\
m_j n_j \left[\frac{\partial \boldsymbol{v}_j}{\partial t} + (\boldsymbol{v}_j \cdot \nabla)\boldsymbol{v}_j \right] &= q_j n_j (\boldsymbol{E} + \boldsymbol{v}_j \times \boldsymbol{B}) - \nabla p_j && (1.2.22)
\end{aligned}$$

$$\frac{\partial n_j}{\partial t} + \nabla \cdot (n_j \boldsymbol{v}_j) = 0 \tag{1.2.23}$$

$$p_j = C_j n_j^{\gamma_j} \tag{1.2.24}$$

where $j = i, e$ are the particle species of each fluid considered, n is the particle density, p is the pressure, v is the velocity, E is the electric field, B is the magnetic field, ϵ_0 and μ_0 are the permittivity and permeability in vacuum respectively. The simultaneous solution of equations above provides a set of motions and corresponding fields in the plasma fluid approximations[Chen, 1975]. The discussions above can be found in [Chen, 1975] and [Krall and Trivelpiece, 1986]

Fluid drift perpendicular to $\boldsymbol{B}$

In this subchapter, the fluid with drifts perpendicular to the magnetic field $\boldsymbol{B}$ will be discussed. This phenomenon also appears in the generation of drift waves which will be introduced in Chapter 1.2.5. The suppression of drift wave turbulence in a fusion device may give rise to the transition to the high confinement mode(H-mode)[Diamond et al., 2005], which is mentioned in Chapter 1.1 and will be discussed in 1.2.4 and 1.2.5 in detail. The theory of fluid drifts, particularly perpendicular to the magnetic field, is one of the most important topics underpinning the transport phenomena for energy and particles in fusion plasmas. The discussions in this subchapter appear in [Chen, 1975].

We start the derivation from the equation of motion.

$$mn\left[\frac{\partial \boldsymbol{v}}{\partial t} + (\boldsymbol{v} \cdot \nabla)\boldsymbol{v}\right] = qn(\boldsymbol{E} + \boldsymbol{v} \times \boldsymbol{B}) - \nabla p \tag{1.2.25}$$

Consider the ratio of the first term on the left-hand side to the first term on the right-hand side for a periodic motion of angular frequency ω:

$$Ratio \simeq \left|\frac{mni\omega v_\perp}{qnv_\perp B}\right| \simeq \frac{\omega}{\omega_c} \tag{1.2.26}$$

where ω_c is the cyclotron frequency. We have taken $\partial/\partial t = i\omega$ and are concerned with $\boldsymbol{v}_\perp$ only. For this drift, which is slow compared with the time scale of ω_c, we can neglect the first term on the left-hand side of Eq.(1.2.25). The advective term $(\boldsymbol{v} \cdot \nabla)\boldsymbol{v}$ on the left-hand side is assumed to be ignored as well, see discussion below

Eq.(1.2.31). Let the electric field $\boldsymbol{E}$ and the magnetic field $\boldsymbol{B}$ be uniform, while assuming density n and pressure p have non-zero gradients. The set of assumptions mentioned above is commonly adopted for in the magnetic confined plasma column. Please see Fig.1.2.1 for details. Taking the cross product of Eq.(1.2.25) with the magnetic field strength $\boldsymbol{B}$, we have

$$0 = qn\left[\boldsymbol{E} \times \boldsymbol{B} + (\boldsymbol{v}_\perp \times \boldsymbol{B}) \times \boldsymbol{B}\right] - \nabla p \times \boldsymbol{B} \tag{1.2.27}$$

then

$$0 = qn\left[\boldsymbol{E} \times \boldsymbol{B} - \boldsymbol{v}_\perp B^2\right] - \nabla p \times \boldsymbol{B} \tag{1.2.28}$$

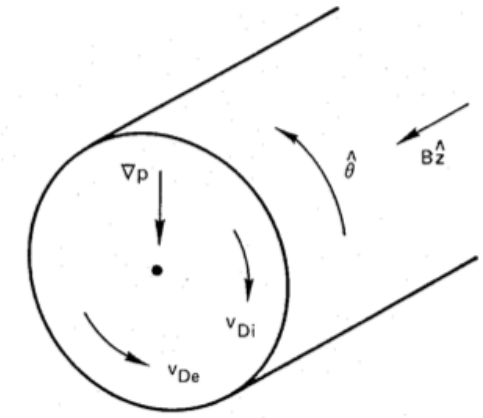

Figure 1.2.1: Fig.3.4 in [Chen, 1975], the diamagnetic drifts in a cylindrical plasma

Therefore,

$$\boldsymbol{v}_\perp = \frac{\boldsymbol{E} \times \boldsymbol{B}}{B^2} - \frac{\nabla p \times \boldsymbol{B}}{qnB^2} \equiv \boldsymbol{v}_E + \boldsymbol{v}_D \tag{1.2.29}$$

where

$$\boldsymbol{v}_E \equiv \frac{\boldsymbol{E} \times \boldsymbol{B}}{B^2} \tag{1.2.30}$$

$$\boldsymbol{v}_D \equiv -\frac{\nabla p \times \boldsymbol{B}}{qnB^2} \tag{1.2.31}$$

Equations (1.2.30) and Eq.(1.2.31) define the $\boldsymbol{E} \times \boldsymbol{B}$ drift and diamagnetic drift respectively. The drift velocity $\boldsymbol{v}_E$ is the same as for guiding centres, in addition there is a new drift velocity $\boldsymbol{v}_D$ called the diamagnetic drift. Since $\boldsymbol{v}_D$ is perpendicular to the gradient direction, the neglect of $(\boldsymbol{v} \cdot \nabla)\boldsymbol{v}$ is justified if $\boldsymbol{E} = 0$. Because under this situation, we have $\boldsymbol{v} = \boldsymbol{v}_D$ and $\boldsymbol{v}_D \cdot \nabla = 0$. $(\boldsymbol{v} \cdot \nabla)\boldsymbol{v}$ can still be neglected if $\boldsymbol{E} = -\nabla\phi \neq 0$ and $\nabla\phi$, ∇p are in the same direction. Because $\boldsymbol{v}_D \perp \nabla$, then $(\nabla p \times B) \perp \nabla$, then $(\nabla\phi \times B) \perp \nabla$, thus we have $\boldsymbol{v}_E \perp \nabla$. Using Eq.(1.2.15), we can rewrite the diamagnetic drift velocity in Eq.(1.2.31) as

$$\boldsymbol{v}_D = \pm\frac{\gamma KT}{eB}\frac{\hat{z} \times \nabla n}{n} \tag{1.2.32}$$

where K is the Boltzmann's constant and T is the temperature. In particular, for an isothermal plasma($\gamma = 1$) in the geometry of Fig.1.2.1, where $\nabla n = n'\hat{\boldsymbol{r}}$, we have the following formulas for a cylindrical plasma:

$$\boldsymbol{v}_{Di} = \frac{KT_i}{eB}\frac{n'}{n}\hat{\theta} \tag{1.2.33}$$

$$\boldsymbol{v}_{De} = -\frac{KT_e}{eB}\frac{n'}{n}\hat{\theta} \tag{1.2.34}$$

where $n' \equiv \dfrac{\partial n}{\partial r} < 0$[Chen, 1975]. The discussions above can be found in [Chen, 1975]. The applications of this physical mechanism will be discussed in Chapter 1.2.5 in detail.

1.2.2 Magnetohydrodynamics description

Magnetohydrodynamics(MHD) is the level of description that is used to model the dynamics of electrically conducting fluids, and is a major subfield in plasma physics. MHD research was initiated and developed by Swedish plasma physicist Hannes Alfvén in 1940s. While plasma can sometimes be taken as an MHD fluid, electric and magnetic forces, acting at the particle kinetic level of description, can also play an important role. In order to investigate this kind of complex phenomenon, we have to consider and solve electric, magnetic and fluid equations simultaneously. The MHD equations can also be developed from the kinetic equations by calculating

the moments of the kinetic equations. The discussions here appear in [Li et al., 2006].

We start from the classical Maxwell's equations,

$$\nabla \cdot \boldsymbol{E} = \frac{\rho_q}{\epsilon_0} \tag{1.2.35}$$

$$\nabla \times \boldsymbol{E} = -\frac{\partial \boldsymbol{B}}{\partial t} \tag{1.2.36}$$

$$\nabla \cdot \boldsymbol{B} = 0 \tag{1.2.37}$$

$$\nabla \times \boldsymbol{B} = \epsilon_0 \mu_0 \frac{\partial \boldsymbol{E}}{\partial t} + \mu_0 \boldsymbol{J} \tag{1.2.38}$$

where $\boldsymbol{E}$ and $\boldsymbol{B}$ are electric field and magnetic field respectively, $\boldsymbol{J}$ is the current density, ρ_q is density of free charge and ϵ_0 and μ_0 are permittivity and conductivity in vacuum respectively. In a frame of reference O, which is stationary with respect to fluid flow, the Ohm's law is

$$\boldsymbol{J} = \sigma \boldsymbol{E} \tag{1.2.39}$$

and Lorenz force is

$$\boldsymbol{f} = \rho_q \boldsymbol{E} + \boldsymbol{J} \times \boldsymbol{B} \tag{1.2.40}$$

We note that, in general, the Ohm's law can take more general form, which may include electron pressure, Hall's term, and Ohmic heating term, for example.

We now introduce another frame of reference $O^{'}$, the $O^{'}$ has a velocity $\boldsymbol{u}$ with respect to O. Then in the frame of reference $O^{'}$, we have

$$\boldsymbol{J}^{'} = \sigma \boldsymbol{E}^{'} \tag{1.2.41}$$

where $\boldsymbol{J'}$ and $\boldsymbol{E'}$ are current density and electric field in $O^{'}$. Then for electric field and current in $O^{'}$, we have

$$\boldsymbol{E}^{'} = \boldsymbol{E} + \boldsymbol{u} \times \boldsymbol{B} \tag{1.2.42}$$

$$\boldsymbol{J}^{'} = \rho_q \boldsymbol{v}^{'} = \rho_q \left(\boldsymbol{v} - \boldsymbol{u}\right) = \boldsymbol{J} - \rho_q \boldsymbol{u} \tag{1.2.43}$$

Substituting Eqs.(1.2.42-1.2.43) into Eq.(1.2.41), we get

$$\boldsymbol{J} = \sigma \left(\boldsymbol{E} + \boldsymbol{u} \times \boldsymbol{B}\right) + \rho_q \boldsymbol{u} \tag{1.2.44}$$

We use the following approximations to make simplifications:

$$\frac{|\epsilon_0 \partial \boldsymbol{E}/\partial t|}{|\boldsymbol{J}|} \simeq \frac{\epsilon_0 |\boldsymbol{E}/T|}{\sigma |\boldsymbol{E}|} = \frac{\epsilon_0}{\sigma T} \ll 1 \tag{1.2.45}$$

$$\frac{|\rho_q \boldsymbol{u}|}{|\boldsymbol{J}|} \simeq \frac{|\boldsymbol{u}| \epsilon_0 |\nabla \cdot \boldsymbol{E}|}{|\nabla \times \boldsymbol{B}|/\mu_0} \simeq \frac{\epsilon_0 \mu_0 L}{T} \left|\frac{\boldsymbol{E}}{\boldsymbol{B}}\right| \simeq \left(\frac{L}{cT}\right)^2 \ll 1 \tag{1.2.46}$$

$$\frac{|\rho_q \boldsymbol{E}|}{|\boldsymbol{J} \times \boldsymbol{B}|} \simeq \frac{\epsilon_0 |\nabla \cdot \boldsymbol{E}||\boldsymbol{E}|}{|\boldsymbol{B}||\nabla \times \boldsymbol{B}|/\mu_0} \simeq \epsilon_0 \mu_0 \left(\left|\frac{\boldsymbol{E}}{\boldsymbol{B}}\right|\right)^2 \simeq \left(\frac{L}{cT}\right)^2 \ll 1 \tag{1.2.47}$$

In the approximations above, we assume that the wave length $\lambda \sim c/\omega$ of the field frequency ω is much larger than the characteristic length L of fluid motion. We also assume that the ratio of electric conductivity σ to field frequency ω satisfies $\dfrac{\sigma}{\epsilon_0 \omega} \gg 1$, which means the characteristic time of field change is much larger than the particle collision time and the fluid is considered to be good electrical conductor. Thus the displacement current $\epsilon_0 \partial \boldsymbol{E}/\partial t$, the current $\rho_q \boldsymbol{u}$ and electrical force $\rho_q \boldsymbol{E}$ can be neglected.

So the Maxwell's equations, Ohm's law and Lorenz force equation can be transformed in an electrically conducting fluid as follows:

$$\nabla \cdot \boldsymbol{E} = \frac{\rho_q}{\epsilon_0} \tag{1.2.48}$$

$$\nabla \times \boldsymbol{E} = -\frac{\partial \boldsymbol{B}}{\partial t} \tag{1.2.49}$$

$$\nabla \cdot \boldsymbol{B} = 0 \tag{1.2.50}$$

$$\nabla \times \boldsymbol{B} = \mu_0 \boldsymbol{J} \tag{1.2.51}$$

$$\boldsymbol{J} = \sigma\left(\boldsymbol{E} + \boldsymbol{u} \times \boldsymbol{B}\right) \tag{1.2.52}$$

$$\boldsymbol{f} = \boldsymbol{J} \times \boldsymbol{B} \tag{1.2.53}$$

From now on, we consider the fluid equation with electric and magnetic forces. A fluid plasma should obey the equation of continuity, which is

$$\frac{\partial \rho}{\partial t} + \nabla \cdot (\rho \boldsymbol{u}) = 0 \tag{1.2.54}$$

The motion equation of an electrically neutral and non-conducting fluid is

$$\rho \frac{d\boldsymbol{u}}{dt} = \nabla \cdot \boldsymbol{P} + \rho \boldsymbol{g} \tag{1.2.55}$$

where $\boldsymbol{P}$ is defined as tensor of stress, $\boldsymbol{P} = 2\eta \boldsymbol{S} - \left(p + \frac{2}{3}\eta \nabla \cdot \boldsymbol{u} - \eta^{'} \nabla \cdot \boldsymbol{u}\right) \boldsymbol{I}$ and $S_{ij} = \frac{1}{2}\left(\frac{\partial u_i}{\partial x_j} + \frac{\partial u_j}{\partial x_i}\right)$. Here we consider the additional electric and magnetic forces and omit the force due to gravity, so that the new equation is

$$\rho \frac{d\boldsymbol{u}}{dt} = \nabla \cdot \boldsymbol{P} + \rho_q \boldsymbol{E} + \boldsymbol{J} \times \boldsymbol{B} \tag{1.2.56}$$

This takes following form if the fluid has no viscosity and the pressure is isotropic($\eta = 0$, $\boldsymbol{P} = -p\boldsymbol{I}$),

$$\rho \frac{d\boldsymbol{u}}{dt} = -\nabla p + \rho_q \boldsymbol{E} + \boldsymbol{J} \times \boldsymbol{B} \tag{1.2.57}$$

The energy equation of a fluid is

$$\rho \frac{d}{dt}\left(\epsilon + \frac{\boldsymbol{u}^2}{2}\right) = \nabla \cdot (\boldsymbol{P} \cdot \boldsymbol{u}) + \rho \boldsymbol{g} \cdot \boldsymbol{u} - \nabla \cdot \boldsymbol{q} \tag{1.2.58}$$

where $\boldsymbol{q} = -\kappa \nabla T$, or the following form if we consider that magnitude of electric and magnetic forces is much larger than that of force due to gravity

$$\rho \frac{d}{dt}\left(\epsilon + \frac{\boldsymbol{u}^2}{2}\right) = \nabla \cdot (\boldsymbol{P} \cdot \boldsymbol{u}) + \boldsymbol{E} \cdot \boldsymbol{J} - \nabla \cdot \boldsymbol{q} \tag{1.2.59}$$

where $\rho\epsilon$ is the internal energy. Given also an equation of state $p = p(\rho, T)$, we have the complete MHD equations as follows:

$$\begin{aligned}
\frac{\partial \rho}{\partial t} + \nabla \cdot (\rho \boldsymbol{u}) &= 0 && (1.2.60)\\
\rho \frac{d\boldsymbol{u}}{dt} &= \nabla \cdot \boldsymbol{P} + \rho_q \boldsymbol{E} + \boldsymbol{J} \times \boldsymbol{B} && (1.2.61)\\
\rho \frac{d}{dt}\left(\epsilon + \frac{\boldsymbol{u}^2}{2}\right) &= \nabla \cdot (\boldsymbol{P} \cdot \boldsymbol{u}) + \boldsymbol{E} \cdot \boldsymbol{J} - \nabla \cdot \boldsymbol{q} && (1.2.62)\\
p &= p(\rho, T) && (1.2.63)\\
\nabla \cdot \boldsymbol{E} &= \frac{\rho_q}{\epsilon_0} && (1.2.64)\\
\nabla \times \boldsymbol{E} &= -\frac{\partial \boldsymbol{B}}{\partial t} && (1.2.65)\\
\nabla \cdot \boldsymbol{B} &= 0 && (1.2.66)\\
\nabla \times \boldsymbol{B} &= \mu_0 \boldsymbol{J} && (1.2.67)\\
\boldsymbol{J} &= \sigma\left(\boldsymbol{E} + \boldsymbol{u} \times \boldsymbol{B}\right) && (1.2.68)\\
\boldsymbol{f} &= \boldsymbol{J} \times \boldsymbol{B} && (1.2.69)
\end{aligned}$$

where

$$\begin{aligned}
\boldsymbol{P} &= 2\eta \boldsymbol{S} - \left(p + \frac{2}{3}\eta \nabla \cdot \boldsymbol{u} - \eta' \nabla \cdot \boldsymbol{u}\right) \boldsymbol{I} && (1.2.70)\\
S_{ij} &= \frac{1}{2}\left(\frac{\partial u_i}{\partial x_j} + \frac{\partial u_j}{\partial x_i}\right) && (1.2.71)\\
\boldsymbol{q} &= -\kappa \nabla T && (1.2.72)
\end{aligned}$$

If we assume the plasma to be an ideal conducting fluid, which means it has no viscosity, no heat conduction and is ideally conducting for current, the MHD equations transform to the ideal MHD equations which are shown here:

$$\begin{aligned}
\frac{\partial \rho}{\partial t} + \nabla \cdot (\rho \boldsymbol{u}) &= 0 && (1.2.73)\\
\rho \frac{d\boldsymbol{u}}{dt} &= -\nabla p + \rho_q \boldsymbol{E} + \boldsymbol{J} \times \boldsymbol{B} && (1.2.74)\\
p\rho^{-\gamma} &= const. && (1.2.75)\\
\nabla \times \boldsymbol{E} &= -\frac{\partial \boldsymbol{B}}{\partial t} && (1.2.76)
\end{aligned}$$

$$\nabla \times \boldsymbol{B} = \mu_0 \boldsymbol{J} \tag{1.2.77}$$

$$\boldsymbol{E} + \boldsymbol{u} \times \boldsymbol{B} = 0 \tag{1.2.78}$$

The discussions above can be found in [Li et al., 2006].

1.2.3 L-mode

The transition from low confinement mode(L-mode) to high confinement mode(H-mode) is one of the most significant topics in fusion plasma physics. In comparison with L-mode, H-mode has higher temperature(T) and density(n) at the edge of plasma. This can contribute to a doubling of the confinement time(τ)[Wesson, 2011].

For the purpose of reaching the ignition mentioned in Chapter 1.1, it is necessary to heat the plasmas by externally additional heating, for example, neutral beam injection and radio-frequency heating. However, with increasing heating power, the confinement time decreases[Freidberg, 2007], please see the reviews[Doyle et al., 2007]. By analysing the experimental results from Tokamak devices, Goldston proposed the confinement scaling[Goldston, 1984],

$$\tau_G = 0.037 \frac{I R^{1.75} \kappa^{0.5}}{P^{0.5} a^{0.37}} \tag{1.2.79}$$

where τ_G is the confinement time in second, I is the toroidal current in MA, P is the external heating power in MW and $\kappa = b/a$ is the plasma elongation.

The Goldston's law was found to predict the experimental data from Tokamak quite well even before the operation of JET[Wesson, 2011]. Another time scaling called ITER89-P proposed in [Wagner et al., 1990] predicts the confinement time more precisely,

$$\tau_E^{ITER89-P} = 0.048 \frac{I^{0.85} R^{1.2} a^{0.3} \kappa^{0.5} \left(n/10^{20}\right)^{0.1} B^{0.2} A^{0.5}}{P^{0.5}} \tag{1.2.80}$$

where $\tau_E^{ITER89-P}$ is in second, I and P are in MA and MW respectively, A is the atomic mass of the ions, B is the toroidal magnetic field. The comparisons[Yushmanov et al., 1990] of confinement times in various Tokamaks are given in Figure 1.2.2.

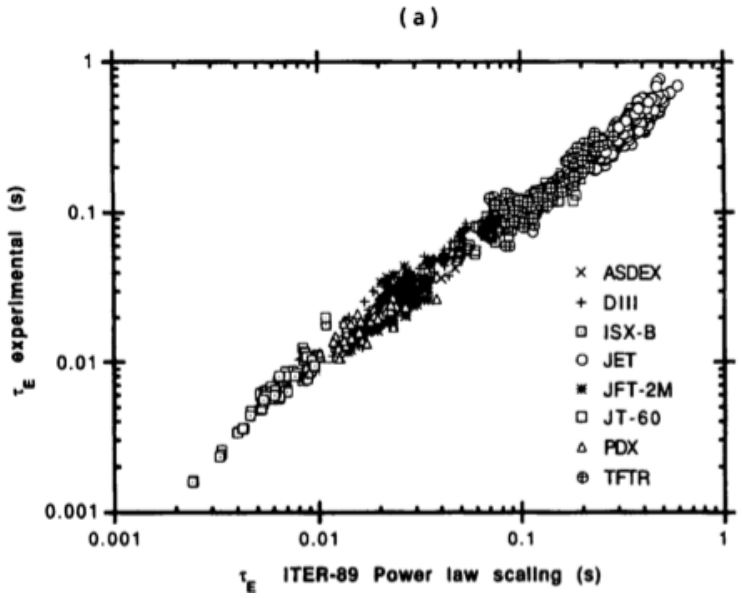

Figure 1.2.2: Fig.2(a) in [Yushmanov et al., 1990], the comparisons of confinement times($\tau_E^{ITER89-P}$ and τ_E^{exp}) in different fusion devices.

1.2.4 H-mode

In the year 1982, Wagner discovered a new confinement regime called H-mode when utilizing neutral beam heating on ASDEX in Germany. He found an increase in density caused by a sudden improvement in particle confinement[Wagner et al., 1982]. Also, the confinement time is twice that in L-mode. In the year 1984, a similar H-mode was observed in PDX Tokamak[Kaye et al., 1984], in DIII-D Tokamak in 1986[Burrell et al., 1987] and in JET Tokamak in 1987[Tanga et al., 1987b].

In recent years, transitions from L-mode to H-mode have been discovered in many Tokamaks like Alcator A[Mossessian et al., 2003], JT-60U[Tsuji et al., 1990], DIII-D[Doyle et al., 1991], ASDEX[Wagner et al., 1984], TFTR[Bush et al., 1990], JET[Cordey et al., 1999], ASDEX-Upgrade[Dux et al., 1999; Angioni et al., 2011], MAST[Dudson et al., 2005], HL-2A[Duan et al., 2010], EAST[Wang et al., 2012] and KSTAR[Yun et al., 2011] and Stellarators like W7-AS[Erckmann et al., 1993], TJ-II[Happel et al., 2011], Heliotron[Sano et al., 2005] and LHD[Motojima et al., 2003]. For further discussions about experimental data on the L-H transition, please see reviews[Carlstrom, 1996; Connor and Wilson, 2000]. For additional analysis of experimental results and theoretical models for improved confinement modes, please see reviews[Connor et al., 2004; Wolf, 2003]. We will discuss L-H transitions in terms of predator-prey models in detail in Chapter 2.4 and Chapters 3–4.

In the H-mode, the change in magnetic confinement happens at the edge of plasmas, where there is an abrupt increase in the pressure gradient(∇p) associated with increasing density on the edge[Doyle et al., 2007]. The question of the H-mode formation is still open, although many scientists believe this improvement on the edge can be taken as a transport barrier[Xu et al., 2012a; Dux et al., 2014], which is a narrow region with considerably reduced transport and steep gradient by the shear effect. It generates an enhancement in stored energy, on the time scale of the confinement time[Wesson, 2011]. The reason for the formation of transport barrier is thought to be the generation of flow shear that suppresses turbulent transport in the H-mode[Diamond et al., 2005; Wesson, 2011]. For further information about the relationship between the turbulence and flow shear, please see Chapter 1.2.5. For actual applications, please see Chapters 3.2–3.3 and Chapters 4.2–4.4.

In order to realise the L-H transition, the external heating power must exceed a threshold. An empirical scaling for the threshold has been acquired from datasets of many Tokamaks[Doyle et al., 2007; Wesson, 2011], as given below

$$P_{thr} = 1.38(n/10^{20})^{0.77} B^{0.92} R^{1.23} a^{0.76} \tag{1.2.81}$$

where P_{thr} is in MW. For the comparisons of the scaling and the experimental thresholds in different Tokamaks, please see Fig.1.2.3.

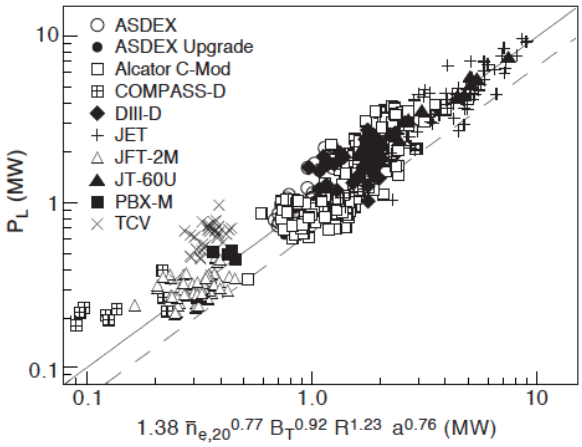

Figure 1.2.3: Fig.7 in [Doyle et al., 2007], the comparison of experimental power threshold for L-H transition with the scaling expression Eq.(1.2.81)[Wesson, 2011].

Besides the abrupt transition from L-mode to H-mode, another regime called

I-phase has been observed in many Tokamaks in recent years[Conway et al., 2011; Kallenbach et al., 2011; Zhang et al., 2013; Cheng et al., 2013]. The I-phase, which is a type of limit cycle oscillation, is an intermediate phase between L-mode and H-mode. The I-phase will appear if the heating power is a little lower than the threshold for L-H transition. Sometimes the I-phase is the final states and sometimes not. It depends on the circulation direction of the limit cycle manifold, see Fig.1.2.4 for further information. The H-mode can only appear after I-phase if the circulation direction of the limit cycle(I-phase) is counter-clockwise[Cheng et al., 2013]. For the applications of L-I-H transitions and further details about the I-phase, please see Chapters 3.2–3.3 and Chapter 4.4.

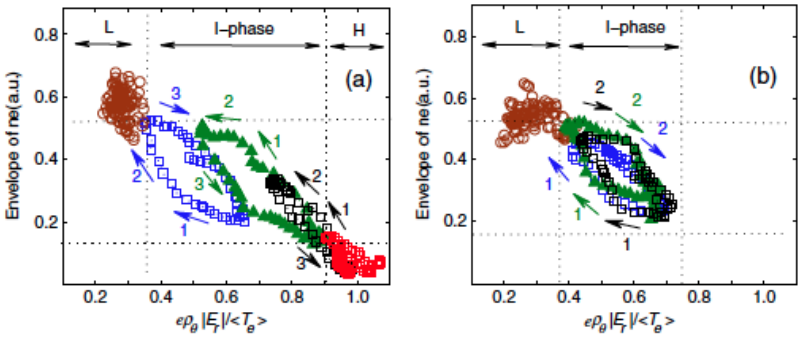

Figure 1.2.4: Fig.3 in [Cheng et al., 2013], the transitions of L-I-H and L-I.

As mentioned earlier, H-mode has been found in Stellarators as well as Tokamaks. There is no toroidal current in Stellarators, see Chapter 1.3.2, which might indicate that the toroidal current plays a minor role in the transition physics[Wagner, 2007]. In ASDEX, strong isotopic effects in transport with deuterium have been discovered which yield a better confinement. Lower transport in deuterium plasmas allows to reach H-mode at lower external heating power[Wagner, 2007]. It is reported that in JET with tritium plasmas this trend still exists[Righi et al., 1999]. In addition, Stellarator plasmas do not demonstrate an isotopic effect in the confinement. Also the power threshold, mentioned in Eq.(1.2.81), does not depend on the mass of isotopes[Wagner, 2007].

There is another form of H-mode called QH-mode(Quiescent H-mode), which was observed for the first time on DIII-D Tokamak in the USA in the year 2001. The QH-mode is obtained by applying neutral beam injection in the direction opposite to the plasma current(counter injection), plus cryopumping to reduce the density[Burrell et al., 2002]. In contrast to the ordinary H-mode, QH-mode is edge

localised modes(ELMs)-free, and the transport barrier can be produced for longer periods of time[Burrell et al., 2002, 2004]. To be explained, ELMs are significant expulsions of heat and particles with deleterious consequences for the vessel wall and machine operation[Burrell et al., 2005; Zohm, 1996], please Chapter 1.4.5. The disadvantage of QH-mode is the impurity accumulation[Burrell et al., 2002]. QH-mode are also observed in, for instance, ASDEX Upgrade Tokamak[Suttrop et al., 2004], JET Tokamak[Suttrop et al., 2005] and W7-AS Stellarator[Hirsch et al., 2008].

1.2.5 Interactions of drift wave turbulence and zonal flow

In fluid dynamics, turbulence is defined in terms of flow regimes characterized by chaotic property changes[Bradshaw, 2013]. In plasmas, turbulence is usually considered to be driven by the temperature gradient(∇T), which must also evolve in a way which is consistent with changes in the heat flux[Malkov and Diamond, 2009]. Therefore, the variation of the heat flux and its corresponding temperature gradient are both important for energy transport in fusion plasmas. At the same time, the energy transport phenomena are typically turbulent, and these are intrinsic nonlinear and non-diffusive[Dendy et al., 2013]. For further information in relation to the heat flux and temperature gradient, please see Chapters 2.4–2.5.

Drift waves are the most widely investigated forms of plasma turbulence in the magnetized confined plasmas[Horton et al., 2012]. The transitions from L-mode to H-mode, see Chapters 1.2.3–1.2.4, are supposed to be induced by interactions of drift wave turbulence and zonal flows[Wesson, 2011; Malkov and Diamond, 2009; Zhu et al., 2013, 2014]. A short introduction to generation of drift waves will be given as shown in [Chen, 1975].

Drift waves have a small but finite component of $\boldsymbol{k}$ along $\boldsymbol{B}_0$. Hence, the constant density surface resembles fluted column with a slight helical twist, see Fig.1.2.5. Then we can enlarge the cross section enclosed by the box in Fig.1.2.5 and envisage it in Cartesian coordinates, see Fig.1.2.6. The driving force for this instability is temperature gradient $Kn\nabla T_0$ if we assume $Kn = const.$; or the force can be density gradient $KT\nabla n_0$ if assuming $KT = const.$. Here we adopt the latter assumption for simplicity.

Since drift waves have a finite k_z, electrons can flow along the $\boldsymbol{B}_0$ direction to establish a thermodynamic equilibrium. Under this situation, they will obey Boltzmann's relation in the linearised approximation,

$$\frac{n_1}{n_0} = \frac{e\phi_1}{kT_e} \tag{1.2.82}$$

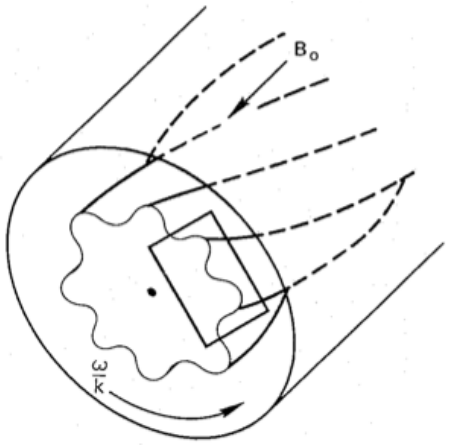

Figure 1.2.5: Fig.6-13 in [Chen, 1975], the geometry of drift instability in a cylinder. The rectangular region is also shown in Fig.1.2.6.

In Fig.1.2.6, n_1 and ϕ_1 are both positive at point A which is in the denser region. Based on this logic, we know that B is in the less dense region, so n_1 and ϕ_1 are negative. The difference of electric potential produces an electric field $\boldsymbol{E_1}$ between point A and point B. This electric field $\boldsymbol{E_1}$ will cause a drift velocity $\boldsymbol{v}_1 = \boldsymbol{E}_1 \times \boldsymbol{B}_0/B_0^2$ in the x-direction. As the drift waves pass by, travelling in the y-direction, oscillations of n_1 and ϕ_1 will be observed at point A. Also, the drift $\boldsymbol{v}_1$ will oscillate in time, and it is $\boldsymbol{v}_1$ that causes the oscillating density.

Since there is ∇n_0 in the $-x$-direction, the plasmas of different density will be brought to a point A by drift $\boldsymbol{v}_1$. Although the wave travels in the y-direction, a drift wave has a motion such that the fluid moves back and forth in the x-direction. The magnitude of v_{1x} is

$$v_{1x} = \frac{E_y}{B_0} = -i\frac{k_y\phi_1}{B_0} \tag{1.2.83}$$

Then we assume that v_{1x} does not vary with x and k_z is quite small by comparison with k_y, so the fluid oscillates incompressibly in the x-direction and therefore,

$$\frac{\partial n_1}{\partial t} = -v_{1x}\frac{\partial n_0}{\partial x} \tag{1.2.84}$$

This is the equation of continuity of guiding centres which do not have a fluid

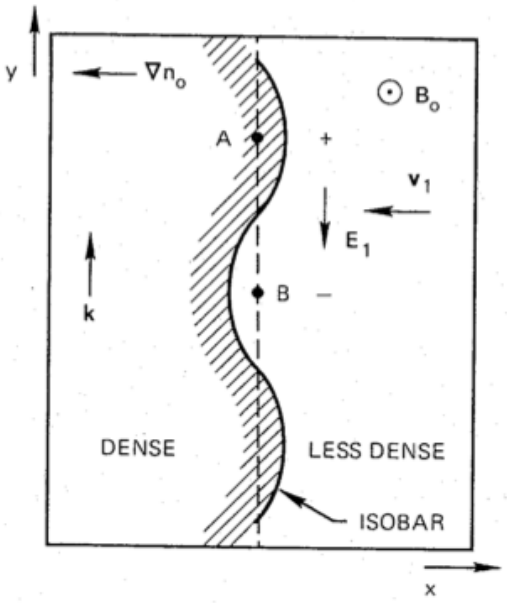

Figure 1.2.6: Fig.6-14 in [Chen, 1975], the physical mechanism of drift waves.

drift $\boldsymbol{v}_D$. Since $\boldsymbol{v_1}$ is a transverse oscillation, that is $\boldsymbol{v_1}$ is in +/- x-direction, while the wave vector is in the y-direction, the term $n_0 \nabla \cdot \boldsymbol{v_1}$ will vanish. We can rewrite Eq.(1.2.84) by using Eq.(1.2.82) and Eq.(1.2.83),

$$-i\omega n_1 = \frac{ik_y \phi_1}{B_0} n_0' = -i\omega \frac{e\phi_1}{KT_e} n_0 \tag{1.2.85}$$

so that we have,

$$\frac{\omega}{k_y} = -\frac{KT_e}{eB_0} \frac{n_0'}{n_0} = v_{De} \tag{1.2.86}$$

These waves are called drift waves that travel with the electron diamagnetic drift velocity, see Chapter 1.2.1. This drift velocity is in the y-direction, which corresponds to the azimuthal direction in cylindrical geometry[Chen, 1975]. The discussions above can be found in [Chen, 1975].

In the ideal Tokamak plasmas, the density fluctuation will cause particles to drift around the perturbation to generate a turbulent eddy[Gallagher, 2013]. This turbulent eddy will be discussed in the following paragraphs.

For an externally heated plasma that develops a temperature gradient ∇T_e

or ∇T_i, a relevant thermodynamic concept is the Carnot engine shown in Fig.1.2.7. There is an input energy Q on the left side. The vortices cycle over the correlation length l_c, connecting T_1 and T_2[Horton et al., 2012]. That means the drift wave turbulence is driven by the temperature gradient[Malkov and Diamond, 2009]. For further discussions of this relationship, see [Diamond et al., 1994; Kim and Diamond, 2003; Diamond et al., 2005, 2011; Zhu et al., 2013, 2014]. See also [Tynan et al., 2009] for a review of the drift wave turbulence.

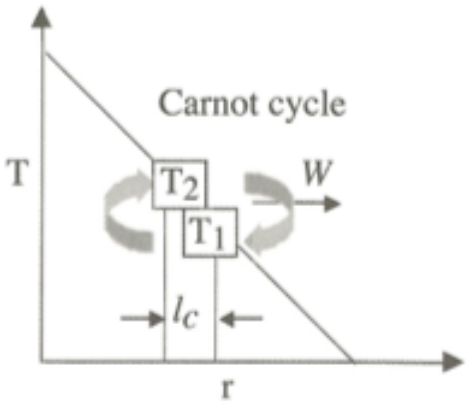

Figure 1.2.7: Fig.3.3 in [Horton et al., 2012], the diagram of the Carnot cycle for ∇T driven drift waves. W is the maximum energy released to the plasma turbulence.

As we also know, there exists a radial electric field in fusion plasmas that is often associated with the improved confinement H-mode. This radial electric field is consistent with the radial force balance equation for an ion of charge $Ze(E_r = \frac{1}{nZe}\frac{dp_i}{dr} - V_{\theta i}B_\phi + V_{\phi i}B_\theta)$. The radially varying E_r profile reduces the anomalous transport, which is partly raised by drift wave turbulence in fusion plasmas[Wesson, 2011]. A shear effect produced by the $\boldsymbol{E} \times \boldsymbol{B}$ force distorts the circular turbulent eddy of diameter L into an elongated elliptical shape after time t. The sheared velocity S_v is superimposed on an isotropic turbulent eddy, being perpendicular to the magnetic field[Wesson, 2011], see Fig.1.2.8 for further information. The minor axis of Fig.1.2.8(c) is reduced to $L_\perp$ and the major axis can be calculated by $L_\ell = L\sqrt{1 + S_v^2 t^2}$, see [Itoh et al., 1999]. Then the turbulent eddies can be suppressed or even destroyed. A fine scale poloidal $\boldsymbol{E} \times \boldsymbol{B}$ flow then can be self-generated by the turbulence nonlinearly via the Reynold stress. These flows are called zonal flows and are found to strongly reduce the saturated level of the turbulence by shear[Diamond et al., 2005]. The zonal flows have the following features: (1) radially localized, (2) axisymmetric($k_\phi = 0, n = 0$), (3) poloidally symmetric($k_\theta = 0, m = 0$) potential

and density, where k_ϕ and k_θ are the toroidal and poloidal components of the wave vector, respectively, such that n and m are the corresponding mode numbers[Zhao et al., 2006]. There is also a high-frequency zonal flow called the geodesic acoustic mode(GAM). The temporal frequency of a GAM is approximately proportional to the product of the sound speed(c_s) and the reciprocal of the major radius(R) of a toroidal fusion device[Miyamoto, 2006]. Unlike low frequency zonal flow, GAM has $n = 1$ perturbation in density[Krämer-Flecken et al., 2006]. The propagation directions of both classes of zonal flow are parallel[Zhu et al., 2014], furthermore both low and high-frequency zonal flows can suppress the drift wave turbulence intensity by shear[Itoh and Itoh, 2011]. In addition to zonal flows, mean sheared flows also play crucial roles in turbulence suppression. These mean flows are driven by the background gradients[Kim and Diamond, 2003]. Besides their shearing effects which act on turbulence, mean shear flows also affect the formation of zonal flows[Hsu and Diamond, 2015]. Please see review[Diamond et al., 2005] about zonal flows and Chapters 3–4 in this thesis for further applications to confinement regime transitions from L-mode to H-mode.

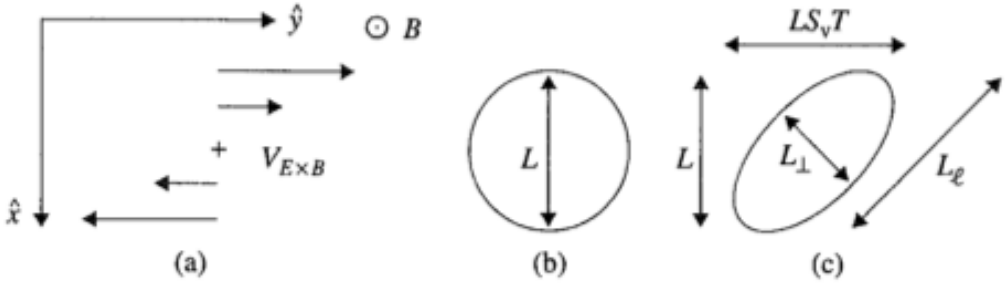

Figure 1.2.8: Fig.18.2 in [Itoh et al., 1999], the effect of a sheared $\boldsymbol{E}\times\boldsymbol{B}$ flow, $V_{\boldsymbol{E}\times\boldsymbol{B}}$ on a turbulent eddy. (a) illustrates the Cartesian coordinate with magnetic field and shear velocity. (b) the circular turbulent eddy with the size L. (c) distorted turbulent eddy by sheared flow.

As mentioned before, drift wave turbulence is driven by the temperature or density gradient. The zonal flows are self-generated by the turbulence nonlinearly, and act to suppress it[Diamond et al., 2005]. Thus, the relationship between the drift wave turbulence and zonal flows is similar to prey and predators[Diamond et al., 1994], see Chapter 2.2 for a description of the Lotka-Volterra or predator-prey model. This relationship is intrinsically nonlinear, not only because of the interactions between drift wave turbulence and zonal flows, but also because the damping of drift wave turbulence is nonlinear[Kaw et al., 2002]. We attach a schematic di-

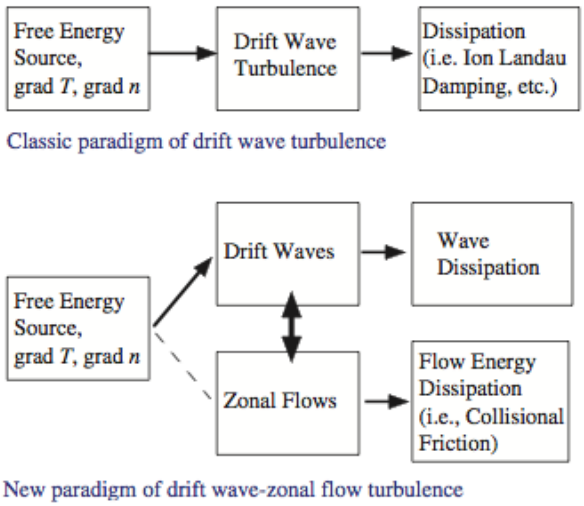

Figure 1.2.9: Fig.1 in [Diamond et al., 2005], classic and new paradigm for plasma turbulence.

agram to show this relationship, see Fig.1.2.9. In the classic paradigm, the drift wave turbulence is driven by the free energy source and dissipated by the Landau damping. The new paradigm illustrates two relationships: the one is the relationship between drift wave turbulence and free energy; the other is the predator-prey relationship between zonal flows and drift waves. In Chapter 1.2.4, it was discussed how zonal flow–drift wave interactions are commonly used to explain the L–H transition. Fig.1.2.9 illustrates why, in principle, we only need drift wave turbulence, zonal flow and a free energy source such as the temperature gradient to explain that phenomenon. As a result, reduced models provide an effective and interesting test of the conventional plasma physics narrative that is used to interpret the L–H transition.

We will give introductions to two representative reduced models, those of [Malkov and Diamond, 2009] and [Itoh and Itoh, 2011] in Chapter 2.4.1 and Chapter 2.4.2 respectively. For further discussion of these models, please see Chapter 3 and Chapter 4.

1.2.6 Heat pulse experiments and anomalous transport

In order to deepen understanding of anomalous transport phenomena in fusion plasmas, experiments involving heat pulse propagation have been implemented on many Tokamaks, for example, TFTR[Fredrickson et al., 1986, 1990; Kissick et al., 1996], JET[Tubbing et al., 1987; Rebut et al., 1988], ASDEX-Upgrade[Ryter et al., 2000],

JT-60U[Inagaki et al., 2006] and RTP[Gorini et al., 1993; Mantica et al., 1999; Hogeweij et al., 2000]. For Stellarators, we can take LHD[Inagaki et al., 2004, 2006, 2010; Tamura et al., 2007; Dendy et al., 2013] and W7-AS[Walter et al., 1998] for examples.

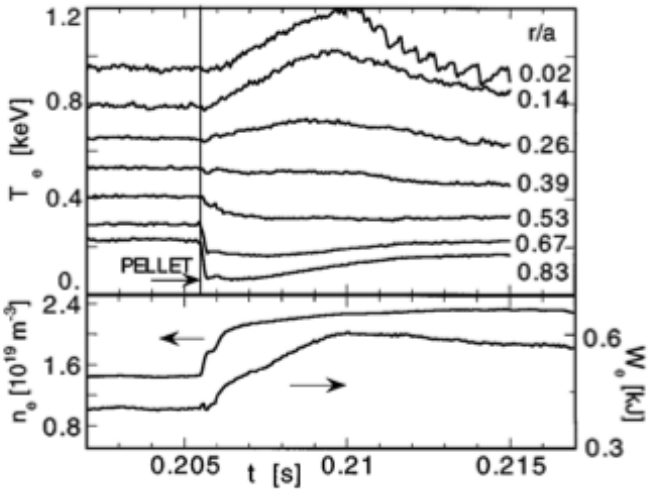

Figure 1.2.10: Fig.1 in [Mantica et al., 1999], the time evolution of electron temperature T_e, the averaged electron density $\bar{n}_e$ and the electron energy stored in the plasmas W_e for RTP discharge r19970224.024. A hydrogen pellet is injected at $t = 0.2054$ second in target plasmas.

In the experiments mentioned above, we can observe either a negative or a positive excursion in the core electron temperature from its steady state value, depending on the confinement properties of the plasmas as discussed in e.g.[Dendy et al., 2013] if we decrease the edge electron temperature by, for example, pellet injection. See Fig.1.2.10 and Fig.1.2.11 for detailed information on electron densities and electron temperatures in the RTP Tokamak and LHD Stellarator respectively.

From Fig.1.2.10, it can be seen that the trend of time series of the electron density n_e and the electron temperature T_e is quite different: T_e returns to the level before pellet injection while n_e is still rising. Hence it is not possible to give a phenomenological interpretation of the T_e rise as due to a dependence of electron density[Mantica et al., 1999]. However, similar phenomena are not observed in Fig.1.2.11(b) and Fig.1.2.11(e). This is an indication of the differences between heat pulse experiments in Tokamaks and Stellarators. The reason might be the distinction in q-profiles. There is larger q in outer plasmas in Tokamaks, whereas the q in outer plasmas in Stellarators is smaller than that in inner plasmas[Wesson, 2011].

For the further information about comparisons of heat pulse experiments between Tokamaks and Stellarators, please see [Inagaki et al., 2006]. It is apparent from Fig.1.2.11(a) that the transport process which underlies the heat pulse experiment is not diffusive. Consequently, the heat pulse propagation of electron temperature, which can be taken as a strong form of anomalous transport, is non-local and non-diffusive[Dendy et al., 2013].

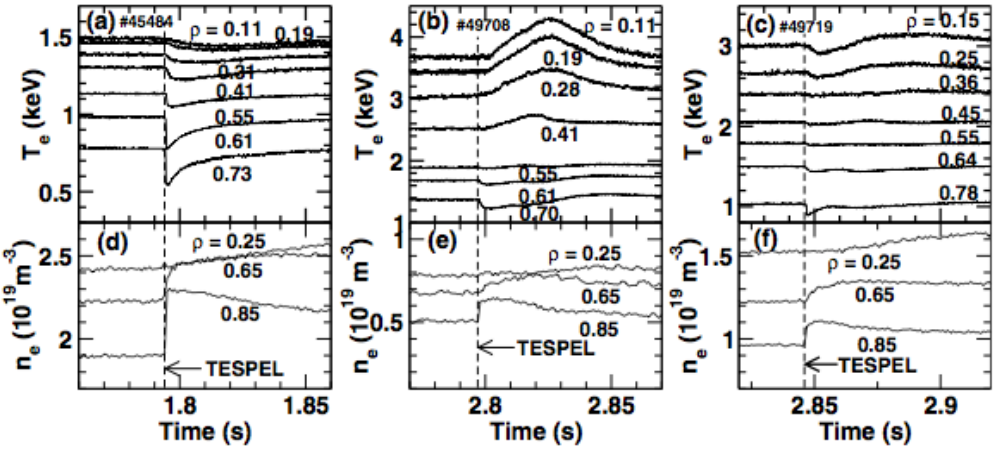

Figure 1.2.11: Fig.1 in [Inagaki et al., 2010], typical electron temperature T_e response to the pellet injection in (a) the local diffusive case (b) the abrupt T_e rise case and (c) the abrupt T_e drop case.

Further heat pulse propagation experiments indicate that the core electron temperature T_e rises following the edge cooling, which happens through the formation of a large temperature gradient(implying a thermal transport barrier) in a radially localized region of the RTP plasmas[Mantica et al., 1999]. It is also found that the electron transport is changed in heat pulse propagation experiments in which core T_e rises. That is to say, a significant decrease in electron heat diffusivity χ_e in the thermal transport barrier region may be required to explain the observations[Mantica et al., 1999]. Fig.5(a) in [Mantica et al., 1999] is a concrete evidence that core electron temperature T_e rise case observed in Fig.1.2.10 during rapid edge cooling by pellet injection is accompanied by a reduction in the electron heat diffusivity in the thermal transport barrier in RTP plasmas[Mantica et al., 1999].

Similar results are obtained when analysing datasets from heat pulse propagation experiments on LHD. It is found that the electron heat diffusivity χ_e has a nonlinear dependence on electron temperature T_e and electron temperature gradient ∇T_e. Furthermore, evidence of a reduction of electron heat diffusivity χ_e inside

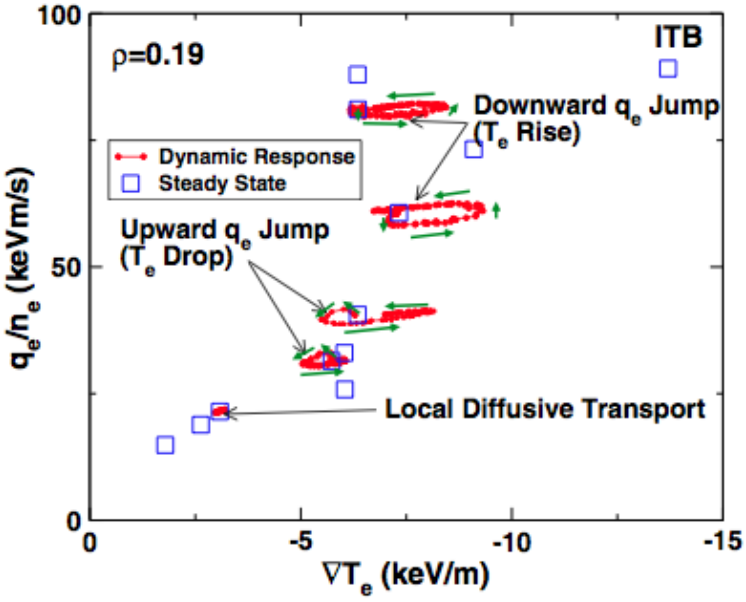

Figure 1.2.12: Fig.2 in [Inagaki et al., 2010], the bifurcation diagram containing stationary and dynamic state. This is expressed by the relationship between heat flux average by electron density q_e/n_e and electron temperature gradient ∇T_e in the core plasma($\rho = 0.19$) in LHD. The green arrows denote the variation directions.

the thermal transport barrier is also found in the experiments[Inagaki et al., 2004]. Consequently a linear diffusive model, which describes diffusion phenomena in terms of $q_e = -n_e\chi_0(r)\nabla T_e$, cannot explain the physics of the heat pulse[Inagaki et al., 2004]. It is also suggested that the electron heat diffusivity χ_0 inside(outside) the transport barrier decreases(increases) with the increasing electron temperature T_e in LHD. Thus the properties of transport inside the barrier are qualitatively different from outside the barrier in LHD[Inagaki et al., 2004]. In conclusion, the thermal transport barrier is indeed the region in which the value of the implied electron heat diffusivity $\chi_0 \simeq -\nabla T_e/q_e$ is reduced in the LHD Stellarator as well as in the RTP Tokamak[Inagaki et al., 2004].

In [Inagaki et al., 2010], a bifurcation(See Chapter 2.2.3) phenomenon is found, see Fig.1.2.12 for the details. If the value of electron temperature gradient ∇T_e is approximately less than 5keV/m, only local diffusive transport would be observed. Therefore, the $|\nabla T_e| = 5\text{keVm}^{-1}$ is the threshold or bifurcating point for diffusive/non-diffusive transport. For the branch where $|\nabla T_e| \geq 5\text{keVm}^{-1}$, the core T_e rise case is found if electron density averaged heat flux q_e/n_e is larger than 50keVm/s; the core T_e drop case is observed if q_e/n_e is smaller than 50keVm/s

approximately[Inagaki et al., 2010].

1.3 Magnetic confinement fusion devices

As we mentioned earlier in Chapter 1.1, magnetic confinement fusion(MCF) plasmas should be heated up to several hundred million kelvin to achieve fusion condition[McCracken and Stott, 2012]. However, there is no material which can sustain its physical properties at such a high temperature. Instead magnetic fields are used to confine the fully ionized plasmas. This leads to the concepts of Tokamaks and Stellarators, which we now review.

1.3.1 Tokamaks

The Tokamak concept was invented by physicists Andrei Sakharov and Igor Tamm. It uses magnetic field lines to confine high temperature plasmas in the shape of a torus[McCracken and Stott, 2012], see Figure 1.3.1 for a schematic diagram.

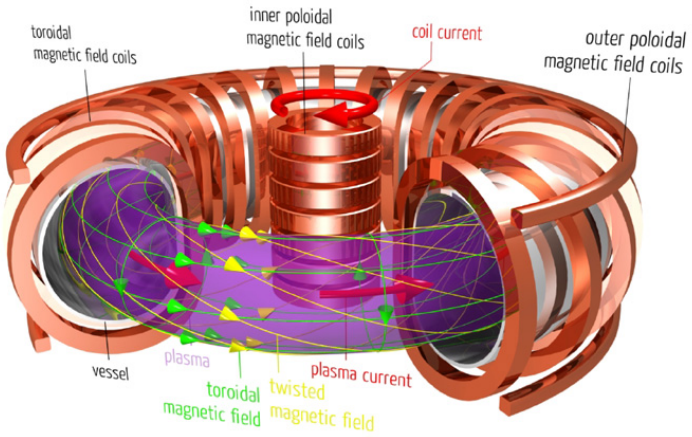

Figure 1.3.1: Schematic diagram of a Tokamak device from Wikipedia.

In order to achieve plasma equilibrium, the toroidal magnetic field B_ϕ is essential[Shafranov, 1963; Mukhovatov and Shafranov, 1971]. The toroidal magnetic field line is produced by the currents in coils linking the plasma. To reach the equilibrium where the plasma pressure is balanced by the magnetic forces, it is also necessary to have a poloidal magnetic field B_p[Wesson, 2011]. In Tokamaks, this magnetic field is induced by the plasma current itself and this current flows in the toroidal direction, please see red arrows in Figure 1.3.1. The combination of the

toroidal magnetic field and poloidal magnetic field produces helical or twisted field lines around the torus[Wesson, 2011], see the green and yellow arrows in Figure 1.3.1.

As the source of poloidal magnetic field, the plasma current[Ohkawa, 1970; Jukes, 1970] is driven by a toroidal electric field induced by a transformer in which a magnetic flux change through the torus is generated. The flux change is created by a current passed through primary coil around the torus, see Figure 1.3.2. Control of the shape needs additional toroidal currents, carried by suitable coils[Wesson, 2011]. The entire system of toroidal and poloidal coils, which together generate the Tokamak magnetic field configuration, is shown in Figure 1.3.1. For other auxiliary components of Tokamak, please see Figure 1.3.3 which shows the cross section of a Tokamak and introduction in [Freidberg, 2007] for further information.

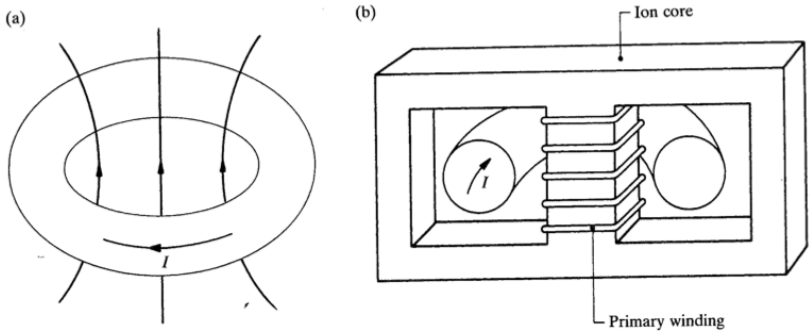

Figure 1.3.2: Figure 1.6.3 in [Wesson, 2011]. (a) The change of flux through the torus induces toroidal electric field which drives the toroidal current. (b) The flux change is produced by primary winding using a transformer core.

In most cases, auxiliary external heating[Mirnov, 1969; Rayle et al., 1969] and current drive are essential to support nuclear fusion. There are six main optional heating methods which are ohmic heating[Artsimovitch et al., 1964], neutral beam heating[Eubank et al., 1979], radio frequency heating[Porkolab, 1977], ion cyclotron resonance heating[Perkins, 1977], lower hybrid resonance heating[Perkins, 1977] and electron cyclotron resonance heating[Ott et al., 1980]. For their applications, please see Chapters 1.2.3–1.2.4 for transitions from low confinement regime(L-mode) to high confinement regime(H-mode), and see Chapters 3 and 4 for the consequences of different levels of external heating flux for predator-prey models. These include period doubling bifurcation and chaotic behaviour of the confinement properties.

Phenomena associated with plasma transport[Rechester and Rosenbluth, 1978; Hirshman and Sigmar, 1981] in Tokamak are important theoretically and experimen-

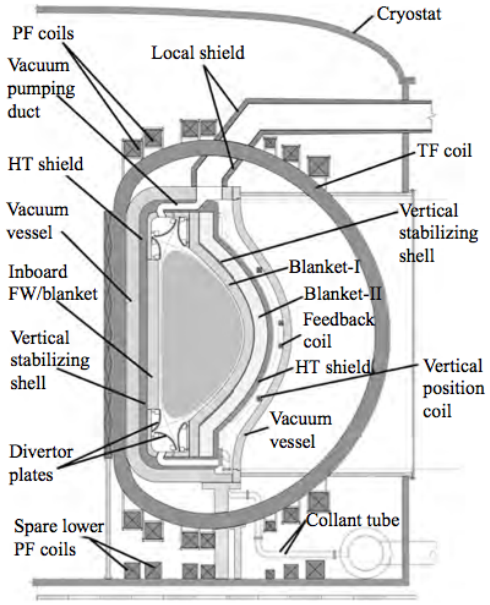

Figure 1.3.3: Figure 5.2 in [Freidberg, 2007]. The cross section of a Tokamak.

tally. In this thesis, we address aspects of the nonlinear interactions between zonal flows and drift wave turbulence in Tokamaks, which can be used to interpret the L-H transition[Diamond et al., 2005].

In Chapters 3 and 4, all the physical quantities in the predator-prey models used to interpret L–H transitions, such as electron temperature gradient, turbulence intensity and energy of meso-scale structures, can be observed directly or indirectly by modern plasma diagnostics. Examples include: for electron temperature, the Thomson scattering technique[Rajesh et al., 2000]; for turbulence intensity, correlative upper hybrid resonance backscattering(UHRBS) technique[Gusakov et al., 2006]; for properties of zonal flows, Langmuir probe array[Guosheng and Baonian, 2006]. For further information about auxiliary heating and diagnostics, please see [Wesson, 2011; Freidberg, 2007]. For further information about plasma transport, please see [Itoh et al., 1999; Yoshizawa et al., 2002; Diamond et al., 2010].

Joint European Torus(JET)

As the world's largest Tokamak device, a brief introduction to the Joint European Torus(JET) Tokamak will be given in this subchapter. The first JET plasma was produced in Oxfordshire, UK in the year 1983[Wesson, 2011]. From Fig.1.3.4, it can be seen that the poloidal section of JET is a D-shape in order to minimize stresses in

the toroidal field coils. The major and minor radii of the torus in JET are $R = 3.0$m and $a = 1.25$m respectively, which means the aspect ratio is $R/a = 2.4$. The toroidal magnetic field is up to 3.5T and the plasma current can reach 3.0MA.

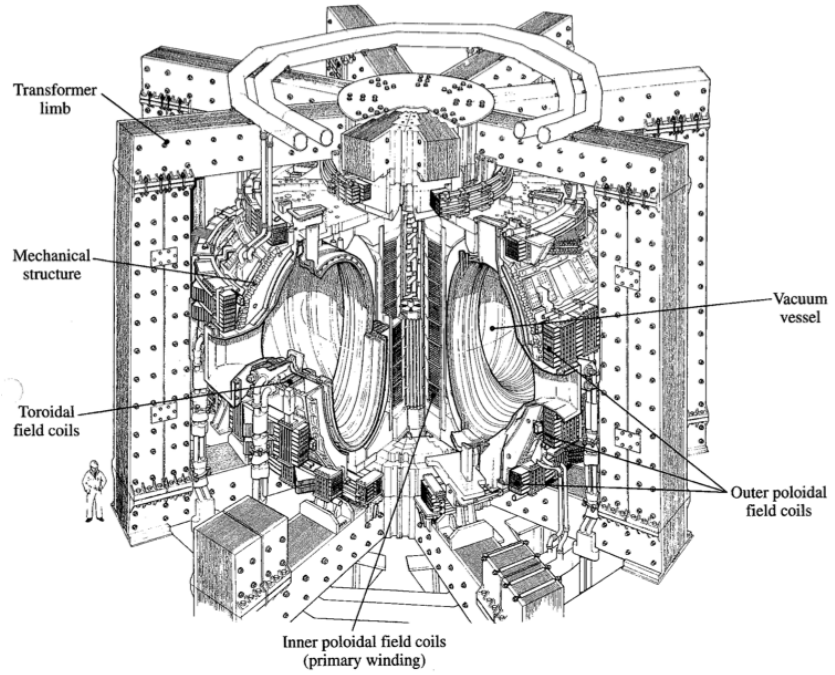

Figure 1.3.4: Fig.12.3.1 in [Wesson, 2011]. The configuration of the Joint European Torus(JET) Tokamak.

Over the past three decades, many significant plasma experiments were carried out on JET. A non-exhaustive list includes: limiter experiments[Borrass et al., 1993; Watson and Whitley, 1986; Cardozo and de Haas, 1990], magnetic separatrix experiments[Tanga et al., 1987b; Davies et al., 1999; Tanga et al., 1987a], transport and confinement experiments[McDonald et al., 2008; Schissel et al., 1991; Tubbing et al., 1991], high performance plasma and deuterium-tritium experiments[Gormezano et al., 1998; Team et al., 1992; Jacquinot et al., 1999], current drive and profile control experiments[Hawkes et al., 2001; Litaudon et al., 2002; Eriksson et al., 2004] and experiments on divertor and plasma-surface interactions[Coad et al., 2006; Hirai et al., 2007; Matthews et al., 2009], for further information about these experiments, please see [Wesson, 2011].

In 1997, during a 50%–50% deuterium-tritium experiment, JET achieved the world record nuclear fusion power of 16 MW[Fasoli et al., 1997], which indicates it attained a fusion energy gain factor Q about 0.7. The factor Q is defined as

$Q \equiv P_{fusion}/P_{heat}$. To reach the breakeven state, which means the energy produced by nuclear fusion can be used as auxiliary external heating, Q value should be greater than 1. In 1998, another Tokamak called JT-60 in Japan achieved a higher equivalent $Q = 1.05$, based however on extrapolation from pure deuterium 50%–50% deuterium-tritium but pure deuterium[Kishimoto et al., 1998]. Pending the appearances of DEMO and ITER, JET is still one of the most successful magnetic confinement devices in the world, and has unique deuterium-tritium capability.

1.3.2 Stellarators

Stellarators are an approach to magnetic confinement fusion which is regarded as complementary to Tokamaks. Like Tokamaks, Stellarators utilize magnetic fields to confine hot plasmas for nuclear reactions. The Stellarator was first proposed by American plasma physicist Lyman Spitzer in 1950s[Spitzer Jr, 1951; Spitzer Jr et al., 1954; Spitzer Jr, 1958]. In contrast to Tokamaks, there are various means to arrange and construct the coils which produce the Stellarator magnetic fields[Grieger et al., 1992]. The different aspects are that in Stellarators there is no plasma current and the relatively large toroidal field $B_\phi(r, \theta)$. In other words, any ohmically or externally driven toroidal current is zero[Freidberg, 2007]. Figs.1.3.5–1.3.6 show that in Stellarator the twisted magnetic field is generated by the helical coil current(blue arrows in Fig.1.3.5) and the toroidal coil current(red arrows in Fig.1.3.5), while in Tokamak the twisted magnetic field is induced by the externally imported toroidal magnetic field and the poloidal magnetic field due to the plasma current[Wesson, 2011].

In Stellarators, both components of the magnetic fields are created by currents flowing solely in external coils. Thus the plasma is inherently nonaxisymmetric[Helander et al., 2012]; the plasma cross section changes shape as it rotates around the magnetic axis. The absence of net plasma currents leads to inherently steady-state operation[Bosch et al., 2010]. There is no need for continuous power input to the plasma to maintain the magnetic configuration, so a large D-T Stellarator plasma could in principle reach rather high Q[Lyon et al., 2000]. Current drive power is zero or minimal, which leads to even higher efficiency, and there would be no current drive related reliability problems. There are also no dangerous current driven disruptions, so a thick vacuum vessel is not required for equilibrium control[Lyon et al., 2000].

In summary, a Stellarator has advantages and disadvantages by comparison to Tokamak. The Stellarator offers two major improvements with respect to the typical Tokamak. First on account of its inherently steady state, it does not require

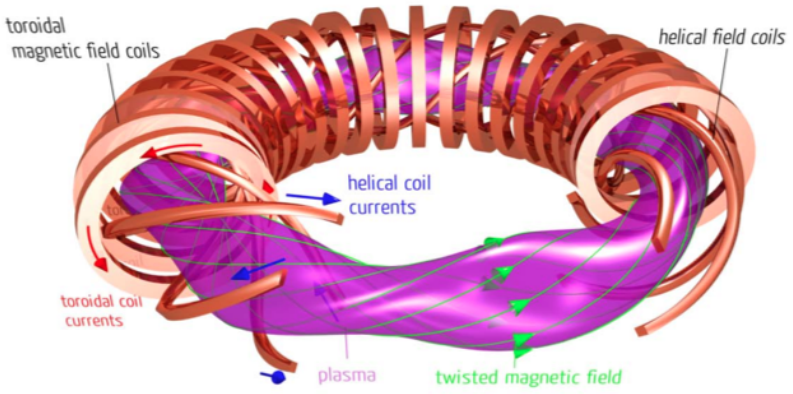

Figure 1.3.5: Schematic diagram of structure of Stellarator from the Wikipedia.

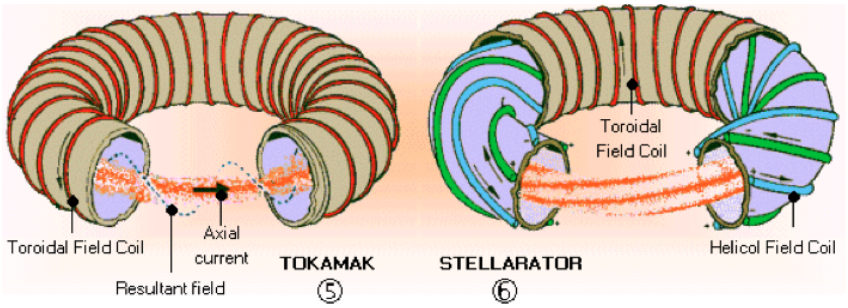

Figure 1.3.6: Comparison of Tokamak and Stellarator from the Wikipedia.

ohmic current and current drive. Second, without net toroidal current flowing, the possibilities of exciting a major disruption[Schuller, 1995] are considerably reduced. Both of these features are highly desirable[Freidberg, 2007]. On the other hand, the Stellarator has its disadvantages. The external coils required to generate magnetic field that are rather complicated technologically compared to Tokamak. The resulting additional costs must compensate for the disadvantages and costs of current drive and of the corresponding possible plasma disruptions in a Tokamak[Freidberg, 2007]. Although the structures of Tokamak and Stellarator are different, the phenomena of transitions from L-mode to H-mode, drift wave turbulence – zonal flow interactions, and heat pulse propagation can be observed in both types of MCF plasma. For the similarities and differences, please see Chapters 1.2.3–1.2.6.

Large Helical Device(LHD)

The final chapter of this thesis relates to heat pulse experiments in the superconductivity Large Helical Device(LHD) in Japan, which contains the largest Stellarator plasmas in the world. For a schematic diagram, please see Figure 1.3.7. The LHD design has a vacuum vessel 3.5m in major radius and 0.6m in minor radius. The strength of the magnetic field generated by the helical coils can reach 3T. The optimum performance of upgraded LHD can reach electron temperature $T_e \simeq 10.0$ keV and confinement time $\tau_E \simeq 0.36$ second[Freidberg, 2007; Iiyoshi et al., 1999].

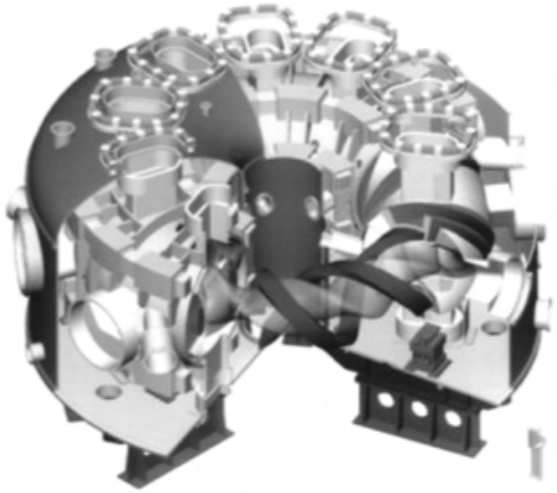

Figure 1.3.7: Schematic diagram of Large Helical Device(LHD).

LHD is thus an experimental almost on the scale of the JET Tokamak. There are correspondingly many experiments operating on the LHD, for instance, divertor physics experiments[Ohyabu et al., 1994; Masuzaki et al., 2002; Morita et al., 2001; Kobayashi et al., 2007], MHD experiments[Sakakibara et al., 2001; Toi et al., 2004; Sakakibara et al., 2008; Watanabe et al., 1992], transport and confinement transitions[Ida et al., 2003; Shimozuma et al., 2003; Yamada et al., 2000, 2001], and interaction of plasmas and surface[Hino et al., 2004, 2007; Nishimura et al., 2005; Kobayashi et al., 2006]. Heat pulse propagation experiments have been carried on LHD recently. In Chapter 5, we will propose a novel model whose outputs provide a good quantitative match to the heat pulse propagation phenomena measured in the LHD.

1.4 Instability in Tokamaks

Trying to contain very hot plasmas within magnetic fields is similar to positioning a ball on the top of a hill – any tiny displacement grows with increasing speed. The plasmas are inherently unstable and try to escape from the magnetic fields. Some kinds of instabilities cause a sudden loss of the whole plasma(plasma disruption); others reduce the energy confinement time; and some become saturated, or can be nonlinearly stabilised[McCracken and Stott, 2012]. There are many types of instabilities in Tokamaks, and the most important include plasma disruption, sawtooth instability, tearing mode, ballooning mode and edge localised modes(ELMs). Here brief introductions, appear in [McCracken and Stott, 2012] and [Wesson, 2011], to the instabilities mentioned above will be given in the Chapter 1.4.

1.4.1 Disruption

A major disruption in a Tokamak is dramatic event where the plasma current abruptly terminates and confinement is lost. It is preceded by a sequence of events with four phases. First, there are changes in the underlying plasma conditions – an increase in the current or the density. When these changes reach some critical value, the second phase starts with an increase of magnetic fluctuations in the plasma, whose growth time is of the order 10ms. The sequence then passes a second critical value and enters the third phase, where the decreasing of electron temperature moves on a faster time scale. The confinement deteriorates and the central temperature decreases dramatically. The plasma current profile flattens and the change in inductance produces a negative voltage spike. Finally comes the quench of the current, meaning that the current in the plasma decays to zero. Disruptions cause very large forces on the wall of the Tokamak, and these forces increase with the plasma size[McCracken and Stott, 2012], please see Fig.1.4.1. The discussions above can be found in [McCracken and Stott, 2012].

1.4.2 Sawtooth instability

The central temperature of a Tokamak plasma may in a periodic way, increasing in a linear ramp to the peak value, dropping abruptly and then starting to increase again. This type of feature is called sawtooth, see Fig.1.4.2 for the sawtooth temperature variation. From observations at different radii, a flattening of the core temperature profile in the plasma is found when the temperature drops. There is also an increase in the temperature further out, which indicates a sudden outflow of energy. In order to explain this phenomenon, Kadomtsev proposed a successful model[Kadomtsev,

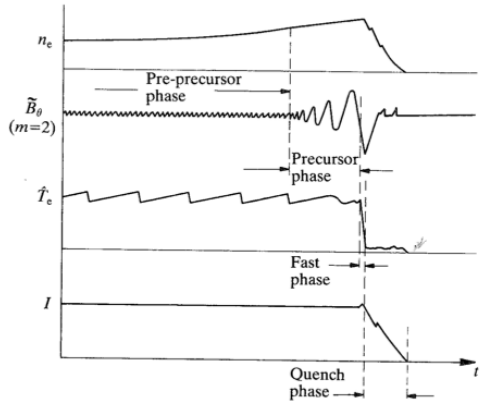

Figure 1.4.1: Fig.7.7.2 in [Wesson, 2011]. Four phases of plasma disruption.

1975]. In his model, the sawtooth phenomenon is taken as the behaviour in terms of magnetic islands, which tangle up the magnetic field lines. Eventually, the field lines sort themselves out by magnetic reconnecting. This reconnection allows plasmas in the hot central region to mix with cold plasmas. It used to be assumed that the sawtooth phenomena are triggered when the safety factor $q = m/n$ reached unity in the plasma core[McCracken and Stott, 2012]. The discussions above can be found in [McCracken and Stott, 2012].

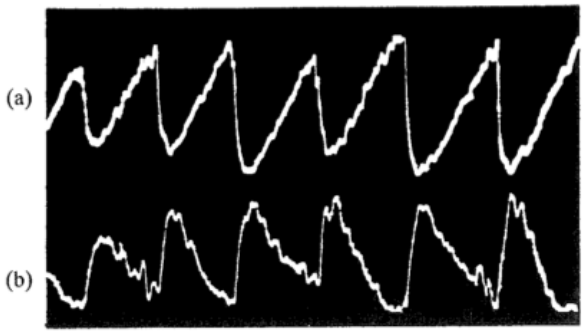

Figure 1.4.2: Fig.7.6.1 in [Wesson, 2011]. The X-ray emission from (a) the central region (b) the outer region of plasma.

1.4.3 Tearing modes

The tearing mode instability in a Tokamak plasma is driven by the radial gradient of the equilibrium toroidal current density. This name is derived from the tearing and rejoining of magnetic field lines which occur during the instability as a conse-

quence of finite resistivity. The growth of this type of instability is rather slow over the most of the plasma because the linear growth rate scales with the resistivity which is very low in a highly conducting plasma. Also, over most of the plasma the resistivity is negligible and the bulk motion can be described in terms of ideal magnetohydrodynamics(MHD). However, at the resonant surface for the mode the $\boldsymbol{v} \times \boldsymbol{B}$ contribution to Ohm's law goes to zero and, in the neighbourhood of this resonant surface, the term of ηj becomes significant in balancing the induced electric field $\boldsymbol{E}$(recall that $\boldsymbol{E} + \boldsymbol{v} \times \boldsymbol{B} = \eta \boldsymbol{j}$). Thus the theories of tearing mode involve solving one set of equations over most of the plasma, and another set in a resistive layer around the resonant surface[Wesson, 2011], please see Fig.1.4.3 for further information. The discussions above can be found in [Wesson, 2011].

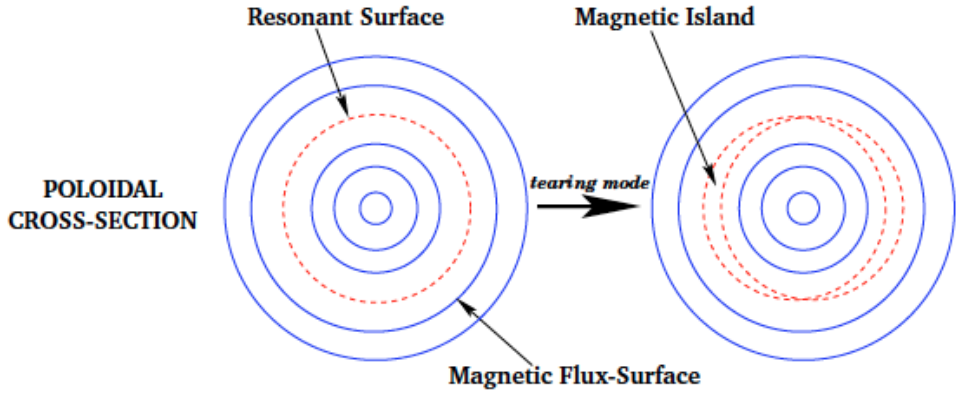

Figure 1.4.3: Schematic diagram of tearing mode in a poloidal cross section of a Tokamak from Richard Fitzpatrick's report.

1.4.4 Ballooning modes

Let us recall that good magnetic field curvature is defined as the centre of curvature(vector $\boldsymbol{R}$ in Fig.1.4.4) being in the opposite direction(from plasma core to inner side of Tokamak) to the pressure gradient. It follows that the conclusion that the curvature is stabilizing on the inner (small R) side of the Tokamak and destabilizing on the outer side, please see Fig.1.4.4 for details. If the pressure gradient is sufficiently high, it is possible for the perturbation to be concentrated in the region of destabilizing curvature. The potential energy thus released can be greater than that required for the line bending inherent in the variation of the perturbation along a field line. The resulting instability is the ballooning mode[Wesson, 2011]. In order to suppress this type of instability, a upper limit of β value($\beta = \dfrac{p}{B^2/2\mu_0}$) should

be applied. The ballooning phenomenon reduces the temperature and pressure in the core of plasmas and contributes to the linear instability underlying the edge localised mode[Snyder et al., 2002], which will be introduced in the next subchapter. The discussions above can be found in [Wesson, 2011].

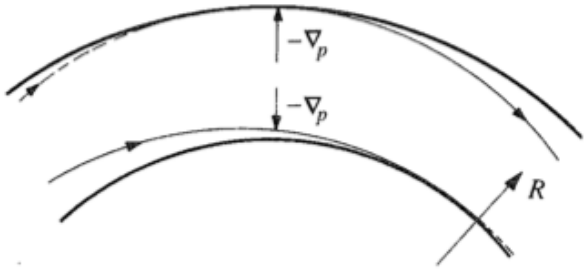

Figure 1.4.4: Fig.6.13.1 in [Wesson, 2011]. Showing the destabilizing curvature on the outer side of the Tokamak and stabilizing on the inner side.

1.4.5 Edge localised modes(ELMs)

The discovery of H-mode(mentioned in the Chapter 1.2.4) of Tokamak operation in ASDEX was accompanied by the observation of short bursts of a new instability called edge localised modes(ELMs).

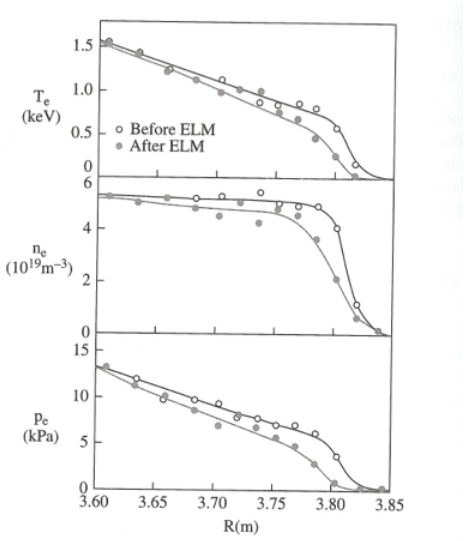

Figure 1.4.5: Fig.7.17.1 in [Wesson, 2011]. This figure demonstrates the falling in temperature, density and pressure respectively resulting from ELMs in JET.

These bursts have been found subsequently in association with H-modes in other Tokamaks. In the H-mode, a transport barrier is formed at the edge, and this leads to steep pressure and current density gradients that are subjected to instability. Each burst causes a reduction in density and temperature in the outer zone of the plasma. A fall in the density and temperature across the plasma radius is also observed and the existence of ELMs causes some deterioration of plasma confinement through reduction of the density, temperature and pressure[Wesson, 2011], please see Fig.1.4.5 for details. The discussions above can be found in [Wesson, 2011].

Chapter 2

Introduction to nonlinear dynamics

2.1 Reviews of reduced models in magnetic confinement fusion

In most cases, energy transport in toroidal magnetically confined fusion plasmas is determined by the effects of micro-scale turbulence and meso-scale coherent nonlinear structures, together with their mutual interactions. These structures include zonal flows(ZFs) and geodesic acoustic modes(GAMs)[Hasegawa and Wakatani, 1987; Coda et al., 2001; Jakubowski et al., 2002; McKee et al., 2003; Conway et al., 2005; Diamond et al., 2005; Gupta et al., 2006; Yamada et al., 2008], which are poloidally localised flows. The importance of these structures for energy transport was highlighted in large scale numerical simulations[Dorland et al., 2000; Jenko et al., 2000]. Zonal flows have been the subject of extensive theoretical and observational work[Hasegawa and Wakatani, 1987; Coda et al., 2001; Jakubowski et al., 2002; McKee et al., 2003; Conway et al., 2005; Diamond et al., 2005; Gupta et al., 2006]. There is now substantial experimental support for the long-standing hypothesis[Diamond and Kim, 1991] that the growth of zonal flows is driven by the averaged Reynolds stress of micro-scale turbulence. The latter can be locally suppressed by the resultant shear flow, thereby generating a temporally quasi-discontinuous enhancement of global energy confinement: the L-H transition[Wagner et al., 1982]. Whether zonal flows or geodesic acoustic modes are preferentially formed under specific plasma conditions, and how they compete, has been addressed from various perspectives[Manfredi et al., 2001; Li et al., 2005; Kasuya et al., 2008], and remains an open question. Both zonal flows and geodesic acoustic modes can

strongly affect the level of turbulent transport, and normally the lower frequency zonal flows have a stronger regulating influence than the high-frequency geodesic acoustic modes[Wesson, 2011]. They can compete with each other indirectly due to the parallelism of poloidal velocities of zonal flows and GAMs[Zhu et al., 2014]. For a recent review of experimental observations of the interaction between mesoscale structures (such as zonal flows and geodesic acoustic modes) and micro-scale structures (such as drift wave turbulence), see [Fujisawa, 2011]; of drift wave turbulence, particularly in relation to transitions in global confinement, see [Tynan et al., 2009]; and of the L-H transition, see [Wagner, 2007]. A recent review of these physics issues in a broad context is provided by [Diamond et al., 2011]. As emphasised in [Fujisawa, 2011; Tynan et al., 2009; Wagner, 2007; Diamond et al., 2011] and references therein, recent diagnostic advances are transforming the experimental study of time evolving micro-turbulence and coherent nonlinear meso-scale structures during confinement transitions. This generates fresh theoretical challenges. In addition, the ability to understand and control this plasma physics phenomenology will be central to the successful operation of the next step magnetic confinement fusion experiment ITER[Doyle et al., 2007].

It is noted by Malkov and Diamond in [Malkov and Diamond, 2009], hereafter referred to as MD, that transport models derived from the fundamental equations of plasma physics continue to add much to our understanding but "tend to be increasingly, if not excessively, detailed. Therefore, there is high demand for a simple, illustrative theoretical model with a minimal number of critical quantities responsible for the transition. Such models usually yield or encapsulate basic insight into complicated phenomena." One approach in fusion plasmas is that of zero-dimensional models for the interaction between microturbulence and coherent nonlinear structures, in particular Lotka-Volterra or predator-prey[Leboeuf et al., 1993; Diamond et al., 1994]. The properties of Lotka-Volterra systems, both mathematically and from the perspective of fusion plasma physics, are by no means fully explored and remain an active field of research[Vano et al., 2006; Hofbauer and So, 1994; Bian and Garcia, 2003; Sprott et al., 2005; Bian, 2010; Itoh and Itoh, 2011; Miki and Diamond, 2011]. For fusion applications, a key step is to establish agreement between the outputs of such models and the observed confinement phenomenology, which should ideally extend to the character of measured time traces of key properties near transitions, for example. Recent experimental results[Schmitz et al., 2012; Xu et al., 2012b] are encouraging in this respect. There is an important additional requirement. The zero-dimensional models used for this application should be robust, in the sense that the character of their outputs remains largely invariant

against minor changes in the formulations of the models. This requirement for robustness has been explicitly noted[Watkins et al., 1999] in the other main class of zero-dimensional heuristic model for magnetised plasma confinement, namely sandpiles, both in fusion[Diamond and Hahm, 1995; Newman et al., 1996; Carreras et al., 1998; Dendy and Helander, 1998; Chapman et al., 1999, 2001; Gruzinov et al., 2002] and in solar-terrestrial[Watkins et al., 1999; Chapman et al., 1998; Hughes et al., 2003; Dendy et al., 2007] contexts, and requires investigation for Lotka-Volterra or predator-prey applications to fusion plasmas.

There are several aspects to the degree of invariance of the phenomenology generated by a zero-dimensional model when aspects of the model are changed. First, what is the long-time behaviour of the system and how sensitive is this to variation in the model parameters[Haken, 1983; Schuster and Just, 2006]? Second, how sensitively does the nature of the system's evolution towards its final state depend on the initial conditions? Is there an attractive fixed point or limit cycle towards which the system flows as time passes? If so, what is its basin of attraction? Third, how sensitive is the path to this attractor? This is particularly important for models which, as here, generate sharp transitions in the values of system variables which may replicate some key features of confinement transitions in tokamaks. If the initial conditions are varied, is the time at which the transition occurs delayed or brought forward, or does its character change, for example? Further, given two zero-dimensional models which are schematically distinct but adjacent, how similar is the phenomenology of their solutions? An example is provided here by our extension of the model of MD[Malkov and Diamond, 2009] to incorporate two variables, rather than one, representing different classes of meso-scale coherent nonlinear field, in a four-variable system. The case of two predators and one prey was considered theoretically in the model of Itoh & Itoh[Itoh and Itoh, 2011], hereafter referred to as II, and by Miki and Diamond[Miki and Diamond, 2011], and there is recent experimental motivation[Schmitz et al., 2012; Xu et al., 2012b]. Insofar as a zero-dimensional model turns out to be robust with respect to the considerations outlined (attractors; initial conditions; structural adjacency), confidence is strengthened in the mapping from model variables to specific plasma properties, and from the time evolving behaviour of the model to that of the plasma system.

The transport of energy across magnetically confined fusion plasmas, and the storage of energy within them, also reflects a wide range of turbulent and nonlinear phenomenology. There is extensive experimental evidence for transport phenomena that are non-diffusive and may be non-local. Examples have been found in many tokamak plasmas, for example JET[Hogeweij et al., 1991; Tubbing et al.,

1987], DIII-D[Luce et al., 1992; DeBoo et al., 2012; Petty and Luce, 1994], JT-60U[Inagaki et al., 2006], HL-2A[Sun et al., 2010], Alcator C-Mod[Rice et al., 2013], TEXTOR[Spakman et al., 2008], TEXT[Brower et al., 1990], RTP[Mantica et al., 1999] and TFTR[Fredrickson et al., 1986], as well as stellarator like LHD[Inagaki et al., 2006, 2010; Dendy et al., 2013; Tamura et al., 2007; Inagaki et al., 2004]. A broad range of techniques for data analysis have been used to identify various forms of perturbation of heat and particle fluxes from their steady states. Measurements of the spatio-temporal propagation of strongly nonlinear localised heat pulses provide a particularly interesting, and potentially fruitful, challenge to theoretical understanding and models.

In the sub-chapter below, we will first introduce the Lotka-Volterra(predator-prey) model in Chapter 2.2. The methodology used throughout this thesis will be given in Chapter 2.3. For the reduced models for energy confinement for low dimensional nonlinear dynamics – the MD model and II model, we will discuss them in Chapter 2.4. The reduced model for heat pulse propagation – Dendy's model[Dendy et al., 2013], is presented in Chapter 2.5.

2.2 Lotka-Volterra models

In order to interpret the nonlinear phenomena mentioned in Chapter 1, an introduction to the relevant nonlinear dynamics will first be given in this Chapter. Nonlinear dynamics methodology for low-dimensional system is becoming increasingly important in the fields of modern mathematics, physics, chemistry and so on, see for example [Strogatz, 2014; Ott, 2002; Guastello et al., 2009; Izhikevich, 2007; Thompson and Stewart, 2002; Tufillaro et al., 1992; Jackson, 1992; Bertuglia and Vaio, 2005; Pike and Lugiato, 1987; Robertson and Combs, 2014; Rasband, 1997; Iooss and Adelmeyer, 1998; Hilborn, 1994; Drazin, 1992]. A key element is that nonlinear system does not obey the principle of superposition and that the input and output are not proportional.

The Lotka-Volterra or predator-prey model was first proposed in 1926 by Volterra [Volterra, 1926] in order to interpret the relationship of populations between predators and preys and independently by Lotka[Lotka, 1925] to describe chemical reactions. Predator-prey models are applied in subjects across physics[McKane and Newman, 2005; Satulovsky and Tomé, 1994], chemistry[Liu et al., 2004], ecology[Yoshida et al., 2003; Vano et al., 2006], neurology[Thatcher, 1998], economics[Anderton, 2003; Mehlum et al., 2003] and so forth.

As mentioned in the Chapter 1.2.5, the interactions between micro-scale drift

wave turbulence, low-frequency zonal flow and high-frequency zonal flow(GAM) are key features of the L-H transition in fusion plasma physics. Zonal flows are driven by the drift wave turbulence via Reynold stress and suppress the turbulence by shear. The suppression of anomalous transport by drift wave turbulence will produce a transport barrier, which can induce the formation of H-mode[Diamond et al., 2005]. The relation of these interactions can be modelled as a predator-prey process. The drift wave turbulence is taken as the prey, and the two kinds of zonal flows are regarded as the predators[Zhu et al., 2013, 2014]. Based on these assumptions, many fusion plasma oriented predator-prey models have been proposed to interpret the relationship, for example, by Diamond[Diamond et al., 1994], Kim[Kim and Diamond, 2003], Malkov[Malkov and Diamond, 2009], Miki[Miki and Diamond, 2011; Miki et al., 2013b], Itoh[Itoh and Itoh, 2011], Zhu[Zhu et al., 2013, 2014] and Douglas[Douglas et al., 2013].

2.2.1 Lotka-Volterra model

The general form of predator-prey model is:

$$\frac{dx_i}{dt} = r_i x_i \left(1 - \sum_{j=1}^{N} a_{ij} x_j\right) \tag{2.2.1}$$

where x_i is the population of species i, r_i is the intrinsic growth rate of species i, N denotes the number of species in the system and a_{ij} is the rate of interaction between species i and j.

Jacobian Matrix

The Jacobian matrix and related concepts are named after German mathematician Carl Gustav Jacob Jacobi. In the vector calculus, the Jacobian matrix is the matrix comprising all first-order partial derivatives of a function of vector values[Arrowsmith and Place, 1992].

Suppose that a given function $\mathbf{F} : \mathbb{R}^n \to \mathbb{R}^m$ which regards as input the vector $\mathbf{x} \in \mathbb{R}^n$ and produces as output the vector $\mathbf{F}(\mathbf{x}) \in \mathbb{R}^m$. The Jacobian matrix $\mathbf{J}$ of $\mathbf{F}$ is an $m \times n$ matrix, defined as follows, see [Arrowsmith and Place, 1992]:

$$\mathbf{J} = \begin{bmatrix} \dfrac{\partial \mathbf{F}}{\partial x_1} & \cdots & \dfrac{\partial \mathbf{F}}{\partial x_n} \end{bmatrix} = \begin{bmatrix} \dfrac{\partial F_1}{\partial x_1} & \cdots & \dfrac{\partial F_1}{\partial x_n} \\ \vdots & \ddots & \vdots \\ \dfrac{\partial F_m}{\partial x_1} & \cdots & \dfrac{\partial F_m}{\partial x_n} \end{bmatrix} \tag{2.2.2}$$

If $m = n$, then the matrix is a square matrix. Moreover, its determinant is called the Jacobian determinant of $\mathbf{F}$, which will be further discussed in the next subchapter. If $m = 1$, $\mathbf{F}$ is a scalar field and the matrix is changed as the gradient of $\mathbf{F}$, which is a row vector of partial derivatives of $\mathbf{F}$, see [Arrowsmith and Place, 1992].

Theoretical analysis of 2-ODE Lotka-Volterra model

The simplest Lotka-Volterra model only comprises two species, i.e. one prey and one predator, see [Kaplan and Glass, 1995]. The model equations are given here. They can be discussed analytically as follows.

$$\frac{dR}{dt} = \alpha R - \beta RF \tag{2.2.3}$$

$$\frac{dF}{dt} = -\gamma F + \delta RF \tag{2.2.4}$$

where R is the prey population, F is the predator population, t is time and α, β, γ and δ are the positive coupling coefficients of the two species.

In order to find the equilibrium points, we let $d/dt = 0$. Then we have

$$\alpha R - \beta RF = 0 \tag{2.2.5}$$

$$-\gamma F + \delta RF = 0 \tag{2.2.6}$$

We solve these equations and obtain two equilibrium points(fixed points), which are

$$R = 0, F = 0 \tag{2.2.7}$$

and

$$R = \frac{\gamma}{\delta}, y = \frac{\alpha}{\beta} \tag{2.2.8}$$

Then we calculate the Jacobian matrix of this 2-ODE Lotka-Volterra model, which gives

$$\mathbf{J}(R, F) = \begin{bmatrix} \alpha - \beta F & -\beta R \\ \delta F & \delta R - \gamma \end{bmatrix} \tag{2.2.9}$$

We will obtain the Jacobian matrix of the first fixed point if we substitute Eq.(2.2.7) into Eq.(2.2.9). The first fixed point indicates that both of the two species are in extinction. The Jacobian matrix of the first fixed point is given below,

$$\mathbf{J}(0, 0) = \begin{bmatrix} \alpha & 0 \\ 0 & -\gamma \end{bmatrix} \tag{2.2.10}$$

and the eigenvalues of this Jacobian matrix are

$$\lambda_1 = \alpha, \lambda_2 = -\gamma \tag{2.2.11}$$

It is illustrated that the fixed point (0,0) is a saddle point due to one positive and one negative real eigenvalues.

Also, in addition we obtain the Jacobian matrix of the second fixed point if we substitute Eq.(2.2.8) into Eq.(2.2.9). The second fixed point indicates both of the two species populations are oscillatory. The Jacobian matrix of the second fixed point is given below,

$$\mathbf{J}\left(\frac{\gamma}{\delta}, \frac{\alpha}{\beta}\right) = \begin{bmatrix} 0 & -\dfrac{\beta\gamma}{\delta} \\ \dfrac{\alpha\delta}{\beta} & 0 \end{bmatrix} \tag{2.2.12}$$

and the eigenvalues of this Jacobian matrix are

$$\lambda_1 = i\sqrt{\alpha\gamma}, \lambda_2 = -i\sqrt{\alpha\gamma} \tag{2.2.13}$$

The eigenvalues of the second fixed point $\left(\frac{\gamma}{\delta}, \frac{\alpha}{\beta}\right)$ are in conjugate pairs and the real parts are zero. The populations of two species oscillate in a cycle, see [Kaplan and Glass, 1995]. For further applications of eigenvalues of Jacobian matrix, please see Chapter 3.4.

Numerical analysis of 2-ODE Lotka-Volterra model

We illustrate the dynamics numerically for the simple 2-ODE Lotka-Volterra model. We assume that the supplies of grass, water, sunshine and air are abundant. The 2-ODE Lotka-Volterra equations are given here.

$$\frac{dR}{dt} = R(\alpha - \beta F) \tag{2.2.14}$$

$$\frac{dF}{dt} = -F(\gamma - \delta R) \tag{2.2.15}$$

R and F are the populations of rabbits and foxes respectively. Let us define α as the intrinsic growth rate of rabbits, γ as the population extinction rate of foxes, β and δ as the positive coupling coefficients.

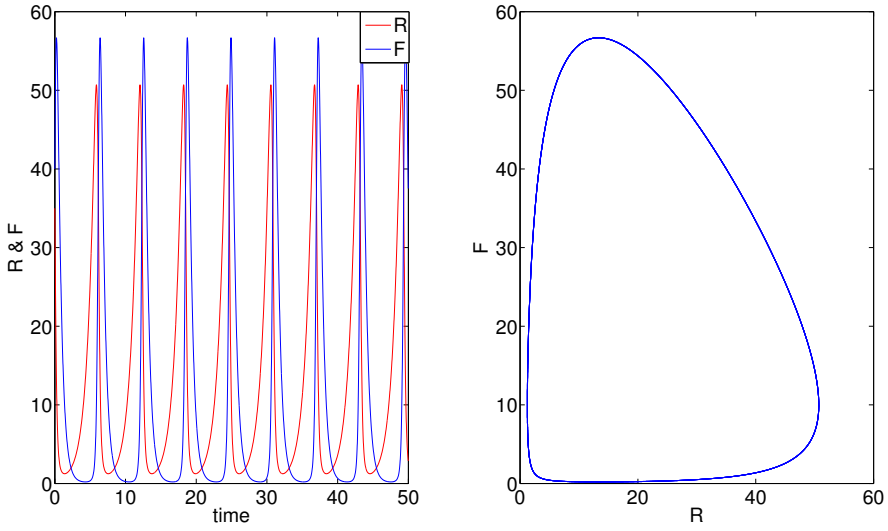

Figure 2.2.1: 2-ODE Lotka-Volterra model. Defining R as rabbits, F as foxes. Left panel: time series of 2-ODE Lotka-Volterra model. Right panel: phase plot of 2-ODE Lotka-Volterra model. The parameters and initial conditions are given as $\alpha = 1, \beta = 0.1, \gamma = 2, \delta = 0.15, R_0 = 35, F_0 = 40$.

We plot numerical solutions for given initial values and coefficients, as shown in Fig.2.2.1. The left panel displays the time series of populations of rabbits and foxes. It is shown that the two time series oscillate with the same amplitude and frequency respectively. The right panel describes the phase plot of two populations. The phase portrait is a closed contour.

Closed contours in the phase plane suggest that there is a constant of motion. From Eqs.(2.2.14-2.2.15), we have

$$\frac{dR}{dF} = -\frac{\frac{\alpha}{F}-\beta}{\frac{\gamma}{R}-\delta} \tag{2.2.16}$$

Make integration on both sides,

$$\int \left(\delta - \frac{\gamma}{R}\right) dR = \int \left(\frac{\alpha}{F} - \beta\right) dF + C' \tag{2.2.17}$$

$$\delta R - \gamma lnR = \alpha lnF - \beta F + C \tag{2.2.18}$$

where $C = \delta R_0 - \gamma lnR_0 - \alpha lnF_0 + \beta F_0$.

There is a ***Constant of Motion*** in 2-ODE Lotka-Volterra model.

Pendulum oscillations

In fact, many second-order ordinary differential equations can be converted into 2-ODE Lotka-Volterra model with a constant of motion, for example, pendulum oscillations. In the elementary course, the nonlinearity of the pendulum is omitted by the small angle approximation i.e. $\theta \simeq sin\theta$. In this subchapter, we analyse not only small angle approximating pendulum system but also large angle regime where the pendulum whirls over the top[Strogatz, 2014]. The discussion here in this subchapter appears in [Strogatz, 2014].

Without the external driving and internal damping forces, the oscillation of a single conservative pendulum can be described as follow:

$$\frac{d^2x}{dt^2} + A\sin x = 0 \tag{2.2.19}$$

where A is defined as g/L, g is the acceleration due to gravity, L is the length of the string, and x is the angle from the downward vertical[Strogatz, 2014].

We make transformations on Eq.(2.2.19) as the Lotka-Volterra model,

$$\frac{dx}{dt} = v \tag{2.2.20}$$

$$\frac{dv}{dt} = -A\sin x \tag{2.2.21}$$

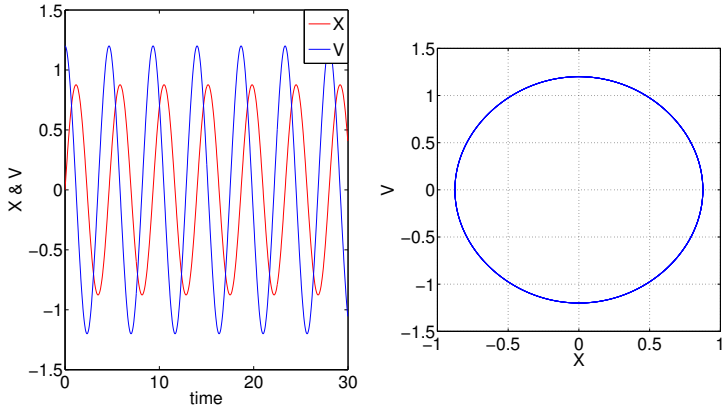

Figure 2.2.2: Pendulum oscillation model with small angle approximation. Left panel: time series of pendulum oscillation model. Right panel: phase plot of pendulum oscillation model. The parameter and initial conditions are $A = 2, x_0 = 0, v_0 = 1.2$.

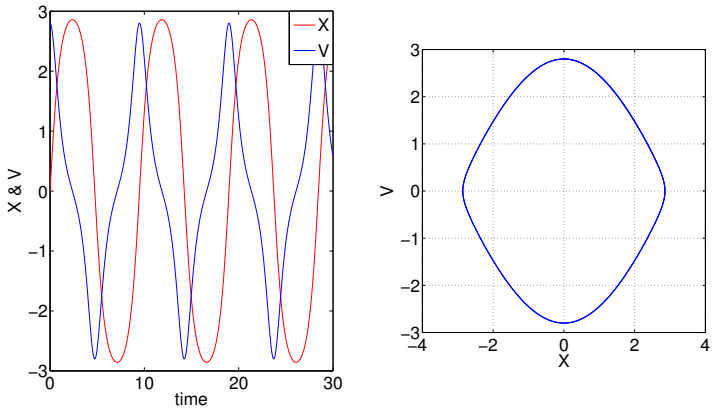

Figure 2.2.3: Pendulum oscillation model with large angle. Left panel: time series of pendulum oscillation model. Right panel: phase plot of pendulum oscillation model. The parameter and initial conditions are $A = 2, x_0 = 0, v_0 = 2.8$.

It is apparent to discover that the initial velocity v_0 is the control parameter. The pendulum will whirl over the top if the v_0 value is large enough. For the small angle regime(small v_0 value), the time series and phase plot of pendulum oscillations are shown in Fig.2.2.2,

However, when the v_0 values increase from $v_0 = 1.2$ to $v_0 = 2.8$ then to $v_0 = 2.8285$, the feature of the system gradually transfers from linear one to nonlinear one. And these scenarios are not the same, as shown in Fig.2.2.3 and Fig.2.2.4 respectively.

Fig.2.2.3 illustrates the pendulum oscillation with initial condition $v_0 = 2.8$. Under this situation the large angle regime appears, the phase plot is not a circle as Fig.2.2.2.

Fig.2.2.4 plots the critical value of pendulum oscillation, the mass point swings over the top point. In this case, the phase plot is no longer a circle but an oscillation.

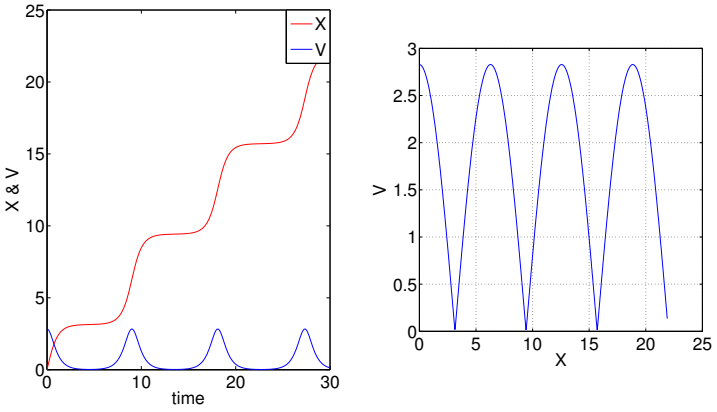

Figure 2.2.4: Pendulum oscillation model in critical angle condition. Left panel: time series of pendulum oscillation model. Right panel: phase plot of pendulum oscillation model. The parameter and initial conditions are $A = 2, x_0 = 0, v_0 = 2.8285$.

The discussions above can be found in [Strogatz, 2014].

2.2.2 Limit cycle manifold

A limit cycle manifold is a type of closed trajectory of which the neighbouring trajectories are not closed[Strogatz, 2014]. The ambient trajectories near the limit cycle would be attracted to itself or be repelled away from it.

Figure 2.2.5 illustrates three types of limit cycle. The left panel is the stable limit cycle, which means all ambient trajectories would be attracted by it. There is an unstable fixed point(source) inside the stable limit cycle. The eigenvalues of Jacobian matrix of this unstable fixed point have a conjugate pair, and their real parts are positive.(Please see the stable limit cycle in transitions from L-mode to H-mode in fusion experiments in Chapter 1.2.4 and their theoretical approaching models in Chapter 2.4.1, Chapters 3 and 4).

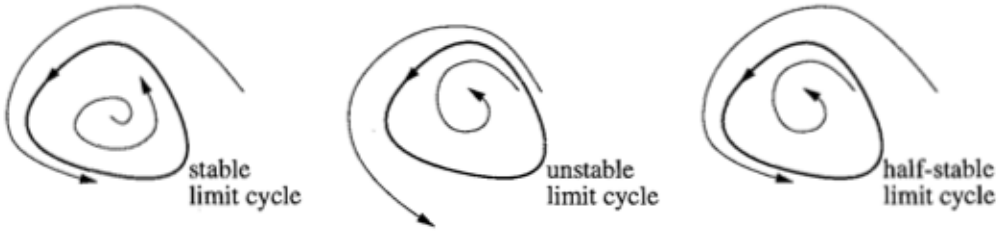

Figure 2.2.5: Figure 7.0.1 in [Strogatz, 2014]. Three types of limit cycles, which are stable limit cycle, unstable limit cycle and half-stable limit cycle.

The unstable limit cycle is demonstrated in the middle panel of Fig.2.2.5. It repels all trajectories away from itself. The fixed point inside the unstable limit cycle must be a stable one(sink). What is more, the eigenvalues of the Jacobian matrix of stable fixed point have a conjugate pair, and their real parts are negative.

The right panel shows an example half-stable limit cycle. Inside of the limit cycle there exists a stable fixed point(sink) and all ambient trajectories outside are attracted by the limit cycle.

Among these three types of limit cycles, the stable limit cycle is scientifically important. This system oscillates in the absence of an external periodic force. Also the whole system always returns to the limit cycle if it is slightly perturbed[Strogatz, 2014].

Van der Pol oscillations

The Van der Pol oscillator was originally proposed by Balthasar Van der Pol[Van der Pol and Van der Mark, 1927] in 1927. The oscillator can be described by a second order ordinary differential equation, see [Drazin, 1992]

$$\frac{d^2x}{dt^2} + \eta(x^2 - 1)\frac{dx}{dt} + x = 0 \tag{2.2.22}$$

where $\eta \geq 0$, then the corresponding Lotka-Volterra form is given below,

$$\frac{dx}{dt} = v \tag{2.2.23}$$

$$\frac{dv}{dt} = -x - \eta(x^2 - 1)v \tag{2.2.24}$$

The time series and phase plot of pendulum oscillations are shown in Fig.2.2.6,

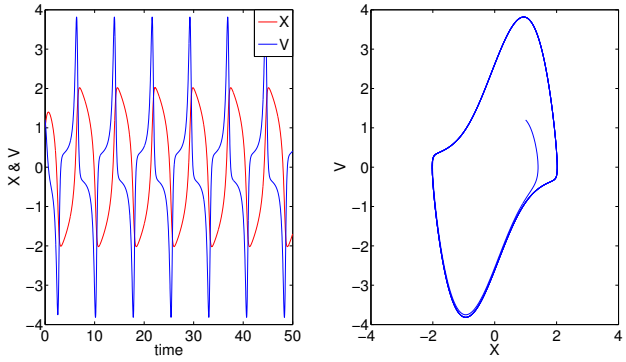

Figure 2.2.6: Van der Pol oscillation model. Left Panel: time series of Van der Pol oscillation model. Right Panel: phase plot of Van der Pol oscillation model. The parameter and initial conditions are $\eta = 2, x_0 = 0, v_0 = 1.2$.

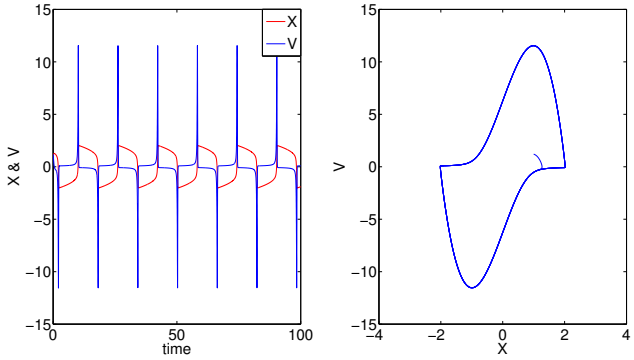

Figure 2.2.7: Van der Pol oscillation model. Left panel: time series of Van der Pol oscillation model. Right panel: phase plot of Van der Pol oscillation model. The parameter and initial conditions are $\eta = 8, x_0 = 0, v_0 = 1.2$.

With the condition of $\eta = 0$, the Van der Pol oscillation is reduced to harmonic oscillation which has no intrinsic damping rate. However, with increasing η

relaxation oscillation appears, as shown in Fig.2.2.7,

One can prove that "*The Van der Pol model has a unique, stable limit cycle for each* $\eta > 0$."[Strogatz, 2014].

We numerically solve the Van der Pol equation by ordering $\eta = 1.5$ and starting from $(\dot{x}, x) = (0.5, 0)$ at $t = 0$ as shown in Fig.2.2.8. These parameters and initial conditions are not identical with those in Figure 2.2.6 and Figure 2.2.7. In Figure 2.2.8, left panel illustrates the phase plot of $\dot{x}$ and x, while right panel demonstrates the time series of x. It is apparent that, although the system starts from inside the Van der Pol circle, the trajectory is ultimately attracted by the circle. We will acquire the identical results if the system starts from the outside of the circle. Numerically, we can conclude that the circle is a stable limit cycle.

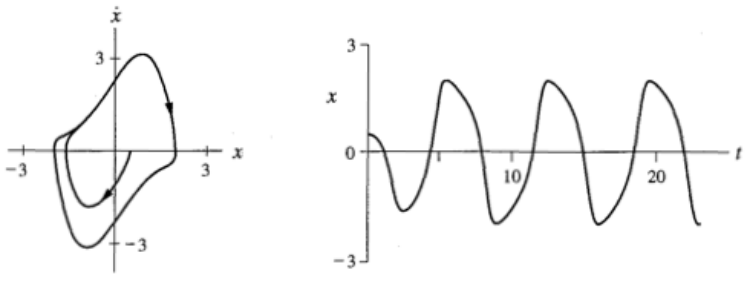

Figure 2.2.8: Figure 7.1.4 and Figure 7.1.5 in [Strogatz, 2014]. Numerical solution of Van der Pol equation for $\eta = 1.5$ and starting from $(\dot{x}, x) = (0.5, 0)$ at $t = 0$.

2.2.3 Period-doubling bifurcation

In order to illustrate period-doubling bifurcation, we will consider a circuit experiment. The apparatus is shown in Fig.2.2.9. The simple circuit consists of a signal generator, a diode and an inductor. The generator produces a voltage varying sinusoidally in time[Hilborn, 1994], see Chapter 4 for the further discussion for the oscillating external heating rate in fusion plasmas. The discussions here in Chapter 2.2.3 appear in [Hilborn, 1994].

The function of voltage is shown below,

$$v(t) = V_0 \sin 2\pi f t \tag{2.2.25}$$

in which V_0 and f are amplitude of the generator voltage and frequency of signal oscillation respectively. Here V_0 is the control parameter. We obtain a period-doubling bifurcation by changing V_0[Hilborn, 1994].

In [Hilborn, 1994], bifurcation is defined as follow:

"*Bifurcation means a splitting into two parts. The term bifurcation is commonly used in the study if nonlinear dynamics to describe any sudden change in the behaviour of the system as some parameter is varied. The bifurcation then refers to the splitting if the behaviour of the system into two regions: one above, the other below the particular parameter value at which the change occurs.*"

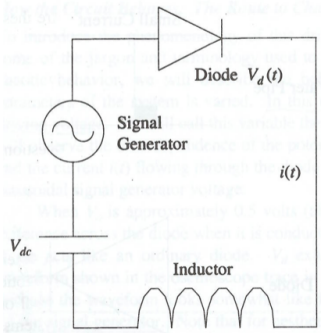

Figure 2.2.9: Figure 1.1 in [Hilborn, 1994]. The inductor-diode circuit. $i(t)$ is the electric current. $V_d(t)$ is the electric potential difference across the diode.

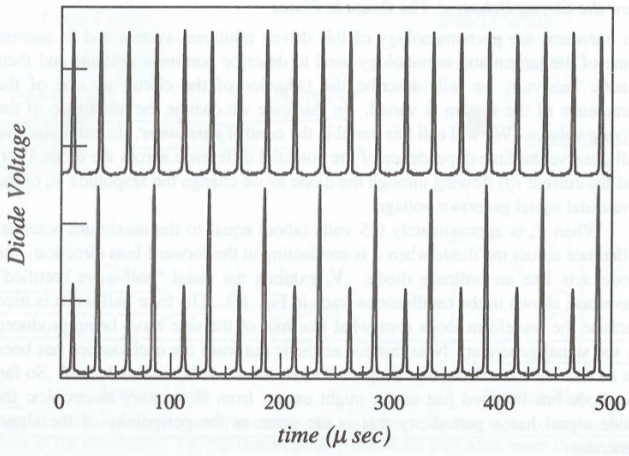

Figure 2.2.10: Figure 1.3 in [Hilborn, 1994]. The time series of diode voltage. Upper panel shows period-1, while lower panel illustrates period-2.

The change from period-1 to period-2 is an instance of period-doubling bifurcation, see Fig.2.2.10. We start from period-1 behaviour. Under this situation, the frequency of diode voltage signal(upper panel of Fig.2.2.10) is identical with that of the signal generator voltage. If the amplitude of signal generator voltage

slightly increases, the time series of diode voltage is split into two segments. The diode voltage signal's repetition period is now twice that of the signal generator, see lower panel of Fig.2.2.10[Hilborn, 1994].

If we continue to increase the amplitude of the signal generator, we will observe period-4 oscillation and period-8 oscillation, see upper and lower panels of Fig.2.2.11 respectively. The period-8 situation is discernible by paying attention to the smallest peaks[Hilborn, 1994].

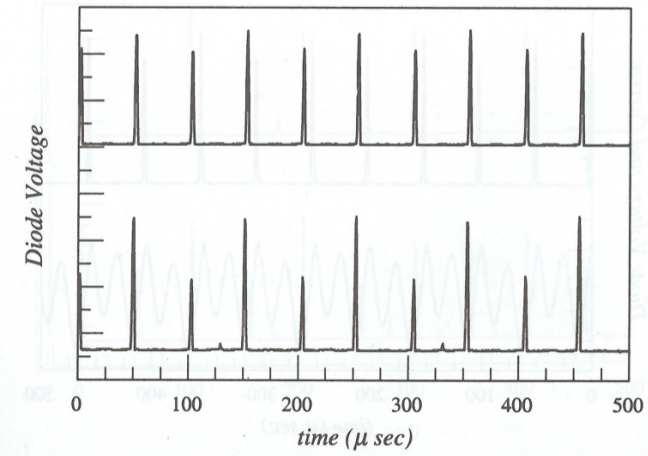

Figure 2.2.11: Figure 1.4 in [Hilborn, 1994]. The time series of diode voltage. Upper panel shows period-4, while lower panel indicates period-8.

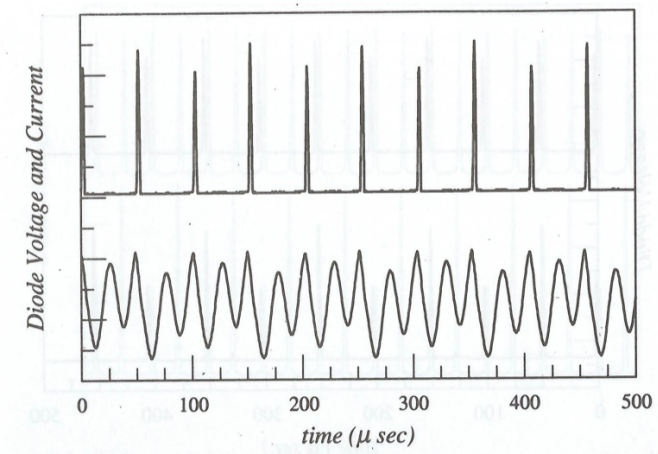

Figure 2.2.12: Figure 1.5 in [Hilborn, 1994]. Upper panel is period-4 time series of diode voltage. Lower panel is the corresponding time series of current.

Fig.2.2.12 merely demonstrate period-4 behaviour. The upper panel plots the time series of diode voltage which is identical with upper panel of Fig.2.2.11. The lower panel indicates the corresponding time series of circuit current. Here the four distinct peaks size are more clearly identified[Hilborn, 1994].

If we still increase the amplitude of the signal generator, the time series of diode voltage become non-periodic, as Figure 2.2.13 shown. This phenomenon is identified as chaotic sequences[Hilborn, 1994], which will be introduced in Chapter 2.2.4.

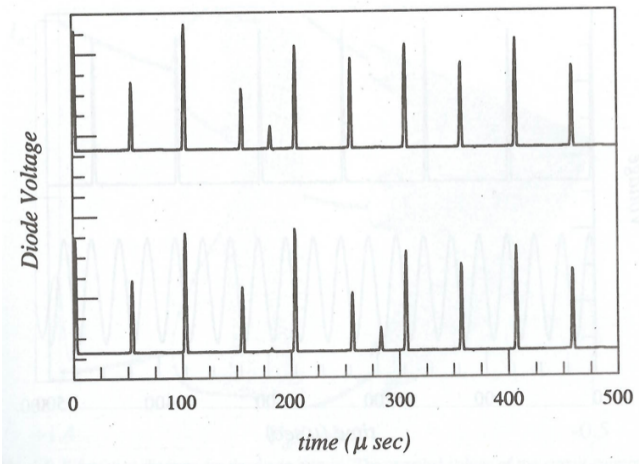

Figure 2.2.13: Figure 1.6 in [Hilborn, 1994]. Diode voltage as a function of time. Both of upper and lower panels are no longer periodic.

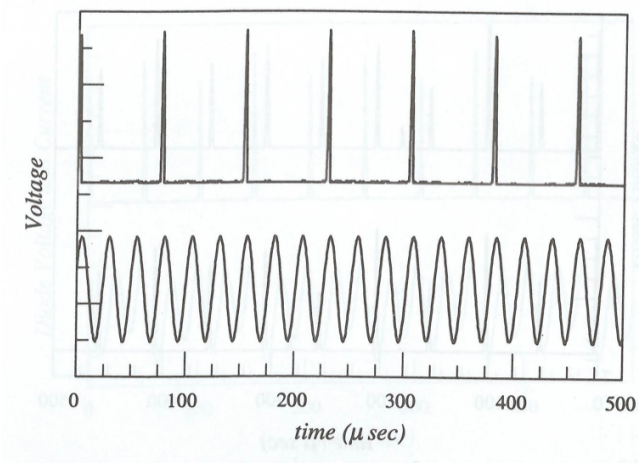

Figure 2.2.14: Figure 1.7 in [Hilborn, 1994]. Upper panel is period-3 time series of diode voltage. Lower panel is the signal generator voltage as a function of time.

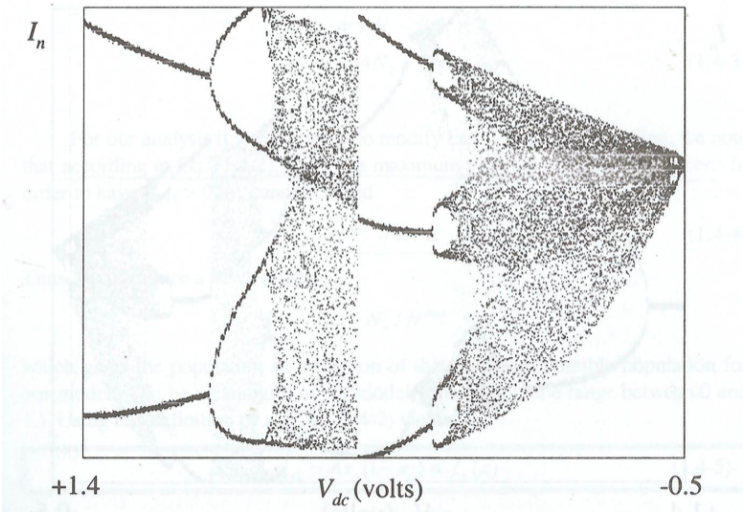

Figure 2.2.15: Figure 1.8 in [Hilborn, 1994]. Bifurcation diagram for the diode circuit.

We can find period-3 oscillations of time series of diode voltage if we keep increasing the amplitude of signal generator. Upper and lower panel of Figure 2.2.14 display the time series of diode voltage and circuit current respectively.

With those time series, we are able to plot bifurcation diagram, which can be utilized to show the bifurcation behaviour with respect to the amplitude of the signal generator. As Figure 2.2.15 presented, period-2 is discovered on the left. The broad, fuzzy regions are chaotic behaviour. Period-3 bifurcating period-6 and finally to more chaos is found near the middle of the diagram. The behaviour goes back to period-1 at the far right[Hilborn, 1994].

The bifurcating phenomenon is not unique if we adjust the control parameter. Figure 2.2.16 shows another bifurcation diagram which is for a smaller amplitude of signal generator[Hilborn, 1994].

Beside the diode circuit, there are numerous processes can exhibit the bifurcation phenomena[Zhu et al., 2014; Linsay, 1981; Giglio et al., 1981; Shraiman et al., 1981], for example, the logistic map[May et al., 1976]. The map equations are given below.

$$x_{n+1} = Ax_n(1 - x_n) \equiv f_A(x) \tag{2.2.26}$$

for logistic map, in which A is the control parameter. The discussions above can be

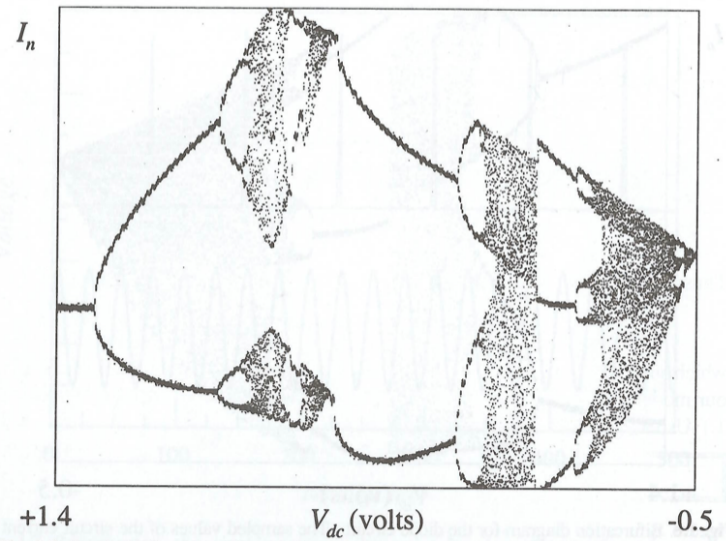

Figure 2.2.16: Figure 1.9 in [Hilborn, 1994]. Another bifurcation diagram for a smaller signal generator amplitude.

found in [Hilborn, 1994].

2.2.4 Chaos

We start our discussion on chaos from the classical Lorenz equations[Lorenz, 1963]:

$$\frac{dx}{dt} = \sigma(y - x) \tag{2.2.27}$$

$$\frac{dy}{dt} = rx - y - xz \tag{2.2.28}$$

$$\frac{dz}{dt} = xy - bz \tag{2.2.29}$$

This model was proposed by Lorenz in 1963 when focusing research on notoriously unpredictable weather forecasts. As mentioned in [Strogatz, 2014],

"*Lorenz found that the solution to his equations never settled down to equilibrium or to a periodic state – instead they continued to oscillate in a irregular, aperiodic fashion. Moreover, if he started his simulation from two slightly different initial conditions, the resulting behaviour would soon become totally different. The implication was that the system was inherently unpredictable – tiny errors in measuring the current state of the atmosphere (or any other chaotic system) would be amplified rapidly, eventually leading to embarrassing forecasts.*

We now attempt to solve Lorenz equation numerically. Here, σ, r, $b > 0$ are parameters. σ and r are Prandtl number and Rayleigh number respectively, while b has no name[Strogatz, 2014]. We adopt the Lorenz's logic and set $\sigma = 10$, $r = 28$ and $b = 8/3$.

Figure 2.2.17 shows the numerical solutions of the Lorenz equation under those parameters given above. The left three panels illustrate the time series of x, y and z. The right panel demonstrates the 3-D phase plot. The initial conditions are $(x_0, y_0, z_0) = (0, 1, 0)$. The butterfly-like trajectory begins from $(0, 1, 0)$ then swings to the right region, and dives in the centre of a spiral on the left region. After a quite slow outward spiral, the trajectory return to the right region, spiral around several times, shoots over to the left region, spiral around, and so on indefinitely[Strogatz, 2014].

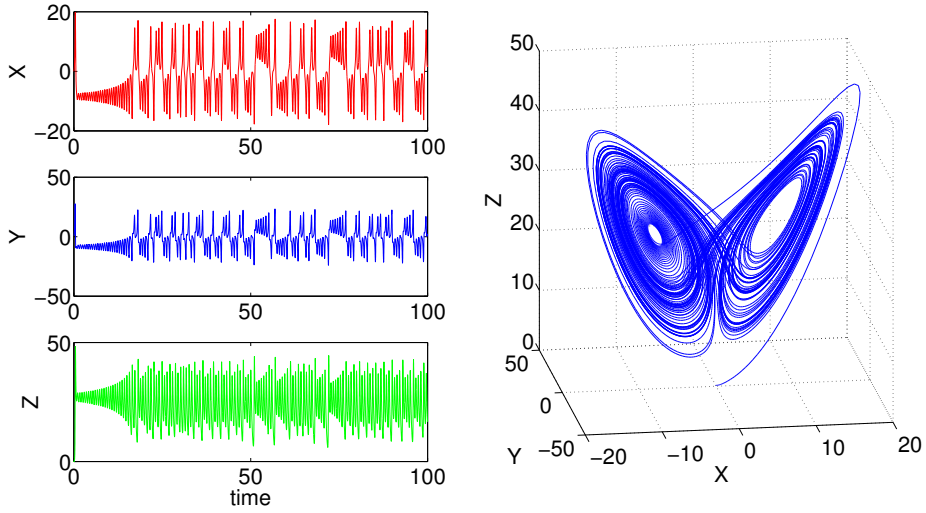

Figure 2.2.17: Lorenz chaotic model. Left panel: irregular time series of Lorenz chaotic model. Right panel: phase plot of Lorenz chaotic model in the type of butterfly. The parameters and initial conditions are $\sigma = 10, b = \frac{8}{3}, r = 28, x_0 = z_0 = 0, y_0 = 1$.

We have a method to identify chaos, which is largest lyapunov exponent(LLE). The lyapunov exponent is defined as $|\delta \boldsymbol{S}(t)| \simeq e^{\lambda t}|\delta \boldsymbol{S}(0)|$, where $\delta \boldsymbol{S}(0)$ and $\delta \boldsymbol{S}(t)$ are the initial and final separations of two trajectories respectively and λ is lyapunov exponent[Strogatz, 2014]. If the LLE is positive(negative), the system will expand(shrink) in that direction exponentially with the scale of the LLE. If at least one of lyapunov exponents is positive, we can conclude that the system is chaotic.

There are more than one route to chaos, which are period-doubling(see Chapter 2.2.3), quasi-periodicity, intermittency and crises and chaotic transients and homoclinic orbits[Hilborn, 1994].

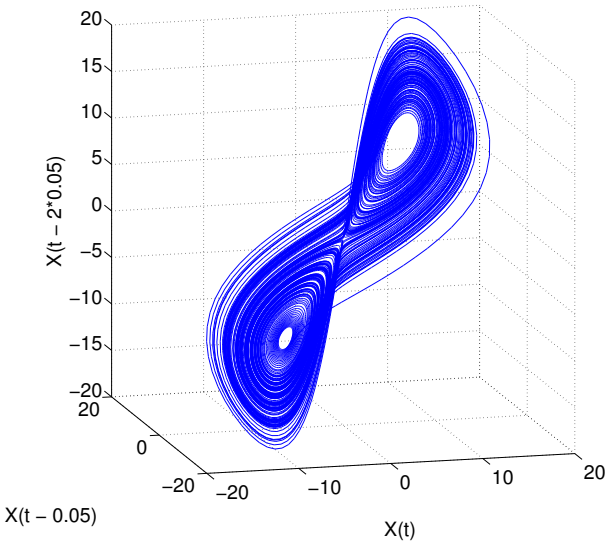

Figure 2.2.18: Reconstruction of phase plot of Lorenz attractor with Takens' Theorem.

In fact, there is no need to plot 3-D phase portrait with all time series like the right panel of Fig.2.2.17. Takens' theorem[Takens, 1981] exhibits that only one of chaotic time series is needed to generate the phase portrait. In brief, Takens proved that instead of $2n+1$ generic time series, the time-delayed versions $[y(t), y(t-\tau), y(t-2\tau), ..., y(t-2n\tau)]$ of one generic time series would suffice to reconstruct phase portrait. Figure 2.2.18 demonstrates the butterfly-like phase portrait with time series of $x(t)$, $x(t-0.05)$ and $x(t-2*0.05)$[Takens, 1981].

2.3 Computational methodology

2.3.1 Taylor series solver

In order to calculate the periods of oscillations appeared in Chapters 3 and 4, we use fixed step Taylor series method to numerically solve first order differential equations(ODEs) throughout this thesis. For the introductions to Taylor series solver in Chapter 2.3.1, we adopt the method appears in [Binegar, 2000].

Recall that the n^{th} order Taylor series of a smooth function $f(x)$ about the point $x = x_0$ is the degree n polynomial defined by

$$T_n(x) = \sum_{i=0}^{n} \frac{1}{i!} f^{(i)}(x_0)(x - x_0)^i \tag{2.3.1}$$

$$= f(x_0) + f'(x_0)(x - x_0) + \frac{f''(x_0)(x - x_0)^2}{2} + \frac{f'''(x_0)(x - x_0)^3}{6} \tag{2.3.2}$$

and that such series are very useful in that they can (for sufficiently small $|x - x_0|$) be used as approximate expression for the original function f. Indeed, Taylor's theorem says

$$f(x) = T_n(x) + \mathcal{O}(|x - x_0|)^{n+1} \tag{2.3.3}$$

and that moreover

$$f(x) = Lim_{n\to\infty} T_n(x) \tag{2.3.4}$$

(so long as $f(x)$ is smooth).

Therefore, one way to get an approximate solution of a differential equations would be to figure out what its Taylor series looks like and this turns out to be a relatively easy thing to do.

Suppose $y(x)$ is a solution of

$$y' = F(x, y) \tag{2.3.5}$$

satisfying the initial condition

$$y(x_0) = y_0 \tag{2.3.6}$$

Since $x = x_0$ implies $y = y_0$, and because the differential equation tells us what $y'(x)$ must be given x and y, we can infer that

$$y'(x_0) = F(x_0, y_0) \tag{2.3.7}$$

Thus, we already know the first two terms of the Taylor expansion of $y(x)$:

$$\begin{aligned} y(x) &= y(x_0) + y'(x_0)(x - x_0) && (2.3.8) \\ &= y_0 + F(x_0, y_0)(x - x_0) && (2.3.9) \end{aligned}$$

To get the second order term we can differentiate the original differential equation with respect to x to get

$$\begin{aligned} y''(x) &= \frac{d}{dx}F(x, y(x)) && (2.3.10) \\ &= \frac{\partial F}{\partial x}\frac{dx}{dx} + \frac{\partial F}{\partial y}\frac{dy}{dx} && (2.3.11) \\ &= \frac{\partial F}{\partial x} + \frac{\partial F}{\partial y}y'(x) && (2.3.12) \\ &= \frac{\partial F}{\partial x} + \frac{\partial F}{\partial y}F(x, y(x)) && (2.3.13) \end{aligned}$$

So

$$y''(x_0) = \left.\frac{\partial F}{\partial x}\right|_{x=x_0, y=y_0} + \left.\frac{\partial F}{\partial y}F(x, y)\right|_{x=x_0, y=y_0} \tag{2.3.14}$$

which after carrying out the partial differentiations and plugging in for x and y is just a number. And thus, we now have the second order term of Taylor expansion of our solution $y(x)$ about $x = x_0$. To get the third order term, we can differentiate the differential equation again to obtain

$$y'''(x) = \frac{d^2}{dx^2}\left(\frac{dy}{dx}\right) = \frac{d^2}{dx^2}F(x, y(x)) \tag{2.3.15}$$

So

$$y'''(x_0) = \left.\frac{d^2}{dx^2}F(x, y(x))\right|_{x=x_0, y=y_0} \tag{2.3.16}$$

The discussions above can be found in [Binegar, 2000]. In this thesis, we adopt from zero order to third order. Thus the error would be $\mathcal{O}(|x - x_0|^4)$.

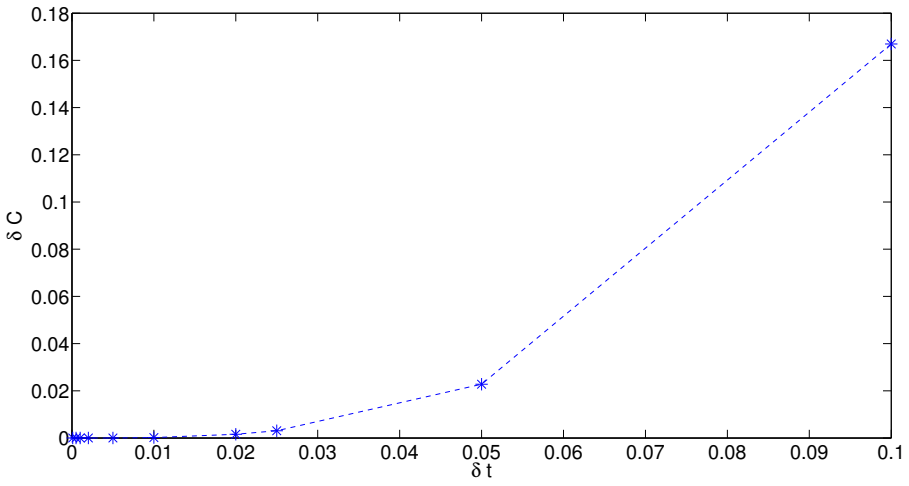

Figure 2.3.1: Deviations of the constant of motion in Eq.(2.2.18) with various fixed step sizes.

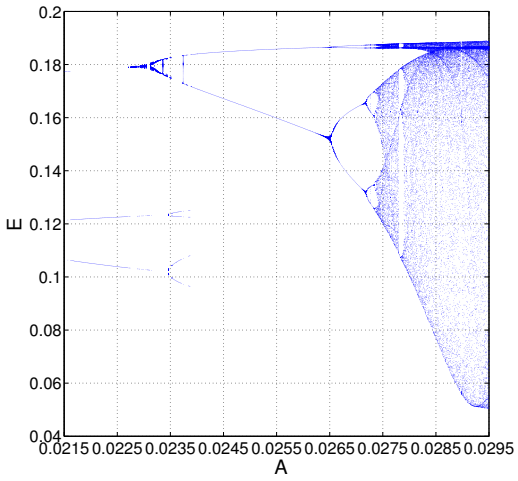

Figure 2.3.2: Bifurcation diagram in Chapter 4.4 with step size $\delta t = 0.5$

To check the convergence of the third order fixed step Taylor series, we recalculate the Eqs.(2.2.14–2.2.15). We use several fixed step sizes from 10^{-3} to 10^{-1} to check the deviations of the constant of motion in Eq.(2.2.18). We define that $\delta C = \delta R - \gamma lnR - \alpha lnF + \beta F - C$, where C is the constant of motion. It demonstrates that the third order Taylor series has good convergence if the step size is small enough, see Fig.2.3.1. Throughout this thesis, we adopt $\delta t = 0.001$ in

all the numerical simulations. Figs.2.3.2–2.3.5 demonstrate the impact of various step sizes on our plots(see Fig.4.6.6). We cannot get the accurate period doubling bifurcation if the step size is too large(Figs.2.3.2-2.3.3).

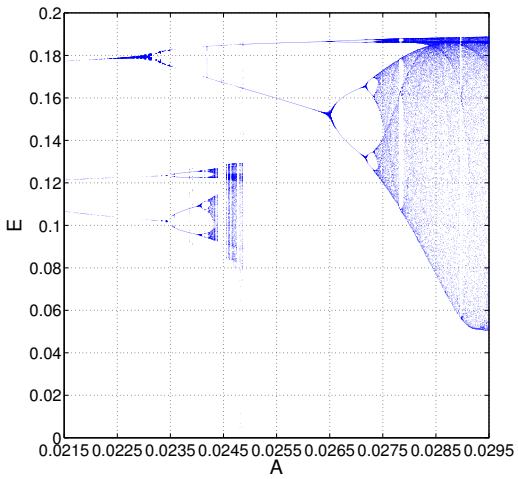

Figure 2.3.3: Bifurcation diagram in Chapter 4.4 with step size $\delta t = 0.1$

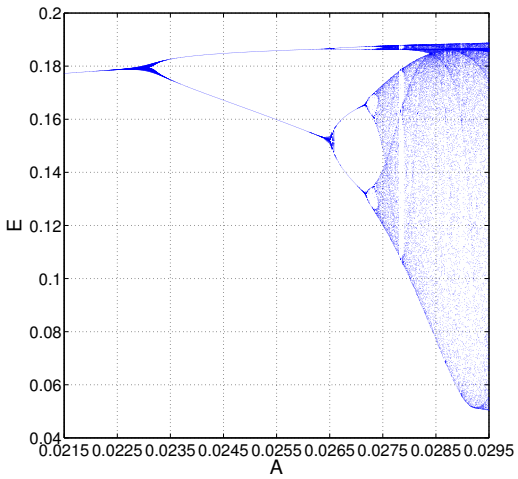

Figure 2.3.4: Bifurcation diagram in Chapter 4.4 with step size $\delta t = 0.01$

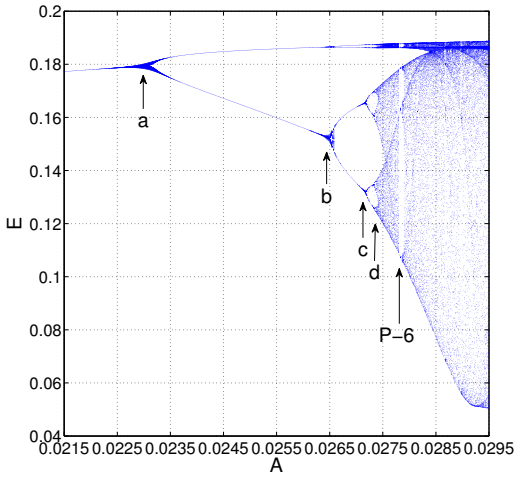

Figure 2.3.5: Bifurcation diagram in Chapter 4.4 with step size $\delta t = 0.001$. This figure is from Fig.4.6.6 in Chapter 4.4.

2.3.2 Other ODE solvers

Besides the Taylor series method mentioned in last subchapter, there are many other ordinary differential equation(ODE) solvers, for example, Runge-Kutta method, Bulirsch-Stoer method and predictor-corrector method. Here we give an brief introduction here in Chapter 2.3.2, appears in [Press, 2007], to the Runge-Kutta method.

The formula of the Euler method is

$$y_{n+1} = y_n + hf(x_n, y_n) \tag{2.3.17}$$

which advances a solution from point x_n to point $x_{n+1} \equiv x_n + h$. There are reasons that the Euler's method is not suitable for practical use, among them, (1) the Euler's method is not very accurate when running at the equivalent step size compared with other methods, and (2) neither it is very stable.

Consider, the use of a step like Eq.(2.3.17) to take a trial step to the midpoint of the interval. Then use the values of x and y at that midpoint to compute the real step.

$$k_1 = hf(x_n, y_n) \tag{2.3.18}$$
$$k_2 = hf(x_n + \frac{1}{2}h, y_n + \frac{1}{2}k_1) \tag{2.3.19}$$
$$y_{n+1} = y_n + k_2 + \mathcal{O}(h^3) \tag{2.3.20}$$

This symmetrization cancels out the first-order error term, making the Euler's method second order. This is the basic idea of the Runge-Kutta method. By far the most ofter used is the classical fourth-order Runge-Kutta method, which is given below

$$k_1 = hf(x_n, y_n) \tag{2.3.21}$$
$$k_2 = hf(x_n + \frac{1}{2}h, y_n + \frac{1}{2}k_1) \tag{2.3.22}$$
$$k_3 = hf(x_n + \frac{1}{2}h, y_n + \frac{1}{2}k_2) \tag{2.3.23}$$
$$k_4 = hf(x_n + h, y_n + k_3) \tag{2.3.24}$$
$$y_{n+1} = y_n + \frac{1}{6}k_1 + \frac{1}{3}k_2 + \frac{1}{3}k_3 + \frac{1}{6}k_4 + \mathcal{O}(h^5) \tag{2.3.25}$$

The fourth-order Runge-Kutta method needs four times of evaluations of the right-hand side per step. This will be superior to the midpoint method mentioned above. However, higher order does not always imply high accuracy[Press, 2007].

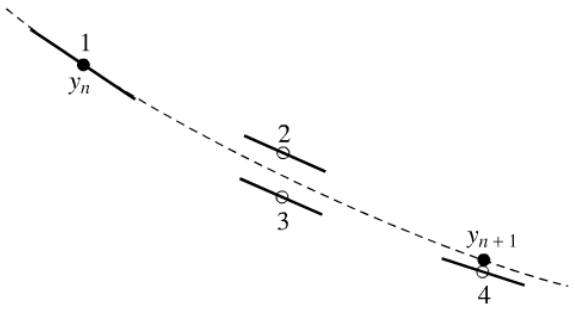

Figure 2.3.6: Fig.17.1.3 in [Press, 2007]. For fourth-order Runge-Kutta method, in each step the derivative is evaluated four times.

For the Bulirsch-Stoer method, this method uses the powerful idea of extrapolating a result to the value that would have been obtained if the step size had been very much smaller than it actually was. Particularly, the extrapolation to zero step

size is the desired target. See the schematics diagram Figure 2.5.3 for the information. For the predictor-corrector method, it stores the solution along the way, and use those results to extrapolate the solution one step advance; then they correct the extrapolation by derivative information at the new point. This is the best for very smooth functions[Press, 2007].

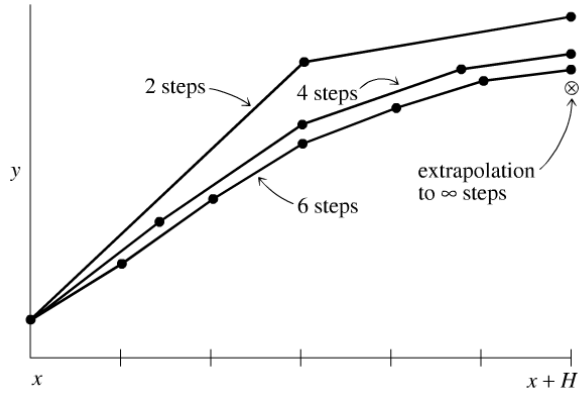

Figure 2.3.7: Fig.17.3.1 in [Press, 2007]. This is extrapolation used in the Bulirsch-Stoer method. A large interval H is spanned by various sequences of finer and finer substeps.

The discussions above can be found in [Press, 2007].

2.3.3 Stiffness

In the nonlinear system, there are two or more time scales. Chaotic systems, for example coupled pendulums, exhibit two or more characteristic frequencies can be observed. These tend to be stiff systems. If the solution contains a term like e^{-1000x}, then it would require a rather small step size $h \ll 1/1000$ to make the method stable, though the term e^{-1000x} might be negligible in determining solution[Press, 2007]. We have checked all the equations that we solved. And none of them has been found to be stiff. Here we will provide an introduction here in Chapter 2.3.3, appears in [Press, 2007], to stiff set of equations.

For example, consider the following equations:

$$u' = 998u + 1998v \tag{2.3.26}$$

$$v' = -999u - 1999v \tag{2.3.27}$$

with the boundary conditions

$$u(0) = 1, \quad v(0) = 1 \tag{2.3.28}$$

By means of the transformations below

$$u = 2y - z, \quad u = -y + z \tag{2.3.29}$$

we get the solutions

$$u = 2e^{-x} - e^{-1000x} \tag{2.3.30}$$

$$v = -e^{-x} + e^{-1000x} \tag{2.3.31}$$

Although the term e^{-1000x} is negligible in the solutions, we have to require a step size $h \ll 1/1000$ to make the method stable. We then give a method to identify this stiffness. Suppose there is a set of linear equations with the constant coefficients:

$$\boldsymbol{y}' = -\boldsymbol{C} \cdot \boldsymbol{y} \tag{2.3.32}$$

Consider the matrix $\boldsymbol{C}$ can be diagonalized by a transformation,

$$\boldsymbol{T} \cdot \boldsymbol{C} \cdot \boldsymbol{T}^{-1} = diag(\lambda_0 ... \lambda_{N-1}) \tag{2.3.33}$$

where λ_i are the eigenvalues of $\boldsymbol{C}$.

Thus, we get the criterion for getting the stable solutions:

$$Re\lambda_i > 0, \quad i = 0, ..., N-1 \tag{2.3.34}$$

If the matrix $\boldsymbol{C}$ cannot be diagonalized, we can transform $\boldsymbol{C}$ to so-called Jordan canonical form, which is the closest it can come to being made diagonal[Press, 2007]. The discussions above can be found in [Press, 2007].

2.4 Reduced models for magnetic confinement regimes

2.4.1 Model proposed by Malkov et al.

In order to interpret the L-H transitions induced by interactions of zonal flow and drift wave turbulence, M.A.Malkov and P.H.Diamond proposed a zero-dimensional model. This model contains three ordinary differential equations for interpreting transitions of various confinement regimes [Malkov and Diamond, 2009]. These equations can model the L-mode, H-mode, transient T-mode, quiescent QH-mode and their interactions to some extent. We could observe and analyse those relations by choosing appropriate parameters and initial conditions. For the theoretical development and improved models from MD models, please see [Zhu et al., 2013; Douglas et al., 2013; Zhu et al., 2014; Dam et al., 2013]. The MD model equations are given below.

$$\frac{d\mathcal{E}}{d\tau} = \left(\mathcal{N} - a_1\mathcal{E} - a_2 d^2\mathcal{N}^4 - a_3 V_{ZF}^2\right)\mathcal{E} \tag{2.4.1}$$

$$\frac{dV_{ZF}}{d\tau} = \left(\frac{b_1\mathcal{E}}{1 + b_2 d^2\mathcal{N}^4} - b_3\right) V_{ZF} \tag{2.4.2}$$

$$\frac{d\mathcal{N}}{d\tau} = -\left(c_1\mathcal{E} + c_2\right)\mathcal{N} + q(\tau) \tag{2.4.3}$$

The model is a closed system of three nonlinear ordinary differential equations that couple time evolution of four different variables. Those variables are drift wave(DW) turbulence intensity $\mathcal{E}$, drift wave driving temperature gradient $\mathcal{N}$, velocity of zonal flow V_{ZF} and mean flow shear V which is slaved to drift wave driving temperature gradient, $V = d\mathcal{N}^2$(d is constant)[Malkov and Diamond, 2009]. The model proposed by Zhu et al,[Zhu et al., 2013, 2014] takes the high-frequency zonal flow(GAM) into consideration. For further discussions of this novel model, please see Chapter 3 and Chapter 4.

The meaning of different terms and parameters of the MD model equations on the right-hand sides are demonstrated in the following Table 2.1.

Here we have defined normalized variables

$$N = a_2^{1/3}\mathcal{N},\ E = a_1 a_2^{1/3}\mathcal{E},\ U = a_2^{1/3} a_3 V_{ZF}^2,$$
$$t = a_2^{1/3}\tau.$$

and the transformed model parameters are

$$\nu = \frac{2b_1}{a_1 a_2^{2/3}},\ \eta = \frac{b_3}{b_1} a_1 a_2^{1/3},\ \rho = \frac{c_2}{a_2^{1/3}},$$

	1^{st} term	2^{nd} term	3^{rd} term	4^{th} term
1^{st} Eqn.	$\mathcal{N}\mathcal{E}$(Turbulence growth rate driven by ∇T)	$-a_1\mathcal{E}^2$(Nonlinear saturation)	$-a_2 d^2\mathcal{N}^4\mathcal{E}$(DW suppression by mean flow)	$-a_3 V_{ZF}^2\mathcal{E}$(DW suppression by zonal flow)
2^{nd} Eqn.	$b_1\mathcal{E}V_{ZF}$(ZF generation by DW turbulence)	$\frac{V_{ZF}}{b_2 d^2\mathcal{N}^4}$(ZF suppression by mean flow)	$-b_3 V_{ZF}$(Linear(collisional) by damping of ZF)	N/A N/A
3^{rd} Eqn.	$-c_1\mathcal{E}\mathcal{N}$($\nabla T$ relaxation by turbulent diffusion)	$-c_2\mathcal{N}$(∇T relaxation by neoclassical transport)	$q(\tau)$(external heating flux)	N/A N/A

Table 2.1: The physical meaning of the terms and parameters in the r.h.s of the MD model.

$$\sigma = \frac{c_1}{a_1 a_2^{2/3}},\ \zeta = \frac{b_2}{a_2^{4/3}},\ d = 1.$$

The corresponding normalized equations are

$$\frac{dE}{dt} = \left(N - N^4 - E - U\right) E \tag{2.4.4}$$

$$\frac{dU}{dt} = \nu \left(\frac{E}{1 + \zeta N^4} - \eta\right) U \tag{2.4.5}$$

$$\frac{dN}{dt} = q - (\rho + \sigma E)\, N \tag{2.4.6}$$

Analytically, Malkov and Diamond analysed the stabilities of the fixed points of Eqs.(2.4.4–2.4.6) and their relations with different confinement regimes like L-mode, T-mode(transient oscillatory mode), H-mode and QH-mode(quiescent H-mode)[Malkov and Diamond, 2009].

In the normalised model, q is external heating rate which is regarded as a control parameter. Numerically, Malkov and Diamond examined the impact of multiple q constant cases on the dynamical system.

Figure 2.4.1 illustrates the transitions under the condition of $q = 0.47$. The system starts from an overpowered H-mode, then transitions to unstable H-mode then unstable L-mode due to appearance of micro-scale turbulence intensity E followed by transient oscillatory mode T-mode[Malkov and Diamond, 2009].

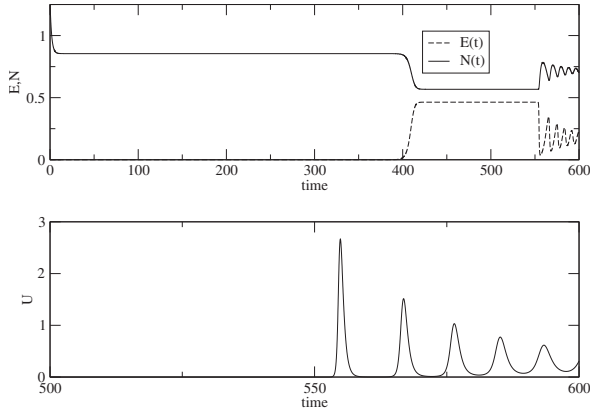

Figure 2.4.1: Fig.2 in [Malkov and Diamond, 2009]. Upper panel indicates time evolution of E(normalised micro-scale turbulence intensity) and N(normalised electron temperature gradient). Lower panel demonstrates the time series of U(energy of zonal flow). The system starts from overpowered H-mode then unstable L-mode then transient oscillatory T-mode.

Figure 2.4.2 demonstrates bursts of zonal flow energy when $q = 0.58$. The time evolutions of E, N and U develop a stable limit cycle[Malkov and Diamond, 2009].

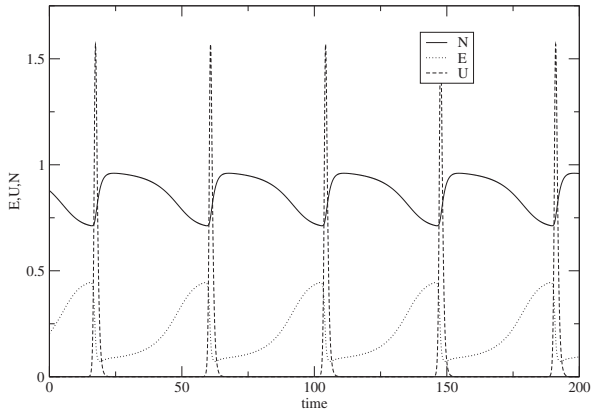

Figure 2.4.2: Fig.3 in [Malkov and Diamond, 2009]. Limit cycle oscillation of E(normalised micro-scale turbulence intensity), N(normalised electron temperature gradient) and U(energy of zonal flow) when $q = 0.58$.

Figure 2.4.3 exhibits collapse of limit cycle oscillations when q slightly increases from 0.58 to 0.582. The dynamical system rests at QH-mode fixed point after increasing bursts of energy of zonal flow[Malkov and Diamond, 2009].

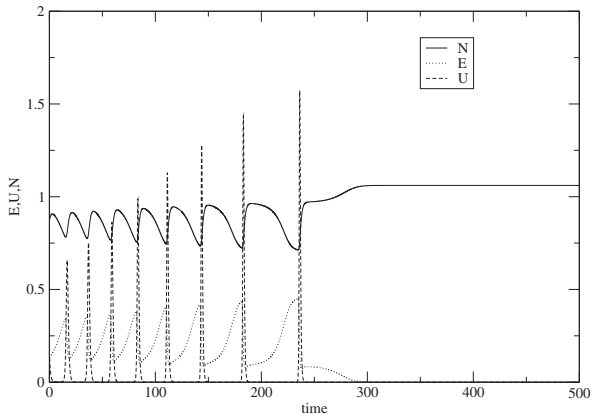

Figure 2.4.3: Fig.4 in [Malkov and Diamond, 2009]. Collapse of limit cycle oscillation and transition to quiescent H-mode(QH-mode), in which only N(normalised electron temperature gradient) exists when $q = 0.582$.

From Figure 2.4.1 to Figure 2.4.3, Malkov and Diamond examined three constant external heating fluxes. In the following cases, they checked the impact of

$q(t)$ on the 3-ODE model. Figure 2.4.4 shows that $q(t)$ slowly vary from $q = 0.47$ to $q = 0.62$ and back. The phenomenology of hysteresis is discovered in time evolutions of E, N and U[Malkov and Diamond, 2009].

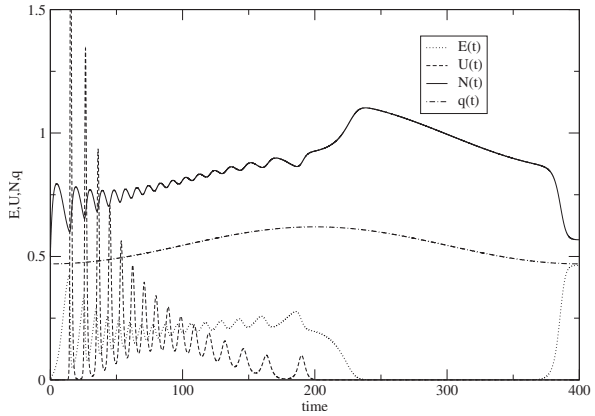

Figure 2.4.4: Fig.6 in [Malkov and Diamond, 2009]. The external heating rate slowly varies from $q = 0.47$(stable L-mode) to $q = 0.62$(stable QH-mode) and back. It is found that the final state is not identical with the initial state, which is identified as hysteresis of the dynamical system.

Figure 2.4.5 demonstrates impact of oscillating $q(t)$ on the MD model[Malkov and Diamond, 2009]. We will also apply oscillating external heating flux $q(t)$ to the model of [Zhu et al., 2014], see Chapter 4.

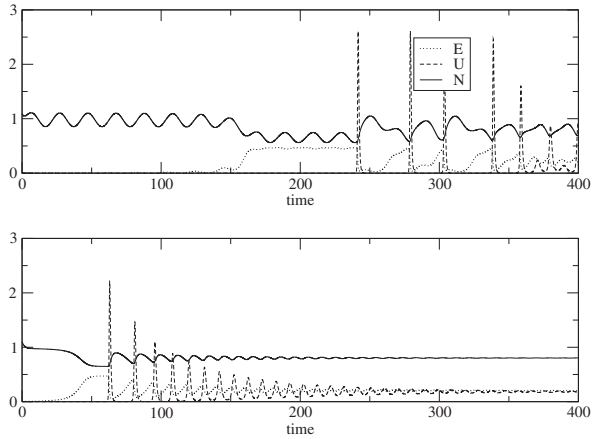

Figure 2.4.5: Fig.7 in [Malkov and Diamond, 2009]. The average and oscillatory parts of q value are 0.54 and 0.08 respectively. The modulation frequency ω is 0.31. The time evolutions of E, U and N indicate apparent irregularity when applying periodic external heating flux.

2.4.2 Model proposed by Itoh et al.

Besides the MD model, Sanae.-I Itoh and Kimitaka Itoh also proposed another zero-dimensional model[Itoh and Itoh, 2011]. This model includes three ordinary differential equations to interpret interactions between micro-scale drift wave turbulence and meso-scale structures, for example, zonal flows and geodesic acoustic modes(GAMs), which are high frequency branches of zonal flows. The II model equations are given here.

$$\frac{\partial}{\partial t}W = \gamma_L W - \Gamma_W W^2 - \alpha ZW - \beta MW \tag{2.4.7}$$

$$\frac{\partial}{\partial t}Z = -\gamma_Z Z - \Gamma_Z Z^2 + \alpha ZW \tag{2.4.8}$$

$$\frac{\partial}{\partial t}M = -\gamma_M M - \Gamma_M M^2 + \beta MW \tag{2.4.9}$$

The II model couples time evolutions of W(normalised energy densities of linear unstable drift waves(DWs)), Z(normalised energy densities of zonal flows(ZFs)) and M(normalised energy densities of geodesic acoustic modes(GAMs)) [Itoh and Itoh, 2011]. Other parameters and terms are illustrated in table 2.2 given below.

In this predator-prey model, the phase space of zonal flows(ZFs) and geodesic acoustic modes(GAMs) has been divided into four segments, which are ZFs-GAMs co-existence region, ZFs distinction region, GAMs distinction region and only turbulence existed region. By theoretical analysis, critical values of γ_Z and γ_M in the phase space mentioned above have been calculated.

Additionally, in Chapter 3, we will propose another predator-prey model[Zhu et al., 2013], which contains four ODEs, aiming to interpret the interactions of zonal flows–drift wave turbulence and the corresponding L-H transitions. The new model adopts the philosophies of both MD model and II model. In our model, we find the stable fixed point in MD model can be transferred to a stable limit cycle which is I-phase in L-H transitions. We also examine the impact of external heating flux on the MD and ZCD models in Chapter 4. What we find is that the final state is quite robust towards the slope of the heating function. Also, a period-doubling bifurcation route to chaos is observed, see also Chapter 2.2.3 for a introduction to bifurcation.

	1^{st} term	2^{nd} term	3^{rd} term	4^{th} term
1^{st} Eqn.	$\gamma_L W$(DW linear growth rate)	$-\Gamma_W W^2$(DW nonlinear damping rate)	$-\alpha ZW$(Lowest-order coupling rates of DW and ZFs)	$-\beta MW$(Lowest-order coupling rates of DW and GAMs)
2^{nd} Eqn.	$-\gamma_Z Z$(ZFs linear and collisional damping rate)	$-\Gamma_Z Z^2$(ZFs nonlinear damping rate)	αZW(Lowest-order coupling rates of DW and ZFs)	N/A N/A
3^{rd} Eqn.	$-\gamma_M M$(GAMs linear resistive damping rate)	$-\Gamma_M M^2$(GAMs nonlinear damping rate)	βMW(Lowest-order coupling rates of DW and GAMs)	N/A N/A

Table 2.2: The physical meaning of the terms and parameters in the r.h.s of the II model.

2.5 Reduced models for heat pulse experiments

2.5.1 Model proposed by Dendy et al.

In order to simulate the heat pulse propagation, several theoretical models are proposed[Gentle, 1988; Iwasaki et al., 1999; Dendy et al., 2013]. Here we present a brief introduction of heat pulse model for LHD in [Dendy et al., 2013]. Further discussions about heat pulse model can be seen in Chapter 5.

In [Dendy et al., 2013], three key observable physical quantities are taken into consideration, which are the deviation from steady state of turbulent flux(heat flux) averaged by density of electron $\delta q_e\left(\rho,t\right)/n_e$, the deviation from steady state of electron temperature gradient $\delta\nabla T_e$ and the deviation from steady state of electron temperature $T_e - T_{e0}$. Firstly, we assume $\delta q_e\left(\rho,t\right)/n_e$ acts to reduce the magnitude of local electron temperature gradient $\delta\nabla T_e$ by carrying away energy and the steady state turbulent transport acts to damp $\delta\nabla T_e$ at rate of γ_{L1}[Dendy et al., 2013]. Hence we have,

$$\frac{\partial}{\partial t}\left(\delta\nabla T_e\right) = \kappa_T\left(T_e,\nabla T_e\right)\frac{\delta\boldsymbol{q_e}}{\chi_0 n_e} - \gamma_{L1}\delta\nabla T_e \tag{2.5.1}$$

where $\kappa_T\left(T_e,\nabla T_e\right)$ is the coupling coefficient that has dimension inverse time. The value of measured steady state turbulent heat diffusivity χ_0 is defined as $\chi_0 = L_c^2/\tau_c$, where L_c is the characteristic scale-length of steady state turbulent transport. τ_c is the associated global energy confinement time[Dendy et al., 2013].

Secondly, δq_e is a proxy for excess turbulence and this is driven by negative temperature gradient ∇T_e and damped by the steady state turbulent transport. Hence we have,

$$\frac{\partial}{\partial t}\left(\frac{\delta\boldsymbol{q_e}}{\chi_0 n_e}\right) = -\kappa_Q\left(T_e,\nabla T_e\right)\delta\nabla T_e - \gamma_{L1}\frac{\delta\boldsymbol{q_e}}{\chi_0 n_e} \tag{2.5.2}$$

where $\kappa_Q\left(T_e,\nabla T_e\right)$ is another coupling factor[Dendy et al., 2013].

Lastly, we assume that the local time derivative of $T_e - T_{e0}$ matches the divergence of local excess turbulent heat flux. We also assume that steady state turbulent transport acts to damp the deviation[Dendy et al., 2013], thus

$$\frac{\partial}{\partial t}\left(T_e - T_{e0}\right) = -\eta\nabla\cdot\left(\frac{\delta\boldsymbol{q_e}}{\chi_0 n_e}\right) - \gamma_{L2}\left(T_e - T_{e0}\right) \tag{2.5.3}$$

with approximations and normalizations, we have the following equations[Dendy et al., 2013],

$$\frac{dx_1}{dt} = \kappa_{T0}x_2 + x_1x_2\frac{\partial\kappa_T}{\partial x_1} + x_2x_3\frac{\partial\kappa_T}{\partial x_3} - \gamma_{L1}x_1 \tag{2.5.4}$$

$$\frac{dx_2}{dt} = -\kappa_{Q0}x_1 - x_1^2\frac{\partial\kappa_Q}{\partial x_1} - x_1x_3\frac{\partial\kappa_Q}{\partial x_3} - \gamma_{L1}x_2 \tag{2.5.5}$$

$$\frac{dx_3}{dt} = -\frac{1}{\tau_c}\frac{\eta}{\chi_0}x_2 - \gamma_{L2}x_3 \tag{2.5.6}$$

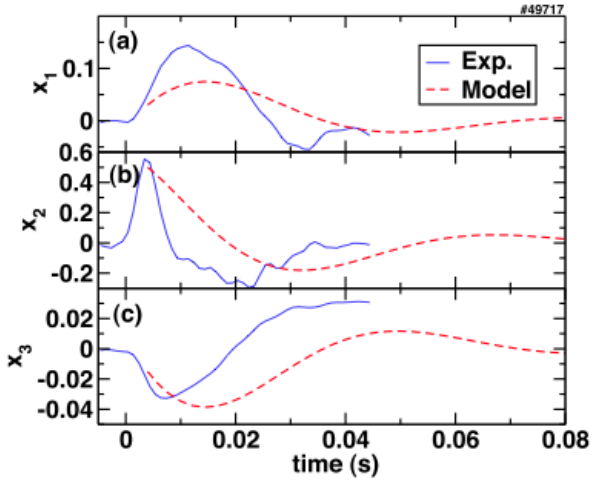

Figure 2.5.1: Fig.1 in [Dendy et al., 2013], time series of normalised (a)$\delta\nabla T_e$, (b)δq and (c)δT_e for the T_e rise case in LHD in $\rho = 0.19$. Blue lines are experimental data and red lines are model outputs. Parameters are: $\chi_0 = 3.2\text{m}^2\text{s}^{-1}$, $T_{e0} = 3.5\text{keV}$, $L_c = 1.1\text{m}$, $\kappa_{T0} = 15, \partial\kappa_T/\partial x_1 = \partial\kappa_T/\partial x_3 = 1.5, \kappa_{Q0} = 225, \partial\kappa_Q/\partial x_1 = \partial\kappa_Q/\partial x_3 = 22.5, \gamma_{L1} = \gamma_{L2} = 35$ and $\eta/\tau_c\chi_0 = 10.5$.

Fig.2.5.1 and Fig.2.5.2 illustrate the comparisons of model outputs and experimental datasets. It is demonstrated that the model can quantitatively simulate experimental data at the normalised radius $\rho = 0.19$. We will modify this model by travelling wave transformation[Zhu et al., 2015] in Chapter 5. It is concluded that the new model can simulate not only one specific radius but also the broad radial range from the plasma edge to the core. This new model can also be employed to simulate and predict heat pulse propagation in other radial locations without Langmuir probes diagnostics.

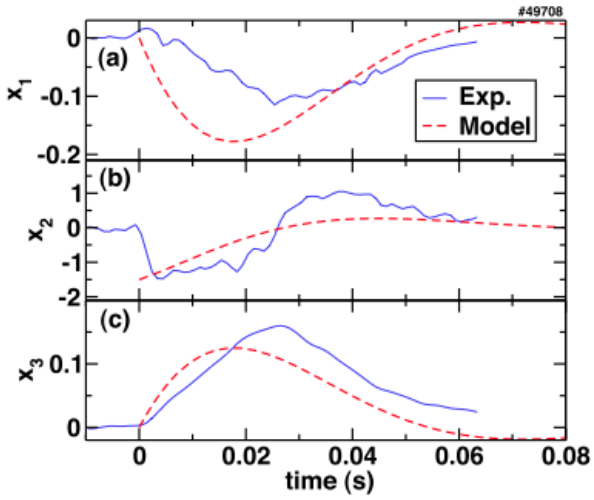

Figure 2.5.2: Fig.2 in [Dendy et al., 2013], time series of normalised (a)$\delta\nabla T_e$, (b)δq and (c)δT_e for the T_e drop case in LHD in $\rho = 0.19$. Blue lines are experimental data and red lines are model outputs. Parameters are: $\chi_0 = 2.4\mathrm{m}^2\mathrm{s}^{-1}$, $T_{e0} = 2.9\mathrm{keV}$, $L_c = 1.1\mathrm{m}$, $\kappa_{T0} = 20, \partial\kappa_T/\partial x_1 = \partial\kappa_T/\partial x_3 = 2.0, \kappa_{Q0} = 400, \partial\kappa_Q/\partial x_1 = \partial\kappa_Q/\partial x_3 = 40, \gamma_{L1} = \gamma_{L2} = 35$ and $\eta/\tau_c\chi_0 = 10.5$.

Chapter 3

Predator-prey models for confinement in fusion plasmas

3.1 Introduction

In this Chapter, we focus from the perspective on the interesting and successful mathematical model proposed in MD, see Chapter 2.4.1. This is constructed in terms of variables representing the magnitude of the plasma electron temperature gradient and the amplitudes of micro-scale drift wave turbulence and of meso-scale coherent nonlinear structures such as zonal flows. Malkov & Diamond proposed[Malkov and Diamond, 2009] certain mappings between different solution regimes of their model and different confinement regimes of tokamak plasmas. In the interest of continuity, we follow the confinement regime nomenclature of MD in relation to model outputs in this Chapter. We investigate the robustness of the phenomenology of the MD model extended as described, for parameter regimes identical or adjacent, to those used in the key figures of MD.

Specifically, the MD model mentioned in Chapter 2.4.1 is a closed system of nonlinear ordinary differential equations which couple the time evolution of three variables: the drift wave(DW)-driving temperature gradient N, the energy density of drift wave turbulence E, and the zonal flow energy U. The three variables of the II model, which is demonstrated in Chapter 2.4.2, exclude N, retain drift turbulence energy density denoted by W, and incorporate the energy densities of two competing classes of coherent nonlinear structure, zonal flows Z and geodesic acoustic modes M. Miki and Diamond[Miki and Diamond, 2011] introduced a zero-dimensional three-variable two-predator, one prey model, where the predators are also identified with zonal flows and geodesic acoustic modes. The aspect of robustness which we first

address can therefore be expressed in physical terms as follows. We adopt the philosophy of MD, II and of [Miki and Diamond, 2011] by introducing two competing classes of coherent nonlinear structure, here identified with zonal flows and geodesic acoustic modes, that replace the single class in MD. The other two MD equations are adjusted only so far as necessary to accommodate these two fields, instead of one, in a mathematically symmetrical way as in II. We investigate how far the model outputs of our new four-variable system differ from those of the three-variable system of MD. A good focus for this study is provided by the time traces captured in Figs.2-4 of MD, which have been mapped to transitions observed between tokamak confinement regimes. How are these traces altered by the inclusion of a second competing class of coherent nonlinear structure? The answers to these questions are conditioned by the underlying phase space structure of families of solutions to the models, as plotted in Fig.5 of MD, for example. In addition to studying time traces, therefore, we seek to characterise the limit cycles and fixed points of our system of equations. We first generalize the un-normalized equations(hereafter ZCD) to:

$$\frac{d\mathcal{E}}{d\tau} = \left(\mathcal{N} - a_1\mathcal{E} - a_2 d^2\mathcal{N}^4 - a_3 V_{ZF}^2 - a_3 V_{GAM}^2\right)\mathcal{E} \tag{3.1.1}$$

$$\frac{dV_{ZF}}{d\tau} = \left(\frac{b_{1Z}\mathcal{E}}{1 + b_{2Z}d^2\mathcal{N}^4} - b_{3Z}\right)V_{ZF} \tag{3.1.2}$$

$$\frac{dV_{GAM}}{d\tau} = \left(\frac{b_{1G}\mathcal{E}}{1 + b_{2G}d^2\mathcal{N}^4} - b_{3G}\right)V_{GAM} \tag{3.1.3}$$

$$\frac{d\mathcal{N}}{d\tau} = -\left(c_1\mathcal{E} + c_2\right)\mathcal{N} + q(\tau) \tag{3.1.4}$$

The physical meanings of terms and parameters are illustrated in Table 3.1. This model encompasses drift wave turbulence level $\mathcal{E}$, drift wave driving temperature gradient $\mathcal{N}$, zonal flow velocity V_{ZF}, geodesic acoustic modes velocity V_{GAM}, and the external heating rate q which is a control parameter of the system. This model thus extends, to the case when zonal flows are joined by geodesic acoustic modes, the key physics encapsulated in the description in [Kim and Diamond, 2003]: "When the drift wave turbulence drive becomes sufficiently strong to overcome flow damping, it generates zonal flows by Reynolds stress. Drift wave turbulence and zonal flows then form a self-regulating system as the shearing by zonal flows damps the drift wave turbulence." We note that this model follows the approach expressed in Eq.(17) of MD[Malkov and Diamond, 2009], in that the zonal flows and geodesic acoustic modes do not explicitly enter the time evolution equation for the temperature gradient, Eq.(3.1.4). The zonal flows and geodesic acoustic modes are

	1^{st} term	2^{nd} term	3^{rd} term	4^{th} term	5^{th} term
1^{st} Eqn.	$\mathcal{N}\mathcal{E}$(Turbulence growth rate driven by ∇T)	$-a_1\mathcal{E}^2$(Nonlinear saturation)	$-a_2 d^2\mathcal{N}^4\mathcal{E}$(DW suppression by mean flow)	$-a_3 V_{ZF}^2\mathcal{E}$(DW suppression by ZF)	$-a_3 V_{GAM}^2\mathcal{E}$(DW suppression by GAM)
2^{nd} Eqn.	$b_{1Z}\mathcal{E}V_{ZF}$(ZF generation by DW turbulence)	$\frac{V_{ZF}}{b_{2Z}d^2\mathcal{N}^4}$(ZF suppression by mean flow)	$-b_3 V_{ZF}$(Linear(collisional) by damping of ZF)	N/A N/A	N/A N/A
3^{rd} Eqn.	$b_{1G}\mathcal{E}V_{GAM}$(GAM generation by DW turbulence)	$\frac{V_{GAM}}{b_{2G}d^2\mathcal{N}^4}$(GAM suppression by mean flow)	$-b_3 V_{ZF}$(Linear(collisional) by damping of ZF)	N/A N/A	N/A N/A
4^{th} Eqn.	$-c_1\mathcal{E}\mathcal{N}$($\nabla T$ relaxation by turbulent diffusion)	$-c_2\mathcal{N}$(∇T relaxation by neoclassical transport)	$q(\tau)$(external heating flux)	N/A N/A	N/A N/A

Table 3.1: The physical meanings of terms and parameters in r.h.s of ZCD model equations(3.1.1-3.1.4).

indirectly coupled to each other through the evolving electron temperature gradient and micro-scale turbulence level. To maximise mathematical congruence with the model of MD, there is no direct cross term in $V_{ZF}V_{GAM}$. We note that our introduction of geodesic acoustic modes into this model is mathematically symmetric with the approach to zonal flows expressed in the model of [Malkov and Diamond, 2009]. This reflects our emphasis in this Chapter on the question of mathematical robustness: we have two predators rather than one, operating on the same mathematical footing. A corollary is that in the present model, neither the zonal flows nor the geodesic acoustic modes explicitly enter the time evolution equation for the temperature gradient, Eq.(3.1.4).

The corresponding normalized equations are

$$\frac{dE}{dt} = \left(N - N^4 - E - U_1 - U_2\right) E \tag{3.1.5}$$

$$\frac{dU_1}{dt} = \nu_1 \left(\frac{E}{1+\zeta N^4} - \eta_1\right) U_1 \tag{3.1.6}$$

$$\frac{dU_2}{dt} = \nu_2 \left(\frac{E}{1+\zeta N^4} - \eta_2\right) U_2 \tag{3.1.7}$$

$$\frac{dN}{dt} = q - (\rho + \sigma E) N \tag{3.1.8}$$

Here we have defined normalized variables

$$N = a_2^{1/3}\mathcal{N},\ E = a_1 a_2^{1/3}\mathcal{E},\ U_1 = a_2^{1/3} a_3 V_{ZF}^2,\ U_2 = a_2^{1/3} a_3 V_{GAM}^2,$$

$$t = a_2^{-1/3}\tau.$$

and the transformed model parameters are

$$\nu_1 = \frac{2b_{1Z}}{a_1},\ \nu_2 = \frac{2b_{1G}}{a_1},\ \eta_1 = \frac{b_{3Z}}{b_{1Z}} a_1 a_2^{1/3},\ \eta_2 = \frac{b_{3G}}{b_{1G}} a_1 a_2^{1/3},$$

$$\rho = c_2 a_2^{1/3},\ \sigma = \frac{c_1}{a_1},\ \zeta = \frac{b_{2Z}}{a_2^{4/3}},$$

$$b_{2Z} = b_{2G},\ q(t) = a_2^{2/3} q(\tau),\ d = 1.$$

This rescaling of variables differs from that in MD, where Eqs.(13) and (14) are rescaled using $t = a_2^{1/3}\tau$ as indicated in MD, whereas Eq.(12) appears to have been rescaled inconsistently, using $t = a_2^{-1/3}\tau$, which is the scaling applied to all four model equations in this Chapter. There appear to be no consequences for the results

in MD. The system of Eqs.(3.1.5-3.1.8) thus generalizes the system of Eqs.(15-17) of MD by introducing two distinct flow variables, U_1 and U_2, to replace the single zonal flow variable U. We refer to U_1 as zonal flows, U_2 as geodesic acoustic modes.

Chapter 3.2 of this thesis addresses transition phenomenology given time-independent coefficients, as characterised primarily by time traces. This requires careful comparison with the specific scenarios identified in Fig.3 to Fig.5 of MD. The MD scenarios predetermine the choice of parameter values and initial conditions that we consider. We typically probe neighbouring phase space by considering in addition eighty-one (three to the fourth power) nearby phase trajectories. In Chapter 3.3 we consider the phase space evolution of our system and establish comparisons between the MD model and ours. In Chapter 3.4 we focus on stability analysis of MD and ZCD models. In Chapter 3.5, we focus on limit cycle analysis of ZCD model.

3.2 Modelling confinement transitions

In the limit where either one of the two parameters that represent distinct classes of coherent nonlinear structures (zonal flows or geodesic acoustic modes) in our model vanishes, it reproduces exactly the results shown in Fig.2 of MD, as required. Figure 3.2.1 displays the corresponding results for the case where both geodesic acoustic modes and zonal flows exist. In the nomenclature of MD, the system starts from an overpowered state near H-mode, with negligible turbulence E and large scale structures U_1, U_2. The eventual growth of turbulence accompanies a sharp drop in N to unstable L-mode, while also providing energy for U_1 and U_2. Drift wave turbulence is later suppressed and the maximum amplitude of large scale flows declines, leaving only the mean flow to support the transport barrier[Diamond et al., 2011]. Finally the stable T-mode, which combines a steady-state level of E with lower N than H-mode, appears after the oscillating transition regime. During this transition, energy is extracted from the initially dominant oscillating geodesic acoustic modes U_2 to the zonal flow U_1 until the former vanishes.

In Fig.3.2.2, we plot the system evolution for the case where the values of ν_2 and η_2 are different from Fig.3.2.1, while all other parameter values are identical. Specifically, in Fig.3.2.1 $\nu_2/\nu_1 = \eta_2/\eta_1 = 1.01$, whereas in Fig.3.2.2 $\nu_2/\nu_1 = 0.01$ and $\eta_2/\eta_1 = 0.1$. This weakens both the drive and the damping of structures U_2 compared to zonal flows U_1 in Fig.3.2.2, with respect to the case of Fig.3.2.1. Before time reaches $t \sim 6000$ time units, the evolution is very similar to Fig.2 of MD. However, at $t \sim 6500$ time units we find a dramatic change. A limit cycle appears after the long-term fixed point time series. The amplitudes of U_1 and U_2

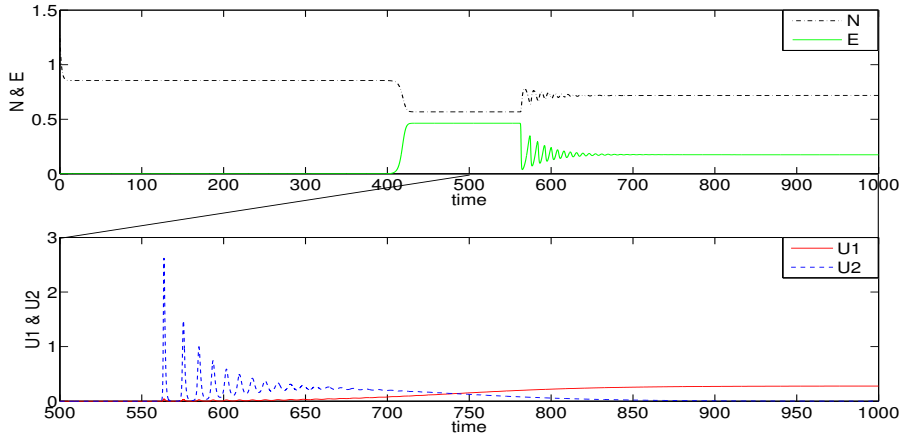

Figure 3.2.1: Upper panel: From a state near overpowered H-mode to unstable H-mode then to unstable L-mode then to T-mode. Lower panel: Transition to T-mode for U_1 and U_2 showing intersection at $t \simeq 750$ time units followed by gradual energy reversal. The model parameters are $\nu_1 = 19$, $\nu_2 = 1.01\nu_1$, $\eta_1 = 0.12$, $\eta_2 = 1.01\eta_1$, $q = 0.47$, $\rho = 0.55$, $\sigma = 0.6$, $\zeta = 1.7$.

exchange rather fast compared to Fig.3.2.1. Furthermore, the period of the limit cycle is rather long: several hundred time units. With the appearance of zonal flows and geodesic acoustic modes, the T-mode becomes unstable.

Figure 3.2.3 shows the case where the heating rate is higher than for Fig.3.2.1, $q = 0.58$, but all other model parameters are the same. At each pulsed occurrence of zonal flows U_1 and geodesic acoustic modes U_2, the former extract energy from the latter, which become extinct after the sixth pulse. Thereafter there are limit cycle oscillations in E, N and U_1 equivalent to the limit cycle for E, N and U in the case in MD.

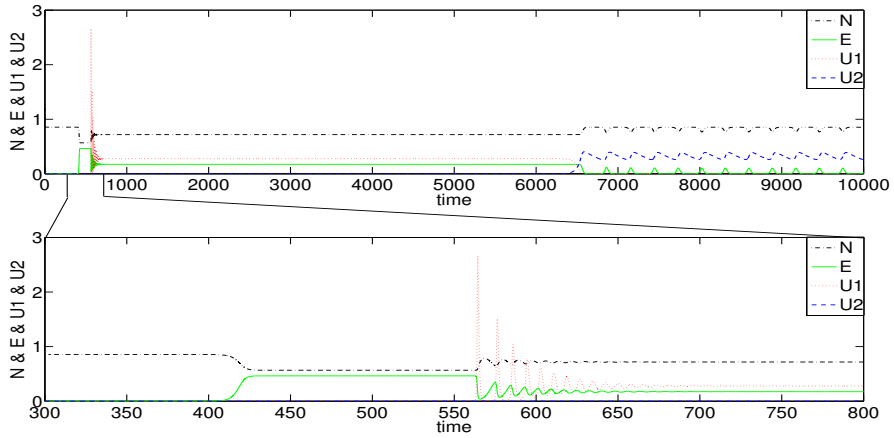

Figure 3.2.2: Upper panel: Transition from unstable fixed point state(T-mode) to unstable limit cycle oscillation state. Lower panel: Zoomed in version from $t = 300$ to $t = 800$. The model parameters are $\nu_1 = 19$, $\nu_2 = 0.01\nu_1$, $\eta_1 = 0.12$, $\eta_2 = 0.1\eta_1$, $q = 0.47$, $\rho = 0.55$, $\sigma = 0.6$, $\zeta = 1.7$.

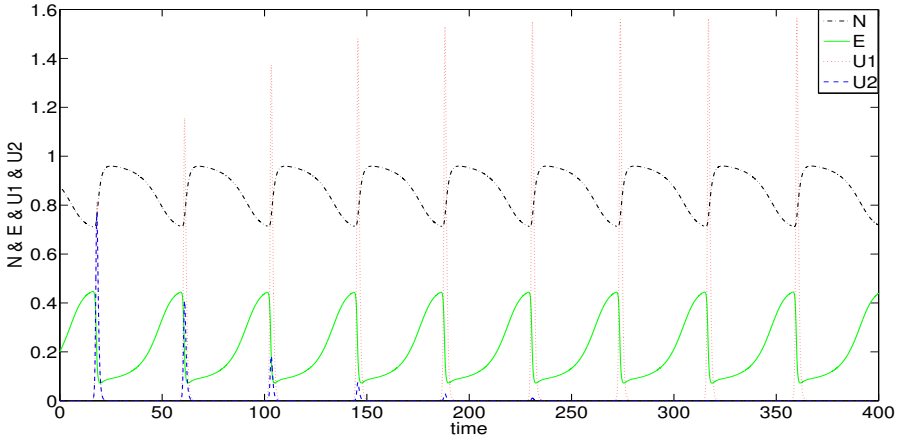

Figure 3.2.3: Burst energy transfer from U_2 to U_1 during strong nonlinear oscillation, followed by limit cycle oscillation in N, E and U_1. The model parameters are $\nu_1 = 19$, $\nu_2 = 1.01\nu_1$, $\eta_1 = 0.12$, $\eta_2 = 1.01\eta_1$, $q = 0.58$, $\rho = 0.55$, $\sigma = 0.6$, $\zeta = 1.7$.

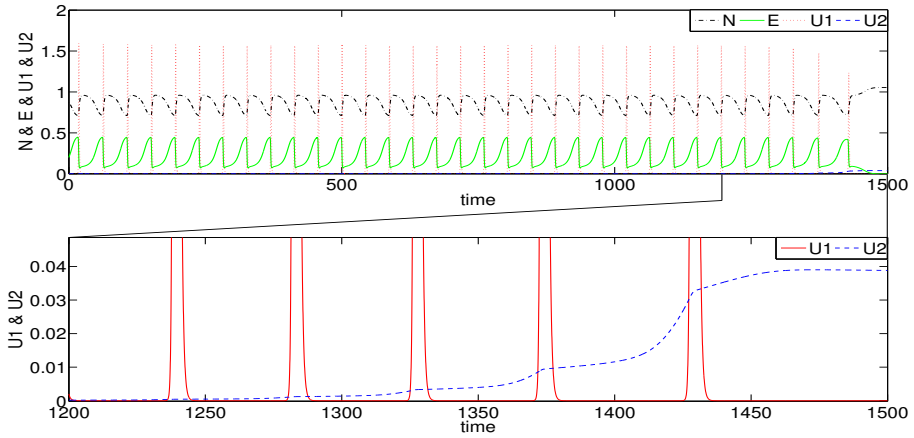

Figure 3.2.4: Upper panel: Collapse of limit cycle in N, E and U_1. Lower panel: Stair increasing of U_2 between every two pulses. The model parameters are $\nu_1 = 19$, $\nu_2 = 0.01\nu_1$, $\eta_1 = 0.12$, $\eta_2 = 0.01\eta_1$, $q = 0.58$, $\rho = 0.55$, $\sigma = 0.6$, $\zeta = 1.7$.

Figure 3.2.4 shows time traces for the case where all parameters, except the heating rate $q = 0.58$ which is the same as in Fig.3.2.3, are those of Fig.3.2.2. Together with Fig.3.2.5, where the heating rate q is slightly increased to $q = 0.582$ instead of $q = 0.58$, this enables us to relate our model to Fig.4 of MD, which showed that if in MD $q = 0.582$ instead of 0.58, the limit cycle eventually collapses after many oscillations. The final state has N finite and the remaining variables are zero; this is designated the QH-mode fixed point in MD. The corresponding cases for our model Eqs.(3.1.5-3.1.8) are shown in Figs.3.2.4 and 3.2.5. A precursor to limit cycle collapse is apparent in Fig.3.2.4 in the growth of the geodesic acoustic modes field U_2 during the episodes of zonal flow quiescence in the last few oscillations of the system.

For the slightly different parameter set used to generate Fig.3.2.5, the pulses of U_1 and U_2 grow and die together. Their peak amplitude increases at each successive cycle, as does the time interval between them. At the final oscillation, U_1 and U_2 collapse promptly together, whereas E survives longer until it is extinguished by damping. The phenomenology of Fig.3.2.5 thus corresponds more closely to that of Fig.4 of MD, compared to our Fig.3.2.4.

Figure 3.2.6 illustrates how system evolution towards the finite-N final state of Fig.3.2.5 depends on the damping rate η_2 of geodesic acoustic modes. We fix all parameters except η_2 and find that, with increasing η_2, there are more peaks of U_2 correlating with cyclic growth of E, which acts as a damping sink of N. Successive

peaks increase in height prior to extinction, which results in a final state similar to Fig.3.2.5.

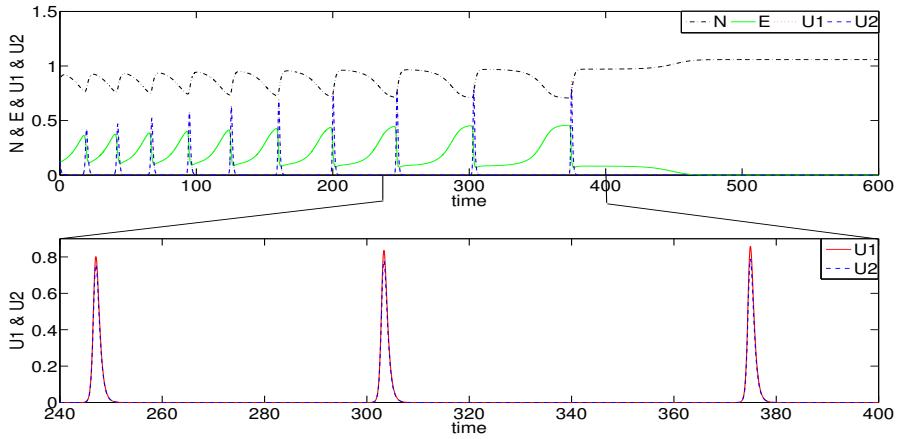

Figure 3.2.5: Upper panel: Collapse of limit cycle with positively correlated growth of pulses of U_1 and U_2. Lower panel: Zoomed in version from $t = 240$ to $t = 400$. The model parameters are $\nu_1 = 19$, $\nu_2 = 1.0001\nu_1$, $\eta_1 = 0.12$, $\eta_2 = 1.0001\eta_1$, $q = 0.582$, $\rho = 0.55$, $\sigma = 0.6$, $\zeta = 1.7$.

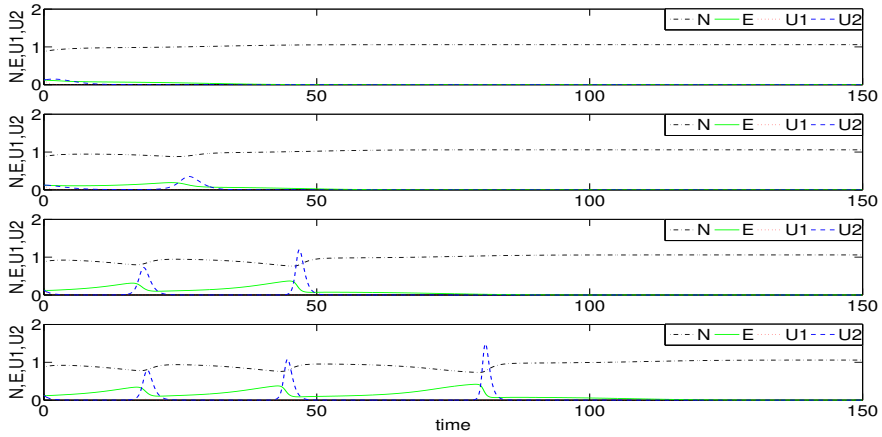

Figure 3.2.6: Evolution to the finite N attractor for different η_2 values. Upper panel: $\eta_2 = 0.05$. Middle upper panel: $\eta_2 = 0.06$. Middle lower panel: $\eta_2 = 0.10$. Lower panel: $\eta_2 = 0.11$. The remaining parameters are identical: $\nu_1 = 19$, $\nu_2 = 1.001\nu_1$, $\eta_1 = 0.12$, $q = 0.582$, $\rho = 0.55$, $\sigma = 0.6$, $\zeta = 1.7$.

3.3 Phase space evolution

The time traces of the individual variables, plotted in Figs.3.2.1 to 3.2.6, represent projections of the evolution in four-dimensional phase space of the system defined by Eqs.(3.1.5) to (3.1.8). In the present subchapter, we capture the global phase space explored by this system, for parameter values corresponding, or adjacent, to those used to generate Figs.3.2.1 to 3.2.6. This approach enables us to identify and characterise the nature of initial and final states, and of the transitional behaviour between them. The relationship between these figures is summarized in Table 3.2. These results are supplemented in the Chapter 3.4 by stability studies. At issue are two main physical concerns, which map directly to the properties of different energy confinement regimes in tokamaks, insofar as the zero-dimensional approach and the identifications made in MD, for example, may be valid. First, what is the nature of the final state that is reached at long times? For example, is it an attractive fixed point or a limit cycle (implying a nearby repulsive fixed point)? Second, there is the question, discussed previously, of robustness of three-variable models against the inclusion of a fourth variable (here, geodesic acoustic modes) in the model. For example, the pioneering work of MD includes identification of a limit cycle (Fig.3 of MD) with a specific confinement regime. Is this limit cycle - and, proceeding by analogy, the confinement regime that it represents - stable against the presence of geodesic acoustic modes in addition to zonal flows?

Figure 3.3.1 displays the generalisation, to the four-variable system, of the case of the three-variable system addressed in Fig.2 of MD. To fix ideas, the two left-hand plots correspond to the three-variable case for the parameters of Fig.2 of MD, showing the attractive fixed point which has finite values of E, N and U. The inward spiral path of the system from a random initial position is shown, both in (E, N, U) space and projected onto the (E, U) plane. It is evident that this path lies on a topological structure in phase space, whose dimensionality is lower by one than that of the full phase space. The two right-hand plots of Fig.3.3.1 show how this system changes when the two variables U_1 and U_2 replace U, for the parameter values used to generate the traces in Fig.3.2.1, which are adjacent to those for Fig.2 of MD, as discussed above. The centre right-hand plot shows initial spiral convergence in (E, U_2) which closely resembles that in the (E, U) plane displayed at centre left. Whereas with three variables this convergence is towards a fixed point, the existence of a fourth variable renders this attractive fixed point unstable. In consequence, the final stage of system evolution consists of injection in the U_1 direction to a fixed point at finite (E, N, U_1) with $U_2 = 0$. The far right plot in

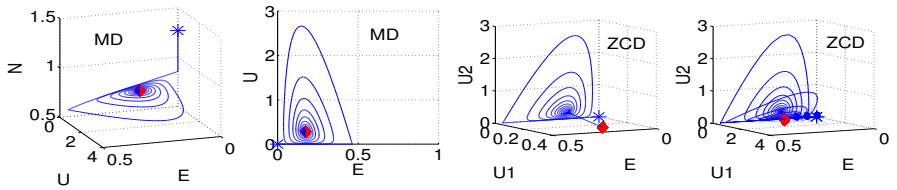

Figure 3.3.1: First panel: Fig.2 in MD. The parameters are $\nu = 19$, $\eta = 0.12$, $q = 0.47$, $\rho = 0.55$, $\sigma = 0.6$, $\zeta = 1.7$. Second panel: Projection of first panel on E-U plane. Third panel: Phase plot of Fig.3.2.1. Last panel: Phase plot of Fig.3.2.1 with 81 initial conditions. Stars denote initial values, blue dots denote trajectories and red diamonds denote final states.

Fig.3.3.1 demonstrates that this is indeed a fixed point, towards which phase space evolution originating from eighty-one different initial points converges. In each case, there is spiral convergence on a manifold followed by injection along U_1. The choice of initial condition affects only the orientation of this convergence manifold with respect to U_1 and U_2. We note also that the final state with finite U_1 differs from the MD final state for which $U = 0$.

Figure 3.3.2 illustrates the phase space evolution of the system whose time traces are plotted in Fig.3.2.2, which like Fig.3.3.1 is a case with parameters adjacent to those used to generate Fig.2 of MD. The initial spiral convergence in the (E, U_1) plane, shown in the centre panel, resembles that in the (E, U) plane for the MD case plotted in the left panel, which is identical to the centre-left panel of Fig.3.3.1. As in Fig.3.3.1, the stable fixed point of the three-variable system is unstable for the four-variable system, for which there is injection along U_2. Unlike Fig.3.3.1, where this injection is towards a stable fixed point, in Fig.3.3.2 the injection is onto a stable limit cycle that has finite slow oscillations in (N, E, U_2) with $U_1 = 0$ in the four-variable system.

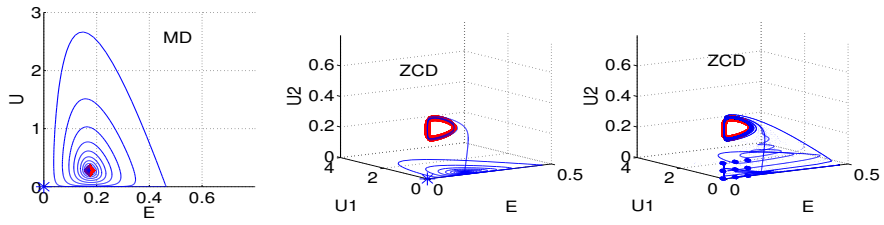

Figure 3.3.2: First panel: Projection of Fig.2 in MD on E-U plane. The parameters are $\nu = 19$, $\eta = 0.12$, $q = 0.47$, $\rho = 0.55$, $\sigma = 0.6$, $\zeta = 1.7$. Second panel: Phase plot of Fig.3.2.2. Last panel: Phase plot of Fig.3.2.2 with 81 initial conditions. Stars denote initial values, blue dots denote trajectories and red diamonds denote final states.

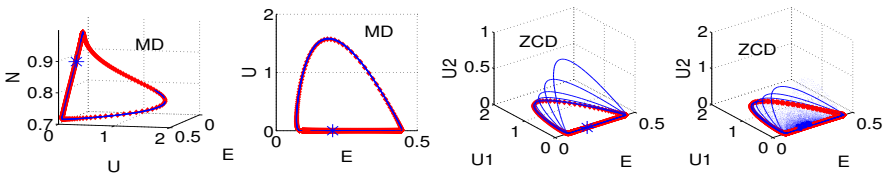

Figure 3.3.3: First panel: Fig.3 in MD. The parameters are $\nu = 19$, $\eta = 0.12$, $q = 0.58$, $\rho = 0.55$, $\sigma = 0.6$, $\zeta = 1.7$. Second panel: Projection of first panel on E-U plane. Third panel: Phase plot of Fig.3.2.3. Last panel: Phase plot of Fig.3.2.3 with 81 initial conditions. Stars denote initial values, blue dots denote trajectories and red diamonds denote final states.

The three-variable MD system has a limit cycle in (N, E, U) for the case shown in Fig.3 of MD. This is re-plotted in the two left panels of Fig.3.3.3 and in

the left panel of Fig.3.3.4. Figures 3.3.3 and 3.3.4 relate to the time traces shown in Figs.3.2.3 to 3.2.4 of the Chapter 3.2, obtained for parameter sets for the four-variable system which are adjacent to those used in MD for the three-variable system. For the parameters of Fig.3.3.3, which is the phase space plot for Fig.3.2.3, it is clear from the two right-hand panels that the limit cycle behaviour is essentially that of the MD system. The transient evolution towards the limit cycle involves circulation on similar planes that have successively lower peak values of U_2. The final limit cycle in (N, E, U_1), with $U_2 = 0$, is essentially that in (N, E, U) for the three-variable system.

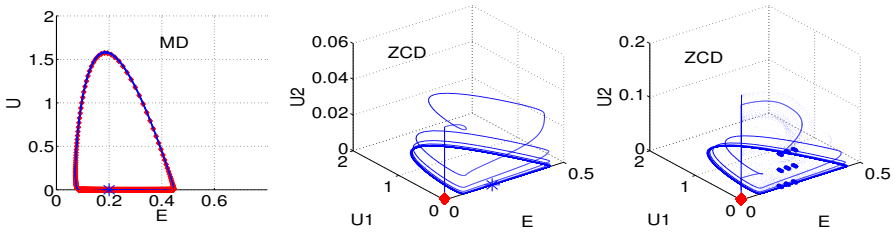

Figure 3.3.4: First panel: Projection of Fig.3 in MD on E-U plane. The parameters are $\nu = 19$, $\eta = 0.12$, $q = 0.58$, $\rho = 0.55$, $\sigma = 0.6$, $\zeta = 1.7$. Middle panel: Phase plot of Fig.3.2.4. Last panel: Phase plot of Fig.3.2.4 with 81 initial conditions. Stars denote initial values, blue dots denote trajectories and red diamonds denote final states.

The three-variable MD attractive limit cycle which manifests in the four-variable system as shown in Fig.3.3.3 is, however, unstable. Figure 3.3.4, which is the phase space plot for Fig.3.2.4, shows that the system leaves the former limit cycle and transiently explores the additional phase space dimension associated with the additional variable, before converging to a new fixed point that has N finite and all other variables zero. This class of attractive fixed point is noted in Fig.4 of MD, shown in the far left panel of Fig.3.3.5 and, projected on the (E, U) plane, in the centre left panel. The two right-hand panels of Fig.3.3.5 are the phase space plots for Fig.3.2.5, showing convergence to the origin in (E, U_1, U_2) space while N remains finite. The final step to the origin is preceded by circulation around and

away from an apparent repulsive fixed point with finite values of E, U_1 and U_2. The far right panel of Fig.3.3.5 shows that the choice of initial conditions merely affects the orientation in (U_1, U_2) space of the plane of this transient circulation.

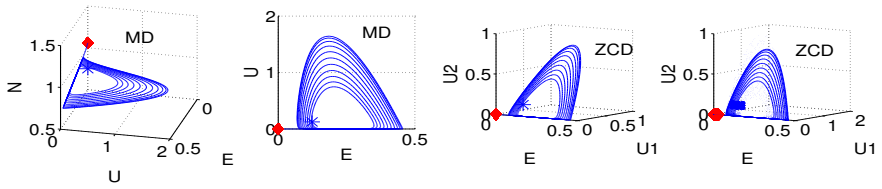

Figure 3.3.5: First panel: Phase plot for Fig.4 of MD. Second panel: Projection of Fig.4 in MD on E-U plane. The parameters are $\nu = 19$, $\eta = 0.12$, $q = 0.582$, $\rho = 0.55$, $\sigma = 0.6$, $\zeta = 1.7$. Third panel: Phase plot of Fig.3.2.5. Last panel: Phase plot of Fig.3.2.5 with 81 initial conditions. Stars denote initial values, blue dots denote trajectories and red diamonds denote final states.

Case	q	ν_2/ν_1	η_2/η_1	Timetraces	Phaseplot	Manifold
1	0.47	1.01	1.01	Fig.3.2.1	Fig.3.3.1	Fixed point
2	0.47	0.01	0.1	Fig.3.2.2	Fig.3.3.2	Limit cycle
3	0.58	1.01	1.01	Fig.3.2.3	Fig.3.3.3	Limit cycle
4	0.58	0.01	0.01	Fig.3.2.4	Fig.3.3.4	Limit cycle
5	0.582	1.0001	1.0001	Fig.3.2.5	Fig.3.3.5	Fixed point
6	0.582	1.001	0.05;0.06;0.1;0.11	Fig.3.2.6	N/A	N/A

Table 3.2: Summary of Figs.3.2.1 to 3.3.5

The phase space behaviour discussed thus far assists us in re-visiting the time traces in Fig.3.2.2, for which the corresponding phase plot is given in Fig.3.3.7. In Fig.3.3.6 we annotate Fig.3.2.2 in light of Fig.3.3.7. These two Figures demonstrate how, for the four-variable system, the T-mode of the three-variable system becomes unstable at long times. The system then evolves towards the newly identified attractive limit cycle in (N, E, U_2). Here slow oscillations in N correlate with those in U_2, both of which remain finite throughout, while bursts of E, feeding on U_2,

occur between extinctions. For the summary of these figures, please see Table 3.4 for details.

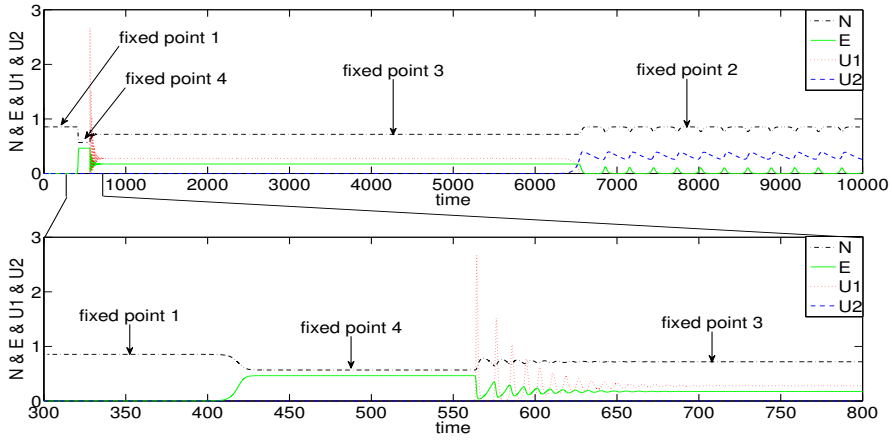

Figure 3.3.6: Time series of Fig.3.2.2 in Chapter 3.2, annotated in light of Fig.3.3.7.

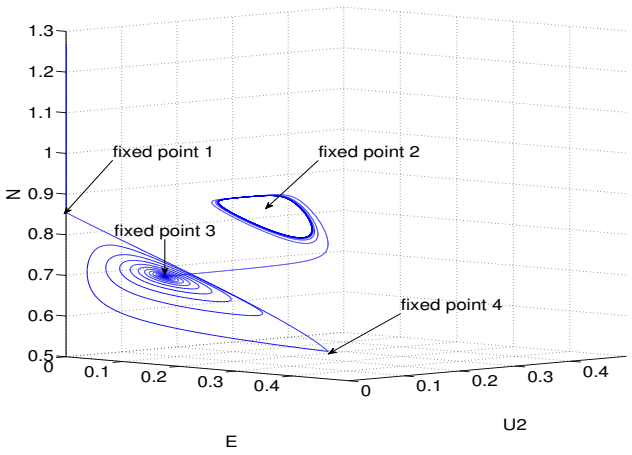

Figure 3.3.7: Phase plot of Fig.3.3.2 in Chapter 3.2.

3.4 Stability analysis in MD and ZCD models

We start from Eqs.(3.1.5-3.1.8), and for simplicity define the normalized equations as

$$\begin{cases} dE/dt = \left(N - N^4 - E - U_1 - U_2\right) E \equiv f\left(E, U_1, U_2, N\right) \\ dU_1/dt = \nu_1 \left(\dfrac{E}{1+\zeta N^4} - \eta_1\right) U_1 \equiv g_1\left(E, U_1, N\right) \\ dU_2/dt = \nu_2 \left(\dfrac{E}{1+\zeta N^4} - \eta_2\right) U_2 \equiv g_2\left(E, U_2, N\right) \\ dN/dt = q - \left(\rho + \sigma E\right) N \equiv h\left(E, N\right) \end{cases} \tag{3.4.1}$$

We regard point $(N_0, E_0, U_{10}, U_{20})$ as a fixed point of the 4D system, and define

$$\begin{cases} f_0 \equiv f\left(E_0, U_{10}, U_{20}, N_0\right) \\ g_{10} \equiv g_1\left(E_0, U_{10}, N_0\right) \\ g_{20} \equiv g_2\left(E_0, U_{20}, N_0\right) \\ h_0 \equiv h\left(E_0, N_0\right) \end{cases} \tag{3.4.2}$$

By construction $f_0 = g_{10} = g_{20} = h_0 = 0$. Near the fixed point, we make a local linear expansion of the model parameters:

$$\triangle E \equiv E - E_0; \triangle U_1 \equiv U_1 - U_{10}; \triangle U_2 \equiv U_2 - U_{20}; \triangle N \equiv N - N_0; \tag{3.4.3}$$

This gives rise to the linearised equations

$$\begin{cases} f \approx f_0 + \frac{\partial f}{\partial E} \triangle E + \frac{\partial f}{\partial U_1} \triangle U_1 + \frac{\partial f}{\partial U_2} \triangle U_2 + \frac{\partial f}{\partial N} \triangle N \\ g_1 \approx g_{10} + \frac{\partial g_1}{\partial E} \triangle E + \frac{\partial g_1}{\partial U_1} \triangle U_1 + \frac{\partial g_1}{\partial N} \triangle N \\ g_2 \approx g_{20} + \frac{\partial g_2}{\partial E} \triangle E + \frac{\partial g_2}{\partial U_2} \triangle U_2 + \frac{\partial g_2}{\partial N} \triangle N \\ h \approx h_0 + \frac{\partial h}{\partial E} \triangle E + \frac{\partial h}{\partial N} \triangle N \end{cases} \tag{3.4.4}$$

To obtain the eigenvalues of the system, we calculate the corresponding Jacobian matrix

$$J = \begin{pmatrix} \frac{\partial}{\partial E} f & \frac{\partial}{\partial U_1} f & \frac{\partial}{\partial U_2} f & \frac{\partial}{\partial N} f \\ \frac{\partial}{\partial E} g_1 & \frac{\partial}{\partial U_1} g_1 & \frac{\partial}{\partial U_2} g_1 & \frac{\partial}{\partial N} g_1 \\ \frac{\partial}{\partial E} g_2 & \frac{\partial}{\partial U_1} g_2 & \frac{\partial}{\partial U_2} g_2 & \frac{\partial}{\partial N} g_2 \\ \frac{\partial}{\partial E} h & \frac{\partial}{\partial U_1} h & \frac{\partial}{\partial U_2} h & \frac{\partial}{\partial N} h \end{pmatrix}_{(E_0, U_{10}, U_{20}, N_0)} \tag{3.4.5}$$

We now identify the fixed points.

① if $E = 0$,

$$\begin{cases} N - N^4 - E - U_1 - U_2 = K \\ U_1 = 0 \\ U_2 = 0 \\ N = \dfrac{q}{\rho} \end{cases} \tag{3.4.6}$$

where K is a constant that can take any value.

② if $E \neq 0$,

$$\begin{cases} N - N^4 - E - U_1 - U_2 = 0 \\ \left(\dfrac{E}{1 + \zeta N^4} - \eta_1 \right) U_1 = 0 \\ \left(\dfrac{E}{1 + \zeta N^4} - \eta_2 \right) U_2 = 0 \\ q - (\rho + \sigma E) N = 0 \end{cases} \tag{3.4.7}$$

From the second and third equations in this group, it follows that U_1 and U_2 cannot be non-zero simultaneously.

(i) if $U_1 = 0$, $U_2 \neq 0$, $E \neq 0$,

$$\begin{cases} N - N^4 - E - U_1 - U_2 = 0 \\ \dfrac{E}{1 + \zeta N^4} - \eta_1 = K \\ \dfrac{E}{1 + \zeta N^4} - \eta_2 = 0 \\ q - (\rho + \sigma E) N = 0 \end{cases} \tag{3.4.8}$$

(ii) if $U_1 \neq 0$, $U_2 = 0$, $E \neq 0$,

$$\begin{cases} N - N^4 - E - U_1 - U_2 = 0 \\ \dfrac{E}{1 + \zeta N^4} - \eta_1 = 0 \\ \dfrac{E}{1 + \zeta N^4} - \eta_2 = K \\ q - (\rho + \sigma E) N = 0 \end{cases} \tag{3.4.9}$$

where K is a constant that can take any value.

(iii) if $U_1 = U_2 = 0$, $E \neq 0$,

$$\begin{cases} N - N^4 - E = 0 \\ U_1 = 0 \\ U_2 = 0 \\ q - (\rho + \sigma E)\, N = 0 \end{cases} \tag{3.4.10}$$

Solutions for the specific cases of the MD and ZCD systems considered in this Chapter are shown in Table 3.3 and Table 3.4 respectively.

MD	Fixed points$(E;U;N)$	Eigenvalues	Property
Fig.2	0;0;0.8545	-2.28;-0.55;0.3213	Saddle point-Index 1
	0.1742;0.2780;0.7181	$-0.0360 \pm 0.8099i$;-0.7567	Spiral node**(final state)**
	0.4638;0;0.5675	$-0.6460 \pm 0.0963i$;5.2111	Inward spiral and source
Fig.3	0;0;0.8545	-2.28;-0.55;-0.1821	Node
	0.2249;0.1077;0.8468	$0.0069 \pm 0.4991i$;-0.9236	Outward spiral and sink**(limit cycle)**
	0.0769;0;0.9729	0.0969;-0.7700;-1.7010	Saddle point-Index 1
	0.4588;0;0.7028	3.8817;-0.3122;-0.9718	Saddle point-Index 1
Fig.4	0;0;1.0582	-2.28;-0.55;-0.1957	Node**(final state)**
	0.2260;0.1036;0.8489	$0.0080 \pm 0.4892i$;-0.9275	Outward spiral and sink
	0.0825;0;0.9708	0.1002;-0.7821;-1.6558	Saddle point-Index 1
	0.4576;0;0.7058	3.8348;-0.3058;-0.9764	Saddle point-Index 1

Table 3.3: Properties of stability analysis of MD system

3.5 Limit cycle analysis in ZCD model

In previous two sub-chapters(Chapter 3.3 and Chapter 3.4), we know that limit cycle oscillations could be discovered if adjusting the ratios of η, ν and q. In this sub-chapter, we try to demonstrate the inherent relationships between ZCD model and limit cycle oscillations. The properties of fixed points and limit cycle oscillations will be illustrated as well.

Figure 3.5.1 shows the parameter space of ν_2/ν_1 and η_2/η_1 when $q = 0.47$. We calculated from $t = 0$ to $t = 500,000$ time units. The red diamonds denote final states that are limit cycles while the black dots denote stable fixed points final states. It is demonstrated that the threshold of the appearance of limit cycle oscillations is $\eta_2/\eta_1 \simeq 0.20$. Limit cycle oscillations cannot be found if η_2/η_1 value is larger than the threshold. We also get the conclusion that ν_2/ν_1 influences much less than η_2/η_1 in the parameter space if calculating in the range of $0 \leq \nu_2/\nu_1 \leq 2$ and $0.18 \leq \eta_2/\eta_1 \leq 0.22$.

ZCD	Fixed points$(E;U_1;U_2;N)$	Eigenvalues	Property
Fig.4.12	0;0;0;0.8545	-2.28;-0.55;0.3213;-2.3258	4D Saddle point-Index 1
	0.1757;0;0.2770;0.7171	$-0.0365 \pm 0.8165i$;-0.7581;0.0228	Inward spiral, source and sink
	0.1742;0.2780;0;0.7187	$-0.0360 \pm 0.8099i$;-0.0230;-0.7567	Spiral node**(final state)**
	0.4638;0;0;0.5675	$-0.6460 \pm 0.0963i$;5.2402;5.2111	Inward spiral and sources
Fig.4.13	0;0;0;0.8545	-2.28;-0.55;0.3213;-0.0023	4D Saddle point-Index 1
	0.0219;0;0.3275;0.8346	$0.0019 \pm 0.0272i$;-0.5888;-2.052	Outward spiral and sinks**(limit cycle)**
	0.1742;0.2780;0;0.7187	$-0.0360 \pm 0.8099i$;0.0205;-0.7567	Inward spiral,source and sink
	0.4638;0;0;0.5675	$-0.6460 \pm 0.0963i$;0.0726;5.2111	Outward spiral and sources
Fig.4.14	0;0;0;1.0545	-2.28;-0.55;-2.3258;-0.1821	Node
	0.2265;0;0.1078;0.8456	$0.0062 \pm 0.5045i$;0.0228;-0.9248	Outward spiral, source and sink
	0.2249;0.1077;0;0.8468	$0.0069 \pm 0.4991i$;-0.0230;-0.9236	Outward spiral and sinks**(limit cycle)**
	0.0769;0;0;0.9729	0.0969;-0.7700;-1.7010;-1.741	4D Saddle point-Index 1
	0.4588;0;0;0.7028	-0.3122;-0.9718;3.8817;3.8975	4D Saddle point-Index 2
Fig.4.15	0;0;0;1.0545	-2.28;-0.55;-0.1821;-0.0002	Node**(final state)**
	0.2249;0.1077;0;0.8468	$0.0069 \pm 0.4990i$;0.0226;-0.9236	Outward spiral, source and sink
	0.4588;0;0;0.7028	-0.3122;-0.9718;3.8817;0.0614	4D Saddle point-Index 2
	0.0769;0;0;0.9729	0.0969;0.0056;-0.7700;-1.7010	4D Saddle point-Index 2
Fig.4.16	0;0;0;1.0582	-2.28;-0.55;-2.2805;-0.1957	Node**(final state)**
	0.2260;0;0.1036;0.8489	$0.0080 \pm 0.4892i$;0.0002;-0.9275	Outward spiral, source and sink
	0.2260;0.1036;0;0.8489	$0.0080 \pm 0.4892i$;-0.0002;-0.9275	Outward spiral and sinks
	0.0825;0;0;0.9708	0.1002;-0.7821;-1.6558;-1.6562	4D Saddle point-Index 1
	0.4576;0;0;0.7058	-0.3058;-0.9764;3.8348;3.8349	4D Saddle point-Index 2

Table 3.4: Properties of stability analysis of ZCD system

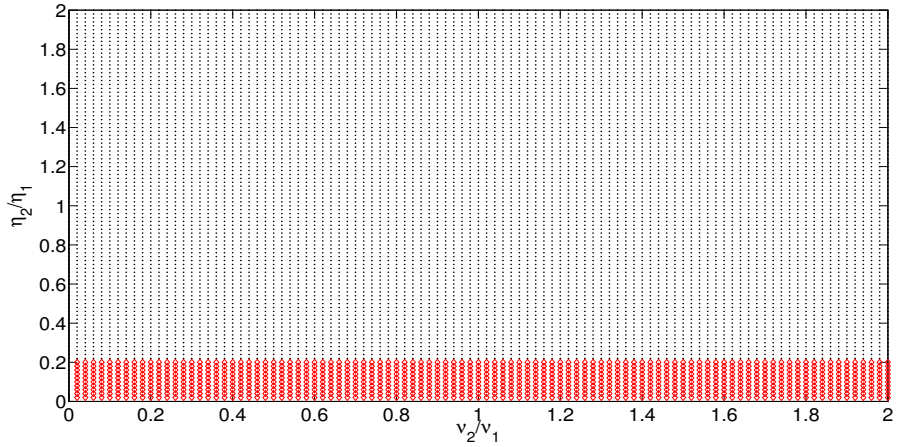

Figure 3.5.1: Parameter space of ν_2/ν_1 and η_2/η_1 when $q = 0.47$.

Figure 3.5.2 demonstrates the parameter space of ratios of η and ν when $q = 0.58$. Like Figure 3.5.1, red diamonds and black dots are limit cycle oscillations final states and stable fixed points final states respectively. The vertical red diamond line in the left corner represents the limit cycle oscillations in MD model when $\nu_2 = 0$, see Chapter 2.4.1. The threshold of this parameter space is $\eta_2/\eta_1 \simeq 1.00$. Similarly, η_2/η_1 influence the properties of final states much more than ν_2/ν_1.

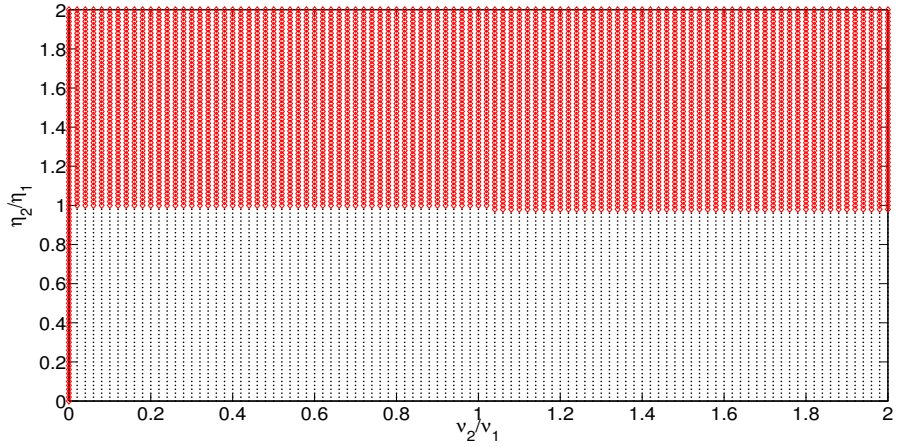

Figure 3.5.2: Parameter space of ν_2/ν_1 and η_2/η_1 when $q = 0.58$.

Figure 3.5.3 is the parameter space when $q = 0.582$. In this case, the limit cycle oscillations final states cannot be discovered in the range of $0 \leq \nu_2/\nu_1 \leq 2$

and $0 \leq \eta_2/\eta_1 \leq 2$. We can conclude that the external heating flux q is a control parameter in the ZCD dynamical system. With the increasing q from $q = 0.58$ in Figure 3.5.2 to $q = 0.582$ in Figure 3.5.3, the properties of final states are totally changed.

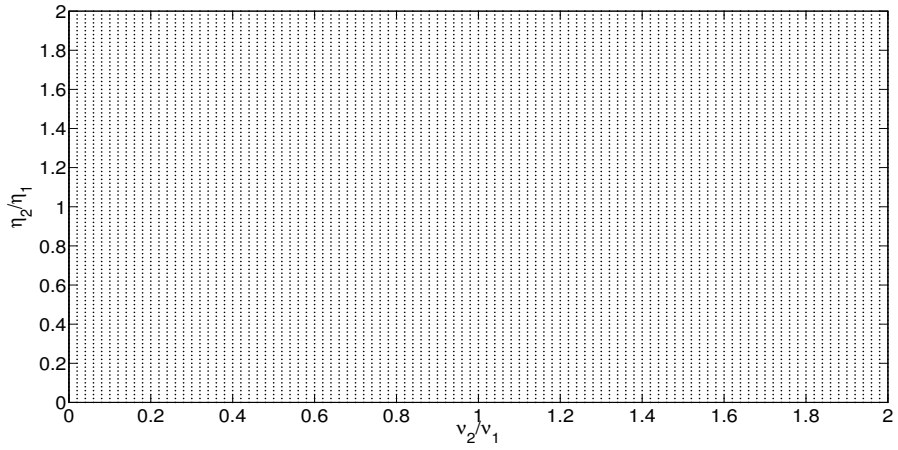

Figure 3.5.3: Parameter space of ν_2/ν_1 and η_2/η_1 when $q = 0.582$.

3.6 Conclusions

Contemporary experimental results from the DIII-D[Schmitz et al., 2012] and HL-2A tokamak devices[Xu et al., 2012b] reinforce the relevance of zero-dimensional predator-prey models to transitions between energy confinement regimes. Understanding how the outputs of related, but different, predator-prey models for plasma confinement phenomenology may resemble or deviate from each other is therefore important. In Chapter 3, we have focused on the consequences of adding a second predator, and hence a fourth field variable, to the three-field MD[Malkov and Diamond, 2009] model. Quantitative studies have been presented for parameter sets that are maximally adjacent to those in MD, which yield the time traces shown in Figs.3.2.1 to 3.2.6 and Fig.3.3.6. These are projections of the phase space dynamics shown in Figs.3.3.1 to 3.3.5 and Fig.3.3.7. It is found that both congruences and deviations can occur between the three-field and four-field models. For example, Fig.3.3.4 shows how a limit cycle in the three-field system is unstable for four fields in the relevant parameter range, where the attractor is a fixed point. Conversely Fig.3.3.2 shows a three-field fixed point mapping to a four-field limit cycle. Figure 3.3.7 shows the complex, but resolved, phase space dynamics underlying a

generalisation to four fields of the three-field scenario modelled in Fig.2 of MD. We conclude that exploration of the linkages between different zero-dimensional models, capturing full phase space properties so far as computationally possible, needs to keep pace with the continuing development and refinement of individual zero-dimensional models in fusion plasma physics.

Zero-dimensional models remain attractive because they embody physically motivated narratives that may account for global fusion plasma confinement phenomenology. Ideally the end states (attractors) of zero-dimensional models, together with the transitional behaviour en route from the initial configurations, should be robustly identifiable with fusion plasma confinement states and transitions. Zero-dimensional predator-prey models, constructed in terms of a small number of variables representing global quantities such as the drift wave turbulence level $\mathcal{E}$, drift wave driving temperature gradient $\mathcal{N}$, zonal flow velocity V_{ZF}, geodesic acoustic modes velocity V_{GAM}, and the heating rate q in Eqs.(3.1.1) to (3.1.4), are intrinsically nonlinear. This nonlinearity implies the potential for a rich and varied set of attractors and transitional behaviour, together with strong dependence on the numerical values of model parameters. This Chapter has taken steps to explore this potential for the model of interest in the case of parameter sets close to those studied previously in MD, with a view to strengthening the links between families of zero-dimensional models on the one hand, and fusion plasma confinement phenomenology on the other. We note finally that some of the considerations addressed here may carry over to other fields where it is hoped to develop zero-dimensional models that have descriptive, or even predictive, power for global phenomena in macroscopic multiscale driven-dissipative systems. A topical instance is provided by zero-dimensional modelling in climate science, see for example [Eliseev and Mokhov, 2007] and references therein, where some general circulation models incorporate Lotka-Volterra features[Cox et al., 2000].

Chapter 4

Heating induced confinement transitions in MD and ZCD models

4.1 Introduction

Zero-dimensional models[Malkov and Diamond, 2009; Diamond et al., 1994; Bian and Garcia, 2003; Bian, 2010; Itoh and Itoh, 2011; Miki and Diamond, 2011; Kim and Diamond, 2003; Miki and Diamond, 2010; Miki et al., 2012, 2013c,a,d,b; Zhu et al., 2013; Douglas et al., 2013] – that is, systems of coupled nonlinear differential equations with a single independent parametric coordinate representing time – play an important role in interpreting fusion plasmas behaviour. By choosing variables to represent key macroscopic quantities such as the electron temperature gradient N, the intensity of micro-scale turbulence E, and the magnitude of meso-scale coherent nonlinear structures U, zero-dimensional models can be constructed in a manner that reflects the global phenomenology of, for example, L-mode and H-mode confinement physics. This enables empirically inspired physical models, which typically include predator-prey or Lotka-Volterra dynamics, to be tested and explored quantitatively: a necessary step, given that the dynamics can be strongly nonlinear. It has not previously been established whether, in zero-dimensional models, rapid substantial increases in externally applied heating can engender sharp transitions in confinement properties, akin to heating-induced transition from L-mode to H-mode confinement in tokamak plasmas. First identified in [Wagner et al., 1982], the role of heating in this transition has been examined experimentally in all large tokamak plasmas, including DIII-D[Burrell, 1994], JT-60U[Fukuda et al., 1997], Alcator

C-Mod[Greenwald et al., 1997] and ASDEX-U[Ryter et al., 1998], and in a range of tritium, deuterium-tritium and hydrogen plasmas in JET[Righi et al., 1999]. For recent reviews of the H-mode and related fundamental plasma phenomena, see for example [Tynan et al., 2009; Wagner, 2007; Diamond et al., 2011]. Here we address heating-induced transitions in the framework of the well-established zero-dimensional model of Diamond, Kim and Malkov[Malkov and Diamond, 2009; Kim and Diamond, 2003], hereafter KD/MD, which couples the three variables (N, E, U) introduced above, and is driven by the external heating flux $q(t)$, using the normalization of [Malkov and Diamond, 2009]. The model of ZCD will be analysed as well, see [Zhu et al., 2013]. In the normalization mentioned above, the correspondence between the E^2 terms in equation (4.1.1) and equation (1) of [Diamond et al., 1994], implies that the time scale throughout this system of equations scales with the inverse of the parameter a_1 defined in [Diamond et al., 1994]. Table 1 of [Diamond et al., 1994] provides expressions for this parameter in terms of physical quantities.

$$\frac{dE}{dt} = \left(N - N^4 - E - U\right) E \tag{4.1.1}$$

$$\frac{dU}{dt} = \nu \left(\frac{E}{1+\zeta N^4} - \eta\right) U \tag{4.1.2}$$

$$\frac{dN}{dt} = q\left(t\right) - \left(\rho + \sigma E\right) N \tag{4.1.3}$$

The meso-scale coherent nonlinear structures U are induced by micro-scale turbulence intensity E. The growth of micro-scale turbulence E is suppressed and meso-scale structures U as well as being self suppressed. External heating drives this system, and the external heating rate acts as a control parameter. The KD/MD model was recently extended in [Zhu et al., 2013], to include a fourth variable representing a second predator population U_2 of coherent nonlinear structures, for example geodesic acoustic modes(GAMs), in addition to the KD/MD population(denoted U_1 in ZCD) originally intended to represent zonal flows(ZFs). The introduction of these distinct classes of nonlinear structure in a zero-dimensional model follows the philosophy of Itoh & Itoh[Itoh and Itoh, 2011]. We note that there is no direct interaction between U_1 and U_2 due to the parallelism of ZFs and GAMs[Diamond et al., 2005].

The ZCD extension[Zhu et al., 2013] of the KD/MD model is written as:

$$\frac{dE}{dt} = \left(N - N^4 - E - U_1 - U_2\right) E \tag{4.1.4}$$

$$\frac{dU_1}{dt} = \nu_1 \left(\frac{E}{1+\zeta N^4} - \eta_1\right) U_1 \tag{4.1.5}$$

$$\frac{dU_2}{dt} = \nu_2 \left(\frac{E}{1+\zeta N^4} - \eta_2\right) U_2 \tag{4.1.6}$$

$$\frac{dN}{dt} = q\left(t\right) - \left(\rho + \sigma E\right) N \tag{4.1.7}$$

In this Chapter we investigate how sharp step changes in heating power $q(t)$ in the KD/MD model, and its ZCD extension, can induce confinement transitions. We also examine the impact of an oscillating heating rate on the ZCD extension, obtaining results for the system dynamics which differ significantly from those found in [Douglas et al., 2013] for the KD/MD model. We quantify the dynamics, both in terms of the underlying (N, E, U) phase space and in terms of the energy confinement time τ_c which is the key figure of merit. We identify the scaling of τ_c with heating power in the different confinement regimes of the KD/MD model and its ZCD extension. This is an important first step towards direct comparison between the global energy confinement times implicit in zero-dimensional models and the empirical confinement time scalings determined from multiple tokamak plasma experiments. We establish that the heating-induced confinement transitions are not strongly sensitive to the timescale on which heating power is increased. The results in this Chapter are a significant step in the validation of the zero-dimensional approach, and of the KD/MD model and its ZCD extension, together with the physical identifications and assumptions which zero-dimensional models embody.

A new result of [Zhu et al., 2013] concerned the attractive fixed point of the KD/MD model referred to as the transient mode (T-mode). It was found in ZCD that the introduction of a second coherent field U_2, acting as an additional predator on the micro-scale turbulence E, transforms the post-heating T-mode into a repulsive fixed point. A new attractive fixed point (see Figure 4.3.1 in Chapter 4.3) or limit cycle (see Figure 4.3.2 in Chapter 4.3) appears in ZCD, compare e.g. Fig.13 of ZCD. Here we refer to this new attractor as the oscillation mode (O-mode). Unlike the low confinement T-mode in KD/MD, the O-mode in ZCD has good confinement properties, as we discuss below. In the stable O-mode, N is finite, as is U_2, with E zero or very small, and U_1 zero. The present Chapter therefore also explores heating-induced transitions that can give rise to the O-mode in the ZCD extension of the KD/MD model.

We find that in the ZCD model, when the external heating rate includes a component that oscillates sinusoidally in time, as in [Douglas et al., 2013], a period-doubling path to chaos exists. The amplitude A of the oscillatory component of the heating rate is the control parameter. The micro-scale turbulence level E bifurcates with increasing A, and the ratio of values of A at successive bifurcations is found to yield the first Feigenbaum's constant[Feigenbaum, 1978] to high accuracy.

4.2 Analytical confinement properties of the models

The energy confinement time in the KD/MD model and its ZCD extension can be addressed analytically, to some extent. We may define the energy confinement time τ_c at any instant by analogy with the fusion context[Freidberg, 2007], using

$$\tau_c = \frac{N}{q - dN/dt} \tag{4.2.1}$$

The structure of Eq.(4.2.1) is standard; in the present context, it reflects the fact that the electron temperature gradient N is a physical proxy for stored energy, whose time evolution is driven by q in Eq.(4.1.3). It follows from Eqs.(4.1.3), (4.1.7) and (4.2.1) that the confinement time in both KD/MD and ZCD is

$$\tau_c = \frac{1}{\rho + \sigma E} \tag{4.2.2}$$

for all t. At the fixed point, $dN/dt = 0$ and

$$\tau_F = \frac{N_F}{q_F} = \frac{1}{\rho + \sigma E_F} \tag{4.2.3}$$

where subscript F denotes evaluation at the fixed point.

We will need to solve numerically the system of equations Eqs.(4.1.1) to (4.1.3), and their ZCD counterparts Eqs.(4.1.4) to (4.1.7), in order to establish whether fixed points are accessible and how transitions between them (induced by changes in heating or otherwise) occur. However, provided the system can access the fixed point, Eq.(4.2.3) will hold and we can find τ_F for that fixed point. As discussed in KD/MD[Malkov and Diamond, 2009; Kim and Diamond, 2003], the QH-mode fixed point has $E = U = 0$. It therefore follows from Eq.(4.1.3) that in QH-mode there is linear scaling of stored energy with heating power,

$$q_{QH} = \rho N_{QH} \tag{4.2.4}$$

and from Eq.(4.2.3), $\tau_{QH} = 1/\rho$. In contrast the T-mode fixed point[Malkov and Diamond, 2009] has E and U finite, and Eq.(4.2.3) then yields

$$\tau_T = \frac{1}{\rho + \sigma\eta\left(1 + \zeta N_T^4\right)} = \frac{\tau_{QH}}{1 + (\sigma\eta/\rho)\left(1 + \zeta N_T^4\right)} \tag{4.2.5}$$

This reflects the degradation of confinement in T-mode compared to QH-mode, associated with the level of T-mode turbulence $E_T = \eta\left(1 + \zeta N_T^4\right)$. It further follows from Eq.(4.1.3) that

$$q_T = \rho N_T\left[1 + (\sigma\eta/\rho)\left(1 + \zeta N_T^4\right)\right] \tag{4.2.6}$$

in contrast to Eq.(4.2.4).

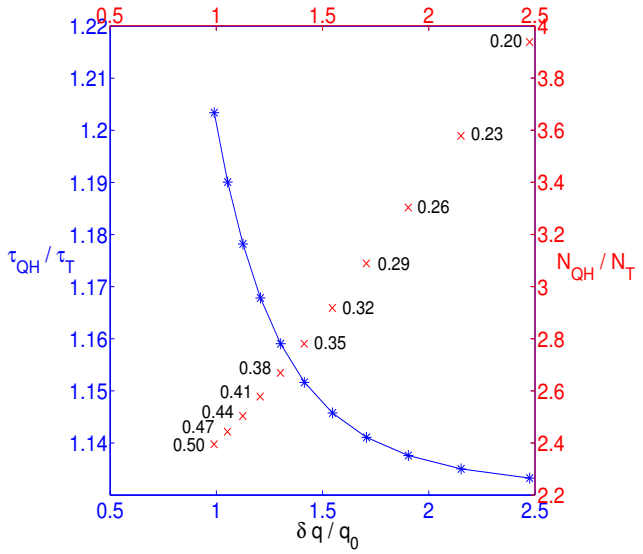

Figure 4.2.1: KD/MD model dependence of ratios of confinement time τ_{QH}/τ_T (blue stars; left scale) and temperature gradient N_{QH}/N_T (red crosses; right scale) on the normalised increase in heating rate $\delta q/q_0$. Solid line for τ_{QH}/τ_T is inferred from Eqs.(4.2.5) and (4.2.6). Points are obtained from numerical results for $\delta q = 0.495$, $\tau_{QH} = 1.8182$, q_0 values are shown in figure; other parameter values are $\nu = 19$, $\eta = 0.12$, $\rho = 0.55$, $\sigma = 0.6$, $\zeta = 1.7$.

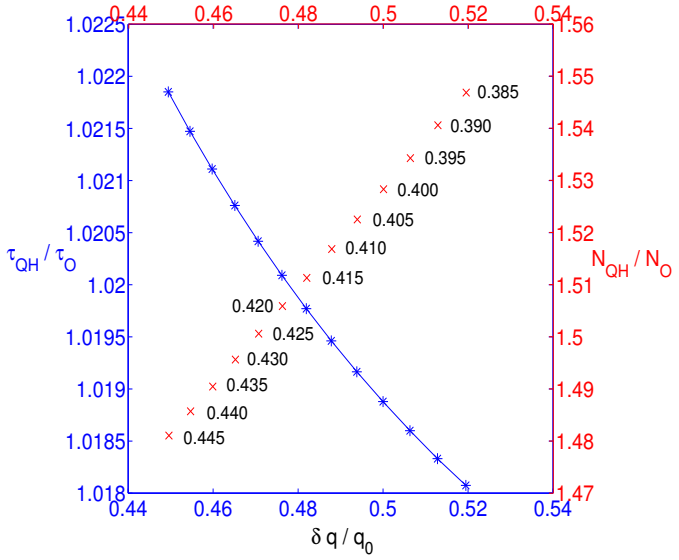

Figure 4.2.2: ZCD model dependence of ratios of confinement time τ_{QH}/τ_O (blue stars; left scale) and temperature gradient N_{QH}/N_O (red crosses; right scale) on the normalised increase in heating rate $\delta q/q_0$. Solid line is inferred from Eqs.(4.2.4) and (4.2.9). Points are obtained from numerical results for $\delta q = 0.20$, $\tau_{QH} = 1.8182$, q_0 values are shown in figure; other parameter values are $\nu_1 = 19$, $\nu_2 = 0.19$, $\eta_1 = 0.12$, $\eta_2 = 0.012$, $\rho = 0.55$, $\sigma = 0.6$, $\zeta = 1.7$.

Inversion of Eq.(4.2.6) to yield N_T as a function of q_T can be achieved numerically. Substitution of this result into Eq.(4.2.5) then yields τ_T as a function of q_T. In Fig.4.2.1 we plot the relative changes in the proxy for stored energy, N_{QH}/N_T, and in confinement time τ_{QH}/τ_T, as functions of the normalised increase in heating power $\delta q/q_0$ in the KD/MD model, where $\delta q = q_{QH} - q_T$ and $q_0 = q_T$. The solid line in Fig.4.2.1 is derived from Eqs.(4.2.4) to (4.2.6), with over-plotted points derived from direct solution of Eqs.(4.1.1) to (4.1.3) and (4.2.1).

The O-mode attractive fixed point or limit cycle of ZCD can be well approximated by $U_1 = 0$ and

$$E_O = \eta_2 \left(1 + \zeta N_O^4\right) \tag{4.2.7}$$

$$U_{2O} = N_O - N_O^4 - E_O \tag{4.2.8}$$

It follows that

$$\tau_O = \frac{1}{\rho + \sigma\eta_2 \left(1 + \zeta N_O^4\right)} \tag{4.2.9}$$

Analysis similar to that for the T-mode following Eq.(4.2.5) is then possible.

In this Chapter, the T-mode is the lower confinement regime, compared to the enhanced confinement QH-mode in KD/MD and ZCD, and also compared to the O-mode in ZCD. The model QH-mode has highly idealised confinement properties embodied in Eq.(4.2.4). Figure 4.2.2 shows that the confinement properties of the ZCD post-heating O-mode are very similar to QH-mode, although weakly dependent on heating. These good confinement regimes effectively provide the benchmark with respect to which the degraded T-mode confinement is normalised. Figures.4.2.1 and 4.2.2 provide a general method to parametrise the energy confinement transition properties of zero-dimensional models in similar terms to experiments, see for example the classic studies of tokamak plasma confinement scaling in [Kaye et al., 1997] for L-mode and [Doyle et al., 2007] for H-mode. We have used parameter values here that correspond to those in [Malkov and Diamond, 2009; Zhu et al., 2013]. Different sets of values of these parameters would correspond to different values of the ratio $\sigma\eta/\rho$ and of ζ, and to different locations of the fixed points in phase space for given $\delta q/q_0$. This suggests that an extensive exploration of parameter space could yield confinement time ratios more nearly consistent with experiment than those in Figure 4.2.1.

4.3 Confinement transition induced by heating in MD model

Understanding the confinement properties of the fixed point attractors and limit cycles of the KD/MD model and its ZCD extension is necessary, but not sufficient, for analysing the mapping from these zero-dimensional approaches to tokamak phenomenology. The transient time evolution of the system variables towards and between fixed points can, as we shall see, be of long duration and may relate to tokamak scenarios. In this sub-chapter, we focus particularly on changes in time evolution that are consequent on rapid changes in heating power q.

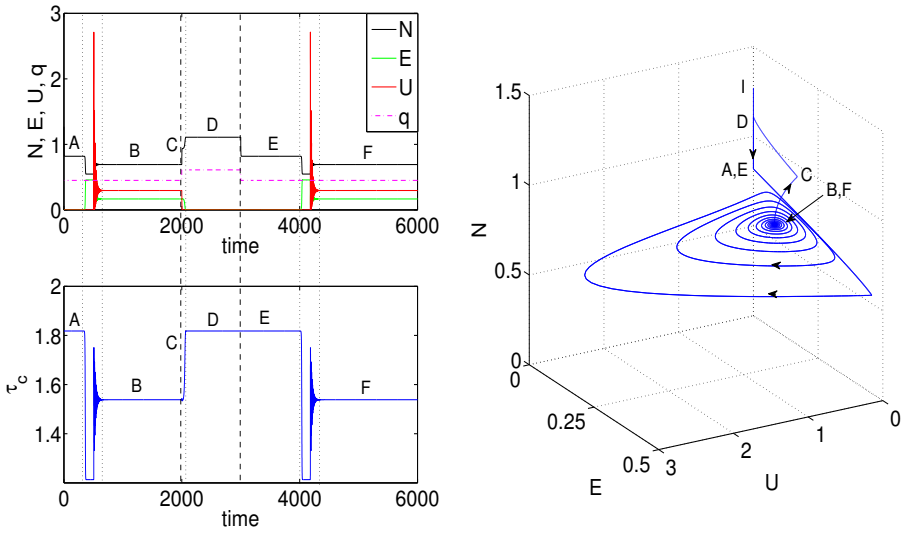

Figure 4.3.1: Time traces and phase space evolution for the KD/MD model, Eqs(4.1.1) to (4.1.3), with a discontinuous increase in heating rate q by amount $\delta q = 0.16$ from $q_0 = 0.45$ at $t = 2000$ time units; q reverts to q_0 at $t = 3000$ time units. Upper left plot shows time traces of variables N (black), q (dashed magenta), U (red) and E (green). Lower left plot shows time trace of energy confinement time τ_c defined by Eq.(4.2.1). Right plot shows time evolution of the system in (N, E, U) phase space. The sequence of key phases is labelled in all three plots in this Figure as follows. A is the initial transient evolution from the over-powered H-mode point I, leading to convergent cyclic motion towards fixed point attractor B corresponding to T-mode. At C the instantaneous increase in heating rate q induces rapid departure from the T-mode attractor B to the QH-mode (increased N; $E = U = 0$) attractor D with improved confinement time. Instantaneous reversion of q to initial value q_0 brings the end of phase D and results in immediate transition to a QH-mode by exponential decrease in N, labelled E, with a lower value of N and the same confinement time as phase D. There is later a spontaneous back transition from E at $t = 4000$ time units, followed by convergent cyclic motion F to the T-mode attractor B.

Figures 4.3.1 to 4.3.3 display an example of the responses, in the KD/MD model, to a substantial instantaneous rise δq in heating power q, which is then sustained at this higher level before later returning instantaneously to its initial level q_0. The resulting system dynamics – a proxy for plasma phenomenology – is characterised in each Figure in terms of time traces of N, E, U and q (upper plot), and of τ_c (lower plot). The heating power q_0 is successively larger in the system shown in Fig.4.3.1 through Fig.4.3.3. Before δq is applied, the system has relaxed to its attractor for q_0. For the particular parameter values chosen, in Figs.4.3.1 to

4.3.3 this fixed point is a state with relatively low N, and non-zero turbulence level E and zonal flow amplitude U. In KD/MD, this low confinement fixed point is referred to as the transient mode (T-mode).

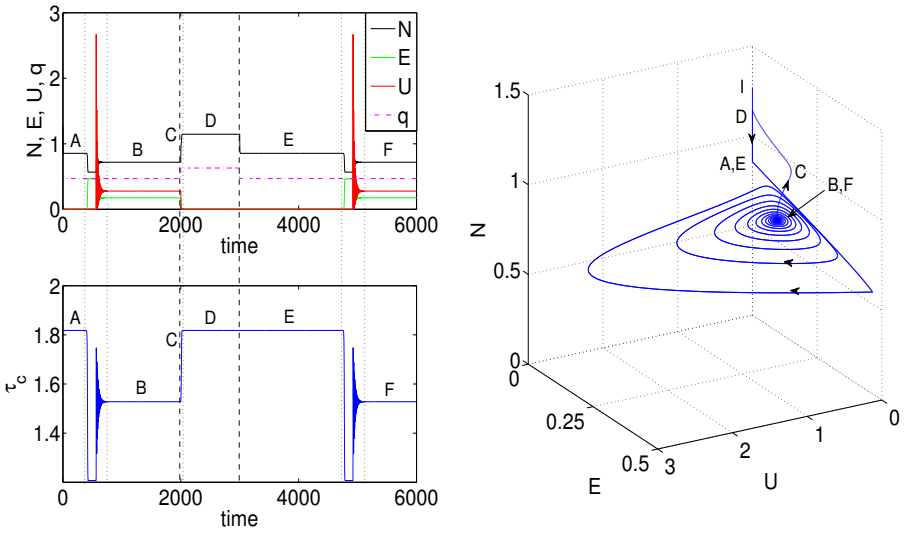

Figure 4.3.2: As Fig.4.3.1, for the case where $q_0 = 0.47$. The major difference is the longer duration of the post-heating QH-mode phase E, after reversion of q to its initial value.

Figure 4.3.1 shows that instantaneous application of $\delta q = 0.16$ to the $q_0 = 0.45$ T-mode causes a transition to an improved confinement regime which is identified by KD/MD with the quiescent H-mode (QH-mode). This is a fixed point which has larger N, while $E = U = 0$. As a consequence (from Eq.(4.2.4)), the value of τ_c rises instantly by about twenty per cent. At the termination of additional heating when $q \to q_0$, the system is still at this fixed point but now at lower N, with E and U still zero, hence still a QH-mode. The value of τ_c remains constant at its value for the additionally heated QH-mode, since $\tau_{QH} = 1/\rho$ is independent of N. This second QH-mode phase persists for some time after the heating power has reverted to the lower initial value $q_0 = 0.45$. Eventually the system returns to the initial T-mode.

In Figure 4.3.2, the duration of the QH-mode after the heating has reverted to its initial value q_0 is substantially longer than in Fig.4.3.1. Here the only parameter difference from Fig.4.3.1 is that $q_0 = 0.47$, implying a slightly higher maximum power $q_0 + \delta q$ and slightly lower fractional change $\delta q/q_0$. For the case shown in Fig.4.3.3, where $q_0 = 0.49$, the system remains in the post-heating QH-mode until

the run ends. An eventual back transition to T-mode after the heating power reverts to $q_0 = 0.49$ has not had time to occur.

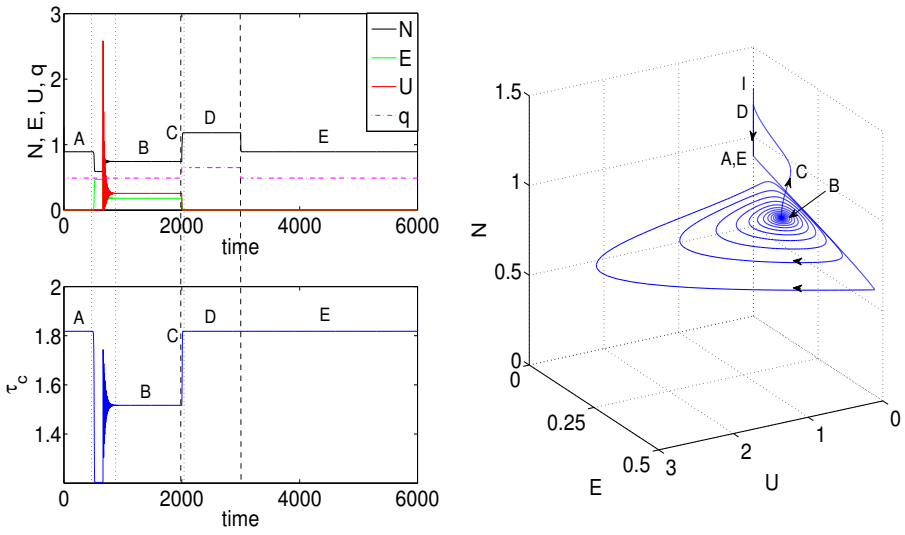

Figure 4.3.3: As Fig.4.3.2, for the case where $q_0 = 0.49$. The major difference is that the back transition from the post-heating QH-mode phase E, which is not a stable attractor, has not yet occurred by the end of this run.

In conclusion, in Figs.4.3.1 to 4.3.3, the initial T-mode with confinement time τ_T is sustained by the heating rate $q_0 = q_T$. The sharp rise in heating rate to $q_0 + \delta q = q_{QH}$ triggers the transition to the QH-mode at higher N and with improved confinement time τ_{QH}.

4.4 Confinement transition induced by heating in ZCD model

Figures 4.4.1 to 4.4.3 show the counterparts to Figs.4.3.1 to 4.3.3 that are obtained from the ZCD extension of the KD/MD model; that is, when a fourth variable U_2 representing a second coherent field predator is added to the KD/MD model, see Eqs.(4.1.4) to (4.1.7). The phenomenology of the heating-induced QH-mode and post-heating QH-mode in Figs.4.4.1 to 4.4.3 is very similar to that in the corresponding Figs.4.3.1 to 4.3.3 for the KD/MD model.

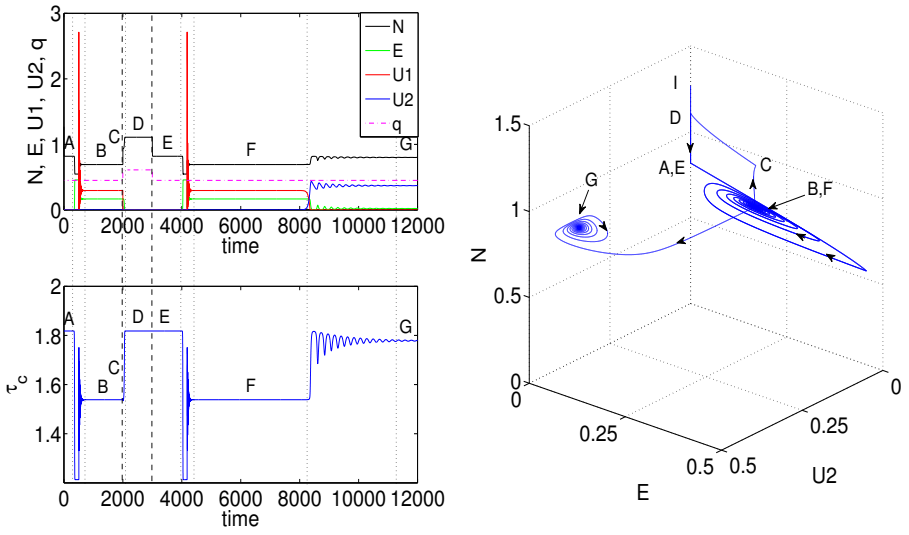

Figure 4.4.1: As Fig.4.3.1, for the two-predator ZCD model, Eqs(4.1.4) to (4.1.7), with a sharp heating transition where $q_0 = 0.45$, $\delta q = 0.16$. The second predator field U_2 is traced in blue in the upper left plot. The major difference from Fig.4.3.1 is that the post-heating T-mode state F is a repulsive fixed point, from which the system spontaneously transitions and converges cyclically to the fixed point G. This is known from [Zhu et al., 2013] and has enhanced N and finite U_2, with E very small. Here we refer to the attractive fixed point G as an example of O-mode.

From this we can infer that the induction of enhanced confinement by additional heating in the KD/MD model is robust against the introduction of a fourth variable as in ZCD. It is known[Zhu et al., 2013] that the eventual post-heating T-mode is a fixed point attractor in KD/MD but is a repulsive fixed point in ZCD. Figures 4.4.1 and 4.4.2 capture the transition from T-mode to the new ZCD fixed point (phase G in Fig.4.4.1) or limit cycle (phase G in Fig.4.4.2). This is the O-mode, with good confinement, as discussed in Chapter 4.2.

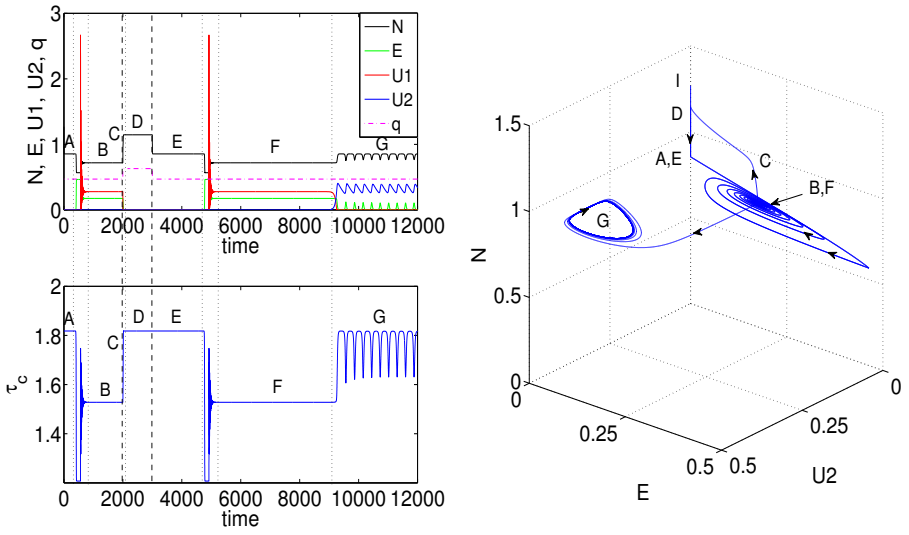

Figure 4.4.2: As Fig.4.3.2, for the two-predator ZCD model[Zhu et al., 2013] with a sharp heating transition where $q_0 = 0.47$, $\delta q = 0.16$. The major difference from Fig.4.3.2 is that the post-heating T-mode state F is a repulsive fixed point, from which the system spontaneously transitions and converges cyclically to the limit cycle G. This is known from [Zhu et al., 2013] and has oscillations of enhanced N and finite U_2, accompanied by small pulses of E. Here we refer to the attractive limit cycle G as an example of O-mode.

We have repeated this analysis using a smooth function for the transition in heating, represented by $q(t) = A_0 + A_1 \tanh(t/T)$, where T is the time scale for the heating transition (ramp up), see Chapter 4.5. We obtain essentially the same results as those reported above, for a broad range of T values. This suggests that, for the parameter sets considered in this Chapter, this model would not generate a smooth transition between confinement regimes in response to a heating rate which slowly rises or falls over time. Whether such phenomenology can be generated by this model in other parameter regimes remains to be investigated.

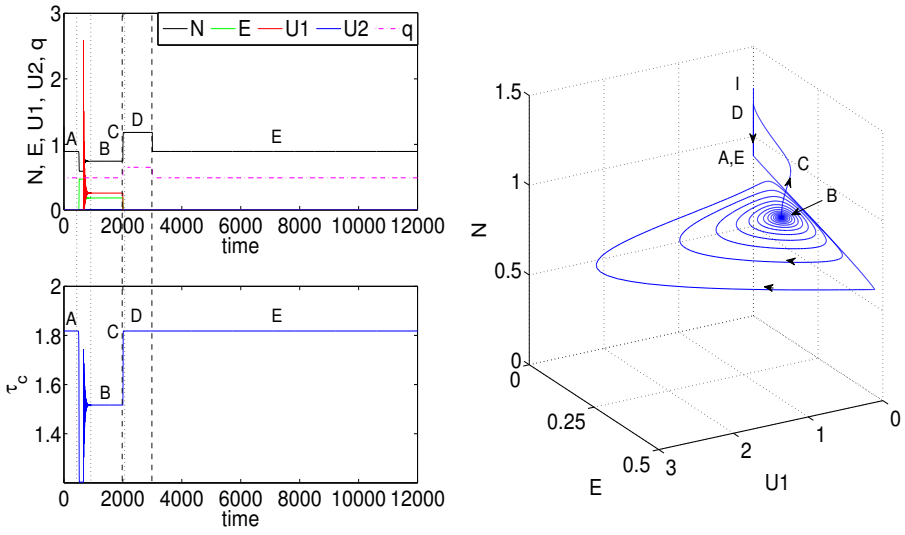

Figure 4.4.3: As Fig.4.3.3, for the two-predator ZCD model[Zhu et al., 2013] with a sharp heating transition where $q_0 = 0.49$, $\delta q = 0.16$. There is insufficient run time for the phase E QH-mode to transition to T-mode and then to the O-mode attractor, unlike Figs.4.4.1 and 4.4.2.

4.5 Impact of smoothed changes of external heating flux on MD model

We test that the heating-induced transitions between confinement regimes are not strongly sensitive to the temporal sharpness of the change in heating rate from q_0 to $q_0 + \delta q$. We repeat the numerical experiments of Chapter 4.3 and Chapter 4.4 for the same parameters, except that the heating transition up and down is now a continuous tanh function. Specifically $q(t) = q_0 + \delta q(t)$ where

$$\delta q(t) = 0.08\{\tanh\left[16 + 0.03\,(t - 2500)\right]\}; 0 \leq x \leq 2500 \quad (4.5.1)$$

$$= 0.08\{\tanh\left[16 - 0.03\,(t - 2500)\right]\}; 2500 < x \leq 5000 \quad (4.5.2)$$

Thus there is a finite timescale over which the heating power increases and, later, reverts to its initial value.

The sequence of key phases is labelled as follows in all three plots in Fig.4.5.1, which is the counterpart to Fig.4.3.1. A is the initial transient evolution from the over-powered H-mode point I, leading to convergent cyclic motion towards fixed

point attractor B corresponding to T-mode. The smooth increase in heating rate q induces immediate departure from the T-mode attractor B to a mode C, which has higher N but lower confinement time than T-mode B. The system slowly diverges cyclically from C before transitioning rapidly to QH-mode D with improved confinement time. Smooth reversion of q to initial value q_0 brings the end of phase D and results in transition to a QH-mode, labelled E, with a lower value of N and the same confinement time as phase D. There is later a spontaneous back transition from E at $t = 3500$ time units, followed by convergent cyclic motion F to the T-mode attractor B.

The primary difference between Fig.4.5.1 and its counterpart Fig.4.3.1 is the transition to the distinct long-lived phase C which is triggered by the smooth increase in heating power. Figure 4.5.1 shows that phase C is associated with a repulsive fixed point, from which the system eventually evolves to the same QH-mode D that is found in Fig.4.3.1.

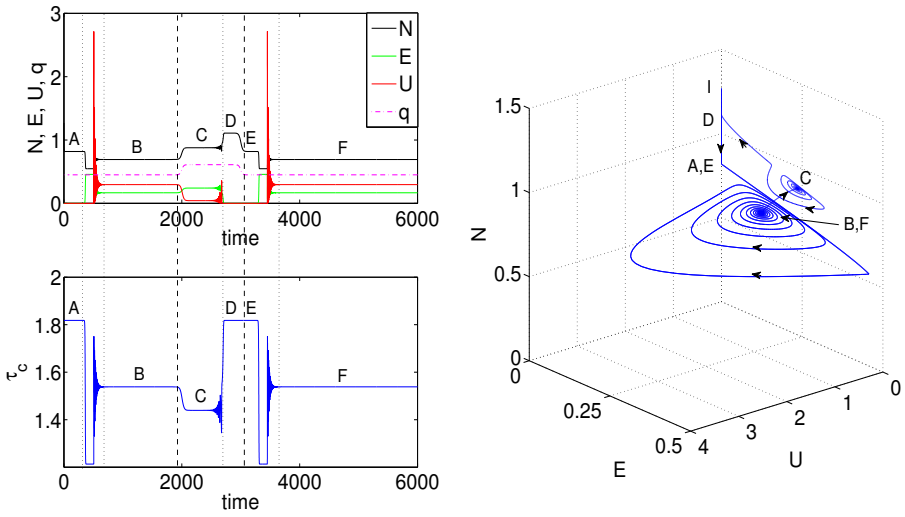

Figure 4.5.1: Time traces and phase space evolution for the MD model, Eqs(4.1.1) to (4.1.3), with a smooth increase, represented by the tanh function in Eqs.(4.5.1) and (4.5.2), in the heating rate q by an amount $\delta q = 0.16$ from $q_0 = 0.45$ around $t = 2000$ time units; q reverts to q_0 around $t = 3000$ time units. Upper left plot shows time traces of variables N (black), q (dashed magenta), U (red) and E (green). Lower left plot shows time trace of energy confinement time defined by Eq.(4.2.1). Right plot shows time evolution of the system in (N, E, U) phase space.

Fig.4.5.2 differs from Fig.4.5.1 in that phase C is transient. The post-heating QH-mode E lasts longer than in Fig.4.5.1. Unlike in Fig.4.3.3, there is time for the

eventual back transition to T-mode phase F to occur in Fig.4.5.2. We conclude that discontinuous (Figs.4.3.1 to 4.3.3) and slightly smoothed (Figs.4.5.1 and 4.5.2) changes of heating rate with time produce essentially similar results.

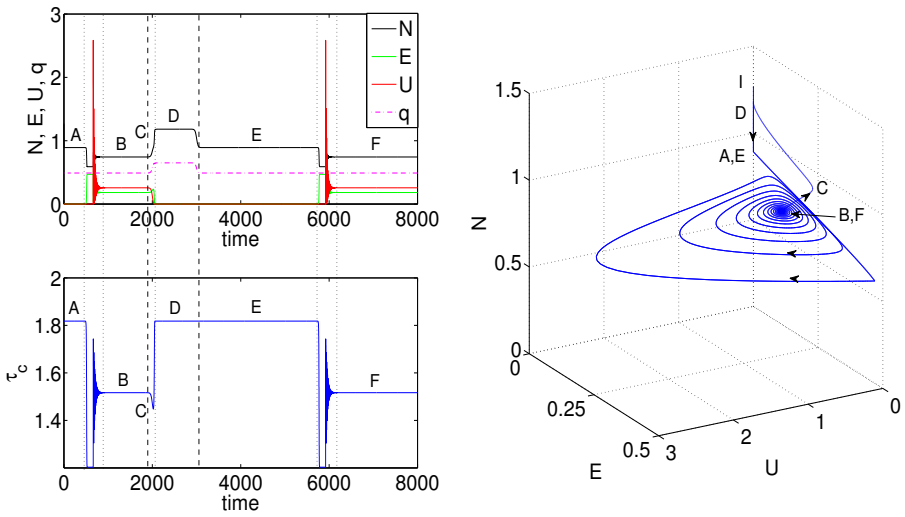

Figure 4.5.2: As Fig.4.5.1, for the case where $q_0 = 0.49$. There are two major differences from Fig.4.3.3. First, confinement time τ_c during phase C experiences a transient drop before jumping to higher confinement regime. Second, a spontaneous back-transition F to T-mode appears after long duration phase E QH-mode.

4.6 Impact of oscillating heating rate on ZCD model

A topical question concerns the system response to oscillations, in time, of the heating rate about a constant value. The resultant changes in the phenomenology generated by zero-dimensional models are of interest both theoretically and, potentially, experimentally. Repeated on-off switching of electron cyclotron heating is now routine[Leuterer et al., 2001], so that quasi-oscillatory ECH scenarios are becoming realisable. If one can identify distinctive signatures in the system response of a zero-dimensional model in such scenarios, this could assist a potential future experimental probe of the physical assumptions embodied in that model. We now examine the ZCD model in this context, and find that such a signature indeed exists, in the form of a classical period-doubling path[Hilborn, 1994] to chaos in the electron temperature gradient N, coherent meso-scale field amplitude U_2, and level of micro-scale turbulence intensity E, as the amplitude of the oscillatory component of the heating rate is increased. The response of the MD model, which has one

fewer variable and does not appear to exhibit this distinctive phenomenology, was investigated in [Douglas et al., 2013].

We represent the heating rate by

$$q(t) = q_0 + A\sin(\omega t) \tag{4.6.1}$$

where $q_0 = 0.47$, $\omega = 0.05$ and all other coefficients and initial conditions take the values that were used to generate Fig.4.4.2. This oscillatory time scale is fast compared to the duration of quasi-stationary phase in Figs.4.4.1 to 4.4.3. Specifically, the ratio of period of oscillating heating rate and that of limit cycle in Fig.4.4.2 is approximately 43.6 per cent. The control parameter in the following study is thus the amplitude A of the oscillatory component of the heating rate defined in Eq.(4.6.1). Figures 4.6.1 to 4.6.3 show the initial period-doubling path from period-1, via period-2, to period-4 as the value of A is increased from 0.0215 through 0.0240 to 0.0270. We note that these values of A are correspond to a few per cent of the steady heating rate $q_0 = 0.47$. Figures 4.6.1 to 4.6.3 all show: on the left, the power spectrum of N; on the right, the full attractor in (N, U_2, E) space; and, inset, the time series of N. Figure 4.6.4 provides an additional perspective on this period-doubling by showing the power spectra of N from Figs.4.6.1 to 4.6.3 over-plotted in the frequency range from 0.04 to 0.08. The fully chaotic attractor is shown in Fig.4.6.5, obtained for $A = 0.0295$. Figure 4.6.6 provides a comprehensive diagram of the period-doubling bifurcation path to chaos in the value of micro turbulence level E as A is increased from 0.0215 to 0.0295 in the ZCD model. We have obtained the values of A_n at which the nth period-doubling bifurcations occur, from period-1 to period-8. We find $A_1 = 0.0230, A_2 = 0.0265, A_3 = 0.0272$ and $A_4 = 0.0273$, giving the ratios 4.666 which is within 0.05 per cent of the expected value 4.669[Feigenbaum, 1978].

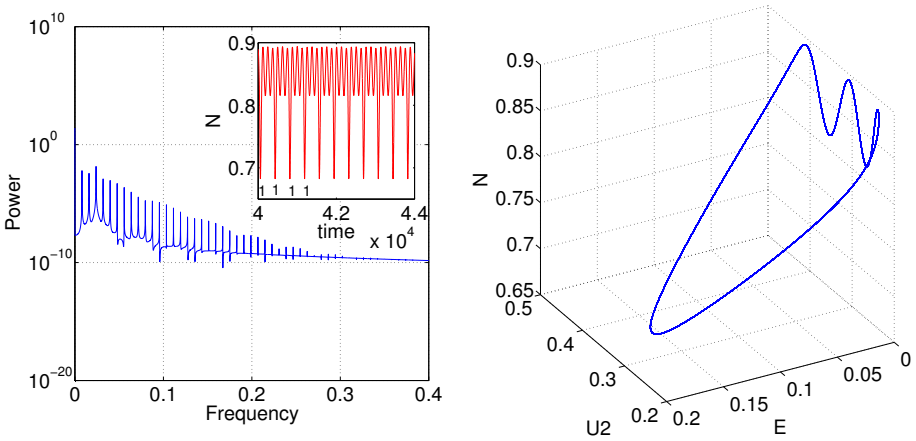

Figure 4.6.1: Period-1 oscillation in ZCD system dynamics in response to the varying heating rate defined by Eq.(4.6.1) with $A = 0.0215$; other parameter values are as for Fig.4.4.2. Left, the power spectrum of N; right, the full attractor in (N, U_2, E) space; inset, the time series of N.

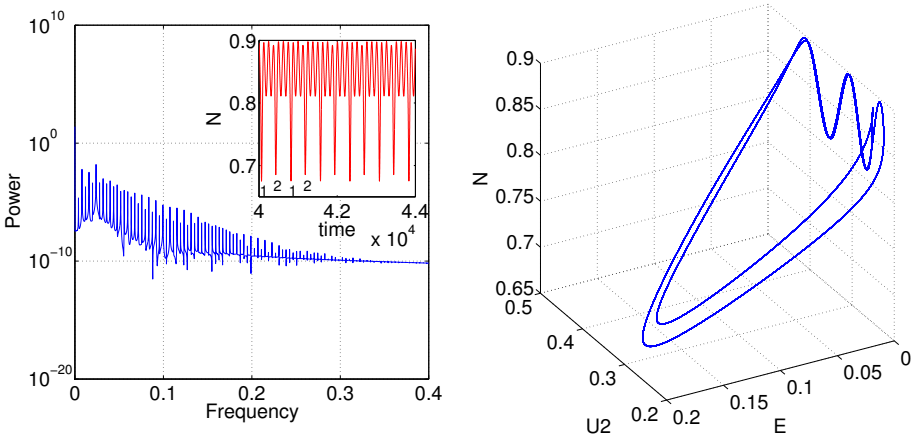

Figure 4.6.2: As Fig.4.6.1, showing period-2 oscillation in ZCD system dynamics when $A = 0.0240$.

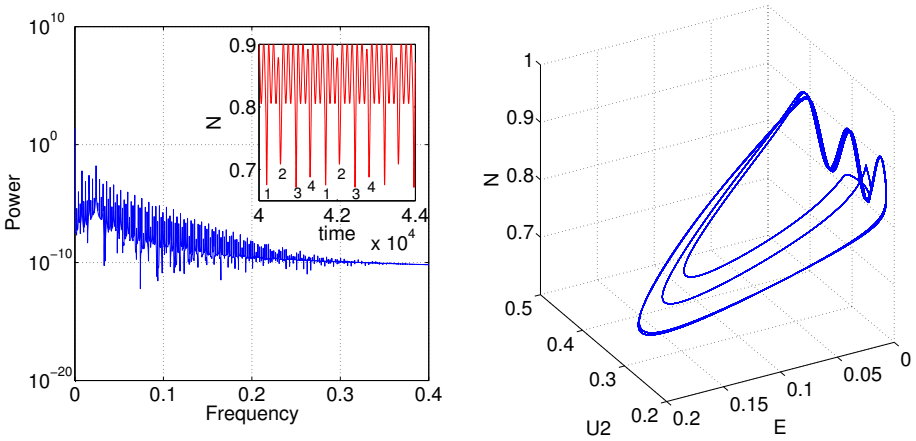

Figure 4.6.3: As Fig.4.6.1, showing period-4 oscillation in ZCD system dynamics when $A = 0.0270$.

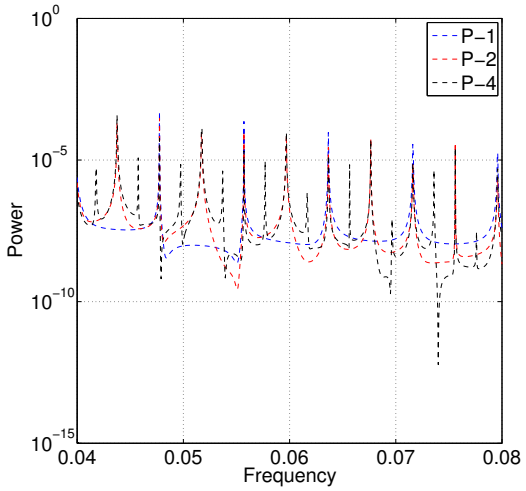

Figure 4.6.4: Period-doubling illustrated by the power spectra of N from Figs.4.6.1 to 4.6.3, over-plotted in the frequency range from 0.04 to 0.08. Blue, red and black dash lines denote spectra of period-1, period-2 and period-4 respectively.

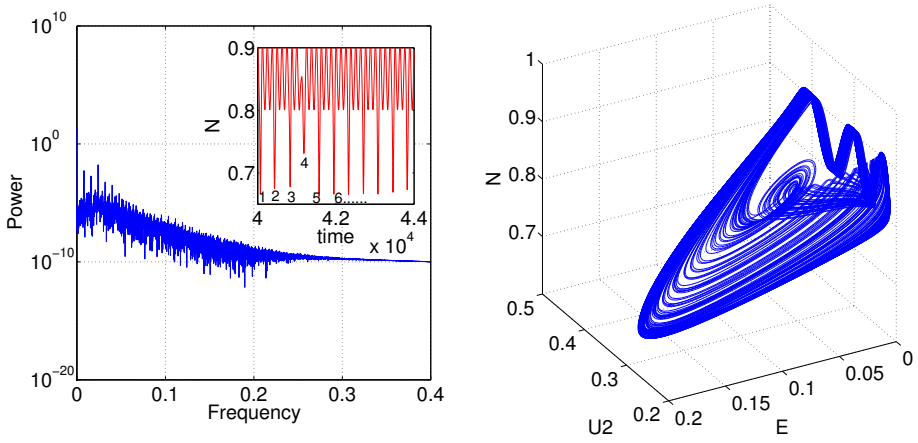

Figure 4.6.5: As Fig.4.6.1, showing chaotic attractor of the ZCD system dynamics when $A = 0.0295$.

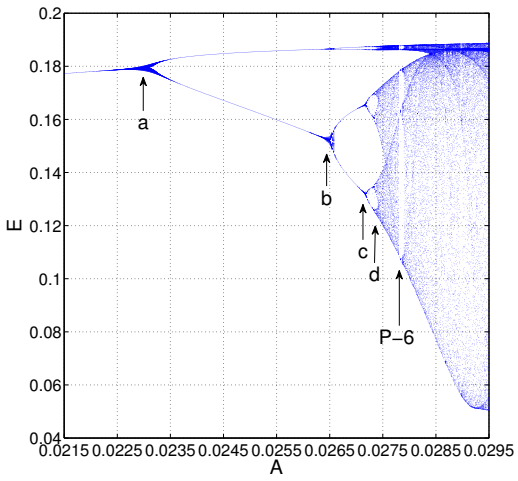

Figure 4.6.6: Period-doubling bifurcation path to chaos of ZCD system dynamics. Micro-turbulence level E is plotted versus amplitude A of oscillatory heating component in Eq.(4.6.1), in the range 0.0215 to 0.0295. The first four arrows indicate successive bifurcations, which occur at values $A = 0.0230, 0.0265, 0.0272$ and 0.0273. These yield Feigenbaum's ratio to within 0.05 per cent. The fifth arrow marks a period-6 window within the chaotic region.

4.7 Conclusions

In this Chapter we have shown that the KD/MD model and its ZCD extension capture a key feature of tokamak plasma confinement phenomenology, additional to those previously noted in [Malkov and Diamond, 2009; Kim and Diamond, 2003] and [Zhu et al., 2013]. Specifically, a rapid substantial change in heating power can trigger a transition to an enhanced confinement regime having steeper electron temperature gradient N, longer energy confinement time τ_c, and suppressed micro-scale turbulence level E. Enhanced confinement is sustained throughout the duration of the heating pulse. It can continue after heating reverts to its initial level, retaining the same value of τ_c but with lower N, for a time whose duration depends on the values of the initial and additional levels of heating. Importantly, this tokamak plasma-like enhanced confinement phenomenology is robust: both against minor variations of the switch-on time scale for the additional heating, and against inclusion of a second predator field in the model. The latter step also creates a new attractive fixed point or limit cycle which has enhanced confinement characteristics. This O-mode has higher values of N and τ_c than the lower confinement T-mode which precedes it, with nonlinear structure amplitudes $U_1 = 0$ and U_2 finite, and micro-scale turbulence level small or zero. The KD/MD model and its ZCD extension also possess well defined scaling relations between energy confinement time and heating power, which can be calculated. We emphasise again that numerical solution of the time evolving system, as well as knowledge of its fixed points, are necessary for these studies.

From a dynamical systems perspective, we have identified a confinement time parameter τ_c which depends only on the values of the macroscopic fields (E, U, N, q). The value of τ_c at the fixed points can be used to characterise the confinement states of the model. Since these values can be found analytically for any zero-dimensional model, we have provided a procedure to obtain the dependence of confinement time on the heating enhancement $\delta q/q_0$. If these fixed points are attractors in the model, then the duration of these confinement states will be long and will be insensitive to the detailed time dependence of heating $q(t)$. If on the other hand these fixed points are repulsive, then full numerical solution of the given zero-dimensional model equations is required to determine the duration of the corresponding confinement states, and whether this is sensitive to the detailed time dependence of the heating $q(t)$.

When a small oscillatory-in-time component is added to the steady heating rate, we find that the ZCD model can exhibit a classic period-doubling path to chaos

in, for example, the level of micro-turbulence E as the amplitude of oscillation is increased. In this, the ZCD model may differ from the MD model, for which oscillatory heating was studied in [Douglas et al., 2013]. This distinctive phenomenology may offer a path to future experimental testing of the assumptions of zero-dimensional models, and perhaps distinguishing between them.

We infer that the heating-induced transitions between confinement regimes are not strongly sensitive to the temporal sharpness of the change in heating rate from q_0 to $q_0 + \delta q$. We have repeated the numerical experiment of Chapters 4.3 to 4.4 for the same parameters, except that the heating transition up and down is now a continuous tanh function. We conclude that discontinuous and slightly smoothed changes of heating rate with time produce essentially similar results. Resilience against noise fluctuations in the heating has also been investigated. We find that the results are effectively invariant against noise in the heating at levels of 1% to 10%.

The results in this chapter reinforce the apparent validity of the conceptually simple (albeit strongly nonlinear) physical picture embodied in the KD/MD model. Very few simple first principles models can spontaneously generate tokamak-like enhanced confinement phenomenology; the sandpile of [Chapman et al., 1999, 2001] is an example. It is increasingly clear that the KD/MD model is in this category.

Chapter 5

Heat pulse model in the Large Helical Device

5.1 Introduction

In this Chapter, we analyse a recent successful zero-dimensional model[Dendy et al., 2013] by applying travelling wave transformation to show the intrinsic links in anomalous transport of heat and particle. The zero-dimensional model of [Dendy et al., 2013], which incorporates only time dependence, is successful in quantitatively capturing the local time evolution of $\delta\nabla T_e$ and $\delta \boldsymbol{q_e}$ at a specific radius. We refer in particular to Figs.3 and 5 of [Dendy et al., 2013]. This motivates the following optimistic physical conjecture, which we test in the present Chapter. The zero-dimensional model is known to work at the best diagnosed spatial location, capturing the time evolution of the pulse there, where $t = 0$ is defined to be the local arrival time of the initial impulsive perturbation. Therefore we conjecture that the zero-dimensional model ought to work at each location across the radial domain of the plasma within which the same physical processes determine the behaviour of the pulse. From this we infer that the model ought to apply in a frame co-moving radially with the heat pulse across this region. This final step in the conjecture provides a simple path to construct a spatio-temporally dependent model from the tested time-dependent-only model of [Dendy et al., 2013]. We replace t in Eqs.(1-3) of [Dendy et al., 2013] by $\xi = x + v_0 t$; here v_0 is to be considered as a proxy of pulse propagation velocity in the radial direction x, and the sign convention adopted for t assists consideration of inward propagation. Importantly, as we shall show, the mathematical structure of the resultant model equations, combined with the choice of physical model parameters that carries over from [Dendy et al., 2013], yields a

formula for v_0 that aligns with prior empirical expectations.

The normalised zero-dimensional model[Dendy et al., 2013] examined below is constructed in terms of the three key physical quantities that were measured[Inagaki et al., 2010] so as to characterise pulse propagation in LHD. These are the deviation from steady state of the electron temperature gradient $\delta\nabla T_e$, the excess turbulent heat flux $\delta \boldsymbol{q_e}$, and the deviation of electron temperature δT_e, from its steady-state value. The dimensionless counterparts of these variables are denoted by x_1, x_2 and x_3 respectively, as defined in [Dendy et al., 2013]. This model shows quantitative agreement between its outputs and experimental measurements of the time evolution of these variables at fixed locations in the LHD plasma, after rapid cooling at the edge. It is successful both when core electron temperature rises and when it drops. However, for given parameters and initial conditions, the model only simulates the time evolution of a passing heat pulse at a specific radius, for example $r/a = 0.19$ in [Dendy et al., 2013]. Spatial dependence is eliminated from the physical picture underlying the model in [Dendy et al., 2013] by using the parameter $1/L_c$ as a proxy for divergence in the heat flux energy conservation equation; here L_c is the characteristic scale-length of steady-state turbulent transport. The model equations (5) to (7) of [Dendy et al., 2013] are as follows

$$\frac{dx_1}{dt} = \kappa_{T0}x_2 + x_1x_2\frac{\partial\kappa_T}{\partial x_1} + x_2x_3\frac{\partial\kappa_T}{\partial x_3} - \gamma_{L1}x_1 \tag{5.1.1}$$

$$\frac{dx_2}{dt} = -\kappa_{Q0}x_1 - x_1^2\frac{\partial\kappa_Q}{\partial x_1} - x_1x_3\frac{\partial\kappa_Q}{\partial x_3} - \gamma_{L1}x_2 \tag{5.1.2}$$

$$\frac{dx_3}{dt} = -\frac{1}{\tau_c}\frac{\eta}{\chi_0}x_2 - \gamma_{L2}x_3 \tag{5.1.3}$$

The physical significance of the various coefficients is described in the discussion of equations (1) to (4) of [Dendy et al., 2013]. We note that, from Eq.(5.1.3) above, x_3 is slave to x_2 because the electron temperature deviation from steady state is damped linearly and by excess turbulent transport which scales with x_2. Thus x_3 is not an independent variable in the model, although plotting x_3 is valuable for model validation.

Central to the present Chapter is the adoption of travelling wave transformations as a method for generating (x,t)–dependence from the t–dependent model of Eqs.(5.1.1) to (5.1.3). We assume that

$$x_i\left(x,t\right) = y_i\left(\xi\right), \xi = x + v_0t \qquad i = 1,2,3 \tag{5.1.4}$$

Here x and t are considered to be independent variables, and we refer to v_0 as the pseudo-velocity of the pulse. This pseudo-velocity is expected to be similar, but not identical, to the real measured velocity of the pulse. It then follows that

$$\frac{dx_i}{dt} = \frac{dy_i}{d\xi}\frac{\partial \xi}{\partial t} = v_0\frac{dy_i}{d\xi} \qquad i = 1, 2, 3 \tag{5.1.5}$$

Due to the fact that y_3 is a dependent variable, we choose to simplify by neglecting all y_3 related terms in Eqs.(5.1.1) to (5.1.3), and substitute Eq.(5.1.5) into Eqs.(5.1.1-5.1.2), yielding

$$-v_0\frac{dy_1}{d\xi} = \kappa_{T0}y_2 + y_1y_2\frac{\partial \kappa_T}{\partial y_1} - \gamma_{L1}y_1 \tag{5.1.6}$$

$$-v_0\frac{dy_2}{d\xi} = -\kappa_{Q0}y_1 - y_1^2\frac{\partial \kappa_Q}{\partial y_1} - \gamma_{L1}y_2 \tag{5.1.7}$$

Our new model Eqs.(5.1.6-5.1.7) comprises only two independent variables: y_3 values are deduced using Eq.(5.1.3) directly from the timeseries of y_2 and Eq.(5.1.3) above. Let us now operate on Eq.(5.1.6) with $d/d\xi$ and multiply Eq.(5.1.7) by κ_{T0}, then eliminate $dy_2/d\xi$ by substitutions. This yields the following equation to leading order approximation, see Chapter 5.2 for further details:

$$v_0\frac{d^2y_1}{d\xi^2} - \gamma_{L1}\frac{dy_1}{d\xi} + \left(\frac{\kappa_{T0}}{v_0}\frac{\partial \kappa_Q}{\partial y_1} + \frac{\kappa_{Q0}}{v_0}\frac{\partial \kappa_T}{\partial y_1}\right)y_1^2 + \frac{\kappa_{T0}\kappa_{Q0}}{v_0}y_1 = -\frac{\kappa_{T0}\gamma_{L1}}{v_0}y_2 + \frac{\kappa_{T0}}{v_0}\frac{\partial \kappa_T}{\partial y_1}y_2^2 \tag{5.1.8}$$

The second coupled nonlinear ordinary differential equation is derived by applying similar procedures, see Chapter 5.2 for further details:

$$v_0\frac{d^2y_2}{d\xi^2} - \gamma_{L1}\frac{dy_2}{d\xi} + \frac{\kappa_{T0}\kappa_{Q0}}{v_0}y_2 = \frac{\kappa_{Q0}\gamma_{L1}}{v_0}y_1 - y_1y_2\left(\frac{\kappa_{Q0}}{v_0}\frac{\partial \kappa_T}{\partial y_1} + 2\frac{\kappa_{T0}}{v_0}\frac{\partial \kappa_Q}{\partial y_1}\right) \tag{5.1.9}$$

Equations (5.1.8) and (5.1.9) comprise our mathematical model for the propagating heat pulse. Its physical motivation is that of [Dendy et al., 2013], combined with the co-moving conjecture outlined above and expressed in Eq.(5.1.4). The mathematical structure of Eqs.(5.1.8) and (5.1.9) can be linked, in certain approximations, to the Korteweg-de Vries-Burgers(KdV-Burgers) equation[Kudryashov,

2009] and to a damped wave equation in the co-moving frame, respectively. The left hand side of Eq.(5.1.8) corresponds to that in the formulation of the KdV-Burgers equation in Eq.(5.3) of [Kudryashov, 2009]. This is known to support soliton pulses that move at a speed determined by the coefficient of the term which is linked to y_1. This motivates the following conjecture regarding heat pulse velocity in our model:

$$v_0 \sim (\kappa_T \kappa_Q)^{1/2} \tag{5.1.10}$$

This scaling has previously been noted empirically from heat pulse experiments [Lopes Cardozo, 1995; Garbet et al., 2007]. From those references, we can also assume that $v_0 \sim \left(\chi_0 (\kappa_T \kappa_Q)^{1/2}\right)^{1/2}$ or $v_0 \sim \left(\eta (\kappa_T \kappa_Q)^{1/2}\right)^{1/2}$. The numerical value of v_0, which may be expected to align with Eq.(5.1.10), is obtained empirically below.

5.2 Travelling wave transformations on the model

The zero-dimensional model in [Dendy et al., 2013], shown below, is constructed in terms of three key unnormalised plasma quantities which are directly measured in the LHD experiments: the excess electron temperature gradient($\delta \nabla T_e$), excess turbulence heat flux($\delta \boldsymbol{q_e}$) and electron temperature deviation from steady state(δT_e).

$$\frac{\partial}{\partial t}(\delta \nabla T_e) = \kappa_T (T_e, \nabla T_e) \frac{\delta \boldsymbol{q_e}}{\chi_0 n_e} - \gamma_{L1} \delta \nabla T_e \tag{5.2.1}$$

$$\frac{\partial}{\partial t}\left(\frac{\delta \boldsymbol{q_e}}{\chi_0 n_e}\right) = -\kappa_Q (T_e, \nabla T_e) \delta \nabla T_e - \gamma_{L1} \frac{\delta \boldsymbol{q_e}}{\chi_0 n_e} \tag{5.2.2}$$

$$\frac{\partial}{\partial t}(T_e - T_{e0}) = -\eta \nabla \cdot \left(\frac{\delta \boldsymbol{q_e}}{\chi_0 n_e}\right) - \gamma_{L2} (T_e - T_{e0}) \tag{5.2.3}$$

Coupling coefficients are denoted by κ_T and κ_Q, which are functions of the election temperature and its local spatial gradient. η and χ_0 are parameters which represent diffusivity. Background turbulent transport give rise to damping rates which are denoted by γ_{L1} and γ_{L2}. We infer to [Dendy et al., 2013] for further discussion. By adopting normalization coefficients below[Dendy et al., 2013], the normalised model equations Eqs.(5.2.4) to (5.2.6) follow [Dendy et al., 2013].

$x_1 = L_c \delta \nabla T_e / T_{e0}, x_2 = L_c \delta q_e / \chi_0 n_e T_{e0}, x_3 = (T_e - T_{e0}) / T_0,$
$\kappa_T (T_e, \delta \nabla T_e) = \kappa_{T0} + (T_e - T_{e0}) (\partial \kappa_T / \partial T_e) + \delta \nabla T_e (\partial \kappa_T / \partial \nabla T_e),$
$\kappa_Q (T_e, \delta \nabla T_e) = \kappa_{Q0} + (T_e - T_{e0}) (\partial \kappa_Q / \partial T_e) + \delta \nabla T_e (\partial \kappa_Q / \partial \nabla T_e).$

$$\frac{dx_1}{dt} = \kappa_{T0}x_2 + x_1x_2\frac{\partial\kappa_T}{\partial x_1} + x_2x_3\frac{\partial\kappa_T}{\partial x_3} - \gamma_{L1}x_1 \tag{5.2.4}$$

$$\frac{dx_2}{dt} = -\kappa_{Q0}x_1 - x_1^2\frac{\partial\kappa_Q}{\partial x_1} - x_1x_3\frac{\partial\kappa_Q}{\partial x_3} - \gamma_{L1}x_2 \tag{5.2.5}$$

$$\frac{dx_3}{dt} = -\frac{1}{\tau_c}\frac{\eta}{\chi_0}x_2 - \gamma_{L2}x_3 \tag{5.2.6}$$

These are Eqs.(5.1.1) to (5.1.3) in the Chapter 5.1. Using the travelling wave transformations Eqs.(5.1.4-5.1.5) and neglecting all y_3 related terms as discussed in the main text, Eq.(5.2.4) and Eq.(5.2.5) reduce to

$$-v_0\frac{dy_1}{d\xi} = \kappa_{T0}y_2 + y_1y_2\frac{\partial\kappa_T}{\partial y_1} - \gamma_{L1}y_1 \tag{5.2.7}$$

$$-v_0\frac{dy_2}{d\xi} = -\kappa_{Q0}y_1 - y_1^2\frac{\partial\kappa_Q}{\partial y_1} - \gamma_{L1}y_2 \tag{5.2.8}$$

We operate on Eq.(5.2.7) with $d/d\xi$, and multiply Eq.(5.2.8) by κ_{T0}:

$$-v_0\frac{d^2y_1}{d\xi^2} = \kappa_{T0}\frac{dy_2}{d\xi} + \left(\frac{dy_1}{d\xi}y_2 + y_1\frac{dy_2}{d\xi}\right)\frac{\partial\kappa_T}{\partial y_1} - \gamma_{L1}\frac{dy_1}{d\xi} \tag{5.2.9}$$

$$\kappa_{T0}v_0\frac{dy_2}{d\xi} = \kappa_{T0}\kappa_{Q0}y_1 + \kappa_{T0}y_1^2\frac{\partial\kappa_Q}{\partial y_1} + \kappa_{T0}\gamma_{L1}y_2 \tag{5.2.10}$$

Substituting Eq.(5.2.10) into Eq.(5.2.9) to eliminate $dy_2/d\xi$ yields

$$-v_0\frac{d^2y_1}{d\xi^2} = \frac{1}{v_0}\left(\kappa_{T0}\kappa_{Q0}y_1 + \kappa_{T0}\frac{\partial\kappa_Q}{\partial y_1}y_1^2 + \kappa_{T0}\gamma_{L1}y_2\right) + \left(\frac{dy_1}{d\xi}y_2 + y_1\frac{dy_2}{d\xi}\right)\frac{\partial\kappa_T}{\partial y_1} - \gamma_{L1}\frac{dy_1}{d\xi} \tag{5.2.11}$$

After leading order approximations and transposition,

$$\frac{dy_1}{d\xi}y_2 = -\frac{\kappa_{T0}}{v_0}y_2^2 + ..., \tag{5.2.12a}$$

$$\frac{dy_2}{d\xi}y_1 = \frac{\kappa_{Q0}}{v_0}y_1^2 + ... \tag{5.2.12b}$$

we obtain Eq.(5.1.8).

We operate on Eq.(5.2.8) with $d/d\xi$, and multiply Eq.(5.2.7) by κ_{Q0}:

$$-v_0\frac{d^2y_2}{d\xi^2} = -\kappa_{Q0}\frac{dy_1}{d\xi} - 2\frac{\partial\kappa_Q}{\partial y_1}y_1\frac{dy_1}{d\xi} - \gamma_{L1}\frac{dy_2}{d\xi} \tag{5.2.13}$$

$$-v_0\kappa_{Q0}\frac{dy_1}{d\xi} = \kappa_{Q0}\kappa_{T0}y_2 + \kappa_{Q0}\frac{\partial\kappa_T}{\partial y_1}y_1y_2 - \kappa_{Q0}\gamma_{L1}y_1 \tag{5.2.14}$$

Substituting Eq.(5.2.15) into Eq.(5.2.14) to eliminate $dy_1/d\xi$ yields

$$-v_0\frac{d^2y_2}{d\xi^2} = \frac{1}{v_0}\left(\kappa_{Q0}\kappa_{T0}y_2 + \kappa_{Q0}\frac{\partial\kappa_T}{\partial y_1}y_1y_2 - \kappa_{Q0}\gamma_{L1}y_1\right) - 2\frac{\partial\kappa_Q}{\partial y_1}y_1\frac{dy_1}{d\xi} - \gamma_{L1}\frac{dy_2}{d\xi} \tag{5.2.15}$$

After leading order approximation and transposition,

$$2\frac{\partial\kappa_Q}{\partial y_1}y_1\frac{dy_1}{d\xi} = -2\frac{\kappa_{T0}}{v_0}\frac{\partial\kappa_Q}{\partial y_1}y_1y_2 + ... \tag{5.2.16}$$

we obtain Eq.(5.1.9).

5.3 Comparison of model results with the LHD experimental data

Recall that y_1, y_2 and y_3 are the dimensionless counterparts of $\delta\nabla T_e, \delta\boldsymbol{q_e}$ and δT_e respectively. Solution of our model, embodied in the two coupled nonlinear ordinary differential equations Eqs.(5.1.8) and (5.1.9), proceeds as follows. First, the numerical values for κ_T, κ_Q and their derivatives, together with the numerical values of $\gamma_{L1}, \gamma_{L2}, \eta, \tau_c$ and χ_0, carry over identically from [Dendy et al., 2013], to which we refer for the experimental motivation for these values. See Table 5.1 for detailed information.

The new model embodied in Eqs.(5.1.8) and (5.1.9) is strongly nonlinear. In solving it, we have three kinds of degrees of freedom. First, there are the initial values of $y_i^{'}(\xi = 0)$. Secondly, there is the value of the pseudo-velocity v_0. Third, it is possible to apply fixed horizontal and vertical shifts in the values of the electron temperature and time, provided these shifts are applied uniformly to all outputs of a simulation, as a way of reducing systematic errors introduced by parameter choices.

We optimise model outputs, for comparison with the experimental measurements, in these three ways. These model outputs (time traces of y_1, y_2 and y_3) reflect the underlying phase space structure of the solutions of the nonlinear system of equations. We recall also that the great majority of model parameter values, see e.g. Table 5.1, are determined by experimental measurements.

	κ_{T0}	$\partial\kappa_T/\partial x_1$	κ_{Q0}	$\partial\kappa_Q/\partial x_1$	$\gamma_{L1}=\gamma_{L2}$	χ_0	$\eta=2\chi_0/3$	$\eta/\tau_c\chi_0$
T_e Rise(R)	15	1.5	225	22.5	35	3.2	2.13	10.5
T_e Drop(D)	20	2.0	400	40.0	35	3.2	2.13	10.5

Table 5.1: Experimentally inferred parameter values[Dendy et al., 2013] for both T_e rise and T_e drop cases. We have $\partial\kappa_T/\partial x_1 = \partial\kappa_T/\partial x_3$, $\partial\kappa_Q/\partial x_1 = \partial\kappa_Q/\partial x_3$.

The boundary conditions on the $y_i,\ i = 1, 2, 3$ and their derivatives, evaluated at $\xi = 0$ and $\xi = 10$ which define the solution domain, coincide with the experimentally motivated values in [Dendy et al., 2013] where these carry over. Specifically $y_1(\xi = 0) = y_1(\xi = 10) = 0$; $y_2(\xi = 0) = -1.5, y_2(\xi = 10) = 0$ and $y_3(\xi = 0) = 0.01$ for the core electron temperature Rise(R) case in LHD plasma 49708 and $y_1(\xi = 0) = y_1(\xi = 10) = 0$; $y_2(\xi = 0) = 1, y_2(\xi = 10) = 0$ and $y_3(\xi = 0) = -0.01$ for the core electron temperature Drop(D) case in LHD plasma 49719. Boundary conditions unspecified in [Dendy et al., 2013] in order to satisfy boundary conditions above are assumed to be as follows here: $y_1'(\xi = 0) = -1.496$ and $y_2'(\xi = 0) = 3.552$ for R case; $y_1'(\xi = 0) = 0.668$ and $y_2'(\xi = 0) = -1.156$ for D case. Table 5.2 lists all boundary conditions.

	$y_1(\xi=0)$	$y_2(\xi=0)$	$y_2(\xi=10)$	$y_3(\xi=0)$	$y_1^{'}(\xi=0)$	$y_2^{'}(\xi=0)$
T_e Rise(R)	0	-1.5	0	0.01	-1.496	3.552
T_e Drop(D)	0	1.0	0	-0.01	0.668	-1.156

Table 5.2: Boundary conditions of both T_e rise and T_e drop cases. We have $y_1(\xi = 0) = y_1(\xi = 10)$.

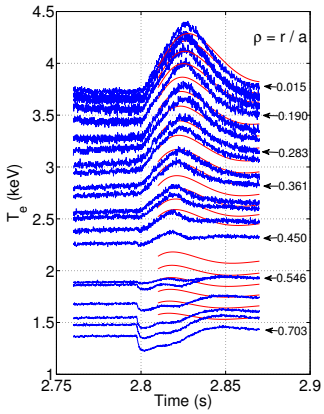

Figure 5.3.1: Time evolution of electron temperature at multiple radial locations, derived from LHD data(blue) and the model(red) for the core temperature rise(R) heat pulse propagation experiment in plasma 49708. Radial locations range from edge($\rho = 0.703$) to core($\rho = 0.015$), where $\rho = r/a$, r is the radial co-ordinate and $a \sim 0.6$m is minor radius of LHD. Model results match experimental data well from $\rho = 0.450$ inwards to the plasma core, especially amplitudes and the time structure of pulse decay. The amplitudes of model time traces increase from edge to core, as in the measured electron temperature profiles. Model results do not fit experimental data outwards from $\rho = 0.546$ to $\rho = 0.703$, implying that different physics applies in the outer LHD plasma.

Figure 5.3.1 compares time traces of the evolving electron temperature at multiple radial locations, obtained from the model and from experimental data(# Te49708) for the R case. Several representative radii are marked by arrows on the right hand side. The model results are able to match raw data from $\rho = 0.45$ inward to the core, if we uniformly apply horizontal(+0.01) and vertical(+0.20) shifts, suggesting that the model applies over this broad radial range. It is also clear that electron temperature profiles from $\rho = 0.546$ outward to $\rho = 0.703$ are not be simulated by the model. This suggests that different physics dominates heat pulse propagation in the outer region of this plasma. We could use cross-correlation function, which is defined as $R(\tau) = (1/T)\int_0^T [f(t)g(t+\tau)]dt$, to check the similarity between the model outputs and experimental data. However, it is impractical to adopt that method here due to the quite noisy data, especially the T_e drop case in Figure 5.3.2. Figure 5.3.2 demonstrates the comparison of model results and experimental data(# Te49719) for the D case. In common with the R case shown Fig.5.3.1, the model results are good from $\rho = 0.450$ inward to the core, with uniformly applied horizontal(+0.04) and vertical(+0.07) shifts, but not in the outer region of this plasma. Fig.5.3.3 and Fig.5.3.4 are zoomed-in electron temperature

pulse plots at three specific radii, selected from Fig.5.3.1 and Fig.5.3.2 respectively.

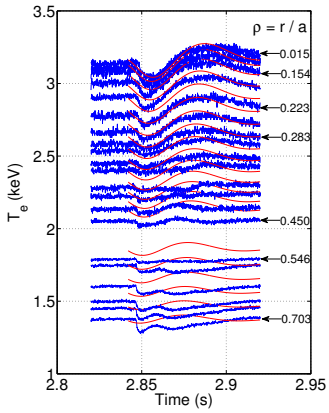

Figure 5.3.2: Time evolution of electron temperature at multiple radial locations, derived from LHD data(blue) and the model(red) for the core temperature drop(D) heat pulse propagation experiment in plasma 49719. Radial locations range from edge($\rho = 0.703$) to core($\rho = 0.015$), where $\rho = r/a$, r is the radial co-ordinate and $a \sim 0.6$m is minor radius of LHD. As in Fig.5.3.1, model results match experimental data well from $\rho = 0.450$ inwards to the plasma core. Again, model results do not fit experimental data outwards from $\rho = 0.546$ to $\rho = 0.703$, reinforcing that different physics dominates in the outer LHD plasma.

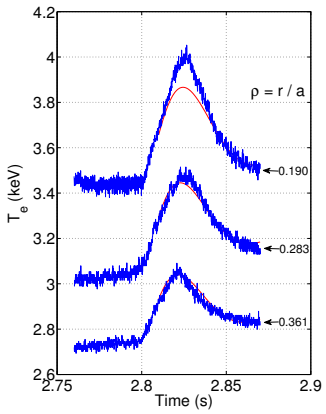

Figure 5.3.3: Time evolution of electron temperature at three specific radii selected from Fig.5.3.1 for the central temperature rise(R) case, during the heat pulse propagation experiment in LHD plasma #Te49708. Data and model output are denoted by blue and red lines respectively.

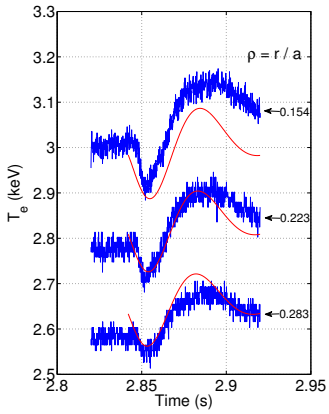

Figure 5.3.4: Time evolution of electron temperature at three specific radii selected from Fig.5.3.2 for the central temperature drop(D) case, during the heat pulse propagation experiment in LHD plasma #Te49719. Data and model output are denoted by blue and red lines respectively.

Empirically, we approach v_0 by identifying a best fit straight line linking the positions of the peak or trough of the heat pulse temperature profile in the two cases, see Figs.5.3.5 and 5.3.6. The effect of data noise on peak location is minimised by taking a five per cent running window. The width of the filter window determines the horizontal error bars. It can be seen that the straight line fit to the radial location of the pulse peak versus time is good. The inward radial propagation velocity of the heat pulse is thus almost invariant across the plasma volume of interest perhaps implying soliton-type characteristics for this strongly nonlinear phenomenon. We find from Figs.5.3.5 and 5.3.6 that $v_0 = 15$ for the temperature rise case and $v_0 = 30$ for the temperature drop case. These dimensionless pseudo-velocities are in the same magnitude with measured heat pulse propagating velocities in ms^{-1}. The ratio 2 between these two velocities is broadly consistent with that inferred from Eq.(5.1.10). We have $v_0^D/v_0^R \sim \left(\kappa_T^D \kappa_Q^D / \kappa_T^R \kappa_Q^R\right)^{1/2} = 1.54 \simeq 2$, referring also to Table 5.1, where R and D denote the core T_e rise and drop cases respectively. We note that the empirically determined velocities v_0^R and v_0^D of heat pulse propagation need not necessarily coincide with the optimal value of the mathematical transformation parameter v_0 in Eq.(5.1.4).

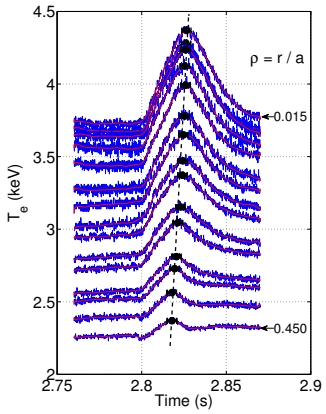

Figure 5.3.5: Data analysis underpinning calculation of pulse velocity from the experimental data, which requires a statistically robust identification of the time of the pulse peak from the noisy data at each radius $0.450 \geq \rho \geq 0.015$. Blue lines show timeseries of electron temperature data versus time from the R case(Te49708). Red lines denote timeseries smoothed over a window whose span is 5% of the total sample points, so that approximately 50 sample points generate the moving average. Black dots mark the maximum values, at each radius, of each smoothed time-evolving electron temperature pulse. The width of the horizontal error bars is defined by span of the moving window. The black dash line is the best fit straight line joining all the peaks. From it we infer the pulse propagation speed, which is nearly independent of radius, to be $(32.62 \pm 9.89)\text{ms}^{-1}$.

Mathematically, we may treat v_0 as a free parameter in Eqs.(5.1.8) and (5.1.9), which we label the "pseudo-velocity". We solve Eqs.(5.1.8) and (5.1.9) repeatedly for different values of this pseudo-velocity, see for example Fig.5.3.7 for the R case, and identify the best fit value. To test sensitivity with respect to ξ, three other cases($\xi = 5; \xi = 15; \xi = 20$) are examined, see for example Figure 5.3.8. All three cases share the same properties with the cases of $\xi = 10$. Various combinations of initial conditions and pseudo-velocities are tested. For the phase plots, circulation directions are identical with those of experimental data for R and D cases.

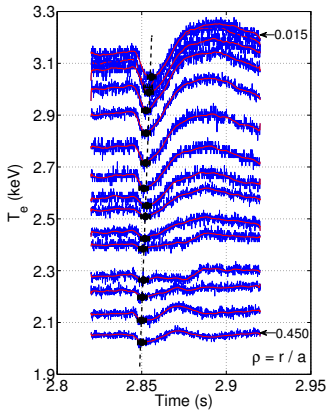

Figure 5.3.6: As Fig.5.3.5, demonstrating the calculation of the pulse velocity for the electron temperature data for the D case. Despite data which is more noisy than in Fig.5.3.5, the pulse propagation velocity calculated from the dashed line is approximately constant across all radii in this region $0.450 \geq \rho \geq 0.015$ of LHD plasma 49719. We infer a pulse velocity $(53.50 \pm 20.97)\mathrm{ms}^{-1}$.

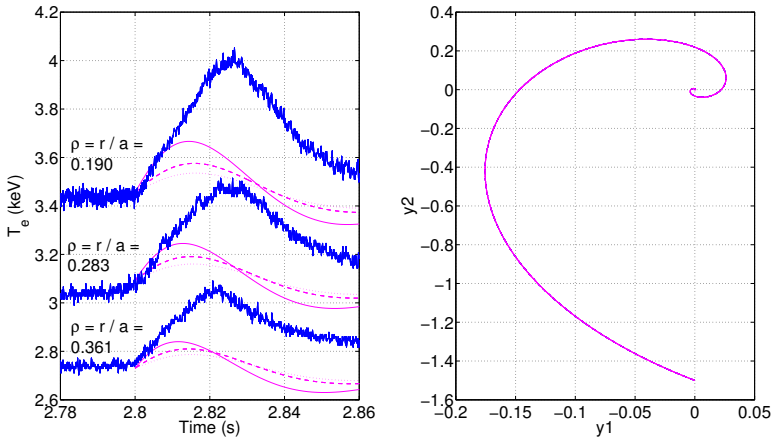

Figure 5.3.7: Variation and robustness of nonlinear pulse phenomenology in the model, for three different values of pseudo-velocity v_0 at three radial locations(Left panel). Blue lines show experimental data for R case in plasma 49708. Solid, dash and dot magenta lines denote simulation outputs for $v_0 = 15, v_0 = 30$ and $v_0 = 45$ respectively. The boundary condition for R case is $y_2(0) = 1.5$, and no horizontal or vertical shift is applied to the model outputs. Right panel: Phase plot of model outputs from left plots, all of which lie on the same orbit. Circulation direction of this phase plot is identical with Fig.6(a) of [Dendy et al., 2013], where the sign of the horizontal axis is reversed.

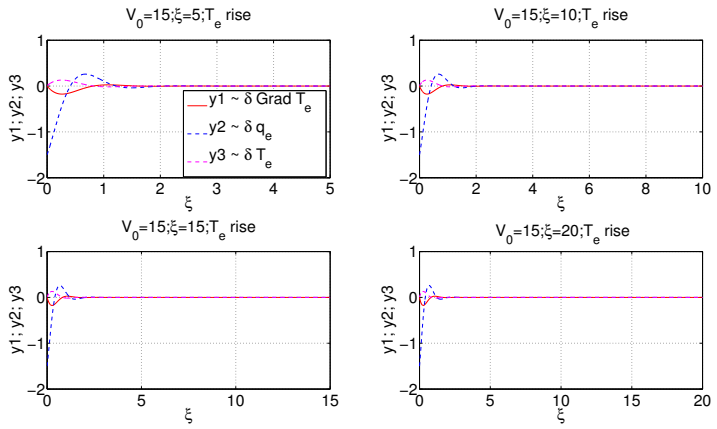

Figure 5.3.8: Impact of different ξ values on the heat pulse model in R case, four cases($\xi = 5; \xi = 10; \xi = 15; \xi = 20$) are examined. Red solid, dash blue and dash magenta lines denote y_1, y_2 and y_3 respectively.

5.4 Conclusion

We have derived from first principles a time-dependent model in one spatial dimension, which is able to describe quantitatively the radial inward propagation of heat pulses in the core of two plasmas[Inagaki et al., 2010] in the Large Helical Device(LHD). In one plasma the central electron temperature rises, in the other it falls. This new model is derived from a travelling wave transformation of the zero-dimensional model of [Dendy et al., 2013], which is known to capture the time-evolution of the heat pulse as it passes through a fixed radial location in these two plasmas. From the experimental data, we infer that the velocity of the propagating pulse is constant in both the electron temperature rise and drop cases. The pulse velocity in the electron temperature rise case is smaller than in the drop case by a factor $\simeq 2$. This aligns with Eq.(5.1.10), which reaches back into the mathematical structure of our model, and also coincides with empirical expectations given the values of the heat conduction parameters for these two plasmas. A pseudo-velocity parameter is introduced in the travelling wave transformations, in order to model heat pulse propagation across spatial location as well as in time. From numerical tests, we discover that real pulse velocity is about two times the best estimate of the travelling-wave transformation parameter v_0, referred to as the pseudo-velocity. Comparison between model outputs and raw experimental data suggests that our model is able to describe heat pulse propagation well, within a broad radial range of the LHD core plasma from $r/a \simeq 0.5$ to the centre.

The results of this Chapter provide additional support to the physical proposals, described in Sec.2 of [Dendy et al., 2013], which motivate the simple model equations reproduced as Eqs.(5.1.1) to (5.1.3) above. Central to these proposals is the conjecture that heat pulses are structures which are so strongly nonlinear that their evolution is primarily determined by the reactions of the perturbed heat flux and the perturbed temperature gradient on each other, while turbulent transport plays a relatively minor dissipative role. It is this mutually coupled interaction that governs the local plasma dynamics of the heat pulse in space, equivalent to the local up-and-down dynamics of a water wave under gravity. We have shown in this Chapter that this coupling model lends itself readily to a travelling wave transformation, yielding spatio-temporal pulse propagation, and that the pulse velocity that emerges mathematically provides an adequate match to empirical results and expectations. This aspect of the analysis also provides guidance on a previously unanswered question, namely the generic character of the heat pulse: we have shown that it may be closely related to a Korteweg-de Vries-Burgers soliton. Two avenues of investigation would repay immediate attention. First, this model has been tested on, and motivated by, measurements from only two plasmas in LHD - albeit plasmas with exceptionally high quality measurements. The simplicity of the model encourages one to hope that it may be more widely applicable, and clearly it should now be tested on a broader range of heat pulse experimental datasets, provided that they possess the required spatial and temporal resolution and that the other relevant plasma parameters are well diagnosed, as in LHD. Second, while gyrokinetic or other computationally intensive transport simulations have not yet (to the authors' knowledge) been applied to heat pulse experiments, the outputs of any future simulations of heat pulses could be tested directly against the analytical model presented here, which is constructed in terms of variables that are directly measurable, as distinct from the first-principles particle and field distributions of gyrokinetic theory.

Chapter 6

Conclusion

The reason for L-H transition would be the formation of transport barrier, which is the result of interactions between drift wave turbulence and zonal flows. Zonal flows are induced by turbulence via Reynold stress and suppress the turbulence by shear. This is a typical predator-prey relation. The positive or negative large deviation of electron temperature in heat pulse propagation experiments in both of Tokamak and Stellarator are described as well. The reason for this non-local and non-diffusive phenomena may be the reduction of electron heat diffusivity in transport barrier.

We have also introduced the basic nonlinear dynamics. We have analysed the predator-prey model(Lotka-Volterra model) which was firstly proposed by ecologist Volterra for investigating the populations of predators(like foxes) and prey(like rabbits). This is a simple model, which is applied in many subjects like mathematics, physics, chemistry, as well as ecology itself.

Research about energy transport and confinement is crucial in MCF plasmas physics. In this thesis, we have explored interactions between micro-scale turbulence and nonlinear meso-scale structures such as zonal flows and geodesic acoustic modes(GAMs), using a predator-prey (or Lotka-Volterra) model. A novel model, which embodies not only zonal flows, micro-scale turbulence and temperature gradient, but in addition GAMs, has been developed and analysed in terms of its nonlinear dynamics. We have studied the long-time behaviours of model results, their evolutions towards the final state, their fixed points and limit cycles. Also, we have explored the sensitivities of routes to attractors, that is, the "error bars" for this nonlinear system. This builds confidence in the read-across to tokamak confinement phenomenology, which we examined.

For heating induced transition phenomena from L-mode to H-mode, we have investigated the effects of how precisely the heating changes with time. We have

also shown that low frequency oscillating changes in external heating can drive the level of micro-scale turbulence through a period-doubling route to chaos, where the control parameter is the amplitude of the oscillatory component of the external heating flux. We have suggested how this could be tested experimentally, yielding diagnostic information.

Also, we have explored heat pulse propagation phenomena, which are widely discovered in Tokamak fusion devices and more recently in the Large Helical Device (LHD). We have carried out a travelling wave transformation of an existing zero-dimensional model. It is demonstrated that our model is able to simulate heat pulse propagation phenomena from edge to core. Experimental data from LHD are well matched by the time series that are deduced from our theoretical model.

In summary, the main body of this thesis has followed two themes, both of which are relevant to the edge transport phenomena. The first one is about modelling global Tokamak transport phenomenology using predator-prey models. Here the aim has been to identify the essential physics underlying confinement transitions, for example, using strongly nonlinear zero-dimensional models for the coupled time evolution of the temperature gradient, micro-scale turbulence level and amplitudes of zonal flows and GAMs. We have published "Robustness of predator-prey models for confinement regime transitions in fusion plasmas" and "Transitions to improved confinement regimes induces by changes in heating in zero-dimensional models for tokamak plasmas" in *Physics of Plasmas* **20**, 042302 (2013) and *Physics of Plasmas* **21**, 062307 (2014) respectively. The second one is achieving a quantitative match between a first principles model for heat pulse propagation and specific datasets from Large Helical Device (LHD). We have submitted "A quantitative model for heat pulse propagation across Large Helical Device plasmas" to *Physics of Plasmas* in 2015.

Chapter 7

Publications during Ph.D. studies

During the period of Ph.D. studies from October 2011 to April 2015, two peer-reviewed journal articles have been published on *Phys. Plasmas* in 2013 and 2014 respectively. Another paper has been submitted to *Phys. Plasmas* in 2015.

Also, seven conference proceedings have been published on European Physical Society Conference(EPS), American Physical Society(APS) Conference, Institute of Physics(IoP) Conference and International Toki Conference. One conference proceeding has been accepted by the 42nd European Physical Society Conference(EPS).

7.1 Peer-reviewed journals

[1] **H. Zhu**, S.C. Chapman and R.O. Dendy, *Phys. Plasmas* **20**, 042302 (2013).

[2] **H. Zhu**, S.C. Chapman, R.O. Dendy and K. Itoh, *Phys. Plasmas* **21**, 062307 (2014).

[3] **H. Zhu**, R.O. Dendy, S.C. Chapman and S. Inagaki, "A quantitative model for heat pulse propagation across Large Helical Device plasmas." (submitted to *Phys. Plasmas*).

7.2 Conference proceedings

[1] **H. Zhu**, S.C. Chapman and R.O. Dendy, Proceedings of the 40th EPS Conference on Plasma Physics, Espoo, Finland, Europhysics Conference Abstracts.

Vol.37D, P5.406. ISBN: 2-914771-84-3 (2013).

[2] R.O. Dendy, **H. Zhu** and S.C. Chapman, 55th Annual Meeting of the APS Division of Plasma Physics, Denver CO, USA, Bulletin of the American Physical Society. Vol.58, No.16, GP8.00015 (2013).

[3] **H. Zhu**, S.C. Chapman and R.O. Dendy, 23rd International Toki Conference (ITC-23) on Large-scale Simulation and Fusion Science, Toki-city, Gifu, Japan, P1-79 (2013).

[4] **H. Zhu**, S.C. Chapman, R.O. Dendy and K. Itoh, 41st IOP Plasma Physics Conference, London, UK, P-39 (2014).

[5] **H. Zhu**, S.C. Chapman, R.O. Dendy and K. Itoh, Proceedings of the 41st EPS Conference on Plasma Physics, Berlin, Germany, Europhysics Conference Abstracts. Vol.38F, P1.036. ISBN: 2-914771-90-8 (2014).

[6] **H. Zhu**, R.O. Dendy, S.C. Chapman and S. Inagaki, 56th Annual Meeting of the APS Division of Plasma Physics, New Orleans LA, USA, Bulletin of the American Physical Society. Vol.59, No.14, UP8.00040 (2014).

[7] **H. Zhu**, S.C. Chapman, R.O. Dendy and S. Inagaki, 42nd IOP Plasma Physics Conference, Milton Keynes, UK, P-06 (2015).

[8] **H. Zhu**, R.O. Dendy, S.C. Chapman and S. Inagaki, Proceedings of the 42nd EPS Conference on Plasma Physics, Lisbon, Portugal, Europhysics Conference Abstracts (2015).(accepted)

Bibliography

Charles H Anderton. Conflict and trade in a predator/prey economy. *Review of Development Economics*, 7(1):15–29, 2003.

C Angioni, RM McDermott, E Fable, R Fischer, T Pütterich, F Ryter, G Tardini, et al. Gyrokinetic modelling of electron and boron density profiles of h-mode plasmas in asdex upgrade. *Nuclear Fusion*, 51(2):023006, 2011.

David Arrowsmith and Colin M Place. *Dynamical systems: differential equations, maps, and chaotic behaviour*, volume 5. CRC Press, 1992.

LA Artsimovitch, SV Mirnov, and VS Strelkov. Investigation of ohmic heating of the plasma in the tokamak-3 toroidal assembly. *Soviet Atomic Energy*, 17(3): 886–892, 1964.

Cristoforo Sergio Bertuglia and Franco Vaio. Nonlinearity, chaos, and complexity: the dynamics of natural and social systems. *OUP Catalogue*, 2005.

NH Bian. On-off intermittent regulation of plasma turbulence. *Physics of Plasmas (1994-present)*, 17(4):044501, 2010.

NH Bian and OE Garcia. Confinement and dynamical regulation in two-dimensional convective turbulence. *Physics of Plasmas (1994-present)*, 10(12):4696–4707, 2003.

B Binegar. Taylor series methods. *Lecture notes*, 0:00, 2000.

K Borrass, DJ Campbell, S Clement, and GC Vlases. Scrape-off layer based modelling of the density limit in beryllated jet limiter discharges. *Nuclear fusion*, 33 (1):63, 1993.

H-S Bosch, V Erckmann, Ralf WT Konig, Felix Schauer, Reinhold J Stadler, and A Werner. Construction of wendelstein 7-xengineering a steady-state stellarator. *Plasma Science, IEEE Transactions on*, 38(3):265–273, 2010.

Peter Bradshaw. *An Introduction to Turbulence and Its Measurement: Thermodynamics and Fluid Mechanics Series*. Elsevier, 2013.

DL Brower, SK Kim, KW Wenzel, ME Austin, MS Foster, RF Gandy, NC Luhmann Jr, SC McCool, M Nagatsu, WA Peebles, et al. Experimental evidence for coupling of plasma particle and heat transport in the text tokamak. *Physical review letters*, 65(3):337, 1990.

KH Burrell. Summary of experimental progress and suggestions for future work (h mode confinement). *Plasma physics and controlled fusion*, 36(7A):A291, 1994.

KH Burrell, S Ejima, DP Schissel, NH Brooks, RW Callis, TN Carlstrom, AP Colleraine, JC DeBoo, H Fukumoto, RJ Groebner, et al. Observation of an improved energy-confinement regime in neutral-beam–heated divertor discharges in the diii-d tokamak. *Physical review letters*, 59(13):1432, 1987.

KH Burrell, ME Austin, DP Brennan, JC DeBoo, EJ Doyle, P Gohil, CM Greenfield, RJ Groebner, LL Lao, TC Luce, et al. Quiescent h-mode plasmas in the diii-d tokamak. *Plasma physics and controlled fusion*, 44(5A):A253, 2002.

KH Burrell, WP West, EJ Doyle, ME Austin, P Gohil, CM Greenfield, RJ Groebner, R Jayakumar, DH Kaplan, LL Lao, et al. Edge radial electric field structure in quiescent h-mode plasmas in the diii-d tokamak. *Plasma physics and controlled fusion*, 46(5A):A165, 2004.

KH Burrell, WP West, EJ Doyle, ME Austin, TA Casper, P Gohil, CM Greenfield, RJ Groebner, AW Hyatt, RJ Jayakumar, et al. Advances in understanding quiescent h-mode plasmas in diii-da). *Physics of Plasmas (1994-present)*, 12(5): 056121, 2005.

CE Bush, RJ Goldston, SD Scott, ED Fredrickson, K McGuire, J Schivell, G Taylor, Cris W Barnes, MG Bell, RL Boivin, et al. Peaked density profiles in circular-limiter h modes on the tftr tokamak. *Physical review letters*, 65(4):424, 1990.

NJ Lopes Cardozo and JCM de Haas. Heat pulse analysis in jet limiter and x-point plasmas. *Nuclear fusion*, 30(3):521, 1990.

TN Carlstrom. Transition physics and scaling overview. *Plasma physics and controlled fusion*, 38(8):1149, 1996.

BA Carreras, B Van Milligen, MA Pedrosa, R Balbín, C Hidalgo, DE Newman, E Sánchez, M Frances, I García-Cortés, J Bleuel, et al. Long-range time correlations in plasma edge turbulence. *Physical review letters*, 80(20):4438, 1998.

SC Chapman, NW Watkins, RO Dendy, P Helander, and G Rowlands. A simple avalanche model as an analogue for magnetospheric activity. *Geophysical Research Letters*, 25(13):2397–2400, 1998.

SC Chapman, RO Dendy, and G Rowlands. A sandpile model with dual scaling regimes for laboratory, space and astrophysical plasmas. *Physics of Plasmas (1994-present)*, 6(11):4169–4177, 1999.

SC Chapman, RO Dendy, and B Hnat. Sandpile model with tokamaklike enhanced confinement phenomenology. *Physical review letters*, 86(13):2814, 2001.

Francis F Chen. Introduction to plasma physics and controlled fusion, volume 1: Plasma physics. *Plenum Press,*, 2:3, 1975.

J Cheng, JQ Dong, K Itoh, LW Yan, M Xu, KJ Zhao, WY Hong, ZH Huang, XQ Ji, WL Zhong, et al. Dynamics of low-intermediate–high-confinement transitions in toroidal plasmas. *Physical review letters*, 110(26):265002, 2013.

JP Coad, J Likonen, M Rubel, E Vainonen-Ahlgren, DE Hole, T Sajavaara, T Renvall, GF Matthews, and JET EFDA Contributors. Overview of material redeposition and fuel retention studies at jet with the gas box divertor. *Nuclear fusion*, 46(2):350, 2006.

S Coda, Miklos Porkolab, and Keith H Burrell. Signature of turbulent zonal flows observed in the diii-d tokamak. *Physical review letters*, 86(CRPP-ARTICLE-2001-065):4835–4838, 2001.

JW Connor and HR Wilson. A review of theories of the lh transition. *Plasma physics and controlled fusion*, 42(1):R1, 2000.

JW Connor, T Fukuda, X Garbet, C Gormezano, V Mukhovatov, M Wakatani, et al. A review of internal transport barrier physics for steady-state operation of tokamaks. *Nuclear Fusion*, 44(4):R1, 2004.

GD Conway, B Scott, J Schirmer, M Reich, A Kendl, et al. Direct measurement of zonal flows and geodesic acoustic mode oscillations in asdex upgrade using doppler reflectometry. *Plasma physics and controlled fusion*, 47(8):1165, 2005.

GD Conway, C Angioni, F Ryter, P Sauter, J Vicente, and ASDEX Upgrade Team. Mean and oscillating plasma flows and turbulence interactions across the l-h confinement transition. *Physical review letters*, 106(6):065001, 2011.

JG Cordey, B Balet, DV Bartlett, RV Budny, JP Christiansen, GD Conway, L-G Eriksson, GM Fishpool, CW Gowers, JCM De Haas, et al. Plasma confinement in jet h mode plasmas with h, d, dt and t isotopes. *Nuclear fusion*, 39(3):301, 1999.

Peter M Cox, Richard A Betts, Chris D Jones, Steven A Spall, and Ian J Totterdell. Acceleration of global warming due to carbon-cycle feedbacks in a coupled climate model. *Nature*, 408(6809):184–187, 2000.

Magnus Dam, Morten Brøns, Jens Juul Rasmussen, Volker Naulin, and Guosheng Xu. Bifurcation analysis and dimension reduction of a predator-prey model for the lh transition. *Physics of Plasmas (1994-present)*, 20(10):102302, 2013.

SJ Davies, SK Erents, PC Stangeby, J Lingertat, GF Matthews, RD Monk, and GC Vlases. Behaviour of upstream separatrix density in jet h-mode plasmas. *Journal of nuclear materials*, 266:1028–1033, 1999.

JC DeBoo, CC Petty, AE White, KH Burrell, EJ Doyle, JC Hillesheim, C Holland, GR McKee, TL Rhodes, L Schmitz, et al. Electron profile stiffness and critical gradient studies. *Physics of Plasmas (1994-present)*, 19(8):082518, 2012.

Richard O Dendy. *Plasma dynamics*. Clarendon Press Oxford, 1990.

RO Dendy and P Helander. Appearance and nonappearance of self-organized criticality in sandpiles. *Physical Review E*, 57(3):3641, 1998.

RO Dendy, Sandra C Chapman, and M Paczuski. Fusion, space and solar plasmas as complex systems. *Plasma Physics and Controlled Fusion*, 49(5A):A95, 2007.

RO Dendy, Sandra C Chapman, and S Inagaki. Modelling the measured local time evolution of strongly nonlinear heat pulses in the large helical device. *Plasma Physics and Controlled Fusion*, 55(11):115009, 2013.

Patrick H Diamond and TS Hahm. On the dynamics of turbulent transport near marginal stability. *Physics of Plasmas (1994-present)*, 2(10):3640–3649, 1995.

Patrick H Diamond, Sanae-I Itoh, and Kimitaka Itoh. *Modern Plasma Physics: Volume 1, Physical Kinetics of Turbulent Plasmas*. Cambridge University Press, 2010.

PH Diamond and Y-B Kim. Theory of mean poloidal flow generation by turbulence. *Physics of Fluids B: Plasma Physics (1989-1993)*, 3(7):1626–1633, 1991.

PH Diamond, Y-M Liang, BA Carreras, and PW Terry. Self-regulating shear flow turbulence: A paradigm for the l to h transition. *Physical review letters*, 72(16): 2565, 1994.

PH Diamond, SI Itoh, K Itoh, and TS Hahm. Zonal flows in plasmaa review. *Plasma Physics and Controlled Fusion*, 47(5):R35, 2005.

PH Diamond, A Hasegawa, and K Mima. Vorticity dynamics, drift wave turbulence, and zonal flows: a look back and a look ahead. *Plasma Physics and Controlled Fusion*, 53(12):124001, 2011.

W Dorland, F Jenko, M Kotschenreuther, and BN Rogers. Electron temperature gradient turbulence. *Physical Review Letters*, 85(26):5579, 2000.

Sarah Douglas, Mabruka Mohamed, and Eun-jin Kim. Confinement improvement by fluctuating input power. *Physics of Plasmas (1994-present)*, 20(11):114504, 2013.

EJ Doyle, RJ Groebner, KH Burrell, P Gohil, T Lehecka, NC Luhmann Jr, H Matsumoto, TH Osborne, WA Peebles, and R Philipona. Modifications in turbulence and edge electric fields at the l–h transition in the diii-d tokamak. *Physics of Fluids B: Plasma Physics (1989-1993)*, 3(8):2300–2307, 1991.

EJ Doyle, WA Houlberg, Y Kamada, V Mukhovatov, TH Osborne, A Polevoi, G Bateman, JW Connor, JG Cordey, T Fujita, et al. Plasma confinement and transport. *Nuclear Fusion*, 47(6):S18, 2007.

Philip G Drazin. *Nonlinear systems*, volume 10. Cambridge University Press, 1992.

XR Duan, JQ Dong, LW Yan, XT Ding, QW Yang, J Rao, DQ Liu, WM Xuan, LY Chen, XD Li, et al. Preliminary results of elmy h-mode experiments on the hl-2a tokamak. *Nuclear Fusion*, 50(9):095011, 2010.

BD Dudson, RO Dendy, A Kirk, H Meyer, and GF Counsell. Comparison of l-and h-mode plasma edge fluctuations in mast. *Plasma physics and controlled fusion*, 47(6):885, 2005.

R Dux, A Gude Peeters, A Gude, A Kallenbach, R Neu, and ASDEX Upgrade Team. Z dependence of the core impurity transport in asdex upgrade h mode discharges. *Nuclear Fusion*, 39(11):1509, 1999.

R Dux, A Loarte, E Fable, and A Kukushkin. Transport of tungsten in the h-mode edge transport barrier of iter. *Plasma Physics and Controlled Fusion*, 56(12): 124003, 2014.

AV Eliseev and II Mokhov. Carbon cycle–climate feedback sensitivity to parameter changes of a zero-dimensional terrestrial carbon cycle scheme in a climate model of intermediate complexity. *Theoretical and applied climatology*, 89(1-2):9–24, 2007.

V Erckmann, F Wagner, J Baldzuhn, R Brakel, R Burhenn, U Gasparino, P Grigull, HJ Hartfuss, JV Hofmann, R Jaenicke, et al. H mode of the w 7-as stellarator. *Physical review letters*, 70(14):2086, 1993.

L-G Eriksson, A Mueck, O Sauter, S Coda, MJ Mantsinen, M-L Mayoral, E Westerhof, RJ Buttery, D McDonald, Thomas Johnson, et al. Destabilization of fast-ion-induced long sawteeth by localized current drive in the jet tokamak. *Physical review letters*, 92(23):235004, 2004.

H Eubank, R Goldston, V Arunasalam, M Bitter, K Bol, D Boyd, N Bretz, J-P Bussac, S Cohen, P Colestock, et al. Neutral-beam-heating results from the princeton large torus. *Physical Review Letters*, 43(4):270, 1979.

A Fasoli, D Borba, C Gormezano, R Heeter, A Jaun, J Jacquinot, W Kerner, Q King, JB Lister, S Sharapov, et al. Alfvén eigenmode experiments in tokamaks and stellarators. *Plasma Physics and Controlled Fusion*, 39(12B):B287, 1997.

Mitchell J Feigenbaum. Quantitative universality for a class of nonlinear transformations. *Journal of statistical physics*, 19(1):25–52, 1978.

ED Fredrickson, JD Callen, K McGuire, JD Bell, RJ Colchin, PC Efthimion, KW Hill, R Izzo, DR Mikkelsen, DA Monticello, et al. Heat pulse propagation studies in tftr. *Nuclear fusion*, 26(7):849, 1986.

ED Fredrickson, K McGuire, A Cavallo, R Budny, A Janos, D Monticello, Y Nagayama, W Park, G Taylor, and MC Zarnstorff. Ballistic contributions to heat-pulse propagation in the tftr tokamak. *Physical review letters*, 65(23):2869, 1990.

Jeffrey P Freidberg. *Plasma physics and fusion energy*. Cambridge university press, 2007.

Akihide Fujisawa. Experimental studies of mesoscale structure and its interactions with microscale waves in plasma turbulence. *Plasma Physics and Controlled Fusion*, 53(12):124015, 2011.

T Fukuda, T Takizuka, K Tsuchiya, Y Kamada, K Nagashima, M Sato, H Takenaga, S Ishida, S Konoshima, S Higashijima, et al. H mode transition threshold power scaling and its relation to the edge neutrals in jt-60u. *Nuclear fusion*, 37(9):1199, 1997.

Stephen J Gallagher. *Zonal flow generation through four wave interaction in reduced models of fusion plasma turbulence*. PhD thesis, University of Warwick, 2013.

X Garbet, Y Sarazin, F Imbeaux, P Ghendrih, C Bourdelle, ÖD Gürcan, and PH Diamond. Front propagation and critical gradient transport models. *Physics of Plasmas (1994-present)*, 14(12):122305, 2007.

KW Gentle. Dependence of heat pulse propagation on transport mechanisms: Consequences of nonconstant transport coefficients. *Physics of Fluids (1958-1988)*, 31(5):1105–1110, 1988.

Marzio Giglio, Sergio Musazzi, and Umberto Perini. Transition to chaotic behavior via a reproducible sequence of period-doubling bifurcations. *Physical Review Letters*, 47(4):243, 1981.

Robert J Goldston. Energy confinement scaling in tokamaks: some implications of recent experiments with ohmic and strong auxiliary heating. *Plasma Physics and Controlled Fusion*, 26(1A):87, 1984.

G Gorini, P Mantica, GMD Hogeweij, F De Luca, A Jacchia, JA Konings, NJ Lopes Cardozo, and M Peters. Simultaneous propagation of heat waves induced by sawteeth and electron cyclotron heating power modulation in the rtp tokamak. *Physical review letters*, 71(13):2038, 1993.

C Gormezano, YF Baranov, CD Challis, I Coffey, GA Cottrell, AC Ekedahl, CM Greenfield, AC Howman, GTA Huysmans, M Keilhacker, et al. Internal transport barriers in jet deuterium-tritium plasmas. *Physical review letters*, 80 (25):5544, 1998.

Martin Greenwald, RL Boivin, F Bombarda, PT Bonoli, CL Fiore, D Garnier, JA Goetz, SN Golovato, MA Graf, RS Granetz, et al. H mode confinement in alcator c-mod. *Nuclear Fusion*, 37(6):793, 1997.

G Grieger, W Lotz, P Merkel, J Nührenberg, J Sapper, E Strumberger, H Wobig, R Burhenn, V Erckmann, U Gasparino, et al. Physics optimization of stellarators. *Physics of Fluids B: Plasma Physics (1989-1993)*, 4(7):2081–2091, 1992.

I Gruzinov, PH Diamond, and MN Rosenbluth. Sandpiles with bistable automata rules: Towards a minimal model of pedestal formation and structure. *Physical review letters*, 89(25):255001, 2002.

Stephen J Guastello, Matthijs Koopmans, and David Pincus. Chaos and complexity in psychology. *Cambridge, Cambridge University*, 2009.

Xu Guosheng and Wan Baonian. Measurement of zonal flows in a tokamak using langmuir probe array. *Plasma Science and Technology*, 8(1):10, 2006.

DK Gupta, RJ Fonck, GR McKee, DJ Schlossberg, and MW Shafer. Detection of zero-mean-frequency zonal flows in the core of a high-temperature tokamak plasma. *Physical review letters*, 97(12):125002, 2006.

EZ Gusakov, AD Gurchenko, AB Altukhov, VV Bulanin, LA Esipov, M Yu Kantor, DV Kouprienko, SI Lashkul, AV Petrov, and A Yu Stepanov. Investigation of small-scale tokamak plasma turbulence by correlative uhr backscattering diagnostics. *Plasma physics and controlled fusion*, 48(12B):B443, 2006.

Hermann Haken. Synergetics. *Edited by Peter Fulde*, page 341, 1983.

T Happel, T Estrada, E Blanco, C Hidalgo, GD Conway, U Stroth, and TJ-II Team. Scale-selective turbulence reduction in h-mode plasmas in the tj-ii stellarator. *Physics of Plasmas (1994-present)*, 18(10):102302, 2011.

Akira Hasegawa and Masahiro Wakatani. Self-organization of electrostatic turbulence in a cylindrical plasma. *Physical review letters*, 59(14):1581, 1987.

NC Hawkes, BC Stratton, T Tala, CD Challis, G Conway, R DeAngelis, C Giroud, J Hobirk, E Joffrin, P Lomas, et al. Observation of zero current density in the core of jet discharges with lower hybrid heating and current drive. *Physical review letters*, 87(11):115001, 2001.

P Helander, CD Beidler, TM Bird, M Drevlak, Y Feng, R Hatzky, F Jenko, R Kleiber, JHE Proll, Yu Turkin, et al. Stellarator and tokamak plasmas: a comparison. *Plasma Physics and Controlled Fusion*, 54(12):124009, 2012.

Robert C Hilborn. *Chaos and nonlinear dynamics*, volume 2. Oxford University Press New York, 1994.

T Hino, A Sagara, Y Nobuta, N Inoue, Y Hirohata, Y Yamauchi, S Masuzaki, N Noda, H Suzuki, A Komori, et al. Material probe analysis for plasma facing surface in the large helical device. *Nuclear fusion*, 44(4):496, 2004.

T Hino, Y Nobuta, N Ashikawa, K Nishimura, S Masuzaki, A Sagara, Y Hirohata, Y Yamauchi, N Noda, N Ohyabu, et al. Plasma wall interaction study in the large helical device. *Fusion Engineering and Design*, 82(15):1621–1626, 2007.

Takeshi Hirai, H Maier, Marek Rubel, Ph Mertens, R Neu, E Gauthier, J Likonen, C Lungu, G Maddaluno, GF Matthews, et al. R&d on full tungsten divertor and beryllium wall for jet iter-like wall project. *Fusion Engineering and Design*, 82 (15):1839–1845, 2007.

M Hirsch, J Baldzuhn, C Beidler, R Brakel, R Burhenn, A Dinklage, H Ehmler, M Endler, V Erckmann, Y Feng, et al. Major results from the stellarator wendelstein 7-as. *Plasma Physics and Controlled Fusion*, 50(5):053001, 2008.

SP Hirshman and DJ Sigmar. Neoclassical transport of impurities in tokamak plasmas. *Nuclear Fusion*, 21(9):1079, 1981.

J Hofbauer and JW-H So. Multiple limit cycles for three dimensional lotka-volterra equations. *Applied Mathematics Letters*, 7(6):59–63, 1994.

GMD Hogeweij, J O'Rourke, and ACC Sips. Evidence of coupling of thermal and particle transport from heat and density pulse measurements in jet. *Plasma Physics and Controlled Fusion*, 33(3):189, 1991.

GMD Hogeweij, P Mantica, G Gorini, J de Kloe, NJ Lopes Cardozo, et al. Recording non-local temperature rise in the rtp tokamak. *Plasma physics and controlled fusion*, 42(10):1137, 2000.

Claude Wendell Horton, Wendell Horton, and Wendell Horton. *Turbulent transport in magnetized plasmas*. World Scientific, 2012.

Pei-Chun Hsu and PH Diamond. Zonal flow formation in the presence of ambient mean shear. *Physics of Plasmas (1994-present)*, 22(2):022306, 2015.

D Hughes, M Paczuski, RO Dendy, P Helander, and KG McClements. Solar flares as cascades of reconnecting magnetic loops. *Physical review letters*, 90(13):131101, 2003.

K Ida, T Shimozuma, H Funaba, K Narihara, S Kubo, S Murakami, A Wakasa, M Yokoyama, Y Takeiri, KY Watanabe, et al. Characteristics of electron heat transport of plasma with an electron internal-transport barrier in the large helical device. *Physical review letters*, 91(8):085003, 2003.

Atsuo Iiyoshi, A Komori, A Ejiri, M Emoto, H Funaba, M Goto, K Ida, H Idei, S Inagaki, S Kado, et al. Overview of the large helical device project. *Nuclear Fusion*, 39(9Y):1245, 1999.

S Inagaki, K Ida, N Tamura, T Shimozuma, S Kubo, Y Nagayama, K Kawahata, S Sudo, K Ohkubo, et al. Cold pulse experiments in plasma with an electron internal transport barrier on lhd. *Plasma physics and controlled fusion*, 46(5A): A71, 2004.

S Inagaki, H Takenaga, K Ida, A Isayama, N Tamura, T Takizuka, T Shimozuma, Y Kamada, S Kubo, Y Miura, et al. Comparison of transient electron heat transport in lhd helical and jt-60u tokamak plasmas. *Nuclear fusion*, 46(1):133, 2006.

S Inagaki, N Tamura, K Ida, K Tanaka, Y Nagayama, K Kawahata, S Sudo, K Itoh, SI Itoh, A Komori, et al. Characterization of bifurcation induced by long distance correlation between heat flux and temperature gradient in toroidal plasmas. *Plasma Physics and Controlled Fusion*, 52(7):075002, 2010.

Gérard Iooss and Moritz Adelmeyer. *Topics in bifurcation theory and applications*. World Scientific, 1998.

Kimitaka Itoh, Sanae I Itoh, and Atsushi Fukuyama. *Transport and structural formation in plasmas*. Institute of Physics Pub., 1999.

SI Itoh and K Itoh. A mini–max principle for drift waves and mesoscale fluctuations. *Plasma Physics and Controlled Fusion*, 53(1):015008, 2011.

Takuya Iwasaki, Sanae-I Itoh, Masatoshi Yagi, Kimitaka Itoh, and Ulich Stroth. Non-local model analysis of heat pulse propagation and simulation of experiments in w7-as. *Journal of the Physical Society of Japan*, 68(2):478–486, 1999.

Eugene M Izhikevich. *Dynamical systems in neuroscience*. MIT press, 2007.

E Atlee Jackson. *Perspectives of nonlinear dynamics*, volume 1. CUP Archive, 1992.

J Jacquinot, VP Bhatnagar, JG Cordey, LD Horton, DFH Start, R Barnsley, P Breger, JP Christiansen, S Clement, SJ Davies, et al. Overview of iter physics deuterium-tritium experiments in jet. *Nuclear fusion*, 39(2):235, 1999.

M Jakubowski, RJ Fonck, and GR McKee. Observation of coherent sheared turbulence flows in the diii-d tokamak. *Physical review letters*, 89(26):265003, 2002.

Frank Jenko, W Dorland, M Kotschenreuther, and BN Rogers. Electron temperature gradient driven turbulence. *Physics of Plasmas (1994-present)*, 7(5):1904–1910, 2000.

JD Jukes. Stability theory of plasma current multipole. *Nuclear Fusion*, 10(2):131, 1970.

B.B. Kadomtsev. *Fiz. Plazmy*, 1(710), 1975.

A Kallenbach, J Adamek, L Aho-Mantila, S Äkäslompolo, C Angioni, CV Atanasiu, M Balden, K Behler, E Belonohy, A Bergmann, et al. Overview of asdex upgrade results. *Nuclear Fusion*, 51(9):094012, 2011.

Daniel Kaplan and Leon Glass. *Understanding nonlinear dynamics*, volume 19. Springer Science & Business Media, 1995.

Naohiro Kasuya, Masatoshi Yagi, Kimitaka Itoh, and Sanae-I Itoh. Selective formation of turbulent structures in magnetized cylindrical plasmas. *Physics of Plasmas (1994-present)*, 15(5):052302, 2008.

Predhiman Kaw, Raghvendra Singh, and PH Diamond. Coherent nonlinear structures of drift wave turbulence modulated by zonal flows. *Plasma physics and controlled fusion*, 44(1):51, 2002.

SM Kaye, MG Bell, K Bol, D Boyd, K Brau, D Buchenauer, R Budny, A Cavallo, P Couture, T Crowley, et al. Attainment of high confinement in neutral beam heated divertor discharges in the pdx tokamak. *Journal of Nuclear Materials*, 121:115–125, 1984.

SM Kaye, M Greenwald, U Stroth, O Kardaun, A Kus, D Schissel, J DeBoo, G Bracco, K Thomsen, JG Cordey, et al. Iter l mode confinement database. *Nuclear Fusion*, 37(9):1303, 1997.

Eun-jin Kim and PH Diamond. Zonal flows and transient dynamics of the l-h transition. *Physical review letters*, 90(18):185006, 2003.

H Kishimoto, M Nagami, and M Kikuchi. Recent results and engineering experiences from jt-60. *Fusion engineering and design*, 39:73–81, 1998.

MW Kissick, JD Callen, ED Fredrickson, AC Janos, and G Taylor. Non-local component of electron heat transport in tftr. *Nuclear fusion*, 36(12):1691, 1996.

M Kobayashi, J Miyazawa, S Masuzaki, Y Igitkhanov, R Sakamoto, N Ashikawa, T Morisaki, N Ohyabu, H Yamada, H Funaba, et al. Analysis for hydrogen particle balance of plasma-wall system in the large helical device. *Journal of nuclear materials*, 350(1):40–46, 2006.

M Kobayashi, Y Feng, S Masuzaki, M Shoji, J Miyazawa, T Morisaki, N Ohyabu, N Ashikawa, A Komori, O Motojima, et al. Divertor transport study in the large helical device. *Journal of nuclear materials*, 363:294–300, 2007.

NA Krall and AW Trivelpiece. *Principles of plasma physics*. San Francisco press, 1986.

A Krämer-Flecken, S Soldatov, HR Koslowski, O Zimmermann, TEXTOR Team, et al. Properties of geodesic acoustic modes and the relation to density fluctuations. *Physical review letters*, 97(4):045006, 2006.

Nikolai A Kudryashov. On new travelling wave solutions of the kdv and the kdv–burgers equations. *Communications in Nonlinear Science and Numerical Simulation*, 14(5):1891–1900, 2009.

J. D. Lawson. Some criteria for a power producing thermonuclear reactor. *Technical report*, 00(00):0000, 1955.

J-N Leboeuf, LA Charlton, and BA Carreras. Shear flow effects on the nonlinear evolution of thermal instabilities. *Physics of Fluids B: Plasma Physics (1989-1993)*, 5(8):2959–2966, 1993.

F Leuterer, M Beckmann, H Brinkschulte, F Monaco, M Münich, F Ryter, H Schütz, L Empacher, G Gantenbein, W Förster, et al. Experience with the ecrh system of asdex-upgrade. *Fusion engineering and design*, 53(1):485–489, 2001.

D Li, Y Chen, J Ma, and W Yang. *plasma physics*. Higher Education Press, 2006.

JQ Li, Y Kishimoto, N Miyato, T Matsumoto, and JQ Dong. Dynamics of large-scale structure and electron transport in tokamak microturbulence simulations. *Nuclear fusion*, 45(11):1293, 2005.

Paul S Linsay. Period doubling and chaotic behavior in a driven anharmonic oscillator. *Physical Review Letters*, 47(19):1349, 1981.

X Litaudon, F Crisanti, B Alper, JF Artaud, Yu F Baranov, E Barbato, V Basiuk, A Bécoulet, M Bécoulet, C Castaldo, et al. Towards fully non-inductive current drive operation in jet. *Plasma physics and controlled fusion*, 44(7):1057, 2002.

Bing Liu, Yujuan Zhang, and Lansun Chen. Dynamic complexities of a holling i predator–prey model concerning periodic biological and chemical control. *Chaos, Solitons & Fractals*, 22(1):123–134, 2004.

NJ Lopes Cardozo. Perturbative transport studies in fusion plasmas. *Plasma physics and controlled fusion*, 37(8):799–852, 1995.

Edward N Lorenz. Deterministic nonperiodic flow. *Journal of the atmospheric sciences*, 20(2):130–141, 1963.

Alfred J Lotka. Elements of physical biology. 1925.

TC Luce, CC Petty, and JCM De Haas. Inward energy transport in tokamak plasmas. *Physical review letters*, 68(1):52, 1992.

James F Lyon, James A Rome, John L Johnson, David T Anderson, and Paul R Garabedian. 2. stellarator physics. *TRANSPORT*, 2:30, 2000.

MA Malkov and PH Diamond. Weak hysteresis in a simplified model of the lh transition. *Physics of Plasmas (1994-present)*, 16(1):012504, 2009.

Giovanni Manfredi, CM Roach, and RO Dendy. Zonal flow and streamer generation in drift turbulence. *Plasma physics and controlled fusion*, 43(6):825, 2001.

P Mantica, P Galli, G Gorini, GMD Hogeweij, J De Kloe, NJ Lopes Cardozo, RTP Team, et al. Nonlocal transient transport and thermal barriers in rijnhuizen tokamak project plasmas. *Physical review letters*, 82(25):5048, 1999.

S Masuzaki, T Morisaki, N Ohyabu, A Komori, H Suzuki, N Noda, Y Kubota, R Sakamoto, K Narihara, K Kawahata, et al. The divertor plasma characteristics in the large helical device. *Nuclear fusion*, 42(6):750, 2002.

GF Matthews, P Edwards, H Greuner, A Loving, H Maier, Ph Mertens, V Philipps, V Riccardo, M Rubel, C Ruset, et al. Current status of the jet iter-like wall project. *Physica Scripta*, 2009(T138):014030, 2009.

Robert M May et al. Simple mathematical models with very complicated dynamics. *Nature*, 261(5560):459–467, 1976.

Garry McCracken and Peter Stott. *Fusion: the Energy of the Universe*. Academic Press, 2012.

DC McDonald, L Laborde, JC DeBoo, F Ryter, M Brix, CD Challis, P De Vries, C Giroud, J Hobirk, D Howell, et al. Jet confinement studies and their scaling to high βn, iter scenarios. *Plasma Physics and Controlled Fusion*, 50(12):124013, 2008.

Alan J McKane and Timothy J Newman. Predator-prey cycles from resonant amplification of demographic stochasticity. *Physical review letters*, 94(21):218102, 2005.

George R McKee, Raymond J Fonck, Marcin Jakubowski, Keith H Burrell, Klaus Hallatschek, Rick A Moyer, Dmitry L Rudakov, W Nevins, Gary D Porter, Paul Schoch, et al. Experimental characterization of coherent, radially-sheared zonal flows in the diii-d tokamak. *Physics of Plasmas (1994-present)*, 10(5):1712–1719, 2003.

Halvor Mehlum, Karl Moene, and Ragnar Torvik. Predator or prey?: Parasitic enterprises in economic development. *European Economic Review*, 47(2):275–294, 2003.

K Miki and PH Diamond. Role of the geodesic acoustic mode shearing feedback loop in transport bifurcations and turbulence spreading. *Physics of Plasmas (1994-present)*, 17(3):032309, 2010.

K Miki and PH Diamond. Novel states of pre-transition edge turbulence emerging from shearing mode competition. *Nuclear Fusion*, 51(10):103003, 2011.

K Miki, PH Diamond, ÖD Gürcan, GR Tynan, T Estrada, L Schmitz, and GS Xu. Spatio-temporal evolution of the l i h transition. *Physics of Plasmas (1994-present)*, 19(9):092306, 2012.

K Miki, PH Diamond, N Fedorczak, ÖD Gürcan, M Malkov, C Lee, Y Kosuga, G Tynan, GS Xu, T Estrada, et al. Spatio-temporal evolution of the l h and h l transitions. *Nuclear Fusion*, 53(7):073044, 2013a.

K Miki, PH Diamond, S-H Hahn, WW Xiao, ÖD Gürcan, and GR Tynan. Dynamics of stimulated l h transitions. *Physics of Plasmas (1994-present)*, 20(8):082304, 2013b.

K Miki, PH Diamond, S-H Hahn, WW Xiao, ÖD Gürcan, and GR Tynan. Physics of stimulated l h transitions. *Physical review letters*, 110(19):195002, 2013c.

K Miki, PH Diamond, L Schmitz, DC McDonald, T Estrada, ÖD Gürcan, and GR Tynan. Spatio-temporal evolution of the h l back transition. *Physics of Plasmas (1994-present)*, 20(6):062304, 2013d.

SV Mirnov. Influence of the shape and magnitude of the discharge current pulse on plasma containment and heating in tokamak-3. *Nuclear Fusion*, 9(1):57, 1969.

Kenro Miyamoto. *Controlled fusion and plasma physics*. Taylor & Francis, 2006.

S Morita, M Goto, H Funaba, H Idei, K Ikeda, S Inagaki, O Kaneko, K Kawahata, A Komori, S Kubo, et al. Effect of carbon divertor plates on impurities, zeff and density limit in large helical device. *Physica Scripta*, 2001(T91):48, 2001.

DA Mossessian, P Snyder, A Hubbard, JW Hughes, M Greenwald, B LaBombard, JA Snipes, S Wolfe, and H Wilson. High-confinement-mode edge stability of alcator c-mod plasmas. *Physics of Plasmas (1994-present)*, 10(5):1720–1726, 2003.

Osamu Motojima, N Ohyabu, A Komori, O Kaneko, H Yamada, K Kawahata, Y Nakamura, K Ida, T Akiyama, N Ashikawa, et al. Recent advances in the lhd experiment. *Nuclear fusion*, 43(12):1674, 2003.

V S_ Mukhovatov and VD Shafranov. Plasma equilibrium in a tokamak. *Nuclear Fusion*, 11(6):605, 1971.

DE Newman, BA Carreras, PH Diamond, and TS Hahm. The dynamics of marginality and self-organized criticality as a paradigm for turbulent transport. *Physics of Plasmas (1994-present)*, 3(5):1858–1866, 1996.

K Nishimura, N Ashikawa, S Masuzaki, J Miyazawa, A Sagara, M Goto, BJ Peterson, A Komori, N Noda, K Ida, et al. Development of the plasma operational regime in the large helical device by the various wall conditioning methods. *Journal of nuclear materials*, 337:431–435, 2005.

T Ohkawa. New methods of driving plasma current in fusion devices. *Nuclear Fusion*, 10(2):185, 1970.

N Ohyabu, T Watanabe, Hantao Ji, H Akao, T Ono, T Kawamura, K Yamazaki, K Akaishi, N Inoue, A Komori, et al. The large helical device (lhd) helical divertor. *Nuclear fusion*, 34(3):387, 1994.

Edward Ott. *Chaos in dynamical systems*. Cambridge university press, 2002.

Edward Ott, Bertram Hui, and KR Chu. Theory of electron cyclotron resonance heating of tokamak plasmas. *Physics of Fluids (1958-1988)*, 23(5):1031–1045, 1980.

Francis W Perkins. Heating tokamaks via the ion-cyclotron and ion-ion hybrid resonances. *Nuclear Fusion*, 17(6):1197, 1977.

CC Petty and TC Luce. Inward transport of energy during off-axis heating on the diii-d tokamak. *Nuclear fusion*, 34(1):121, 1994.

E Roy Pike and Luigi A Lugiato. *Chaos, noise and fractals*. CRC Press, 1987.

Miklos Porkolab. Parametric instabilities due to lower-hybrid radio frequency heating of tokamak plasmas. *Physics of Fluids (1958-1988)*, 20(12):2058–2075, 1977.

William H Press. *Numerical recipes 3rd edition: The art of scientific computing*. Cambridge university press, 2007.

R Rajesh, B Ramesh Kumar, SK Varshney, Manoj Kumar, Chhaya Chavda, Aruna Thakkar, NC Patel, Ajai Kumar, and Aditya Team. Electron temperature (t e) measurements by thomson scattering system. *Pramana*, 55(5-6):733–740, 2000.

S Neil Rasband. *Chaotic dynamics of nonlinear systems*, volume 1. 1997.

Warren D Rayle, John J Reinmann, and J Reece Roth. Pii. plasma heating and containment. *PLASMAS AND MAGNETIC FIELD IN PROPULSION AND*, 1969.

PH Rebut, PP Lallia, and ML Watkins. The critical temperature gradient model of plasma transport: applications to jet and future tokamaks. *Plasma Physics and Controlled Nuclear Fusion Research*, 2:191, 1988.

AB Rechester and MN Rosenbluth. Electron heat transport in a tokamak with destroyed magnetic surfaces. *Physical Review Letters*, 40(1):38–41, 1978.

JE Rice, Chi Gao, ML Reinke, PH Diamond, NT Howard, HJ Sun, Istvan Cziegler, AE Hubbard, YA Podpaly, WL Rowan, et al. Non-local heat transport, rotation reversals and up/down impurity density asymmetries in alcator c-mod ohmic l-mode plasmas. *Nuclear Fusion*, 53(3):033004, 2013.

E Righi, DV Bartlett, JP Christiansen, GD Conway, JG Cordey, L-G Eriksson, HPL De Esch, GM Fishpool, CW Gowers, JCM De Haas, et al. Isotope scaling of the h mode power threshold on jet. *Nuclear fusion*, 39(3):309, 1999.

Robin Robertson and Allan Combs. *Chaos theory in psychology and the life sciences*. Psychology Press, 2014.

F Ryter, W Suttrop, B Brüsehaber, M Kaufmann, V Mertens, H Murmann, AG Peeters, J Stober, J Schweinzer, H Zohm, et al. H-mode power threshold and transition in asdex upgrade. *Plasma physics and controlled fusion*, 40(5):725, 1998.

F Ryter, R Neu, R Dux, H-U Fahrbach, F Leuterer, G Pereverzev, J Schweinzer, J Stober, W Suttrop, ASDEX Upgrade Team, et al. Propagation of cold pulses and heat pulses in asdex upgrade. *Nuclear fusion*, 40(11):1917, 2000.

S Sakakibara, H Yamada, KY Watanabe, Y Narushima, K Toi, S Ohdachi, M Takechi, S Yamamoto, K Narihara, K Tanaka, et al. Mhd characteristics in the high beta regime of the large helical device. *Nuclear fusion*, 41(9):1177, 2001.

S Sakakibara, KY Watanabe, Y Suzuki, Y Narushima, S Ohdachi, N Nakajima, F Watanabe, L Garcia, A Weller, K Toi, et al. Mhd study of the reactor-relevant high-beta regime in the large helical device. *Plasma Physics and Controlled Fusion*, 50(12):124014, 2008.

F Sano, T Mizuuchi, K Kondo, K Nagasaki, H Okada, S Kobayashi, K Hanatani, Y Nakamura, S Yamamoto, Y Torii, et al. H-mode confinement of heliotron j. *Nuclear fusion*, 45(12):1557, 2005.

Javier E Satulovsky and Tânia Tomé. Stochastic lattice gas model for a predator-prey system. *Physical Review E*, 49(6):5073, 1994.

DP Schissel, JC DeBoo, KH Burrell, JR Ferron, RJ Groebner, H St John, RD Stambaugh, BJD Tubbing, K Thomsen, JG Cordey, et al. H-mode energy confinement scaling from the diii-d and jet tokamaks. *Nuclear Fusion*, 31(1):73, 1991.

L Schmitz, L Zeng, TL Rhodes, JC Hillesheim, EJ Doyle, RJ Groebner, WA Peebles, KH Burrell, and G Wang. Role of zonal flow predator-prey oscillations in triggering the transition to h-mode confinement. *Physical review letters*, 108(15): 155002, 2012.

FC Schuller. Disruptions in tokamaks. *Plasma Physics and Controlled Fusion*, 37 (11A):A135, 1995.

Heinz Georg Schuster and Wolfram Just. *Deterministic chaos: an introduction*. John Wiley & Sons, 2006.

VD Shafranov. Equilibrium of a toroidal plasma in a magnetic field. *Journal of Nuclear Energy. Part C, Plasma Physics, Accelerators, Thermonuclear Research*, 5(4):251, 1963.

T Shimozuma, S Kubo, H Idei, Y Yoshimura, T Notake, K Ida, N Ohyabu, I Yamada, K Narihara, S Inagaki, et al. Formation of electron internal transport barriers by highly localized electron cyclotron resonance heating in the large helical device. *Plasma physics and controlled fusion*, 45(7):1183, 2003.

Boris Shraiman, C Eugene Wayne, and Paul C Martin. Scaling theory for noisy period-doubling transitions to chaos. *Physical Review Letters*, 46(14):935, 1981.

PB Snyder, HR Wilson, JR Ferron, LL Lao, AW Leonard, TH Osborne, AD Turnbull, D Mossessian, M Murakami, and XQ Xu. Edge localized modes and the pedestal: A model based on coupled peeling–ballooning modes. *Physics of Plasmas (1994-present)*, 9(5):2037–2043, 2002.

GW Spakman, GMD Hogeweij, RJE Jaspers, E Westerhof, JE Boom, IGJ Classen, E Delabie, C Domier, M Yu Kantor, Y Liang, et al. Heat pulse propagation studies around magnetic islands induced by the dynamic ergodic divertor in textor. *Nuclear fusion*, 48(11):115005, 2008.

L Spitzer Jr. A proposed stellarator. Technical report, Princeton Univ., NJ Forrestal Research Center, 1951.

Lyman Spitzer Jr. The stellarator concept. *Physics of Fluids (1958-1988)*, 1(4): 253–264, 1958.

Lyman Spitzer Jr, DJ Grove, WE Johnson, L Tonks, and WF Westendorp. Problems of the stellarator as a useful power source. Technical report, Princeton Univ., NJ Project Matterhorn, 1954.

JC Sprott, JC Wildenberg, and Yousef Azizi. A simple spatiotemporal chaotic lotka–volterra model. *Chaos, Solitons & Fractals*, 26(4):1035–1043, 2005.

Steven H Strogatz. *Nonlinear dynamics and chaos: with applications to physics, biology, chemistry, and engineering*. Westview press, 2014.

Hong-Juan Sun, Xuan-Tong Ding, Liang-Hua Yao, Bei-Bin Feng, Ze-Tian Liu, Xu-Ru Duan, and Qing-Wei Yang. Experiment of non-local effect with smbi on hl-2a. *Plasma Physics and Controlled Fusion*, 52(4):045003, 2010.

W Suttrop, GD Conway, L Fattorini, LD Horton, T Kurki-Suonio, CF Maggi, M Maraschek, H Meister, R Neu, Th Pütterich, et al. Study of quiescent h-mode plasmas in asdex upgrade. *Plasma physics and controlled fusion*, 46(5A): A151, 2004.

W Suttrop, V Hynönen, T Kurki-Suonio, PT Lang, M Maraschek, R Neu, A Stäbler, GD Conway, S Hacquin, M Kempenaars, et al. Studies of the'quiescent h-mode'regime in asdex upgrade and jet. *Nuclear fusion*, 45(7):721, 2005.

Floris Takens. *Detecting strange attractors in turbulence*. Springer, 1981.

N Tamura, S Inagaki, K Tanaka, C Michael, T Tokuzawa, T Shimozuma, S Kubo, R Sakamoto, K Ida, K Itoh, et al. Impact of nonlocal electron heat transport on the high temperature plasmas of lhd. *Nuclear fusion*, 47(5):449, 2007.

A Tanga, DV Bartlett, and K Behringer. Experimental studies in jet with magnetic separatrix. In *Plasma physics and controlled nuclear fusion research 1986*. 1987a.

A Tanga, KH Behringer, AE Costley, M Brusati, B Denne, A Edwards, A Gibson, RD Gill, N Gottardi, R Granetz, et al. Magnetic separatrix experiments in jet. *Nuclear fusion*, 27(11):1877, 1987b.

JET Team et al. Fusion energy production from a deuterium-tritium plasma in the jet tokamak. *Nuclear Fusion*, 32(2):187, 1992.

Robert W Thatcher. A predator–prey model of human cerebral development. *Applications of nonlinear dynamics to developmental process modeling*, pages 87–128, 1998.

John Michael Tutill Thompson and H Bruce Stewart. *Nonlinear dynamics and chaos*. John Wiley & Sons, 2002.

K Toi, S Ohdachi, S Yamamoto, N Nakajima, S Sakakibara, KY Watanabe, S Inagaki, Y Nagayama, Y Narushima, H Yamada, et al. Mhd instabilities and their effects on plasma confinement in large helical device plasmas. *Nuclear fusion*, 44 (2):217, 2004.

S Tsuji, K Ushigusa, Y Ikeda, T Imai, T Itami, M Nemoto, K Nagashima, Y Koide, Y Kawano, T Fukuda, et al. Observation of the limiter h mode in the jt-60 tokamak with lower-hybrid current drive. *Physical review letters*, 64(9):1023, 1990.

BJD Tubbing, NJ Lopes Cardozo, and MJ Van der Wiel. Tokamak heat transport? a study of heat pulse propagation in jet. *Nuclear fusion*, 27(11):1843, 1987.

BJD Tubbing, B Balet, DV Bartlett, CD Challis, S Corti, RD Gill, C Gormezano, CW Gowers, M Von Hellermann, M Hugon, et al. H-mode confinement in jet with enhanced performance by pellet peaked density profiles. *Nuclear Fusion*, 31 (5):839, 1991.

Nicholas Tufillaro, Tyler Abbott, and Jeremiah Reilly. *An experimental approach to nonlinear dynamics and chaos*. Addison-Wesley Redwood City, CA, 1992.

GR Tynan, A Fujisawa, and G McKee. A review of experimental drift turbulence studies. *Plasma Physics and Controlled Fusion*, 51(11):113001, 2009.

Balth Van der Pol and J Van der Mark. Frequency demultiplication. *Nature*, 120: 363–364, 1927.

JA Vano, JC Wildenberg, MB Anderson, JK Noel, and JC Sprott. Chaos in low-dimensional lotka–volterra models of competition. *Nonlinearity*, 19(10):2391, 2006.

Vito Volterra. Fluctuations in the abundance of a species considered mathematically. *Nature*, 118:558–560, 1926.

F Wagner. A quarter-century of h-mode studies. *Plasma Physics and Controlled Fusion*, 49(12B):B1, 2007.

F Wagner, G Becker, K Behringer, D Campbell, A Eberhagen, W Engelhardt, G Fussmann, O Gehre, J Gernhardt, G v Gierke, et al. Regime of improved confinement and high beta in neutral-beam-heated divertor discharges of the asdex tokamak. *Physical Review Letters*, 49(19):1408, 1982.

F Wagner, G Fussmann, T Grave, M Keilhacker, M Kornherr, K Lackner, K McCormick, ER Müller, A Stäbler, G Becker, et al. Development of an edge transport barrier at the h-mode transition of asdex. *Physical review letters*, 53(15): 1453, 1984.

F Wagner, AR Field, G Fussmann, JV Hofmann, ME Manso, O Vollmer, and José Matias. Recent results of h-mode studies on asdex. 1990.

H Walter, U Stroth, J Bleuel, R Burhenn, T Geist, L Giannone, H Hartfuss, JPT Koponen, L Ledl, G Pereverzev, et al. Transient transport phenomena induced by cold pulses in w7-as. *Plasma physics and controlled fusion*, 40(9):1661, 1998.

L Wang, GS Xu, HY Guo, R Chen, S Ding, KF Gan, X Gao, XZ Gong, M Jiang, P Liu, et al. Particle and power deposition on divertor targets in east h-mode plasmas. *Nuclear Fusion*, 52(6):063024, 2012.

K Watanabe, N Nakajima, M Okamoto, Y Nakamura, and M Wakatani. Three-dimensional mhd equilibrium in the presence of bootstrap current for the large helical device. *Nuclear fusion*, 32(9):1499, 1992.

NW Watkins, SC Chapman, RO Dendy, and G Rowlands. Robustness of collective behaviour in strongly driven avalanche models: magnetospheric implications. *Geophysical research letters*, 26(16):2617–2620, 1999.

RD Watson and JB Whitley. Thermal fatigue tests of a prototype beryllium limiter for jet. *Nuclear Engineering and Design. Fusion*, 4(1):49–60, 1986.

John Wesson. *Tokamaks*, volume 149. Oxford University Press, 2011.

RC Wolf. Internal transport barriers in tokamak plasmas. *Plasma Physics and Controlled Fusion*, 45(1):R1, 2003.

GS Xu, HQ Wang, BN Wan, HY Guo, Volker Naulin, PH Diamond, GR Tynan, M Xu, Ning Yan, W Zhang, et al. First observation of a new zonal-flow cycle state in the h-mode transport barrier of the experimental advanced superconducting tokamak. *Physics of Plasmas (1994-present)*, 19(12):122502, 2012a.

M Xu, GR Tynan, PH Diamond, P Manz, C Holland, N Fedorczak, S Chakraborty Thakur, JH Yu, KJ Zhao, JQ Dong, et al. Frequency-resolved nonlinear turbulent energy transfer into zonal flows in strongly heated l-mode plasmas in the hl-2a tokamak. *Physical review letters*, 108(24):245001, 2012b.

H Yamada, KY Watanabe, S Sakakibara, S Murakami, M Osakabe, O Kaneko, K Narihara, K Tanaka, K Ida, T Minami, et al. Energy confinement time and heat transport in initial neutral beam heated plasmas on the large helical device. *Physical review letters*, 84(6):1216, 2000.

H Yamada, KY Watanabe, K Yamazaki, S Murakami, S Sakakibara, K Narihara, K Tanaka, M Osakabe, K Ida, N Ashikawa, et al. Energy confinement and thermal transport characteristics of net current free plasmas in the large helical device. *Nuclear fusion*, 41(7):901, 2001.

Takuma Yamada, Sanae-I Itoh, Takashi Maruta, Naohiro Kasuya, Yoshihiko Nagashima, Shunjiro Shinohara, Kenichiro Terasaka, Masatoshi Yagi, Shigeru Ina-

gaki, Yoshinobu Kawai, et al. Anatomy of plasma turbulence. *Nature Physics*, 4 (9):721–725, 2008.

Takehito Yoshida, Laura E Jones, Stephen P Ellner, Gregor F Fussmann, and Nelson G Hairston. Rapid evolution drives ecological dynamics in a predator–prey system. *Nature*, 424(6946):303–306, 2003.

Akira Yoshizawa, Sanae I Itoh, and Kimitaka Itoh. *Plasma and Fluid Turbulence: Theory and Modelling*. CRC Press, 2002.

GS Yun, Woochang Lee, MJ Choi, J Lee, HK Park, B Tobias, CW Domier, NC Luhmann Jr, AJH Donné, JH Lee, et al. Two-dimensional visualization of growth and burst of the edge-localized filaments in kstar h-mode plasmas. *Physical review letters*, 107(4):045004, 2011.

PN Yushmanov, T Takizuka, KS Riedel, OJWF Kardaun, JG Cordey, SM Kaye, and DE Post. Scalings for tokamak energy confinement. *Nuclear Fusion*, 30(10): 1999, 1990.

T Zhang, X Gao, SB Zhang, YM Wang, X Han, ZX Liu, BL Ling, EAST Team, et al. Characteristics of dithering cycles during the l–i–h transition on experimental advanced superconducting tokamak (east). *Physics Letters A*, 377(28):1725–1735, 2013.

KJ Zhao, T Lan, JQ Dong, LW Yan, WY Hong, CX Yu, AD Liu, J Qian, J Cheng, DL Yu, et al. Toroidal symmetry of the geodesic acoustic mode zonal flow in a tokamak plasma. *Physical review letters*, 96(25):255004, 2006.

Hao Zhu, Sandra C Chapman, and RO Dendy. Robustness of predator-prey models for confinement regime transitions in fusionplasmas. *Physics of Plasmas (1994-present)*, 20(4):042302, 2013.

Hao Zhu, Sandra C Chapman, RO Dendy, and Kimitaka Itoh. Transitions to improved confinement regimes induced by changes in heating in zero-dimensional models for tokamak plasmas. *Physics of Plasmas (1994-present)*, 21(6):062307, 2014.

Hao Zhu, RO Dendy, Sandra C Chapman, and Shigeru Inagaki. A quantitative model for heat pulse propagation across large helical device plasmas(submitted). *Physics of Plasmas (1994-present)*, 00(0):000–000, 2015.

H Zohm. Edge localized modes (elms). *Plasma Physics and Controlled Fusion*, 38 (2):105, 1996.